# OPTICAL CAVITY SOLITON AND ITS DYNAMICS

**A thesis submitted in fulfillment**
**of the requirement for the award of the degree of**

**DOCTOR OF PHILOSOPHY**


Submitted by

**BALDEEP KAUR**
**Registration No.: 901212001**

Under the Supervision of
**Dr. Soumendu Jana**
**Associate Professor**


Submitted to


**School of Physics and Materials Science**
**Thapar University, Patiala-147004, Punjab, India**


**July 2017**

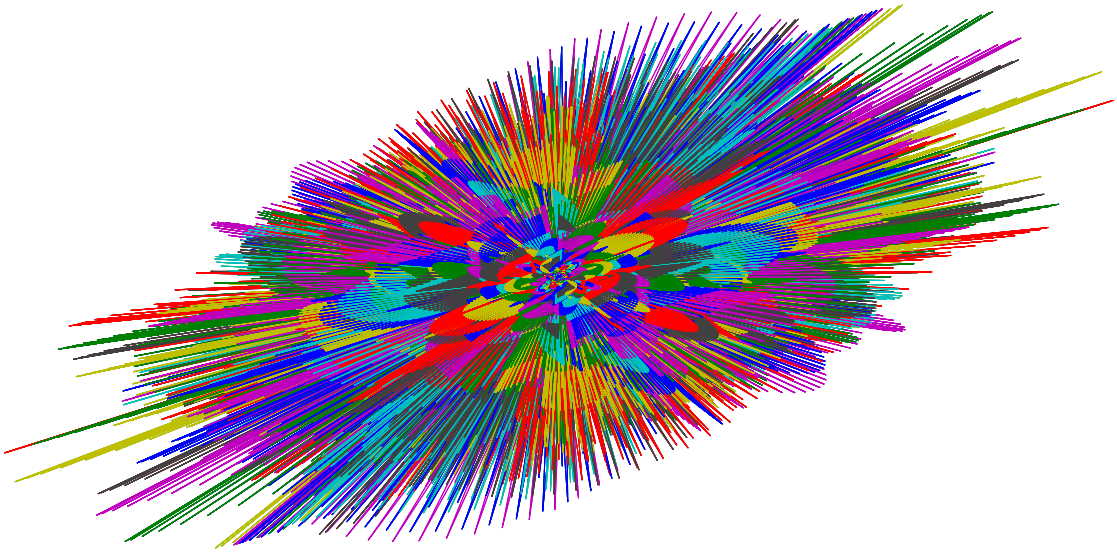

The world is not only nonlinear but changing as well.

## THESIS CERTIFICATION

I, Baldeep Kaur, declare that the work presented in this thesis report entitled, **"OPTICAL CAVITY SOLITON AND ITS DYNAMICS"** submitted in fulfillment of requirement for the award of degree of Doctor of Philosophy in the School of Physics and Materials Science, Thapar University Patiala, is an authentic record of my own work carried out under the supervision of Dr. Soumendu Jana (Associate Professor, School of Physics and Materials Science, Thapar University, Patiala) from July 2012 to July 2017. The matter presented in this thesis has not been submitted either in part or full to any other University or Institute for the award of any other degree.

Baldeep kaur

Baldeep Kaur — Date: July 31, 2017

Registration No. - 901212001

It is certified that the above statement made by the student is correct to the best of my knowledge and belief.

Soumendu Jana

Dr. Soumendu Jana — Date: July 31, 2017

Associate Professor,

School of Physics and Materials Science,

Thapar University, Patiala.

*I affectionately dedicate this thesis to*

*my loving parents*

*for their unconditional love, support and encouragement.*

# ACKNOWLEDGMENTS

I owe my deepest gratitude to my Ph.D. supervisor Dr. Soumendu Jana for his guidance, support and encouragement to discover the new ventures and horizons in research. I would also like to thank him for his patience, motivation and enthusiasm during the entire tenure of my research work with him. He has been always supportive and understanding.

I am thankful to my teacher Mr. Sarabdeep Singh for developing my interest in the subject of mathematics.

I am grateful to the Dr. Soumya Mallick, Dr. Anu Mittal and Mr. Atul Sharma, Particle and Bulk Solids Laboratory, Department of Mechanical Engineering, Thapar University for always being supportive and helpful. I humbly acknowledge Dr. Rehnu Pan, Vice General Manager, Fujian Longking Co., Ltd., China for his collaboration.

I am also thankful to Prof. Peter Wypych, Professor, University of Wollongong, Australia for his valuable support and mentorship.

I appreciate time to time feedbacks offered by Dr. B.C. Mohanty and Dr. B.N. Chudasama, Associate Professors, School of Physics and Materials Science, Thapar University, during the tenure of my research work.

I would like to thank my past and present colleagues, Navjot Kaur, Gurkirpal Singh Parmar, Neeraj Sharma, Arshdeep Kaur, Jaspreet Kaur and Deepakshi Kalyan for making my time at the campus enjoyable and successful.

I am grateful to my siblings, Arpandeep Kaur, Hunardeep Singh and Gurmanav Singh, who have provided me moral and emotional support in my life.

I am also grateful to my friend and fiancé Dr. Jagjit Singh for being always supportive and encouraging.

I acknowledge the financial support from University Grants Commission, Government of India through UGC-BSR Research Fellowships in Sciences (F.4-1/2006(BSR)/7-304/2010(BSR)) and UGC-BSR Research start up grant, ([No. F. 20-1/2012 (BSR)/20-13 (12)/2012(BSR)], PI- Dr. S. Jana) to pursue the research work. I would like to acknowledge the financial support from International Centre for Theoretical Physics for attending 'Spring College on the Physics of Complex Systems'.

I would like to offer my special thanks to Thapar University, Patiala, for providing

me such an amicable atmosphere to learn and perform my research.

Above all I render my gratitude to the Almighty who bestowed upon me the strength and vision to walk on the path of truth.

July 31, 2017 Baldeep Kaur

# Publications and Conference Presentations

## SCI Journals

- **Baldeep Kaur** and Soumendu Jana, "Generation and dynamics of one- and two- dimensional cavity soliton in VCSEL with saturable absorber and frequency-selective feedback", *Journal of Optical Society of America B* **34** 1374-1385 (2017).

- **Baldeep Kaur**, Soumendu Jana, Qin Zhou, Anjan Biswas, Milivoj Belic, "Bright and Exotic Solitons in Laser Cavity with Frequency Selective Feedback", *Journal of Optoelectronics and Advanced Materials*, **18** (5-6), 428-434 (2016).

- Soumendu Jana, Shivani, Gurkirpal Singh Parmar, **Baldeep Kaur**, Qin Zhou, Anjan Biswas, Milivoj Belic, "Evolution of Bell-shaped Dissipative Optical Solitons from super-Gaussian Pulse in Parabolic Law Medium with Bandwidth Limited Amplification", *Optoelectronics and Advanced Materials – Rapid Communications*, **10** (3-4), 143-150 (2016).

- **Baldeep Kaur** and Soumendu Jana, "A Generic Travelling Wave Solution in Dissipative Laser Cavity", *Pramana – Journal of Physics*, **87**, 53 (1-12) (2016).

- **Baldeep Kaur**, Anu Mittal, S.S. Mallick, Renhu Pan and Soumendu Jana, "Numerical Simulation of Fluidized Dense-Phase Pneumatic Conveying of Powders towards Developing Improved Model for Solids Friction Factor", *Particuology* (in press).

- **Baldeep Kaur**, Anu Mittal, Peter Wypych, S.S. Mallick and Soumendu Jana, "On Developing Improved Modelling and Scale-up Procedures for Pneumatic Conveying of Fine Powders", *Powder Technology*, **305**, 270-278 (2017).

- **Baldeep Kaur** and Soumendu Jana, "Cavity Soliton Molecules and All-Optical Push-broom Effect". (Communicated)

- Vichitra Monga, **Baldeep Kaur** and Soumendu Jana, "Pattern and Cavity Solitons inside the Dissipative Cavity". (to be communicated)

- **Baldeep Kaur**, Anu Mittal, Soumendu Jana, S.S. Mallick and Peter Wypych, "Stability and Phase Space Analysis of Fluidized-Dense Phase Pneumatic Transport System". (under review)

## Conference Papers

- **Baldeep Kaur** and Soumendu Jana, "Homonuclear Cavity Soliton Molecules and All-optical Push-Broom", 13th International Conference on Fiber Optics and Photonics, Tu4A.39 (2016).
  (doi: https://doi.org/10.1364/PHOTONICS.2016.Tu4A.39).

- **Baldeep Kaur** and Soumendu Jana, "Cavity Soliton Dynamics in VCSEL", 13th International Conference on Fiber Optics and Photonics, Tu4A.40 (2016).
  (doi: https://doi.org/10.1364/PHOTONICS.2016.Tu4A.40).

- **Baldeep Kaur**, Anu Mittal, Peter Wypych, S.S. Mallick and Soumendu Jana, "Numerical Investigation of Particle Velocity and its Influence on Modelling Solids Friction for Fluidized Dense-Phase Pneumatic Conveying Systems", PGBSIA-2016, Jaipur, Rajasthan, India (2016).

- Kapil Sharma and **Baldeep Kaur**, "Development of Improved System Design for Dense-phase Pneumatic Conveying of Fly Ash", NTPC Global Energy Technology Summit 2016, Noida, India (2016).

- **Baldeep Kaur** and Soumendu Jana, "Generation of Stable Cavity Soliton in Vertical Cavity Surface Emitting Laser: a Variational Approach", Workshop on Recent Advances in Photonics (WRAP), 1-3 (2015).
  (doi: 10.1109/WRAP.2015.7805971)

- **Baldeep Kaur** and Soumendu Jana, "Cosh-Gaussian Solitary Wave Solution in Dissipative Laser Cavity", Conference on Nonlinear Systems and Dynamics (CNSD 2015), IISER Mohali, Punjab, India (2015).

- **Baldeep Kaur** and Soumendu Jana, "Cavity Soliton in VCSEL with Frequency Selective Feedback", WRAP2013, IIT Delhi, New Delhi, India (2013).

# ABSTRACT

This thesis presents a theoretical study of generation and dynamics of cavity solitons in microcavities. We consider a wide area semiconductor cavity system that comprised of a vertical-cavity surface-emitting laser coupled with frequency-selective feedback. Three different cavity nonlinearities; cubic, cubic-quintic and saturating nonlinearities are considered.

Cavity solitons are found in vertical-cavity surface-emitting laser with cubic and cubic-quintic nonlinearity by using variational method. The analytical cavity soliton solutions are validated by numerical split-step Fourier method. Spontaneous fission and subsequent generation of cavity soliton molecules, fusion and annihilation of cavity solitons are observed in the cavity with saturating absorber and frequency-selective feedback. The parametric space for generation of fronts, $\cap$-shaped and flat-top soliton solutions are identified. An alternate approach to generate cavity soliton is formulated by using standing wave method. This approach is shown capable for generation of a large variety of cavity solitons of different profile, ellipticity and power.

A comprehensive stability analysis is done for different cavity soliton systems. Trivial and non-trivial homogeneous steady states of cavity soliton are obtained. Stable, Hopf instable and unstable regions of cavity solitons are marked. Using Lyapunov exponents method in conjugation with Hurwitz's criteria the stability regions are identified for both one and two dimensional cavity solitons. The skill of stability analysis is successfully extended to beyond optics. Stable zones for mechanical and biological systems are identified.

The dynamics of cavity soliton is studied extensively to identify the effect of system parameters, such as, feedback strength, saturation, resonant frequency and amplitude on the dynamics as well as to explore novel phenomena. An intriguing all-optical 'push-broom' effect is demonstrated. The control on 'push-broom' effect by tuning system parameters is shown.

The generated cavity soliton has potential application in all-optical selectively erasable memory and data processing. The wide stability regions identified in this thesis may be of significant benefit to the experimental observation of cavity soliton. The push broom may lead to a novel soliton force microscopy.

# Table of Contents

# List of Figures

# Chapter 1

## Introduction

## 1.1 What is Cavity Soliton?

Cavity solitons (CSs) are localized structure inside dissipative broad area cavity [1, 2, 3, 4]. They can be visualized as bright spots on the homogeneous dark or gray background on the transverse plane of the cavity. CSs belong to a special class of optical dissipative solitons (ODS) [1]. Optical solitons are self-trapped beams (spatial solitons) or pulses (temporal solitons) that preserve their shape during propagation and even after collision with other solitons [2, 5, 6]. These spatial (temporal) solitons are the result of two counteracting phenomena: broadening due to self-diffraction (group velocity dispersion) and contraction owing to the nonlinearity induced self-focusing (self-phase modulation) [2, 7]. These are the manifestation of intensity dependent refractive index [6]. When an intense beam, usually a laser beam propagates through a medium, it gets diffracted due to small cross-section of the beam itself. This self-diffraction causes the beam to broaden. The high intensity beam creates a nonlinear refractive index profile similar to its own intensity profile, for example, Gaussian or sech profile [6]. Since due to its own intensity-induced refractive index profile the beam gets focused, this is referred to as self-focusing. Now, when the self-diffraction induced broadening is equalized by the self-focusing induced compression, we get a self-trapped

beam or spatial soliton, which is confined in space domain.

In a conservative system, this one-fold balance is enough to get a spatial soliton, but in practical systems which are lossy or dissipative, solitons can be generated by applying a proper dose of gain. Optical solitons generated in such 'dissipative system' (a name coined by Prigogine [8]) is referred to as optical dissipative soliton (ODS) [1]. CSs belong to a special class of ODS. The exponential localization, optical bistability and freedom of location in the plane of transverse to the cavity axis make them unique in the ODS family [9, 10, 11]. Generally, CSs are hosted by broad area semiconductor cavity, such as, vertical-cavity surface-emitting laser (VCSEL) [1]. The gain is provided by holding beam [1]; or, frequency-selective feedback (FSF) [4, 9, 12, 13] and/or saturable absorber (SA) [1, 3, 14, 15]) to compensate the loss incurred in the system [1]. The delicate balance between the gain and loss gives rise to the discrete stationary solution points for CS [16].

Recently, CS attracted a significant attention due to its application as 'future bits of light', versatility in orientation and intriguing dynamics. Although the mathematical formulation as well as experimental verification of CS is somewhat difficult, the CS dynamics is very important to realize all-optical tools. For a fixed set of system parameters, the amplitude, width and shape of CS remains unaltered. Once created, the CSs can retain their shape and size for an infinite period of time unless the power is switched off [11]. CS can be erased or drifted individually. They can be written and erased by the same addressing pulse, thus making them suitable for all-optical erasable memory and data processing applications [1, 17]. The introduction of suitable gradients in the semiconductor cavity can change the location and drift velocity of the CS. Such property of CS can be applied to mapping techniques of the surface as well as

volume defects of micro-scale semiconductor devices [1]. The all-optical control of CS along any desired direction multiplies its importance for diverse applications [1, 11].

## 1.2 Journey from 'Wave of Translation' to Cavity Soliton

Solitary waves and solitons is an important subject of theoretical as well as experimental studies in a wide variety of fields, e.g., hydrodynamics [18], nonlinear optics [19, 20, 21], plasma [22], biology [23, 24], chemistry [25], fluid dynamics [26]. The history of soliton started long ago, back in the year 1834. A Scottish engineer, Sir James Scott Russell, while doing work in the Union canal in Glasgow- Edinburgh observed a heap of water moving along the front of bow of the boat. It continued to move with same speed even when the boat was stopped. The heap of water traveled robustly without any distortion in its shape and speed and thereafter diminished gradually. After investigation for a decade, Sir James Scott Russell named such waves as the 'wave of translation' [27]. Such waves were later named as solitary waves. Its properties were explored more comprehensively only after the introduction of suitable mathematical models (Korteweg De-Vries equation) and inverse scattering method (ISM) that was developed in 1960's [28].

Optical solitons and many other nonlinear optical phenomena came into the picture only after the invention of the laser by Maiman in the 1960's [29]. Infact, optical solitons are one of the most important consequence of nonlinear optics. Soon after the invention of laser, the second harmonic generation, the first ever observation of any nonlinear effects was made possible in 1961 by Franken *et al.* [30]. In 1962,

Terhune *et al.* demonstrated the third harmonic generation [31]. In the same year, the stimulated Raman scattering was performed by Woodbury *et al.* [32]. Also in 1962, Armstrong *et al.* formulated the general permutation symmetry relations in nonlinear optics. The amplitude of sum of components of frequency in harmonic generation were explained using appropriate permutation relations in nonlinear optics [33]. A flood gate of nonlinear optical phenomenon was opened by this time that lead to the realization of soliton. Zabusky and Kruskal coined the term 'soliton' to reflect the particle like nature of solitary waves [22]. In 1972, Zakharov and Shabat gave the exact solution of Nonlinear Schrödinger equation (NLSE) using ISM to describe the interaction of solitons [34]. In 1973, Hasegawa and Tappert showed that the propagation of solitons inside the optical fibers is governed by NLSE [19] and subsequently predicted the formation of bright and dark solitons.

In 1976, Gibbs *et al.* demonstrated the optical bistability using sodium-vapor filled Fabry-Perot interferometer [35]. In 1980, the theoretical prediction of solitons in Fabry-Perot interferometer was given by Rozanov *et al.* [36], followed by numerical support from Mclaughlin *et al.*, who analyzed the coherent spatial structures in nonlinear systems of finite dimensions exhibiting chaotic dynamics [37]. In 1980, Mollenauer *et al.* observed the 'self-maintaining structures' or the bright solitons for the first time in optical fibers [38]. They also concluded that the higher order nonlinearity exhibits 'self-maintaining' of pulse shape that leads to periodic solutions during the evolution. The theoretical concept of bistability by Lugiato [39] and Gibbs [40] provided the stronghold to the theory of solitons in the optical systems. In late 1980's and early 1990's, Rozanov, Khodova and Fedorov gave the theoretical concept of 'autosolitons'- a transverse field structures excited by coherent external radiation in nonlinear in-

terferometers [41, 42, 43]. During the this period, the experimental realization of spatio-temporal effects and optical switching was reported in single and multi-mode cavities with saturation absorption using bacteriorhodopsin [44]. Kreuzer *et al.* studied the transverse effects in optically bistable elements, such as, nematic liquid crystals [45]. Neubecker *et al.* compared the theoretical and experimental formation of bright localized structures in Kerr nonlinear medium [46]. With the advent of the theoretical, numerical and experimental techniques of optical solitons, the research on ODSs started to flourish.

The research on cavity soliton was initiated primarily through the work of Moloney [37], Rozanov and their co-workers [36, 41, 42, 43]. Gradually, it achieved good pace and significant amount of work have been done as of today. Rozanov *et al.* significantly contributed towards the theoretical prediction of dissipative optical localized structures in a laser cavity with saturable absorber [36, 41, 47, 48, 49, 50]. Extensive investigation on CS was undertaken by several groups, such, Lugiato, Prati, Tissoni *et al.* [51, 52], Ackemann, Firth, and Oppo [1]. The theoretical concept and the corresponding numerical evidence of cavity soliton laser (CSL) in VCSEL with SA (VCSEL-SA) was studied by Bache *et al.* [14]. Tanguy *et al.* realized the semiconductor based CSL by using frequency selective feedback [53]. Pedaci *et al.* gave the idea of cavity soliton based all-optical delay line [54] and theoretical characterization of prerequisites for CS light bullets [55, 56].

## 1.3 Recent works on Cavity Solitons

The pioneer work in the field of spatial dissipative solitons, and CS stated in the preceding section, paved the way for the more advanced theoretical and experimen-

tal investigations with different configurations of systems. In the current section we summarize the work on CS. Paulav *et al.* demonstrated the motion of CS in VCSEL coupled with FSF (VCSEL-FSF) and studied the changes in the stability behavior of the system due to the induced time delay [57]. In the same year Tlidi *et al.* reported the spontaneous motion of CS in the system considering the time delay in the feedback [58, 59], Caboche *et al.* experimentally proved that the presence of defects in the micro-resonator cavity significantly affects the positioning and drifting of CS [60, 61]. Scroggie *et al.* gave the theoretical concept of traveling wave modes and generation of single frequency solitons in CSL [12]. Genevet *et al.* demonstrated pulsating localized structures in CSL [62]. Prati *et al.* reported the spontaneous motion of CS in a CSL with SA and presented the concept of optical clocks in the CSL with circular cross-section [63]. The theoretical evidence of all-optical delay line in the systems with optical injection was given by McIntyre *et al.* [64]. Experimental demonstration of CS in two face-to-face coupled VCSELs at single longitudinal mode frequency was reported by Genevet *et al.* [65]. The subsequent years witnessed the experimental and theoretical evidence of multistable monochromatic CS in cavity [66]. Firth *et al.* showed the existence and stability of fundamental and vortical solitons in two dimensional system comprising of VCSEL coupled with an external feedback without delay [67]. The 'cavity soliton billards', i.e., spontaneous motion and reflection of CS in the cavity in the closed orbits was demonstrated through numerical simulations by Prati *et al.* [68]. In the next year, Ackeman *et al.* reported the mapping of disorder in VCSEL through CS [69]. In 2013, spontaneous motion of discrete CS has been reported [70]. In 2014, Vladimirov *et al.* experimentally showed the creation and annihilation of CS in VCSEL and the theoretical evidence of spontaneous motion of CS due to time

delayed feedback [71]. Theoretical evidence of formation, motion and interaction of twin cavity solitons in a VCSEL with SA above the energy required for the excitation of single soliton/CS was also reported [15].

The cavity soliton research can be categorized into different sub groups depending on the scheme [1], nature of cavity [72, 73, 74, 75, 76] and condition of operation [14, 77]. As far as the schemes are concerned (which seems to be the most appropriate categorization), three basic schemes attracted significant interest: (1) cavity soliton using injected beam [77], (2) cavity soliton using saturable absorber [14, 47, 78] and (3) cavity soliton with frequency selective feedback [12]. Apart from these three schemes, a fourth scheme consisting of cell with sodium vapour in the magnetic field and feedback mirror was reported to be used for generating the localized structures; however, it is magneto-optic in nature [79, 80].

Initially, the most commonly used scheme was a nonlinear cavity or optical feedback system driven by an external writing beam of high temporal and spatial coherence, and sustained by holding beam. F. Prati *et al.* theoretically as well as experimentally demonstrated the existence of the CSs in the externally driven VCSEL [77]. It was observed that the CSs can be created and annihilated with the same external writing beam, but with opposite phase [81]. For the application point of view, to get self-sustained emission and to make the CSL more simple, there was a need to eliminate the holding beam. However, but in order to sustain excitations in the lossy cavity, there was a need to replace it; therefore work began on new self-sustained schemes in which the holding beam was replaced with the feedback system inside the cavity or using coupled cavity, i.e., coupling the main cavity with the external cavity. Such self-sustained systems lead to the generation of CSL [12, 14]. Therefore, newer schemes,

i.e., CSL with FSF [12] and CSL with SA [14] were devised.

The main advantage of using FSF is to eliminate the requirement of the holding beam, thus making the system more compact. Also, by controlling the feedback strength, one can get a large region of the stable CS and CS cluster. Another prime advantage for the modeling of the CSL with FSF is to sustain excitations in lossy cavity. CSs in self-sustained systems are slaved as their phase, frequency and polarization are dependent on the feedback fed back to the system. Self-driven systems, such as, CSLs originate due to the spontaneous symmetry breaking, therefore it gets freedom to choose its own phase. Coherently self-driven systems are sustained by beam of high temporal and spatial coherence. Thus, the system behaves as a laser with self-sustained emission. Subsequently, in FSF systems the diffraction grating was replaced with Volume Bragg grating (VBG). The advantage of using VBG as FSF element is due to the single frequency soliton generation and frequency stabilization in semiconductor lasers [4]. There is a pure mathematical advantage of using FSF. With the help of separation method, the soliton solutions can be obtained by analytical-graphical approach [81]. The use of FSF, instead of common feedback, helps in achieving single to multiple CS solution points.

Spatial dissipative solitons (SDSs) cannot be generated in a simple free running lasers, because it undergoes the supercritical bifurcation at laser threshold. Hence, free running lasers cannot support optical bistability. In order to sustain optical bistability, the laser should undergo subcritical bifurcation. The presence of SA results in the co-existence of lasing as well as non-lasing solutions in the certain range of pump power. Thus the system exhibits bistability and undergoes subcritical bifurcation. Laser with SA configuration helps in attaining bistability in the system. In such configurations,

the contrast between the CSs and homogeneous cavity background becomes maximum due to pure spontaneous emissions [82]. Elimination of the holding beam makes the CSL with SA more robust and simpler [12]. In such systems, the properties of emitted laser beam depends on radiation-matter interactions, hence, introduces additional thermal losses. Therefore, additional losses arise in the system with SA [14]. In a nutshell, the advantage of using SA or FSF is to create simpler, compact, robust and self-sustaining system, however, but with some limitations [14, 83].

CSs are found with different cavity nonlinearities. Primely, Kerr cavity attracted considerable attention [72, 73, 74, 75, 76, 84]. Thereafter, cubic-quintic nonlinearity was considered [85]. Significant thrust was given on saturable nonlinearity [3, 15, 47, 48, 82].

The generation of CS above and below laser threshold conditions is studied and reported in [77, 86, 87, 88]. It was observed that more than one CS can co-exist in the system. Hence, this may lead to cluster formation [89], thus, leading to two very important studies: the pattern formation and dynamics of the CS cluster [72, 84]. The drift and collision of CSs are interesting as their dynamics can be successfully utilized to fabricate all-optical devices, e.g., optical delay line [64, 90], all-optical push broom [91] etc. A huge potential is foreseen in this direction.

The nonlinear dynamics of CS stated above continuously remained in the focus of research interest during the last two decades. From dynamical point of view, cavity solitons are localized structure that occurs far from equilibrium and arise in the weak dispersive limit. CSs occur in a region where monostable homogeneous steady state shows subcritical Turing instability. In this context, the nature of bifurcation exhibited by the nonlinear dynamical system is an essential characteristic to understand the CS

dynamics. Another generic feature of CS is the homoclinic snaking, which is studied extensively [1, 92, 93, 94, 95].

These interesting features of cavity soliton made them a suitable candidate for several potential applications. One important application is the fabrication of all-optical memory device, which could be erasable [72, 96, 97, 98]. CSs may be used in development of three level logic system with three distinct states: high, low and off state. There is a possibility of CS based optically addressable displays and memories. CSs are stationary structures in the cavity. The presence of inhomogeneity or gradient in the background can induce a drift of CS. CS continues to move until it reaches another equilibrium point or the gradient vanishes. This property of CS is known as plasticity. It makes CS suitable for processing applications including drift and buffer registers and as amplifiers [52]. The drifting of CS can be used to make all-optical delay lines [64]. A new concept of microscopy, named as soliton force microscopy can be realized using cavity solitons [1].

## 1.4 Gaps and Motivation

Although significant theoretical and experimental investigation are reported on CS using VCSEL-SA and VCSEL-FSF, still these models require further investigation in terms of existence of newer CS cluster or alternate methodology of solving. Also, these models have certain limitations. Generally, a VCSEL based system coupled with feedback lacks bistability, which is essential for CS. Now, SA can provide the bistability, but at the cost of increased losses in the system. Since, introduction of FSF can compensate the loss, the combined model (i.e., VCSEL-SA-FSF) has potential to overcome the drawbacks of individual model. However, this combined VCSEL-SA-

FSF model is not explored thoroughly. This leaves an open space for further research towards better modeling as well as exploring novel phenomena. Although different CS clusters are observed. Still there is huge scope for generation of different kind of bound structures or CS molecules. The gradient induced as well as interaction dynamics of CSs in self-sustained systems have enormous potential for novel futuristic applications. The study of the CS would not be complete without addressing these dynamics and interaction. This domain needs further attention. In fact, the CS dynamics available in the literature seems to be only the peak of the iceberg.

Above and beyond the excitation and dynamics, the stability is also an important issue. In many cases, stability can be achieved along only one dimension transverse to the cavity axis. However, a few investigations are reported to stabilize CSs in higher dimensions, i.e., in $(2+1)D$. Other fascinating aspect, like, bistability and multistability of CS are worthy for more research attention.

In view of these gaps in existing state of knowledge of the field and scopes of further research, we propose to investigate the generation and dynamics of the CS in VCSEL based microcavities.

## 1.5 Objectives

Main objectives of this thesis are:

- To explore and establish the existence and stability criteria of cavity soliton and their cluster in micro cavities.
- To study the dynamics of cavity soliton in micro cavities.

## 1.6 Outline of the thesis

**Chapter 1**, i.e., the current chapter, gives general introduction of solitons, DS and CS. The importance of CS in photonics is discussed. The theoretical, numerical and experimental evolution of the solitons, DS and CS are discussed, highlighting the contribution of the eminent researchers in this field. The motivation, objective and the layout of the thesis concludes the chapter.

**Chapter 2**: To understand the CS theory, knowledge of some basic nonlinear phenomena and devices are in order. This chapter gives the introduction of different types of nonlinearities, conservative and dissipative solitons, the generation mechanism of CS and different feedback mechanisms. Mathematical model that present the CS theory is discussed. Analytical (Variational method and He's Variational method) as well as numerical (split-step Fourier method) to solve CS - governing equations are presented. Tools for the stability analysis concludes this chapter.

The subsequent chapters in thesis present our results of investigation on CS generation and dynamics in VCSEL based models exhibiting cubic-quintic and saturating nonlinearity.

**Chapter 3** presents the generation and stability of CSs in VCSEL with higher order (cubic-quintic) nonlinearity and coupled with FSF. The dynamical governing equations of the system (i.e., Complex Ginzburg Landau equation (CGLE)) is solved to find the stable of trivial and non-trivial homogeneous steady state solutions. The dependence of reference frequency, pump power, field intensity and carrier density for the active and passive medium on the feedback strength are studied. In another approach, CS in VCSEL-FSF with cubic and cubic-quintic nonlinearity are studied

first ever using Variational method. The dynamics of CS amplitude, inverse width and wave front chirp is explored. The stability conditions for both the systems are established using the Lyapunov exponents method along with Hurwitzs criteria. The analytical results are validated by the numerical integration of the CGLE with SSFM.

**Chapter 4** presents the generation of CSs in the combined model, i.e., VCSEL-SA-FSF. Such systems exhibit the spontaneous splitting of the input pulse, thus, leading to the occurrence of phenomenon, such as, spontaneous fission, fusion and annihilation of the CSs inside the laser cavity. Generation of CS molecules with newer CS cluster and CS-atoms are demonstrated. Formation of different types of soliton solution, such as, flat-top, $\cap$-shaped solitons and fronts are explored.

**Chapter 5** is dedicated to the investigation on CS dynamics. The phase dependent dynamics is explored in the VCSEL-FSF exhibiting cubic-quintic nonlinearity. The variation in the velocity is studied with respect to the relative phase introduced between the co-propagating CSs. The dynamics of in-phase and out-of-phase CSs and the corresponding phase variation is studied. Also, the spontaneous CS dynamics is explored in VCSEL-SA-FSF. For a certain range of the feedback strength, the spontaneous motion of CSs exhibit a novel phenomenon, namely, all-optical push-broom effect. The variation in the CS velocity with changing feedback strength have been presented.

**Chapter 6** provides an alternate way to generate CS through creating stationary wave by using TW soliton solutions (TWSS). He's method is used to find the TWSSs in the system exhibiting the Kerr or cubic nonlinearity. The stability of the system is established using linear stability analysis with plane wave solutions. Two types of soliton solutions for the system are explored using the sech and cosh-Gaussian ansatz.

Superposition of forward and backward TW creates different standing wave localized structure (SWLS) and subsequently, CS in the dissipative cavity. Such SWLS for various tilt angles and mirror absorption are presented.

**Chapter 7** The stability analysis mechanism used in studying CS dynamics has versatile applications. This skill of stability analysis is extended to study the multi-phase flow dynamics and cancer cell growth dynamics. These are presented in this chapter. In the first section, the stability conditions of gas-solids flow dynamics are presented. Linear stability analysis using the method of Lyapunov's exponents along with the Hurwitz criteria are used. In the second section, another application of the stability analysis is extended to study population dynamics of cancer cells growth. Stability in the absence and presence of immunity cells and at different dosages of drug is shown. The effect of time delay on the growth dynamics is also studied.

**Chapter 8** concludes the thesis. The potential application of the findings is discussed along with the future scope of the work. The CSs presented in this thesis can be used in all-optical memories, delay lines, whereas their dynamics have huge potential applications, such as, relocation in optical memories, mapping the defects in optical, semiconductor materials in micro-devices, optical clocks and soliton-force microscopy.

# Chapter 2

## Essentials of Cavity Solitons

Evolution of CS owes to nonlinearity induced phenomenon, complex mathematical modeling and their solutions. In this chapter, the nonlinearities, fundamentals and generation mechanism of CS and feedback mechanism are discussed. Mathematical modeling, analytical as well as numerical solution methods are portrayed. Stability analysis techniques and bifurcation are also discussed.

## 2.1 Optical Nonlinearity

Nonlinearity is an essential ingredient to study numerous natural phenomenon and so as the nonlinear optics. When a highly intense laser beam interacts with matter, the polarization no longer remains linearly dependent on the field intensity. The nonlinear dependence of polarization can be represented as follows [99]:

$$\vec{P} = (\chi^{(1)} + \chi^{(2)}E + \chi^{(3)}E^2 + \cdots)E, \tag{2.1}$$

and,

$$\chi = \chi(E) \tag{2.2}$$

where, $\chi^{(n)}$ represents the $n^{th}$ order susceptibility. The nonlinear susceptibility leads to the nonlinear refractive index ($n = \sqrt{1+\chi}$) and the resultant nonlinear phenomenon.

CSs are found with different cavity nonlinearities. Initially, Kerr nonlinear cavity attracted considerable attention [67, 72, 73, 74, 75, 100, 101, 102, 103].

### 2.1.1 Kerr Nonlinearity

The simplest form of the optical nonlinearity is represented by Kerr nonlinearity or cubic nonlinearity. This is a third order nonlinearity (due to $\chi^{(3)}$). The nonlinearity function for the this kind can be written in the following intensity dependent form:

$$n(I) = n_0 + n_2 I \tag{2.3}$$

where, $I$ is the intensity of the light. $n_2$ is the optical Kerr coefficient that assumes positive value. Semiconductors doped glass, crystals (for example, GaAs, $TiO_2$, diamond), doped glasses, polymers and organic liquids exhibit third order nonlinearity.

### 2.1.2 Competing and Cubic-Quintic Nonlinearity

The general form of competing nonlinearity can be represented as:

$$n(I) = n_p I^p + n_{2p} I^{2p}. \tag{2.4}$$

where, $p$ is the positive number. $n_p$ and $n_{2p}$ have opposite signs, so that the condition: $n_p n_{2p} < 0$ holds true for the system. The terms related to $n_p$ and $n_{2p}$ compete with each other as the former creates self-focusing, while the later leads to self-defocussing occurring at high intensities. For the simplest case, competing nonlinearity takes the form of cubic-quintic nonlinearity, which is written as:

$$n(I) = n_0 + n_1 I + n_2 I^2. \tag{2.5}$$

Organic dyes and polymers, para toluene sulfonate (PTS), semiconductors (for example, AlGaAs, CdS, $CdS_{1-x}Se_x$) and semiconductor doped glasses exhibit the cubic-quintic nonlinearities [6].

### 2.1.3 Saturable Nonlinearity

Nonlinearity gets saturated at very high intensities. Photo-refractive materials are widely used to induce such kind of saturable nonlinearity in optical systems. Silica and Chalcogenide glasses are generally used to induce the saturating nonlinearity at moderately low intensities [6]. A typical nonlinearity function for saturating nonlinearity can be written as [5]:

$$n(I) = \frac{n_0}{1 + sI}. \tag{2.6}$$

where, $s$ is the saturation parameter. The high intensity of the laser not only saturates the nonlinearity but also reduces the optical loss by depletion of the ground state of the dopant ions of the medium. Such effect leads to saturable absorption and the corresponding material becomes the saturable absorber. Saturable absorber can be used to generate optical bistability in the optical cavities. Since, the second order expansion of the term $(1 + sI)^{-1}$ results in cubic-quintic nonlinearity, sometimes saturable nonlinearity may be approximated as cubic-quintic. Some organic materials can be used as dopants to form SA [6, 104, 105]. Generally, semiconductor saturable absorber mirror (SESAM) provides the saturable absorption in VCSEL [106]. Graphene is a promising SA [107, 108, 109]

## 2.2 Conservative and Dissipative Solitons

Solitons are localized structures in different media, for example, shallow-water waves [110], mechanical vibrations [111], laser beams [1], pulses etc., which can maintain their shape during propagation [6]. Interestingly, even after collision with other solitons it maintains its shape, thus manifests its particle like nature [112].

Self trapping of soliton in one transverse (to the propagation axis) direction is easier to achieve [113]. Difficulty level increases with increase in dimensionality. Thus producing spatial solitons are more challenging than the temporal solitons, but the multi-dimensionality made the spatial solitons more versatile than its temporal counterpart.

In terms of mathematics, solitons are the solutions of NLSE, when the diffraction (for spatial solitons) or dispersion (for temporal solitons) effects are exactly counterbalanced by the nonlinear terms. In frequency domain, the solitons exist in positive domain, whereas, linear waves lie in the negative domain [5]. This indicates that linear waves and solitons cannot interact with each other. Hence the energy of solitons always remain conserved. Therefore, the aforesaid condition is necessary for the existence of stationary soliton solutions in the conservative systems. These solitons are referred to as conservative solitons [114]. In principle, such systems possess infinite conservative entities. The most important are total energy, momentum, etc. However, conservative solitons no longer exist when some perturbations couple the solitons with the radiations [5].

So far, the behavior of solitons in lossless system are discussed. However, ideal conservative systems are rarely found, as practical systems involve in some amount of

loss, whatever small. Still the lossy systems can host a different class of soliton called the dissipative solitons (DS) [1]. DSs are more general than conservative solitons and occur in a wide variety of physical [115, 116, 117], chemical [25], mathematical [118] and biological systems [119] and even in nature. The essential requirement of DS is the continuous supply of external energy that keeps the DS 'alive'. Such energy supply is not necessary for conservative soliton. In this thesis, the core area of interest is optical CSs, which are a special class of spatial dissipative soliton inside laser cavity. To

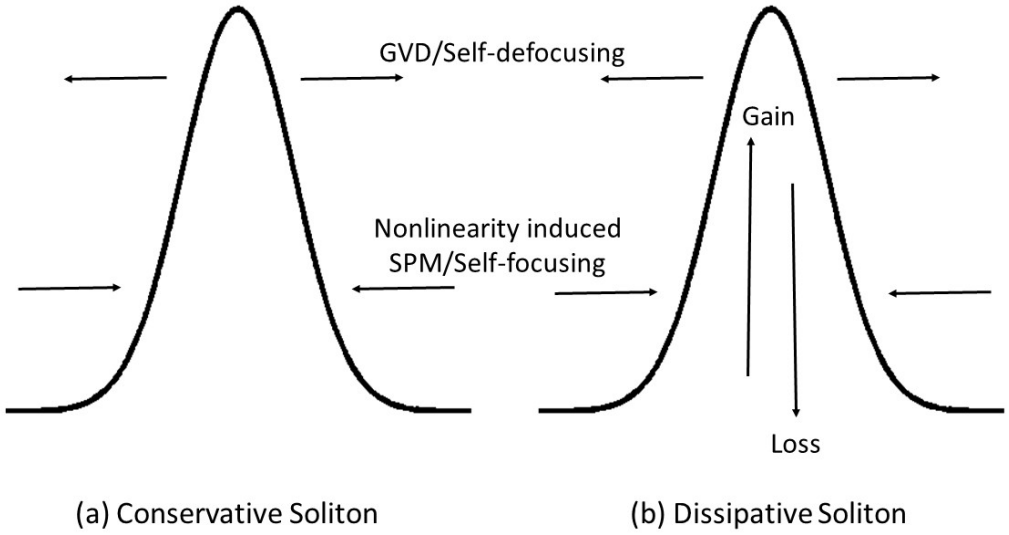


**Figure 2.1:** Generation of ($a$) conservative solitons by balance of counteracting group-velocity dispersion/self-diffraction and nonlinearity induced self-phase modulation or self-focusing, ($b$) dissipative solitons, having additional balance between loss and gain.

sustain DSs (and hence CSs) two-fold balances are required: one, the usual counter-balance between self-diffraction and nonlinearity-induce self-focusing and the other, balance between energy loss and gain in the system (cavity) [17]. Thus, while for conservative solitons a single parameter family of solutions can be obtained, the solution zone of dissipative system is discrete due to the stated two-fold balance (Figures 2.1 and 2.2).

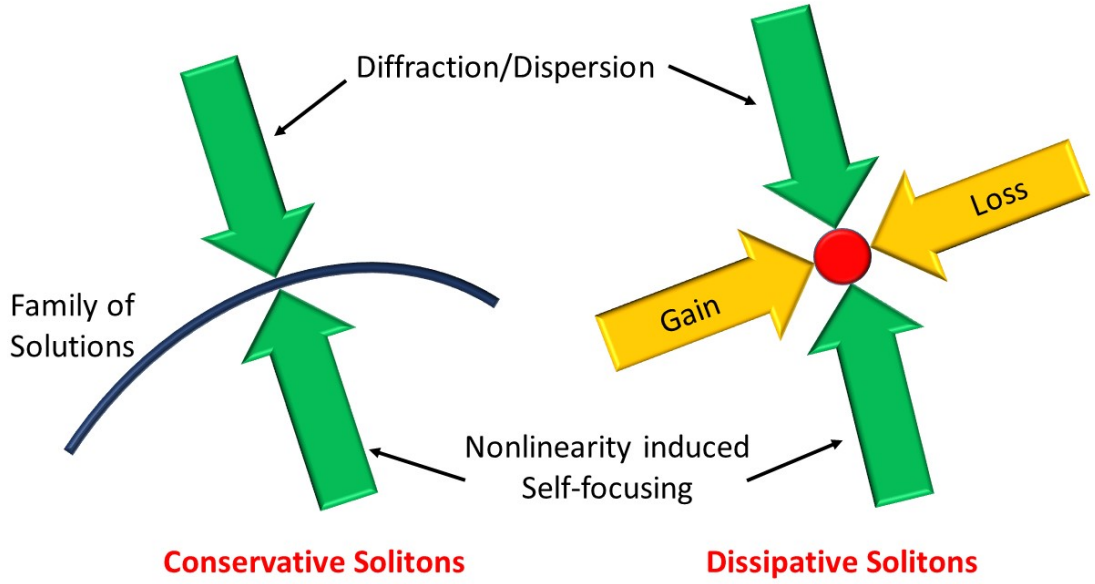


**Figure 2.2:** Continuous and discrete of soliton solutions in conservative and dissipative systems, respectively.

## 2.3 Cavity Solitons

CS belongs to a unique class of spatial optical dissipative solitons observed in broad-area systems, e.g., VCSEL [5, 120]. They are self-localized, non-diffracting and self-organized optical structures observed in dissipative optical cavities with gain and absorption, driven by a holding beam or an optical feedback element. Simply, CSs can be visualized as bright light spots in dark background or conversely, dark spot on a homogeneous bright or gray background. They appear on a plane transverse to the cavity axis. Moreover, one can crop up as many as CS at any desired position on the transverse plane just by shooting at the point with the writing laser beam. They occur in a system that is far-from equilibrium, thus requires continuous supply of energy. In other way, CS can be assumed as conventional propagating soliton bounded by the two mirrors of the cavity, i.e., they are boundary localized along propagating direction. Their localization occurs in the two transverse directions orthogonal to the

propagation direction (Figure 2.3) [1]. CS shares some properties of SDS. However,

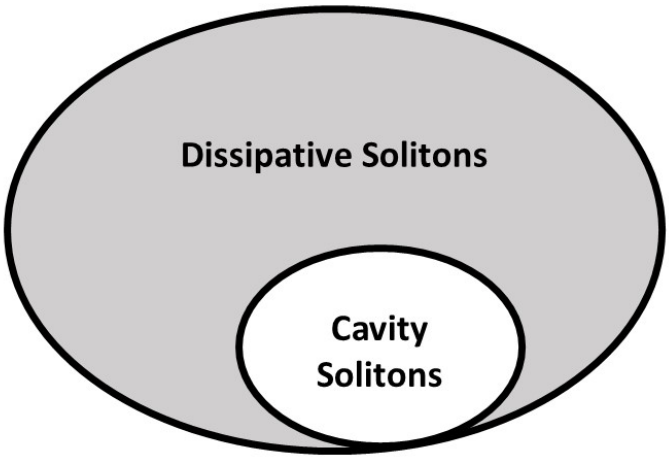


**Figure 2.3:** Classification of dissipative and cavity solitons.

their exponential confinement, plasticity (freedom of occurrence at any point on a plane transverse to cavity axis) and bistability (being 'on' and 'off' at the same condition) make them unique [9]. From the point of view of pattern formation, CSs are localized pattern-state over a co-existing stable homogeneous background state. For investigating generation and dynamics of CS, a VCSEL is usually preferred over edge emitters due to its several advantages, like, long device lifetime, single mode operation, low threshold current, lasing wavelength stability, high efficiency, symmetry of emitted beam profile and high temperature tolerance (usually 80°C). The basic structure of VCSEL consists of semiconductor micro-cavity, enclosed by highly reflective distributed Bragg reflectors (DBR). Typically, cavity thickness is of the order of one wavelength, with aperture size of 100-200 $\mu$m and an approximate emission wavelength of 981 nm at an operating temperature of 80°C [1, 4]. The large transverse area of VCSEL ($\sim 250\mu$m or even more) facilitates the observation of the localized pattern, hence CS ($\sim 5\mu$m) and its dynamics. Ring resonator cavity, single-mirror feedback cavity, double-mirror feedback are some of the commonly available cavity schemes. Among these, owing to the minimum configuration and simplicity of working, a single-mirror

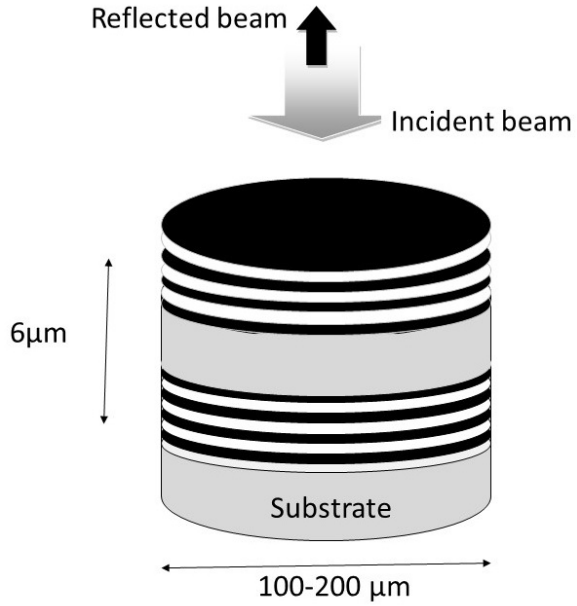


**Figure 2.4:** Schematic of VCSEL.

feedback serves the purpose to its best [1]. Due to the requirement of 'two-fold' balances, CS appears as fixed points or only in a finite narrow range of parameters, usually, referred to as pinning region. Several experimental schemes have been used to generate CS in VCSEL. Generally, holding beam is coupled with VCSEL for providing the continuous power to keep CS 'live'. A simpler but better scheme is the inclusion of an external feedback, for example, a frequency-selective feedback (FSF) element coupled with a VCSEL [121]. The presence of feedback eliminates the need of holding beam and undesired thermal effects and other concomitant complicacies arising due to it [14, 121, 122]. A significant volume of work [1, 4, 9, 12, 57, 67, 77, 123] has been reported on theoretical as well as experimental investigation of CS and cavity soliton laser (CSL) with FSF. Saturable absorber (SA) may also replace the holding beam. SA involves higher order nonlinearities that facilitate in achieving stability of the CS system. Materials with higher order nonlinearities such as some semiconductors [6] and organic materials [124] can be used as dopents to form SA.

## 2.4 Cavity Soliton Generation Schemes

The cavity soliton research can be categorized into different sub groups depending on the scheme, nature of cavity and condition of operation (Figure 2.5).

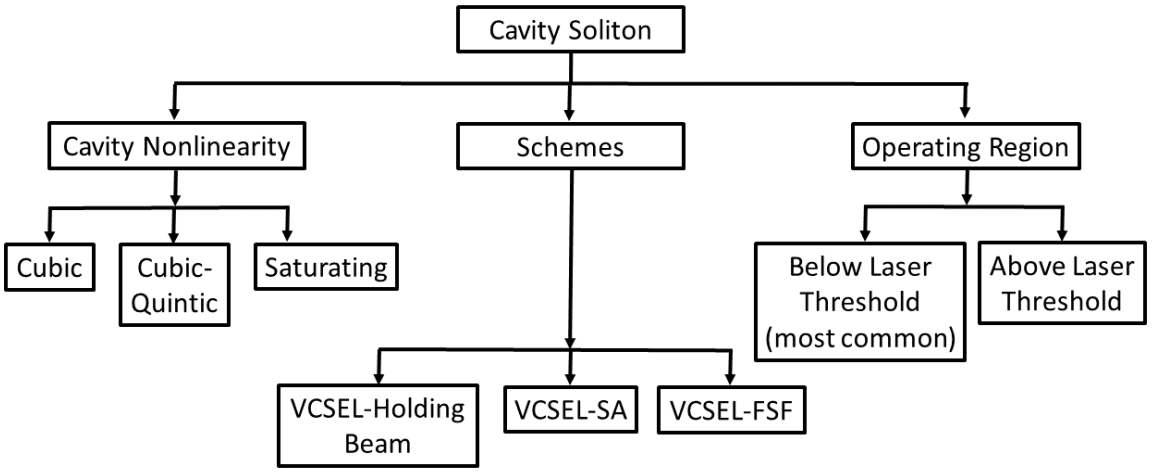


**Figure 2.5:** Classification of cavity soliton.

Initially, the most commonly used scheme was a nonlinear cavity or optical feedback system driven by an external writing beam of high spatial and temporal coherence and sustained by holding beam [1]. For the application point of view, to get self-sustained emission and to make the size of CSL more compact, there was a need to replace the holding beam by self-sustained schemes. The holding beam can be replaced with the feedback system or using coupled cavity, i.e., coupling the main cavity with the external cavity and such systems are known as self-driven systems. Therefore, newer scheme, i.e., CSL with FSF (VCSEL-FSF) was devised (Figure 2.6). Since FSF eliminates the requirement of the holding beam, it makes the system more compact. CSs in self-driven systems are slaved as their phase, frequency and polarization are dependent on the feedback.

Self-driven system, such as, CSL originates due to spontaneous symmetry break-

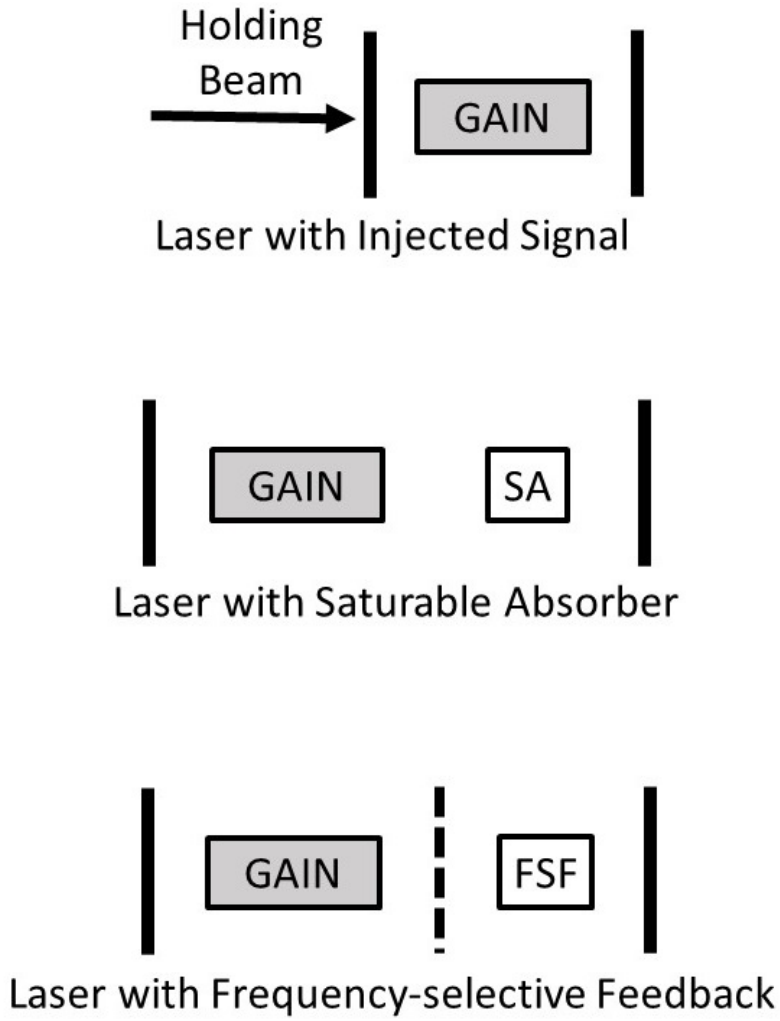


**Figure 2.6:** Schemes for cavity soliton generation.

ing, and therefore it gets freedom to choose its own phase. Coherently self-driven systems are sustained by beam of high temporal and spatial coherence. Thus, the system behaves as a laser with self-sustained emission. In FSF systems, the diffraction grating can be replaced with volume Bragg grating (VBG). The advantage of using VBG as FSF element is seen in the single frequency soliton generation and frequency stabilization in semiconductor lasers [4, 125].

SDSs can not be generated in a simple free running lasers because it undergoes the supercritical bifurcation at laser threshold. Hence, free running lasers cannot support optical bistability. In order to sustain optical bistability, the laser should undergo subcritical bifurcation. The presence of SA results in the coexistence of the lasing

as well as non-lasing solutions in the certain range of pump power. Thus the system exhibits bistability and undergoes subcritical bifurcation. Laser with SA configuration helps in attaining bistability in the system. In such configuration, the contrast between the CSs and homogeneous cavity background is maximum due to pure spontaneous emissions [82]. Elimination of the holding beam makes the CSL-SA more robust and simpler [12]. In such systems, the properties of emitted laser beam depends only on radiation-matter interactions, thus, introduces additional thermal losses. In nutshell, the advantage of using SA or FSF is to create simpler, compact, robust and self-sustaining system, whereas the limitation of using these configurations increases the losses in the system [83].

CS can be generated in different cavity nonlinearities: Kerr (cubic), cubic-quintic and saturable nonlinearity. Primely, Kerr cavity attracted considerable attention [72, 73, 74, 75, 76, 84, 126]. Thereafter, cubic-quintic nonlinearity has been considered [85].

CS can be further classified into two categories in terms of operating region: below and above the laser threshold [77, 86, 127].

## 2.5 Feedback Mechanism

The basic need for modelling of the CSL with FSF is to sustain excitations (CS) in lossy cavity [1] and to control the phase and amplitude gradients of the holding beam [12]. The feedback can be supplied to cavity resonator through diffraction grating, Volume Bragg grating (VBG), distributed Bragg reflectors (DBR). In most of the frequency selective feedback systems, VBG is preferred over diffraction grating because of its compact size and vast range of options for frequency selection. VBGs are optical

devices that consist of a periodic refractive index structure in a bulk and have a wide range of applications such as frequency stabilizer of semiconductor lasers or as beam combiner for fiber or solid state lasers [4]. VBGs have grating period below $1\mu m$ and narrow optical bandwidth of the range $0.1nm$ or $0.01nm$. In most of the cases, its peak reflectivity reaches 99%. It can operate at very high power levels as it experiences very low optical losses related to scattering or absorption. High Fresnel number in the cavity can be maintained through self-image coupling of the VCSEL cavity with the VBG to provide one-to-one mapping. This enables the system in achieving self-localization [4, 125].

## 2.6 Theory of Cavity Solitons

The theory of CS is complex, wide, but elegant. CS theory is a combination of soliton theory, nonlinear dynamics and pattern formation. This section discusses the mathematical formulation and stability analysis.

### 2.6.1 Mathematical Modeling

The theoretical study of CSs has attained a significant height due to its complex yet elegent mathematical formulation, intriguing dynamical behaviour and multidisciplinary characteristics. The mathematical modeling of CS generally involves complex Ginzburg-Landau equation (CGLE) [128], perturbed NLSE [129], complex Swift-Hohenberg equation (CSHE) [130], or Lugiato-Lefever equation (LLE) [131].

The most general form of (2+1)D CGLE used for CS can be written as [132]:

$$\frac{\partial \psi}{\partial t} = \epsilon\psi + (b_1 + ic_1)\nabla_\perp^2\psi - (b_3 - ic_3)|\psi|^2\psi - (b_5 - ic_5)|\psi|^4\psi. \tag{2.7}$$

where, $\psi$ is the input field envelop and the coefficients $b_i$ and $c_i$ are real. $\nabla_\perp^2$ is the transverse component of Laplacian operator in symmetrical coordinates and is represented as $\nabla_\perp^2 = r^{(1-D)}\frac{\partial}{\partial r}(r^{(D-1)}\frac{\partial}{\partial r})$ in $(D+1)$ dimensional system. $x$ and $t$ are space and time coordinates. $\epsilon$ ie the linear gain/loss term, $b_1$ represents diffusive coupling coefficient, $c_1$ represents diffractive coupling coefficient. Cubic gain or loss is represented by $b_3$, whereas, $b_5$ represents quintic gain or loss coefficient. The coefficient $c_3$ is due to cubic nonlinearity, while $c_5$ represents quintic nonlinearity. Equation (2.7) is the general form of cubic-quintic CGLE. Term on left hand side of equation (2.7) is the evolution term. On right hand side, second term is the diffraction term, third and fourth terms represent cubic and quintic nonlinearity. The coefficients $b_i$ and $c_i$ play an important role in the system behavior and stability of different types of solutions. The negative sign in front of cubic non-linearity term results in the supercritical bifurcation at $\epsilon = 0$ in the absence of quintic nonlinearity term, i.e. $b_5 = 0$ and $c_5 = 0$. For a case when real part of the coefficient of cubic nonlinearity term $b_3 < 0$, the system undergoes a subcritical bifurcation, but in this case, to allow stability of the system $b_5$ must be greater than zero.

A few variety of CGLE with different order of nonlinearities are derived in the following subsection.

**Case 1**: The equation (2.7) reduces to cubic CGLE when $b_5 = c_5 = 0$ and takes the form:

$$\frac{\partial\psi}{\partial t} = \epsilon\psi + (b_1 + ic_1)\nabla_\perp^2\psi - (b_3 - ic_3)|\psi|^2\psi. \tag{2.8}$$

Keeping the values of $b_i$'s in equation (2.8) to an absolute unity and $c_1 = c_2 = 0$, the equation (2.8) reduces to real a Ginzburg-Landau equation. The condition describes

the inception of stationary periodic solutions in equation (2.8). Such systems exhibit the reversibility symmetry.

**Case 2**: Equation (2.7) reduces to NLSE when the coefficients $\epsilon = b_i = c_5 = 0$, and takes the following form:

$$\frac{\partial \psi}{\partial t} = ic_1 \nabla_\perp^2 \psi + ic_3 |\psi|^2 \psi. \tag{2.9}$$

Equation (2.9) is both Hamiltonian and completely integrable. For $c_3 < 0$ dark soliton solutions are obtained.

**Case 3**: For $\epsilon = b_i = 0$, equation (2.7) takes the form of cubic-quintic NLSE.

$$\frac{\partial \psi}{\partial t} = ic_1 \nabla_\perp^2 \psi + ic_3 |\psi|^2 \psi + ic_5 |\psi|^4 \psi. \tag{2.10}$$

This is also Hamiltonian in nature. The most general and widely studied solutions of CGLE (and its variants) are of Gaussian and *sech* type [6, 5, 101, 102, 132, 133]. Apart from the soliton solutions, CGLE also supports different types of solutions such as source, fronts or kink or shock, pulses and sinks, which are discussed in details in section 4.2. The TWSS of cubic CGLE and generation of CS are discussed in detail in Chapter 6. Soliton solutions in cubic, cubic-quintic and higher order nonlinearities are discussed in Chapters 4 and 5.

To describe an optical cavity consisting of saturating nonlinearity for active and passive medium coupled with feedback, the following CGLE type dynamical equation can be used:

$$\frac{\partial E}{\partial t} = [-(1 - i\theta) + \frac{\mu(1 - i\alpha)}{1 + |E|^2} - \frac{\gamma(1 - i\beta)}{1 + s|E|^2} + i\nabla_\perp^2]E + F, \tag{2.11}$$

where, the term on L.H.S. is the evolution term. First term on R.H.S. represents the linear gain or loss, second and third terms represent the saturating nonlinearity

corresponding to active and passive medium, respectively, in VCSEL. Fourth term represents the diffraction operator and $F$ represents the feedback field. Expanding the denominators of second and third terms on the R.H.S. of equation (2.11) upto second order results in cubic-quintic CGLE, which can be compared to equation (2.7).

### 2.6.2 Maxwell-Bloch Equations

*Step 1*: The Maxwell's equations in non-magnetic medium without free charges and currents are given as:

$$\nabla \cdot \vec{D} = 0, \tag{2.12}$$

$$\nabla \cdot \vec{B} = 0, \tag{2.13}$$

$$\nabla \times \vec{E} = -\frac{\partial \vec{B}}{\partial t}, \tag{2.14}$$

$$\nabla \times \vec{B} = \mu_0 \frac{\partial \vec{D}}{\partial t}. \tag{2.15}$$

Here, $\vec{D} = \epsilon_0 \vec{E} + \vec{P}$. $\vec{D}$ and $\vec{B}$ are electric and magnetic flux densities. $\vec{E}$ represents the electric field, medium polarization is given by $\vec{P}$. $\epsilon_0$ and $\mu_0$ represent permitivity and permeability in vacuum, respectively.

*Step 2*: Taking the curl of equation (2.14)

$$\nabla \times \nabla \times \vec{E} = -\frac{\partial^2 (\epsilon \vec{E} + \vec{P})}{\partial t^2}. \tag{2.16}$$

The directional derivative is zero for plane waves, whereas, for slowly varying amplitude approximations it is negligibly small, therefore the following relation can be

obtained:

$$-\nabla^2\vec{E} + \frac{1}{c^2}\frac{\partial^2\vec{E}}{\partial t^2} = -\frac{1}{\epsilon_0 c^2}\frac{\partial^2\vec{P}}{\partial t^2}, \tag{2.17}$$

where, $c = \frac{1}{\sqrt{\mu_0\epsilon_0}}$. Magnitude of $\vec{P}$ is very less than the magnitude of $\vec{E}$, such that Maxwell's equation gives $\nabla \cdot \vec{D} \approx \nabla \cdot \vec{E} \approx 0$, which is in agreement with the above approximation. Considering that a wave propagates in the vacuum with frequency $\omega$ and wave-vector $k$, where $k = \omega/c$.

*Step 3*: Introducing the slowly varying complex amplitudes of $E$ and $P$, as following:

$$\vec{E} = [Ee^{-\iota(kz-\omega t)} + c.c.]\vec{z} \tag{2.18}$$

and

$$\vec{P} = [Pe^{-\iota(kz-\omega t)} + c.c.]\vec{z},, \tag{2.19}$$

where, *c.c.* is the complex conjugate. Using equations (2.18) and (2.19), equation (2.17) takes the following form:

$$\begin{aligned} -\nabla_\perp^2 E - [\frac{\partial^2 E}{\partial z^2} - 2ik\frac{\partial E}{\partial z} - k^2 E] + \frac{1}{c^2}[\frac{\partial^2 E}{\partial t^2} + 2i\omega\frac{\partial E}{\partial t} - \omega^2 E] \\ = -\frac{1}{\epsilon_0 c^2}[\frac{\partial^2 P}{\partial t^2} + 2i\omega\frac{\partial P}{\partial t} - \omega^2 P], \end{aligned} \tag{2.20}$$

where, $\nabla_\perp^2$ is the Laplacian operator in the transverse plane to the propagation direction $\vec{z}$.

*Step 4*: Considering the slowly varying amplitude approximation, the frequencies and wavelengths in optical domain satisfy the following relations:

$$|\frac{\partial^2 E}{\partial t^2}| \ll \omega|\frac{\partial E}{\partial t}|, \tag{2.21}$$

$$|\frac{\partial^2 E}{\partial z^2}| \ll k|\frac{\partial E}{\partial z}|, \tag{2.22}$$

$$|\frac{\partial^2 P}{\partial t^2}| \ll \omega|\frac{\partial P}{\partial t}|. \tag{2.23}$$

Considering the slowly varying approximations, equation (2.20) takes the following form:

$$-\nabla_\perp^2 E + 2ik[\frac{\partial E}{\partial z} + \frac{1}{c}\frac{\partial(E + P/\epsilon_0)}{\partial t} = \frac{\omega^2}{\epsilon_0 c^2}P. \tag{2.24}$$

For a medium with linear response ($P = \epsilon_0\chi^1 E$), the above equation takes the following form:

$$-\nabla_\perp^2 E + 2ik[\frac{\partial E}{\partial z} + \partial ck(1+\chi^1)nc^2\frac{\partial E}{\partial t}] = -\nabla_\perp^2 E + 2ik[\frac{\partial E}{\partial z} + \frac{n}{c}\frac{\partial E}{\partial t}] = 0. \tag{2.25}$$

where, $n = \sqrt{1+\chi^{(1)}}$.

*Step 5*: The Optical Bloch equations: Considering the atoms with two energy levels and appropriate wave-function, the time dependent Schrödinger equation for full system can defined as:

$$i\hbar\frac{\partial}{\partial t}|\Psi_s\rangle = (H_0 + H_I)|\Psi_s\rangle, \tag{2.26}$$

where, $H_0$ represents Hamiltonian and $H_I$ is the interaction Hamiltonian. $|\Psi_s\rangle$ is the system wave-function. The equation (2.26) can be written in the form of density matrix form as follows:

$$\frac{\partial\rho}{\partial t} = -\frac{i}{\hbar}[H_I, \rho]. \tag{2.27}$$

*Step 6*: The decay terms: The interaction of the system can be studied by using the Markov approximation. The decay terms in Lindbland form for the dynamics of

density matrix can be represented as:

$$\frac{\partial\rho}{\partial t} = -\frac{i}{\hbar}[H_I, \rho] + \sum i, jq_{i,j}|j\rangle\langle i|\rho|i\rangle\langle j| - \frac{1}{2}\sum i, jq_{i,j}|i\rangle\langle i|\rho - \frac{1}{2}\rho\sum i, jq_{i,j}|i\rangle\langle i| \tag{2.28}$$

where, $i$, $j = 1, 2$ and $q_{i,j}$ are numbers indicating the decays due to external coupling with heat bath. Bloch equations for the medium formed by considering two level atoms is given by:

$$\begin{aligned}
\frac{d\rho_{11}}{dt} &= -i(g^*\rho_{21}e^{i\Delta t} - g\rho_{12}e^{-i\Delta t}) + q_{21}\rho_{22}, \\
\frac{d\rho_{12}}{dt} &= -ig^*(\rho_{22} - \rho_{11})e^{i\Delta t} - \frac{1}{2}(q_{11} + q_{21} + q_{22})\rho_{12}, \\
\frac{d\rho_{21}}{dt} &= -ig^*(\rho_{11} - \rho_{22})e^{-i\Delta t} - \frac{1}{2}(q_{11} + q_{21} + q_{22})\rho_{21}, \\
\frac{d\rho_{11}}{dt} &= -i(g\rho_{12}e^{-i\Delta t} - g^*\rho_{21}e^{i\Delta t}) + q_{21}\rho_{22}.
\end{aligned} \tag{2.29}$$

The time dependence of above equations can be removed by introducing the relations: $R_{12} = \rho_{12}e^{i\Delta t}$ and $R_{21} = \rho_{21}e^{-i\Delta t}$. Assuming that in the dynamics of the system, no other energy levels are involved, therefore, the sum of the probabilities f occupancy of both the levels is unity. This means that $R_{11} + R_{22} = \rho_{11} + \rho_{22} = 1$, thus making the system non-homogeneous. Considering the population inversion variable $n = \rho_{22} - \rho_{11} = R_{22} - R_{11}$, the reduction in the equations can be achieved. Further reduction can be achieved by considering the off diagonal elements occurring in complex conjugate pairs. The final reduced form of Bloch equations take the following form:

$$\frac{dR_{12}}{dt} = -(\gamma_\perp - i\Delta)R_{21} + ign, \tag{2.30}$$

$$\frac{dn}{dt} = -\gamma_\parallel(n - 1) + 2i(g^*R_{21} - gR_{21}^*). \tag{2.31}$$

Here, the decay rates are defined as $\gamma_\perp = \frac{1}{2}(q_{11} + q_{21} + q_{22})$ and $\gamma_\parallel = q_{21}$.

*Step 7*: Combining the Bloch and Maxwell equations: Considering the equations (2.24), (2.30) and (2.31), and introducing the new variables $N = n_a n$, $P = n_a \mu_{12} R12 e^{-ikz}$ and $E = E_0 e^{-ikz}$, the following relation can be obtained:

$$\frac{\partial E}{\partial z} + \frac{1}{c}\frac{\partial (E - 2iP/k)}{\partial t} = \frac{i}{2k}\nabla_\perp^2 E + P, \tag{2.32}$$

$$\frac{\partial P}{\partial t} = \gamma_\perp[-(1 + i\Delta)P + ED], \tag{2.33}$$

$$\frac{\partial D}{\partial t} = -\gamma_\parallel[D - \alpha + \frac{1}{2}(EP^* + E^*P)]. \tag{2.34}$$

The equations (2.32) - (2.34) have been derived in for a laser based on two-level and four level atom models [134, 135].

*Step 8*: Mean Field Limit: The Maxwell-Bloch equations derived in *step 8* gives the propagation of slowly varying amplitude of the electromagnetic wave in two level medium. These equations have now been extended to the medium of length $L$ in an optical ring cavity of length $\mathcal{L}$. At the entry point the longitudinal boundary condition are defined as:

$$\begin{aligned} E(x, y, 0, t) &= e^D E(x, y, L, t - \frac{\mathcal{L} - L}{c}) + \sqrt{T} E_{IN}(x, y), \\ D &= ln\sqrt{R_j} - i\delta_j + (\mathcal{L} - L)\frac{i}{2k}\nabla_\perp^2, \\ \delta &= \frac{\omega_c - \omega}{c}\mathcal{L}, \\ T &= 1 - R. \end{aligned} \tag{2.35}$$

where, $R$ and $T$ represent the mirror reflectivity and transmittivity. $E_{IN}$ is the input field at frequency $\omega$. $\omega_c$ is the longitudinal cavity mode frequency. Transmittivity of

the mirror is considered small, i.e. $\sqrt{T} = \epsilon << 1$. Applying the following mean field limit transformations to the equations (2.35):

$$z' = z,$$
$$t' = t + [\frac{\mathcal{L} - L}{c}]\frac{z}{L}. \tag{2.36}$$

and rearranging, we can obtain the Maxwell-Bloch equations of the following form:

$$\frac{\partial E}{\partial t} = \kappa[E_I + P - (1 - i\theta)E + i\nabla^2 E], \tag{2.37}$$

$$\frac{\partial P}{\partial t} = \gamma_\perp[ED - (1 + i\Delta)P], \tag{2.38}$$

$$\frac{\partial D}{\partial t} = \gamma_\parallel[\mu - D - \frac{1}{2}(EP^* + E^*P)]. \tag{2.39}$$

where, $\kappa = \frac{\gamma c}{\mathcal{L}-(n-1)L}$, $\theta = \frac{(\omega_c-\omega)\mathcal{L}}{c\gamma}$, $\mu = \frac{\alpha L}{\gamma}$ and $E_I = \sqrt{\frac{2E_{IN}}{\gamma}}$.

## 2.7 Methodology

To solve any problem, four approaches can be followed: analytical, numerical, analytical-numerical (combined) and simulation. In view of their complex nature, the governing equations of the cavity systems of this thesis are studied analytically and compared to numerical experiments. Finally, the stability region is identified for CS. In this thesis, variational method [136, 137, 138, 139] is used first ever for complete investigation of CS and its stability in (1+1) and (2+1) dimensions. The traveling wave solutions for CGLE are obtained by He's Variational method [140]. Numerical investigation of CGLE in cubic-quintic and higher order nonlinearities is done using the Split-step

Fourier method (SSFM) [6, 141].

### 2.7.1 Variational Method

Many nonlinear complex systems in physics, cannot be solved using exact methods. Therefore, to solve such problems, approximate methods come handy. In semi-classical and quantum physics, variational method is widely used to get the solution of such problems. In this thesis, we have used the variational method to solve the cubic and cubic-quintic CGLE. The step by step methodology for variational method has been discussed in this section.

In variational method, the nonlinear partial differential equation (PDE) is reduced to a number of coupled ordinary differential equations (ODEs) and then these ODEs are solved to get the solution of the system.

**Step 1**: Consider the nonlinear PDE that describes the beam/pulse dynamics. In this thesis, CGLE describes the system to the best. A general form of the equation used to describe such system is given as:

$$\frac{\partial E}{\partial t} = (m_1 + im_2)E + i\nabla_{\perp}^2 E + (m_3 + im_4)|E|^2 E. \tag{2.40}$$

where, L.H.S represents the evolution. On R.H.S., first term represents linear loss or gain, second term represents the diffraction and third term gives the loss and gain due to cubic nonlinearity.

**Step 2**: Equation (2.40) is separated into conservative and dissipative parts.

**Step 3**: The corresponding Lagrangian density is constructed for conservative and dissipative parts, which are denoted by $\mathbb{L}_C$ and $\mathbb{L}_Q$, respectively.

**Step 4**: A suitable trial function for the system is assumed to proceed further. Gaus-

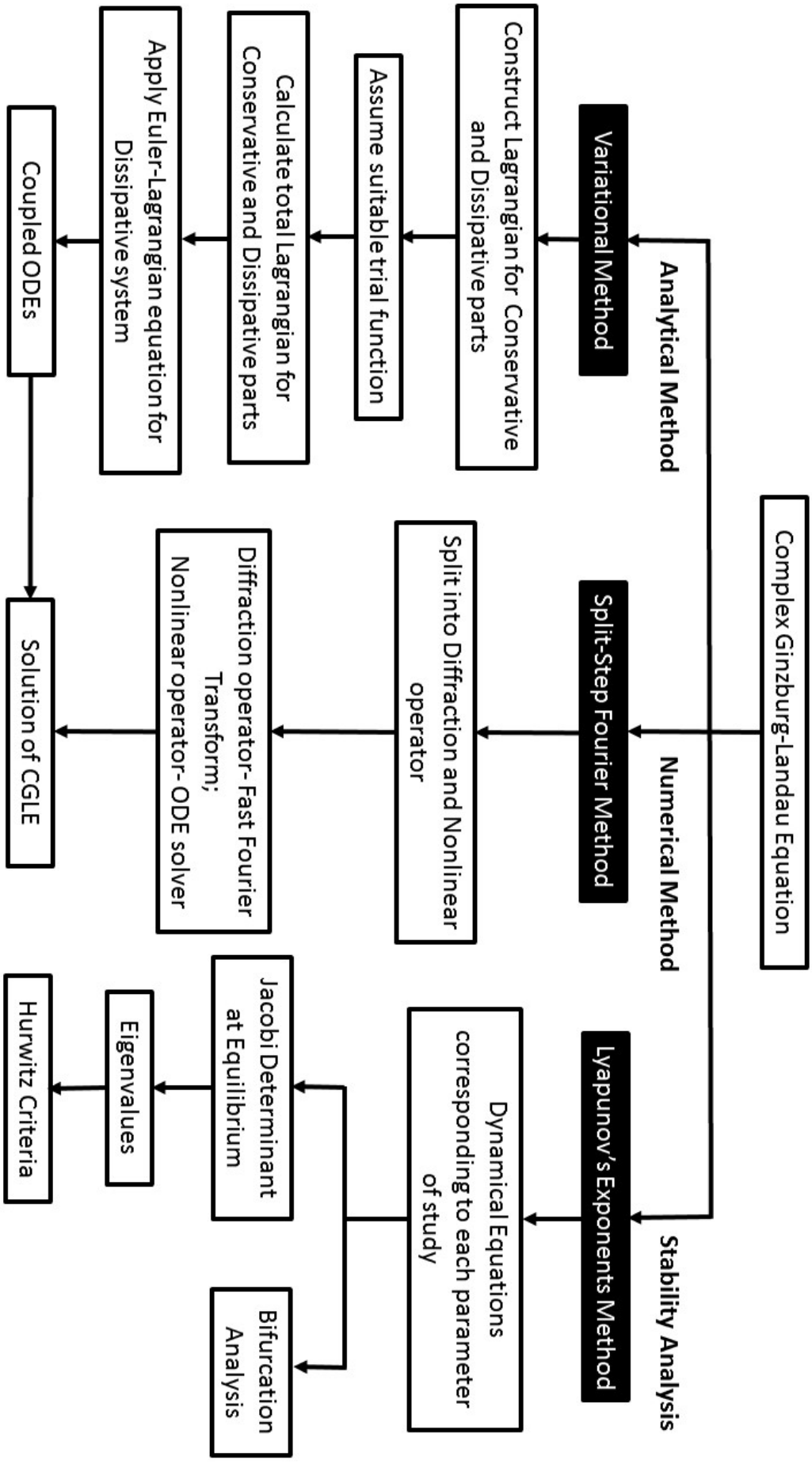


**Figure 2.7:** Schematic representation of stability analysis, analytical and numerical methodology.

sian and *sech* profiles are widely used trial functions for determining the solution with variational method. Typical Gaussian and *sech* trial functions are given below:

$$E = A\ exp\left(-\frac{r^2}{2R^2} + iCr^2 + i\phi\right), \tag{2.41}$$

$$E = A\ sech(r/R). \tag{2.42}$$

Here, $A$, $R$, $C$ and $\phi$ represent the amplitude, inverse width, chirp and phase, respectively, of the input field envelope.

**Step 5**: By substituting the trial function in the Lagrangian density, reduced Lagrangian is calculated.

**Step 6**: The total Lagrangian is calculated by integrating the reduced Lagrangian over the whole available domain, for the system:

$$L_C = \int_{-\infty}^{\infty} \mathbb{L}_C dr. \tag{2.43}$$

**Step 7**: Next, the Euler-Lagrangian equation is used for variation of $L_C$ [136]:

$$\frac{\partial}{\partial t}\left(\frac{\partial L_C}{\partial \eta\prime}\right) - \frac{\partial L_C}{\partial \eta} = 2Re \int r^{(D-1)} Q \frac{\partial E^*}{\partial \eta} dr. \tag{2.44}$$

where, $\eta$ is the soliton parameters and can take the form, i.e., $\eta(t) = A(t)$, $R(t)$, $C(t)$ and $\phi(t)$, where, $\eta\prime = \partial\eta/\partial t$ and $E^*$ is the complex conjugate of $E$. The evolution equations (in the form of coupled ODEs) for soliton parameters ($A(t)$, $R(t)$, $C(t)$ and $\phi(t)$) are then obtained by using equation (2.44).

**Step 8**: From the evolution equations obtained in *step 7*, the steady state values of soliton parameters are obtained. Nature of evolution of the system parameters are

obtained by solving the coupled ODEs, using the steady state values as the initial values.

However, the approximate methods have some limitations as compared to exact methods. However, on the other hand, variational method has its own advantages over the other exact methods. Variational method provides the insight into the nature of the solution individual system parameters.

### 2.7.2 He's Variational Method

A special kind of variational method was formulated by J.H. He to study the traveling wave (TW) solutions in the complex systems [142]. The basic steps for obtaining the TW solutions for NLSE and CGLE are enlisted below:

**Step 1**: NLSE or CGLE presenting the system is considered. A TW ansatz of the following form is substituted in the governing equation:

$$\psi(x,t) = g(\xi)e^{\iota(-kx+\omega t+\theta)}, \tag{2.45}$$

where, $\xi = x - vt$, $x$ and $t$ represent the space and time coordinates, respectively. The amplitude profile function of TW profile has been represented by $g(\xi)$. $k$, $\omega$ and $\theta$ represent the wave number, frequency and phase constant of the TW.

**Step 2**: The real and imaginary parts of the resultant equation (from *step 1*) are separated. The velocity of the TW can be extracted from the imaginary part, whereas, real part is further used to solve the soliton condition.

**Step 3**: $g'(\xi)$ $(= \partial\psi/\partial\xi)$ is eliminated from the real part.

**Step 4**: The resultant equation is multiplied with $g'(\xi)$ and integrated with respect to $\xi$ over the whole space.

**Step 5**: Now, the profile is defined for the amplitude function $g$. For bright soliton conditions *sech* form of ansatz is widely used:

$$g(\xi) = S\ sech(T\xi) \tag{2.46}$$

**Step 6**: The resultant equation from **Step 5** is equated to the physical quantity which is represented by $K$.

**Step 7**: A new quantity J is now defined, such that it satisfies the following condition:

$$J = \int_{\infty}^{-\infty} K d\xi. \tag{2.47}$$

**Step 8**: The principle of variation is applied to the physical quantity $J$, such that $\partial J/\partial S = 0$ and $\partial J/\partial T = 0$. The resultant equations are solved for the soliton parameters: $S$ and $T$.

### 2.7.3 Numerical Integration: Split-step Fourier Method

The numerical integration of the nonlinear dynamical equations is performed using split-step Fourier method (SSFM). In this section a step-by-step procedure is discussed.

**Step 1:** The governing equation (2.40) (CGLE or NLSE) is splitted into diffraction and nonlinear operator, such that:

$$\frac{\partial E}{\partial t} = (\hat{D} + \hat{N})E. \tag{2.48}$$

Here,

$$\hat{D} = (m_1 + im_2) + i\nabla_{\perp}^2 \tag{2.49}$$

and

$$\hat{N} = (m_3 + im_4)|E|^2. \tag{2.50}$$

**Step 2:** The diffraction operator in the equation (2.49) can be solved by the spectral method through Fast Fourier transform (FFT).

**Step 3:** Equation (2.50) has no explicit spatial dependence, therefore it can be solved directly using the technique used to solve the ODEs. In general, the diffraction and nonlinearity act together, but SSFM considered that the diffraction and nonlinearity acts independently without changing the final result.

**Step 4:** As the system moves from $t$ to $t + dt$, the field envelop can be expressed mathematically in the following form:

$$E(t + dt) = e^{\hat{L}dt}E(t), \tag{2.51}$$

where, $\hat{L} = \hat{D} + \hat{N}$. For two non-commuting operators $\hat{a}$ and $\hat{b}$, the Baker-Hausdorff formula states [143]:

$$exp(\hat{a})exp(\hat{b}) = exp(\hat{a} + \hat{b} + \frac{1}{2}[\hat{a}, \hat{b}] + \frac{1}{12}[\hat{a} - \hat{b}, [\hat{a}, \hat{b}]] + ...). \tag{2.52}$$

Assuming that the error introduced in neglecting the commutation of two operators ($[\hat{D}, \hat{N}]$) has been negligible enough, therefore, $E(t + dt)$ can be written as:

$$E(t + dt) = e^{\hat{D}dt}e^{\hat{N}dt}E(t). \tag{2.53}$$

**Step 5:** The error introduced in neglecting $[\hat{D}, \hat{N}]$ can be further reduced by reducing the step-size $h$, therefore, equation (2.53) can be rewritten as:

$$E(t + dt) = e^{\hat{D}\frac{dt}{2}}e^{\hat{N}\frac{dt}{2}}E(t). \tag{2.54}$$

**Step 6:** The final solution for field envelop can be represented in the following form after $n$-times integration:

$$E(t) = e^{\hat{D}\frac{dt}{2}} e^{\hat{N}dt} e^{\hat{D}\frac{dt}{2}} .....e^{\hat{D}\frac{dt}{2}} e^{\hat{N}dt} e^{\hat{D}\frac{dt}{2}} E(0). \tag{2.55}$$

To improve the efficiency of the SSFM, higher order versions can be implemented.

## 2.8 Stability Analysis

Stability of the dynamical system is one of the most important criteria to establish its robustness. The stability analysis of the solutions of the governing equation is inevitable for knowing the system's sustainability. Stability analysis of the system gives the insight of the behavior of the system with respect to the different system parameters. There are a number of established mathematical techniques available to analyze the stability criteria of dynamical systems. Lyapunov exponent's method [8, 144], perturbation method [145], Eckhaus instability criteria [146] and Benjamin-Feir-Newell instability criteria [147], are some of the efficient tools.

### 2.8.1 Lyapunov Exponents Method

The nature of equilibrium points determine the stability of the system. According to Lyapunov, the famous Russian mathematician, the system is stable if and only if all the solution points of the system lie in close proximity to the equilibrium points, otherwise the system is unstable. If the solution points of the system tend to approach the equilibrium point as the time approaches to infinity then the system is asymptotically stable. However, it is necessary to determine the stability of an equilibrium point, which can be determined by linearization about the equilibrium point. The stability

of an autonomous system can be classified into three categories, namely, uniform, uniform asymptotic and exponential stability.

The dynamical equation, in the form of nonlinear partial differential equation (PDE) of second order, describing the system is first transformed into the first order ordinary differential equations (ODEs) through some suitable mathematical technique. We used the variational method to form the first order ODE from the nonlinear PDE. The first order ODE describe the dynamics or evolution of the soliton parameters (for example, see equations (3.54)-(3.57)).

Let us consider the coupled first order ODEs of the form:

$$J_1 = \frac{\partial u_1}{\partial t} = a_{11}u_1 + a_{12}u_2 \tag{2.56}$$

$$J_2 = \frac{\partial u_2}{\partial t} = a_{21}u_1 + a_{22}u_2 \tag{2.57}$$

The corresponding Jacobian determinant at an equilibrium can be written as:

$$|J - \lambda I| = \left| \begin{array}{cc} \frac{\partial J_1}{\partial u_1} - \lambda & \frac{\partial J_1}{\partial u_2} \\ \frac{\partial J_2}{\partial u_1} & \frac{\partial J_2}{\partial u_2} - \lambda \end{array} \right|_{eq} = 0. \tag{2.58}$$

The corresponding eigenvalue equation can be written as:

$$\lambda^2 + \alpha_1\lambda + \alpha_2 = 0 \tag{2.59}$$

where, $\alpha_1 = -(a_{11} + a_{22})$ and $\alpha_2 = a_{11}a_{22} - a_{12}a_{21}$. For a system to be stable, the eigenvalues of Jacobian given by equation (2.58) must possess negative values. Then the coefficients of equation (2.59) should be positive. Even if the polynomial equation (say, $P(\lambda) = \lambda^2 + \alpha_1\lambda + \alpha_2$) have all the positive coefficients at $P(\lambda) = 0$, it is not necessary that the system is stable. The coefficients must satisfy the Hurwitz's

criteria:

$$\Delta_1 = \alpha_1 > 0, \tag{2.60}$$

$$\Delta_2 = \begin{vmatrix} \alpha_1 & 0 \\ 1 & \alpha_2 \end{vmatrix} > 0. \tag{2.61}$$

The system can be stable if and only if all the leading principle minors of Hurwitz's matrices possess positive values.

### 2.8.2 Bifurcation Analysis

In the study of the dynamics of complex system, the distinctions between 'simple' and 'complex'; 'order' and 'disorder' are important. Bifurcation analysis can be employed as a decision making process. Dissipative and irreversible nature of many physical systems made them asymptotically stable. This kind of stability raises an ability to damp the effect of any perturbation acting on the system. Particularly, this property can distinguish the dissipative system from the conservative systems [8].

#### Hopf Bifurcation

At an equilibrium point or steady state, a function posses a fixed value. The next move is to analyze the stability of the system at the equilibrium point. The Jacobian of the dynamical system would be the ingredient to determine the stability of the system at an equilibrium point [148]. The system undergoes Hopf bifurcation when it posses complex conjugate eigenvalues passing through imaginary axis, i.e., $\mathrm{Re}(\lambda) > 0$ and $\mathrm{Im}(\lambda) \neq 0$. In summary, the system should satisfy the condition: $(i)$ A system has an equilibrium point, and $(ii)$ Jacobian determinant $|J - \lambda I|$ should have a pair

of complex conjugate eigenvalues.

To know more about Hopf bifurcation, let us examine a two dimensional system having a stable fixed point. The eigenvalues of the Jacobian of the system $(\lambda_1, \lambda_2)$ have complex values passing through the imaginary axis. The system equations in Cartesian co-ordinates are given by:

$$\frac{\partial x}{\partial t} = \mu x + y - x^3, \tag{2.62}$$

$$\frac{\partial y}{\partial t} = -x + \mu y + 2y^3. \tag{2.63}$$

The equilibrium point for the system can be identified as $(x_0, y_0) = (0, 0)$.

**Supercritical Hopf Bifurcation**

Let us suppose a physical system settles to an equilibrium position–the system tends to stabilize. Now, if a dissipation comes into play, then the system will lose its stability. The supercritical Hopf bifurcation occurs when the stable spiral of phase space changes to unstable spiral. Figure (2.8a) shows the inwards spiral converging towards an equilibrium point. In this example, the equilibrium point lies at an origin. The bifurcation parameter is $\mu$. The phase portraits for $\mu < 0$, $\mu = 0$ and $\mu > 0$ are shown in Figure (2.8). For $\mu < 0$, the origin $(0, 0)$ is a stable spiral, and for $\mu > 0$ an unstable spiral is formed. The Jacobian matrix at origin can be given by:

$$J = \begin{bmatrix} \mu & 1 \\ -1 & \mu \end{bmatrix}. \tag{2.64}$$

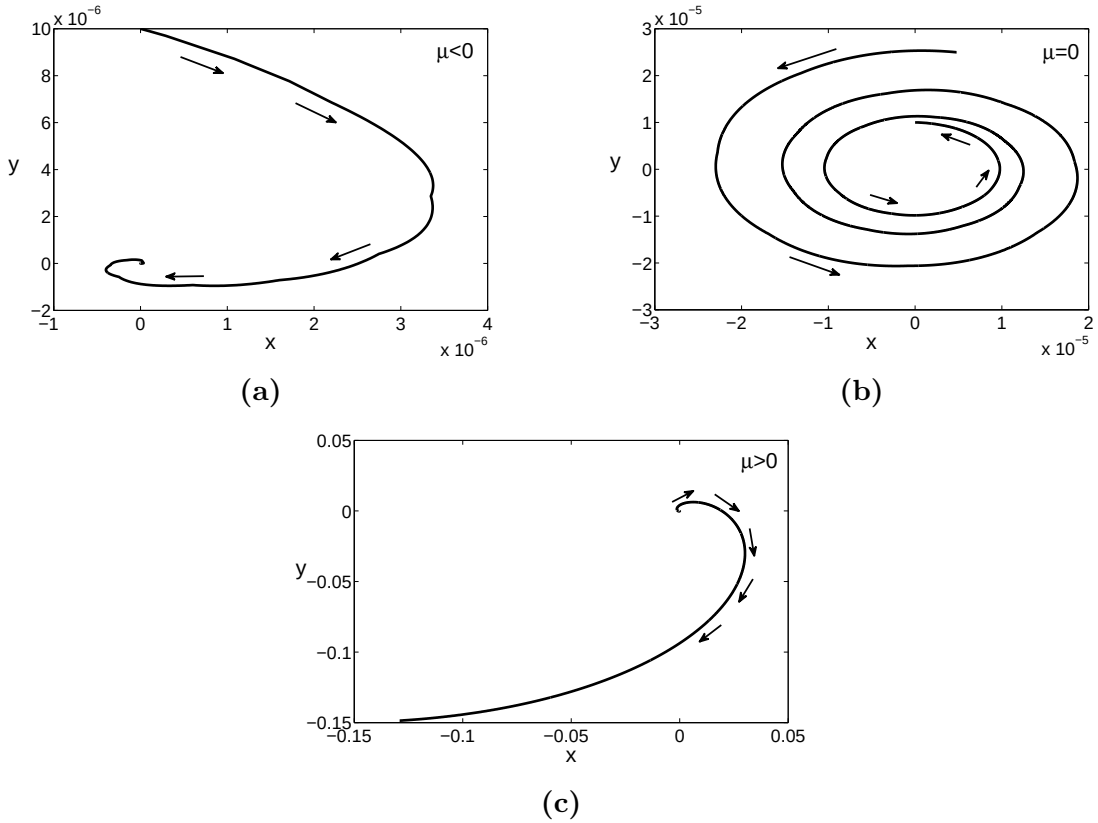


**Figure 2.8:** Phase portraits of equations (2.62) and (2.63). (a) $\mu < 0$ generates the inwards spiral or *supercritical* Hopf bifurcation, (b) $\mu = 0$ generates the limit cycle which shrinks to the equilibrium point, here, the origin or *subcritical* Hopf bifurcation, (c) $\mu > 0$ generates the outward spiral.

The corresponding eigenvalues for the system are given by:

$$\lambda = \mu \pm i. \tag{2.65}$$

As expected for the systems exhibiting Hopf bifurcation, the eigenvalues are complex conjugate with real part lying on the negative real axis for the stable system.

### Subcritical Hopf Bifurcation

A subcritical bifurcation for the system occurs at $\mu = 0$ (Figure (2.8b)). At this point, an unstable cycle shrinks towards the origin or to an equilibrium point. For $\mu > 0$, the large amplitude oscillations start to grow. Interestingly, once large amplitude oscillations start to grow, they can not be reversed by bringing $\mu$ back to zero. These large

oscillations would stop growing at a point where stable and unstable limit cycles meet and annihilate each other. This phenomenon of killing large amplitude oscillations can be described by Global bifurcations, such as, saddle node, infinite period or homoclinic bifurcations [149].

# Chapter 3

## Generation and Stability of Cavity Solitons: Analytical-Numerical Approach

## 3.1 Cavity Soliton in VCSEL-SA-FSF

With the fundamental knowledge of CS and its related mechanism already elaborated in previous chapter, we now proceed to investigate the generation and stability of CS in VCSEL with different nonlinearity and coupled with FSF. We considered a VCSEL with SA and coupled with FSF (VCSEL-SA-FSF) to explore the existence of CS. In context of the mean-field theory, the cavity field ($E(r,t)$) and feedback field ($F(r,t)$) are represented through the following dynamical equations along with the rate equations of the carrier densities for active and passive materials [14, 121, 150, 151].

$$\frac{\partial E}{\partial t} = [-(1-i\theta) + (1-i\alpha)d_a + (1-i\beta)d_p + i\nabla_{\perp}^2]E + F, \tag{3.1}$$

$$\frac{\partial d_a}{\partial t} = c_a[d_a(1+|E|^2) - \mu], \tag{3.2}$$

$$\frac{\partial d_p}{\partial t} = c_p[d_p(1+s|E|^2) + \gamma], \tag{3.3}$$

$$\frac{\partial F}{\partial t} = -(\lambda + i\Omega_0)F + \sigma\lambda E. \tag{3.4}$$

Equations (3.1)- (3.4) can be derived from the Maxwell-Bloch equations for a two level system within the mean field limit where the transmission coefficient assumes very small value. This confines the system within purely dispersive limit and reducing the soliton dynamics to the single longitudnal mode. Also the model holds for a Kerr medium under the generalized mean field limit. A scheme to derive such rate equations is provided in section 2.6.2. Here, an external cavity is considered to be short enough to introduce negligible delay in the system. Otherwise, presence of a significant delay may lead to chaotic behavior of the CS [152]. In view of the cylindrical geometry of VCSEL, symmetric coordinates are best fitted to the dynamical equation. Here, $r$ is the transverse spatial co-ordinate and $t$ is time normalized to the cavity round-trip period. The contribution of different terms in the equations (3.1)- (3.4) is described in the following lines. The first term on right hand side describes the linear losses sustained by the system. The normalized cavity loss is represented by the unity term. The detuning parameter $\theta$ measures the mismatch between the frequencies of the feedback and cavity fields. The value of $\theta$ should to be small in order to reduce linear losses in the system due to detuning. $\alpha$ and $\mu$ , respectively, represent the line-width enhancement factor and pump parameter for active materials, while those for passive materials are given by $\beta$ and $\gamma$, respectively. Usually $\alpha$ and $\beta$ possess positive and large values for VCSEL, while the line-width parameter for active medium is always greater than that in passive medium ($\alpha >> \beta$) [121]. Carrier densities for active and passive material in the VCSEL are represented by second and third terms, respectively, on the right hand side of equation (3.1). In active layer of semi-conductor micro-resonator, the carrier density is represented by $d_a$, whereas, for passive layer, it is represented by $d_p$. $\nabla_\perp^2 (= r^{(1-D)} \frac{\partial}{\partial r}(r^{(D-1)} \frac{\partial}{\partial r}))$ is the transverse Laplacian that acts as an diffraction

operator in D-dimensional system. In equations (3.2) and (3.3), the terms $c_a$ and $c_p$ represent the ratio of the photon lifetime to the carrier lifetime in the active and passive materials, respectively. It is assumed that $c_a > c_p$, as the inverse of the carrier lifetime increases with the carrier density in the semiconductor material [14]. $s$ represents saturation strength of the nonlinearity and is defined as $s = (a_p c_a)/(a_a c_p)$, where, $a_a$ and $a_p$ represent the slopes of differential gain as a function of carrier densities in active and passive materials, respectively [14]. Coupling of the linear feedback field to the cavity field leads to the stability of the system [121]. In most of the cases, the FSF is, generally, provided by a VBG; a glass Bragg reflector with single peak output [4]. In equation (3.4), $\sigma$ represents a positive feedback strength to provide the sustainable gain in the cavity. As the gain cannot be cent percent, therefore, its value always lies in the range of 0 and 1. The frequency selection of feedback element is accomplished by a filter. Here, $\lambda$ represents the band-width of filter reflection, and the corresponding resonance frequency of feedback field is represented by $\Omega_0$ [1, 14, 121]. Pump of suitable duration and transverse profile excites the CS in the system, while the continuous feedback helps in sustaining such localized structures, i.e., CS. The trivial homogeneous steady state (HSS) solutions for the system of equations (3.1)-(3.4) are given as:

$$E_0 = 0,\ d_{a0} = \mu,\ d_{p0} = -\gamma,\ F = 0. \tag{3.5}$$

The system of equations (equations (3.1)-(3.4)) also has a set of non-trivial HSS solution, which are determined as follows:

$$E_0 = \sqrt{I_0} e^{i[qx-(\omega+q^2)t]}, \tag{3.6}$$

$$d_{a0} = \frac{\mu}{1 + I_0}, \tag{3.7}$$

$$d_{p0} = -\frac{\gamma}{1 + sI_0}. \tag{3.8}$$

$$F = \frac{\sigma\lambda}{\lambda + i\Omega_0} E. \tag{3.9}$$

Here, $q$ is the transverse wave vector and hence equation (3.6) represents a tilted traveling wave solution. Equation (3.6) can be further simplified to $E_0 = \sqrt{I_0}e^{-i\omega t}$ by setting $q = 0$. This simplification is allowed for a system having no wave-vector selection mechanism [14]. Moreover, the absence of diffusion term in the cavity field equation preserves the degeneracy of wave-vector. Substituting the non-trivial HSS solution equations (3.7)-(3.9) in the governing equation (3.1), we get:

$$\frac{\partial E}{\partial t} = [-(1 - i\theta) + \frac{\mu(1 - i\alpha)}{1 + |E|^2} - \frac{\gamma(1 - i\beta)}{1 + s|E|^2} + i\nabla_\perp^2]E + (a - ib)E, \tag{3.10}$$

where, $a = \sigma\lambda^2/(\lambda^2 + \Omega_0^2)$ and $b = \sigma\lambda\Omega_0/(\lambda^2 + \Omega_0^2)$. Equation (3.10) resembles with a CGLE with higher order nonlinearity. On right hand side of equation (3.10), the first term describes the linear loss in the system, the second and third terms represent the saturating nonlinearity corresponding to the active and passive materials, respectively. $(a-ib)E$ is the feedback contribution. Equating the real parts on both sides of equation (3.10), one gets the following relation of field intensity $I_0$ with the cavity parameters:

$$\frac{\mu}{1 + I_0} = 1 - a + \frac{\gamma}{1 + sI_0}, \tag{3.11}$$

The imaginary part in equation (3.10) is negligibly small to modify the diffraction coefficient of the cavity field, thus, this can be omitted. On the other hand, the real part is significantly crucial and contribute towards the determination of the diffraction

coefficient of the cavity field [14, 151]. As a result, the reference frequency ($\omega$) of the cavity field is controlled by the imaginary part of the governing equation (equation (3.10)) and can be represented as follows:

$$\omega = \alpha(1-a) - b - \theta + \frac{\gamma(\alpha-\beta)}{1+sI_0}. \tag{3.12}$$

That means that in VCSEL-SA-FSF, the reference frequency of the cavity field is intensity dependent when line-width enhancement parameters for active and passive materials are unequal (i.e. for $\alpha \neq \beta$). Whereas, $\omega$ is always intensity independent for VCSEL-FSF model. Now, the laser frequency is a function of the feedback field parameters ($\sigma$, $\Omega_0$ and $\lambda$) and detuning parameter $\theta$. The increase in feedback strength linearly decreases the value of $\omega$ with a slope of $-0.770$ (Figure (3.1)). Also, for a given feedback strength, $\omega$-value linearly decreases with an increase in the value of detuning parameter.

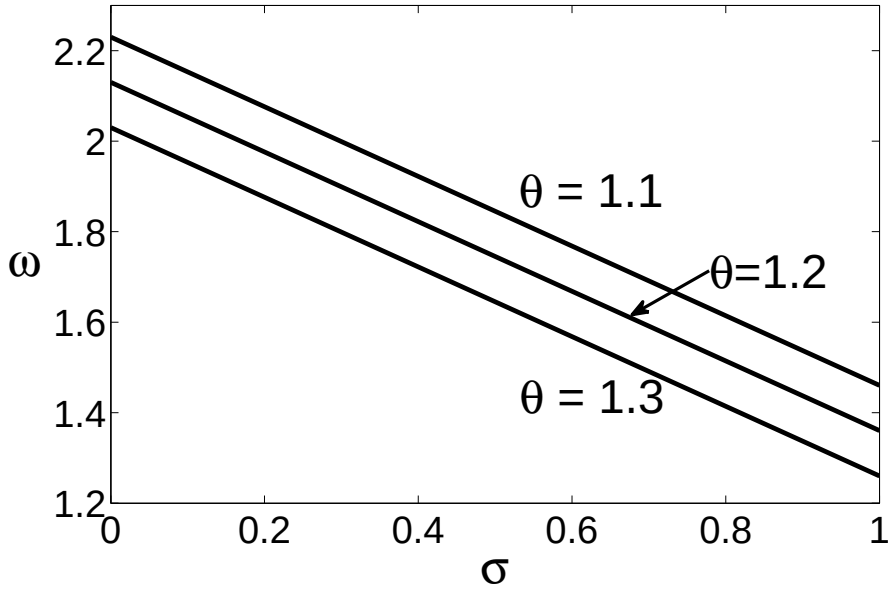


**Figure 3.1:** Variation of reference frequency ($\omega$) with respect to feedback strength ($\sigma$) at a constant laser threshold with varying detuning strength ($\theta$). Here, $\alpha = 2.7$, $\mu = 1.37$, $\gamma = 0.5$, $\beta = 0$, $s = 10$, $\lambda = 0.5$, $\Omega_0 = 1.7$.

However, the stability criteria of non-trivial HSS solution does not depend on the

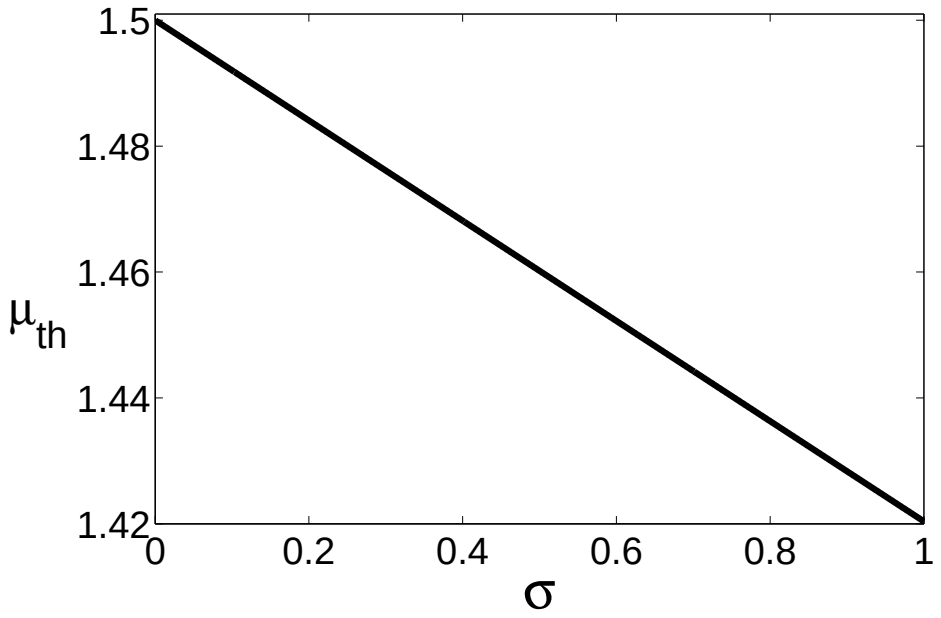


**Figure 3.2:** Variation of threshold pump power ($\mu$) with the varying feedback strength ($\sigma$), rest of parameters are kept same as in Figure (3.1).

modification in the value of $\omega$. Further, using equation (3.11), the pump power at laser threshold ($I_0 = 0$) is found to be:

$$\mu_{th} = 1 - a + \gamma. \tag{3.13}$$

The presence of 'a', i.e., FSF leads to the reduction in the value of $\mu_{th}$ for VCSEL-SA-FSF configuration. The rate of decrease in the $\mu_{th}$-value with respect to $\sigma$-value is linear with a slope of $-0.079$ (Figure (3.2)). On substituting the laser threshold condition (equation (3.13)) in the equation (3.11) the following relation between the saturation parameter $s$ and cavity parameters is obtained:

$$s > 1 + \frac{1 - a}{\gamma}. \tag{3.14}$$

Equation (3.14) gives an essential condition for the bistability in the system. The parabolic shape of non-trivial HSS solution (Figure (3.3)) when plotted with respect to pump parameter $\mu$ leads to bistability. The following equation gives the turning

point value of the pump parameter in the bistable parabolic curve:

$$\mu_{tp} = \frac{(\sqrt{(1-a)(s-1)} + \sqrt{\gamma})^2}{s}. \tag{3.15}$$

Turning point is the point where the variation of function with respect to bifurcation parameter approaches to infinity. At a point where two distinct solution curves intersect or cross each other is known as saddle-node bifurcation. In Figure (3.3), turning point ($\mu_{tp}$ ) represents the saddle-node bifurcation. Such bifurcation is also referred as turning point bifurcation or fold bifurcation [149]. It is evident that turning point

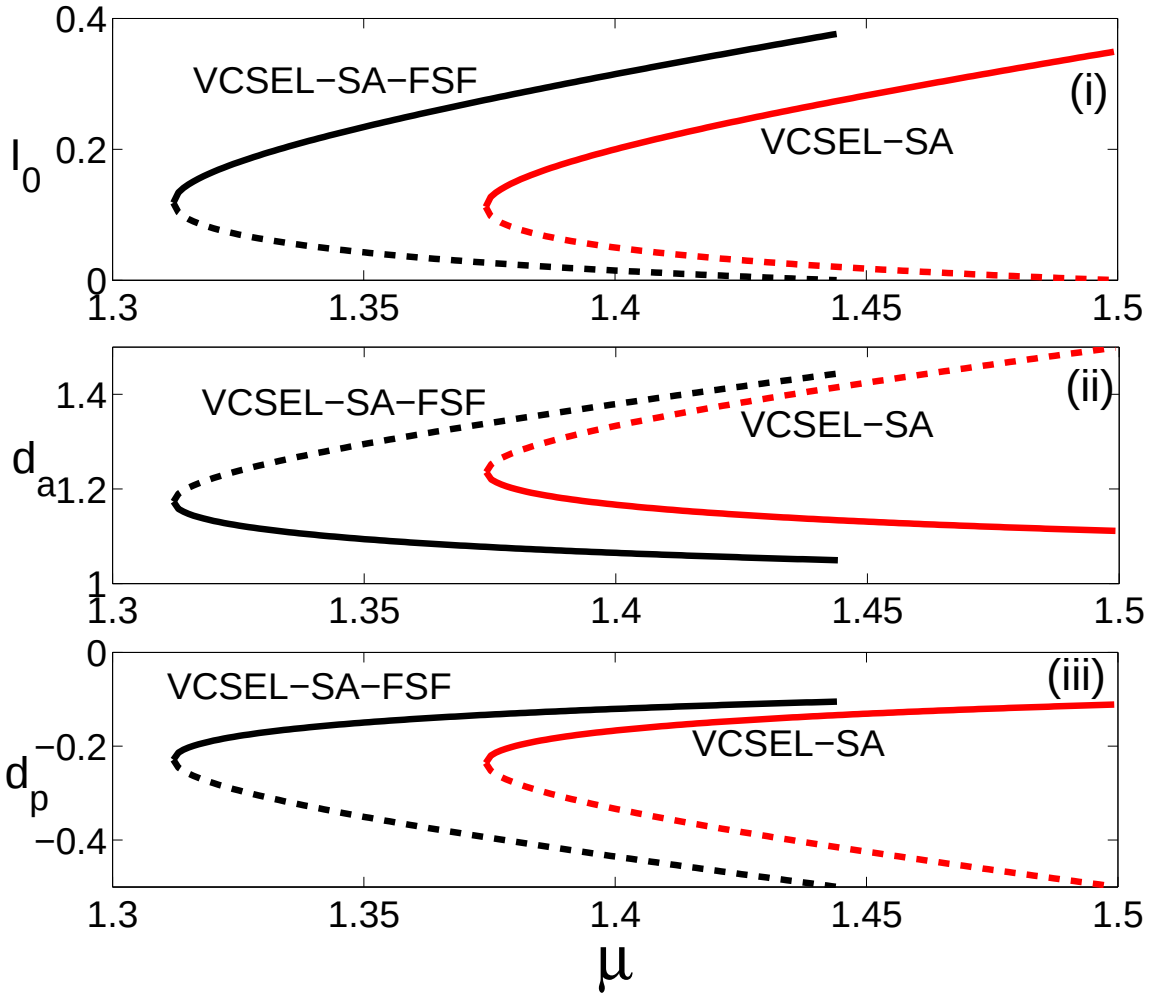


**Figure 3.3:** Comparison of HSS solutions in a model with VCSEL coupled with SA only and SA-FSF: $(i)$ the field intensity ($I_0$), $(ii)$ carrier density for active medium ($d_a$), $(iii)$ carrier density for the passive medium ($d_p$)with respect to pump parameter ($\mu$), at constant feedback strength ($\sigma = 0.7$), rest of parameters are kept same as in Figure (3.1).

of the pump parameter ($\mu_{tp}$) is controlled by parameters of the cavity and feedback field, such as, $s$, $\gamma$, $\sigma$, $\lambda$ and $\Omega_0$. The value of $\mu_{tp}$ linearly decreases with the increase in $\sigma$-value (Figure (3.4) with slope = $-0.088$). Turning back to Figure (3.3) to have an idea of stability as well as comparison between VCSEL-SA and VCSEL-SA-FSF configuration, $\mu_{th} = 1.5$ and $\mu_{tp} = 1.347$ for a model with VCSEL-SA configuration, whereas, $\mu_{th} = 1.458$ and $\mu_{tp} = 1.327$ for model with VCSEL-SA-FSF configuration. Thus, with the inclusion of FSF, both the threshold and turning point values of pump power get lowered down. Moreover, the operating range of pump parameter for sta-

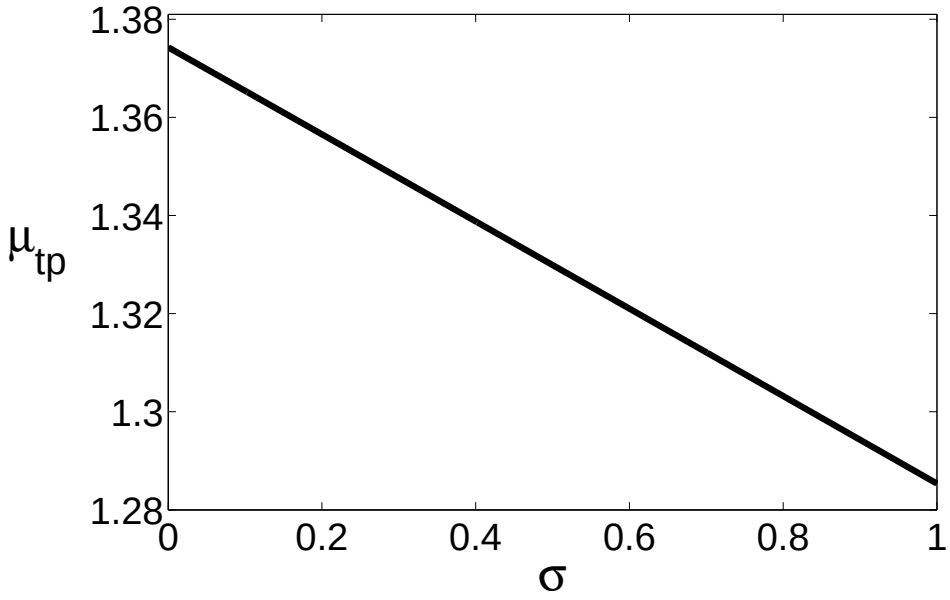


**Figure 3.4:** Variation of turning point value of pump power ($\mu_{tp}$) with respect to the feedback strength ($\sigma$), rest of parameters are kept same as in Figure (3.1).

ble CS, i.e., ($\Delta\mu = \mu_{th} - \mu_{tp}$), extends from 0.126 to 0.131 ($\approx 4\%$). Approximately, around 6% enhancement in the value of $\Delta\mu$ is calculated by increasing the feedback strength. Similar enhancement is determined for both $d_a$ and $d_p$. The solid lines of the curve in Figure (3.3) is Hopf unstable if $\mu < \mu_H$, where $\mu_H = \gamma s$ and $\mu_H$ assumes same value as stated in ref. [14]. The HSS is stable only for $\mu < \mu_{th}$. The dashed lines represent the unstable solution. The regions corresponding to the stable,

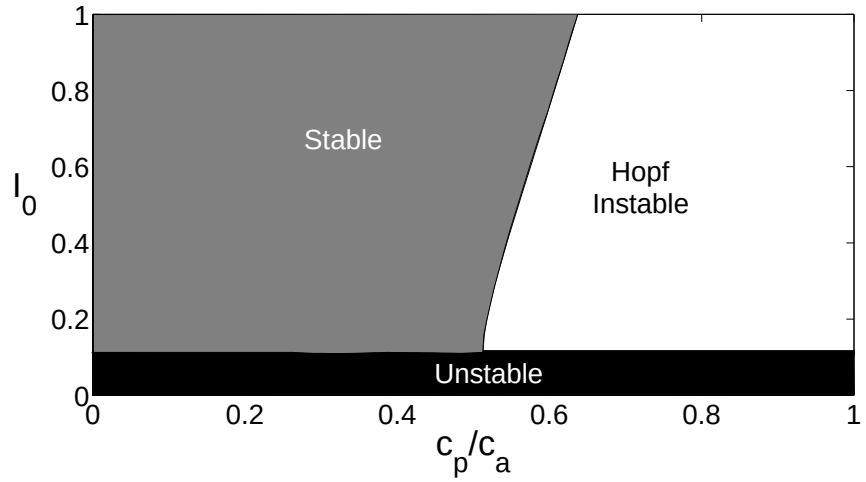


**(a)**

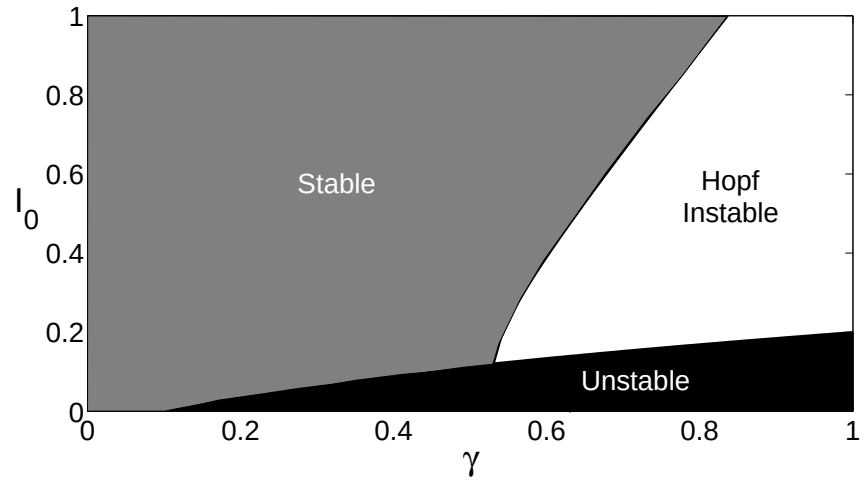


**(b)**

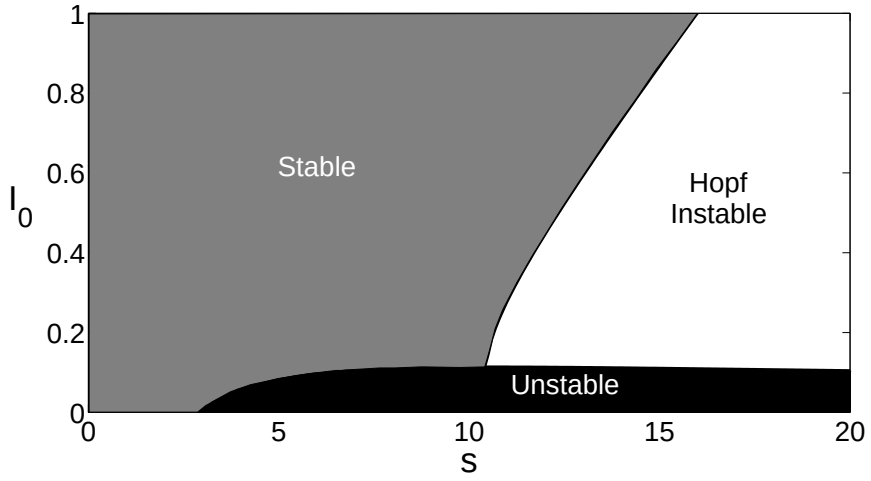


**(c)**

**Figure 3.5:** Stability plots showing the regions corresponding to the stable, Hopf instable and unstable regions for VCSEL-SA-FSF configuration. Plot between $(a)$ the ratio of the photon to carrier lifetime in passive and active medium $(c_p/c_a)$ with respect to field intensity $(I_0)$ at $s = 10$, $\gamma = 0.5$, $(b)$ pump parameter in passive medium with respect to the intensity at $c_p = 0.005$, $s = 10$, $(c)$ saturation parameter with respect to the input field intensity at $c_p = 0.005$, $\gamma = 0.5$, with $c_a = 0.01$ and rest of the parameters are as in Figure (3.1).

unstable and Hopf instability are identified in Figures (3.5a), (3.5b) and (3.5c) with respect to different cavity parameters, such as, ratio of photon to carrier lifetime, field intensity and saturation strength, respectively. Other parameters also significantly affect the stability of the system. However, these parameters were chosen carefully as the limiting conditions for the pump parameters (such as, threshold value, turning point value and Hopf unstable values) are very sensitive to them. Eigenvalues of the system determine the boundaries of the stability region. In Hopf unstable region, the eigenvalues are purely complex. The stable limit cycle decays to attractors (inward spiral) or repellers (outward spiral) as the system moves away from the boundary of the stable region to the Hopf instable region. A comparison with similar Figures for a system with VCSEL-SA model [14] reveals that Hopf instability region increases with the inclusion of FSF in the system as the bifurcation point shift towards the origin with increasing feedback strength parameter.

The modified governing equation (equation (3.10)) can be studied considering the different higher orders of approximations of the SA terms for the active and passive materials. The following sections deal with the analytical analysis of the equation (3.10) with cubic and then with cubic-quintic approximations.

## 3.2 Cavity Soliton in Cubic Nonlinear Microcavity: a Variational Approach

The Kerr or the third order nonlinearity is the lowest order of nonlinearity, which has been studied widely in the context of CS [72, 73, 74, 75, 76, 84]. The stability and dynamics of solitons in Kerr order nonlinear medium has been well explored in the

literature. The existence criteria of 2-D soliton in Kerr cavity was investigated [73] CGLE has an important role in the mathematical modeling of the nonlinear cavity. In general, a solitary pulse is unstable in a CGLE-system. It can be stabilized by coupling a parallel dissipative equation in one dimension. A perturbed NLSE, which is equivalent to CGLE can also be stabilized by the same technique. In this line CGLE in two dimensions has been stabilized by its linear coupling to a linear dissipative equation [101, 102, 103, 153]. Using CGLE, ref. [67] has established the existence and stability of fundamental and vortical solitons in two dimensional system comprising of VCSEL coupled with the external feedback without delay. The analytical and numerical solutions have been reported for the phase invariant system exhibiting cubic nonlinearity. The first order expansion of the saturating nonlinear terms in equation (3.10) takes the following form upon expansion, i.e., $(1+|E|^2)^{-1} = 1-|E|^2$:

$$\frac{\partial E}{\partial t} = (m_1 + im_2)E + i\nabla_\perp^2 E + (m_3 + im_4)|E|^2 E. \tag{3.16}$$

where, $m_1 = \mu - 1 - \gamma + a$, $m_2 = \theta - \alpha\mu + \beta\gamma - b$, $m_3 = s\gamma - \mu$, $m_4 = \alpha\mu + s\gamma\beta$.

For the study of CSs only a few analytical methods are available. Thus, most of the investigation is based on numerical approach. A method based on separation of governing equation into two eigenvalue problems and using graphical solution gives an interesting way to find CS solutions [121]. However, the evolution of CS parameters are not very clear in that method. Variational method can be a suitable approach to study the existence and stability of the CSs. However, other than ref. [73], where variational method has been partially used, there is no report on complete investigation on CS with variational method. Here, equation (3.16) is solved with variational approach. Splitting of equation (3.16) into conservative (real) and dissipative (imaginary) parts

gives:

$$i\frac{\partial E}{\partial t} + m_2 E + \nabla_\perp^2 E + m_4|E|^2 E = Q, \tag{3.17}$$

and,

$$Q = im_1 E + im_3|E|^2 E. \tag{3.18}$$

The corresponding Lagrangian for the conservative and dissipative parts of equation (3.16) are given by the following equations, respectively:

$$\mathbb{L}_C = r^{D-1}\left[\frac{i}{2}\left(E\frac{\partial E^*}{\partial t} - E^*\frac{\partial E}{\partial t}\right) + \left|\frac{\partial E}{\partial r}\right|^2 - m_2|E|^2 - \frac{m_4}{2}|E|^4\right], \tag{3.19}$$

$$\mathbb{L}_Q = ir^{(D-1)}[m_1|E|^2 + \frac{m_4}{2}|E|^4]. \tag{3.20}$$

Assuming the symmetric trial function of Gaussian shape:

$$E = A\ exp\left(-\frac{r^2}{2R^2} + iCr^2 + i\phi\right). \tag{3.21}$$

where, $A$ is the amplitude, $R$ is the inverse width, $C$ is the chirp and $\phi$ is the phase of the input field envelop. In case of the conventional propagating soliton, the evolution axis is the propagation direction $z$, i.e., the evolution term is given by $\partial E/\partial z$, but the evolution of the CS parameter is studied with respect to time, i.e., $\partial E/\partial t$ is the evolution term. Therefore, the $z$ dependent parameters in the trial function are replaced by $t$ dependent parameters. The trial function (equation (3.21)) is substituted to equation (3.19) to get the reduced Lagrangian $L_C$. The total Lagrangian for the system is calculated by the following integration over the whole space in the symmetric co-ordinate system:

$$L_C = \int_\infty^\infty \mathbb{L}_C dr. \tag{3.22}$$

Upon integration, the total Lagrangian for the system exhibiting the Kerr nonlinearity is obtained as:

$$L_C = \left[\frac{A^2R^D}{2}\left(\frac{\partial\phi}{\partial t} - m_2\right) + \frac{D}{4}A^2R^{D+2}\left(\frac{\partial C}{\partial t} + \frac{1}{R^4} + 4C^2\right) - \frac{m_4}{4}A^4R^D 2^{-\frac{D}{2}}\right] \Gamma\left(\frac{D}{2}\right)(1 + (-1)^{D+1}). \tag{3.23}$$

where, $\Gamma$, is the gamma function. The variation of $L_C$ with respect to the amplitude ($A$), inverse width ($R$), chirp ($C$) and phase ($\phi$) gives rise to the following set of differential equations of the first order:

$$AR^D\left(\frac{\partial\phi}{\partial t} - m_2\right) + \frac{D}{2}AR^{D+2}\left(\frac{\partial C}{\partial t} + \frac{1}{R^4} + 4C^2\right) - m_4A^3R^D2^{-\frac{D}{2}} = 0, \tag{3.24}$$

$$\frac{D}{2}A^2R^{D-1}\left(\frac{\partial\phi}{\partial t} - m_2\right) + \frac{D}{4}(D+2)\left(\frac{\partial C}{\partial t} + \frac{1}{R^4} + 4C^2\right) - \frac{m_4}{4}DA^4R^{D-1}2^{-\frac{D}{2}}, \tag{3.25}$$

$$\frac{D}{4}\frac{d}{dt}\left(A^2R^{D+2}\right) - 2DCA^2R^{D+2} = \frac{m_1}{2}DA^2R^{D+2} + \frac{m_3}{4}DA^4R^{D+2}2^{-\frac{D}{2}}, \tag{3.26}$$

$$\frac{1}{2}\frac{d}{dt}(A^2R^D) = m_1A^2R^D + m_3A^4R^D2^{-\frac{D}{2}}. \tag{3.27}$$

The constants $m_3$ and $m_4$ are normalized as follows: $m_{30} = m_3 2^{-\frac{D}{2}-1}$ and $m_{40} = m_4 2^{-\frac{D}{2}-1}$. The equations (3.24) - (3.27) are solved to obtain the following evolution equations:

$$S_1 = \frac{dA}{dt} = 2DAC - m_1A - \left(\frac{D}{2} + 2\right)m_{30}A^4, \tag{3.28}$$

$$S_2 = \frac{dR}{dt} = 4CR - m_{30}A^2R, \tag{3.29}$$

$$S_3 = \frac{dC}{dt} = \frac{1}{R^4} - 4C^2 - m_{40}\frac{A^2}{R^2}, \tag{3.30}$$

$$\frac{d\phi}{dt} = m_2 + \left(\frac{D}{2} + 2\right) m_{40}A^2 - \frac{D}{R^2}. \tag{3.31}$$

The corresponding evolution of the soliton parameters $A$, $R$, $C$ and $\phi$ are shown in Figures (3.6) and (3.7) for $D = 1$ and 2, respectively. The steady state solutions for the system are as follows:

$$A_s = \sqrt{-\frac{m_1}{2m_{30}}}, \tag{3.32}$$

$$C_s = -\frac{m_1}{8}, \tag{3.33}$$

$$R_{s\pm} = \sqrt{\frac{4m_{40} \mp 4\sqrt{m_{40}^2 + m_{30}^2}}{m_1 m_{30}}}. \tag{3.34}$$

These steady state values ($A$, $R$, $C$ and $\phi$) constitute the initial values for solving eqn (3.28)-(3.31). The insets of Figures (3.6) and (3.7) show that $A$, $R$, $C$ and $\phi$ are not constant rather shows small periodic oscillations. For the better insight, A-R phase plot has been drawn for D=1 (Figure (3.8a)) and 2 (Figure (3.8c)). Both the plots confirm bound periodic oscillation of $A$ and $R$ with time. The terms $A^2R^{D+2}$ and $A^2R^D$ in equations (3.26) and (3.27), respectively, represent that the power for the system. Figures (3.8b) and (3.8d) for $D = 1$ and 2, respectively, show that the power does not remain constant, but show bound state oscillations with time.

After obtaining the evolution of the soliton parameters, it is necessary to study the stability of the system. Lyapunov exponents method along with the Hurwitz's

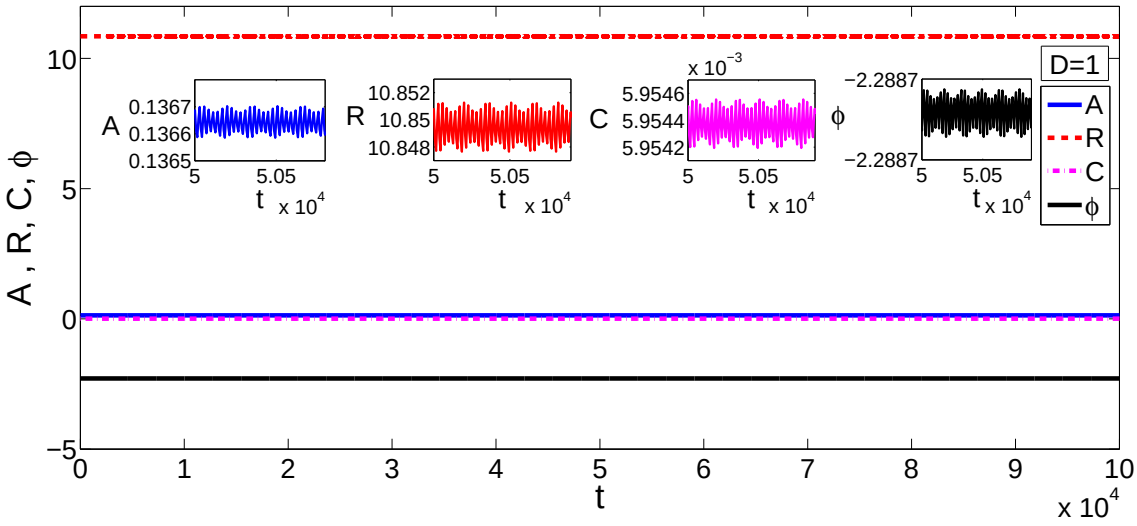


**Figure 3.6:** The steady state evolution of $A$, $R$, $C$ and $\phi$ in D=1. Insets show the zoom in view of the time-evolution of $(a)$ $A$, $(b)$ $R$, $(c)$ $C$ and $(d)$ $\phi$. Here, $\theta = 1.2$, $\alpha = 2.7$, $\beta = 1$, $\lambda = 0.03$, $\gamma = 0.5$, $s = 10$ and $\Omega_0 = 0.1$.

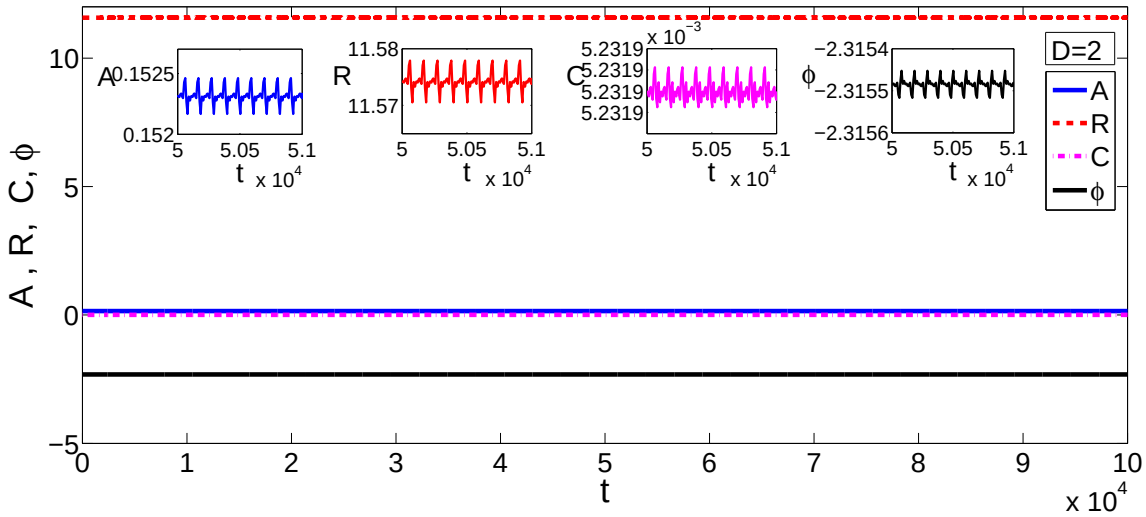


**Figure 3.7:** The steady state evolution of $A$, $R$, $C$ and $\phi$ in D=2. Parameter used are same as stated in Figure (3.6). Insets show the zoom in view of the time-evolution of $(a)$ $A$, $(b)$ $R$, $(c)$ $C$ and $(d)$ $\phi$.

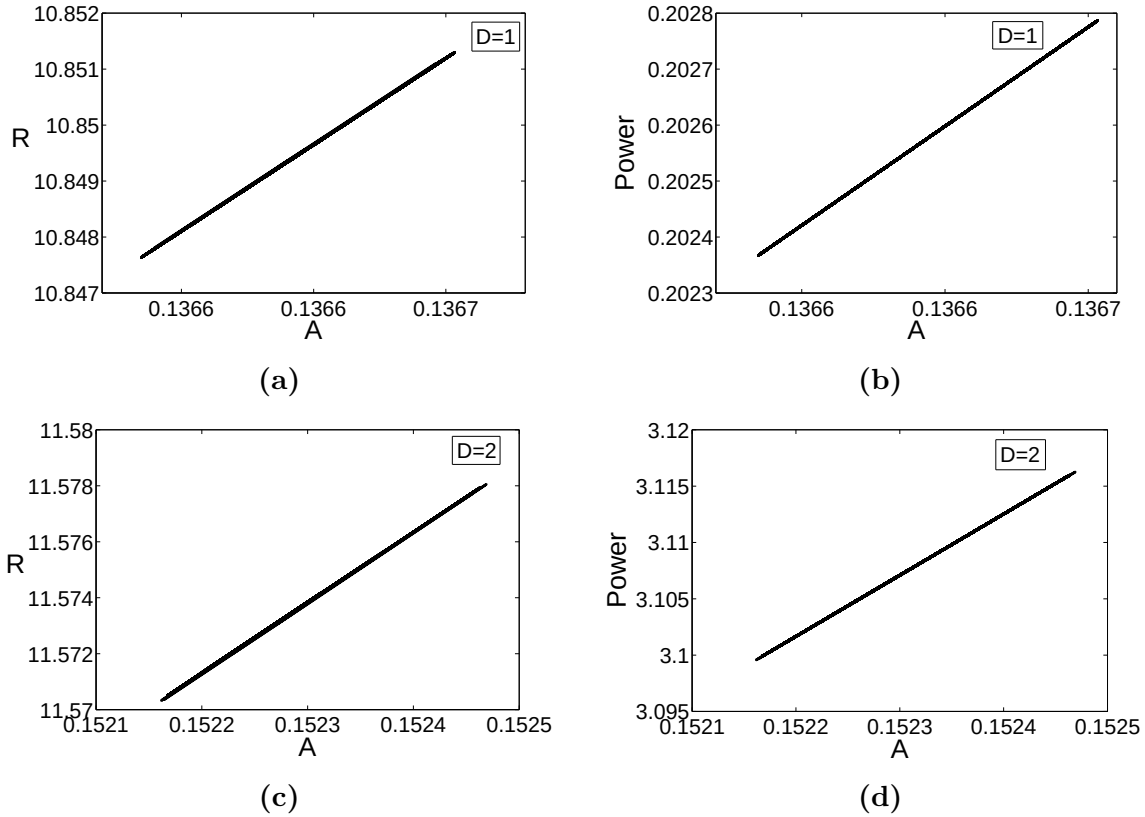


**Figure 3.8:** $(A, R)$ phase plots for (a)$D = 1$ and (c) $D = 2$. Variation of versus soliton power with $A$ for (b)$D = 1$, (d) $D = 2$. Soliton power is not constant, but is bound as the system evolves.

criteria is followed to establish stability of the system. The Jacobian determinant corresponding to the evolution equations (3.28), (3.29) and (3.30) is represented by:

$$\begin{vmatrix} \frac{\partial S_1}{\partial A} - \lambda & \frac{\partial S_1}{\partial R} & \frac{\partial S_1}{\partial C} \\ \frac{\partial S_2}{\partial A} & \frac{\partial S_2}{\partial R} - \lambda & \frac{\partial S_2}{\partial C} \\ \frac{\partial S_3}{\partial A} & \frac{\partial S_3}{\partial R} & \frac{\partial S_3}{\partial C} - \lambda \end{vmatrix}_{eq} = 0. \tag{3.35}$$

where, $\lambda$ is the eigenvalue of the system. The corresponding eigenvalue equation for the system is represented by the following polynomial equation:

$$\lambda^3 + \alpha_1\lambda^2 + \alpha_2\lambda + \alpha_3 = 0. \tag{3.36}$$

where, the coefficients of the eigenvalue equation satisfy the following relations:

$$\alpha_1 = 2(D-2)C - m_1 - \left(\frac{3D}{2}+7\right) m_{30}A^2, \tag{3.37}$$

$$\alpha_2 = 4(D+8)m_{30}A^2C + m_{30}\left(m_1 + 3m_{30}\left(\frac{D}{2}+2\right)\right)A^2 + 4m_{40}(D-2)\frac{A^2}{R^2} \\ -8(D+4)C^2 + 4m_1C + \frac{16}{R^4}, \tag{3.38}$$

$$\alpha_3 = 12m_{30}(-(D+4)+m_{40})\frac{A^4}{R^2} - 8m_1m_{40}\frac{A^2}{R^2} + 8(5D+12)m_{30}\frac{A^2}{R^4} \\ -16m_{30}A^2C^2 + m_{30}(8m_1 - 36(D+4))A^2C + \frac{16}{R^4}(-2DC+m_1) \\ +64DC^2 - 32m_1C. \tag{3.39}$$

The nature of coefficients of the eigenvalue equation determines the stability of the system. To achieve stable CS, Hurwitz's conditions are to be essentially satisfied. In other words, the Hurwitz's coefficients must be positive and real. In the present case, the Hurwitz's constants attain the positive values for the combination of the parameter values: $\alpha = 2.7$, $\beta = 1$, $\mu = 1.3919$, $\gamma = 0.5$, $s = 10$, $\theta = 1.2$, $\lambda = 0.03$ and $\Omega_0 = 0.1$. More detailed stability analysis is studied for the system with cubic-quintic nonlinearity, which is discussed in the following section of this chapter.

## 3.3 Cavity Soliton in Cubic-Quintic Nonlinear Microcavity: a Variational Approach

Higher order nonlinearity has an important role in the generation and stability of CS. The same is investigated and presented in this section. Expanding the terms repre-

senting the saturating nonlinearity, i.e., $((1+|E|^2)^{-1}$ and $(1+s|E|^2)^{-1})$, in equation (3.10) till the second order approximation and rearranging, the following cubic-quintic CGLE (CGLE5) is obtained:

$$\frac{\partial E}{\partial t} = i\nabla_{\perp}^2 E + (m_1 + im_2)E + (m_3 + im_4)|E|^2 E + (m_5 + im_6)|E|^4 E. \qquad (3.40)$$

Here, $m_1 = \mu - 1 - \gamma + a$, $m_2 = \theta - \alpha\mu + \beta\gamma - b$, $m_3 = s\gamma - \mu$, $m_4 = \alpha\mu + s\gamma\beta$, $m_5 = \mu - s^2\gamma$ and $m_6 = s^2\beta\gamma - \alpha\mu$. Although, the magnitude of quintic nonlinearity is much smaller in comparison to the cubic (Kerr) term, the quintic terms significantly modify the dynamics of the system. Moreover, being a higher order nonlinearity, quintic nonlinearity plays an important role in the stability of a soliton solution. The CGLE5 (i.e. equation (3.10)) is non-integrable with respect to available analytical methods. However, the exact solution can be obtained only in some simplified cases [154, 155]. Equation (3.40) and its cubic counterpart equation (3.16) in previous section is well studied in the context of conventional propagating soliton, but it has never been used for the investigation of CS, which can be considered as a "soliton in a box", or a bound state of a propagating soliton bouncing between the cavity mirrors. Noteworthy point is that the evolution of conventional soliton is described along propagation length ($z$), while that for CS is to be described with respect to time. Equation (3.40) is made suitable for such a special case by ($i$) replacing $z$ by time $t$, which is normalized to the cavity round trip time and ($ii$) considering all the CS parameters as a function of the normalized time instead of function of $z$. The same idea was used for equation (3.16). Now, equation (3.40) is not only compatible with CS system, but also can enjoy all the benefits of already known features of CGLE.

The most common approach is to solve the CGLE5 by numerical methods. However, to get deeper insight of the behavior of the individual parameters, the necessity of the analytic approach is indispensable. Therefore, alike previous section, here a complete variational method based approach is again adopted to study the CGLE5. Equation (3.40) can be rewritten as:

$$i\frac{\partial E}{\partial t} + \nabla_{\perp}^{2}E + m_2 E + m_4|E|^2E + m_6|E|^4E = Q, \tag{3.41}$$

where,

$$Q = i(m_1 E + m_3|E|^2E + m_5|E|^4E), \tag{3.42}$$

is the dissipative part of equation (3.40), in absence of which, equation (3.41) turns into a conservative NLSE. The Lagrangian corresponding to the conservative part, i.e., the left hand side of equation (3.41) is given by:

$$\mathbb{L}_C = r^{(D-1)}[\frac{i}{2}(E\frac{\partial E^*}{\partial t} - E^*\frac{\partial E}{\partial t}) + |\frac{\partial E}{\partial r}|^2 - m_2|E|^2 - \frac{m_4}{2}|E|^4 - \frac{m_6}{3}|E|^6]. \tag{3.43}$$

The Lagrangian for the dissipative part of equation (3.40) (i.e., equation (3.42)) can be constructed as:

$$\mathbb{L}_Q = ir^{(D-1)}[m_1|E|^2 + \frac{m_4}{2}|E|^4 + \frac{m_6}{3}|E|^6] \tag{3.44}$$

To proceed ahead, a suitable ansatz or trial function needs to be chosen. The choice of trial function is always crucial for the success of the variational method. The exact soliton ansatz for this kind of equation (3.41) is reported by Pushkarov *et al.* [156] and de Anglis [157]. However, in most of the cases, theoretically predicted and experimentally obtained CSs are of bell-shaped intensity profile. *Sech* is the

most preferred profile function for analytical and numerical modeling [121]. Gaussian profile is also widely used profile function [136, 158] For the present case a Gaussian trial function of the following form, which is very close to *sech* profile yet easier for mathematical treatment, is used [136].

$$E(r,t) = A\ exp(-\frac{r^2}{2R^2} + iCr^2 + i\phi), \tag{3.45}$$

Here, $A(t)$, $R(t)$, $C(t)$ and $\phi(t)$ are functions of $t$ and refer to amplitude, width, chirp and phase of the profile, respectively. Notably, the parameters are presented as functions of time. Substituting the aforesaid trial function equation (3.45) in equation (3.43), the reduced Lagrangian for the conservative part of the dynamical equation takes the following form:

$$\begin{aligned}\mathbb{L}_C = r^{(D-1)}[(\frac{\partial\phi}{\partial t} - m_2)A^2 exp(-\frac{r^2}{R^2}) + (\frac{\partial C}{\partial t} + \frac{1}{R^4} + 4C^2)A^2 r^2 exp(-\frac{r^2}{R^2}) \\ -\frac{m_4}{2}A^4 exp(-\frac{2r^2}{R^2}) - \frac{m_6}{3}A^6 exp(-\frac{3r^2}{R^2})].\end{aligned} \tag{3.46}$$

The total Lagrangian can be determined as:

$$L_C = \int \mathbb{L}_C dr. \tag{3.47}$$

On,

$$\begin{aligned}L_C = [\frac{A^2 R^D}{2}(\frac{\partial\phi}{\partial t} - m_{20}) + \frac{D}{4}A^2 R^{(D+2)}(\frac{\partial C}{\partial t} + \frac{1}{R^4} + 4C^2) \\ -\frac{m_{40}}{2}A^4 R^D - \frac{m_{60}}{2}A^6 R^D]\Gamma(\frac{D}{2})(1 + (-1)^{(D+1)}),\end{aligned} \tag{3.48}$$

where, $\Gamma$, is the gamma function. The cavity parameters $m_1$, $m_2$, $m_3$, $m_4$, $m_5$ and $m_6$ are further normalized, such as $m_{10} = m_1$, $m_{20} = m_2$, $m_{30} = m_3 2^{(-\frac{D}{2}-1)}$,

$m_{40} = m_4 2^{(-\frac{D}{2}-1)}$, $m_{50} = m_5 3^{(-\frac{D}{2}-1)}$ and $m_{60} = m_6 3^{(-\frac{D}{2}-1)}$ . The Euler-Lagrangian equation for dissipative system is defined as [136]:

$$\frac{\partial}{\partial t}(\frac{\partial L_C}{\partial \eta'}) - \frac{\partial L_C}{\partial \eta} = 2Re \int r^{(D-1)} Q \frac{\partial E^*}{\partial \eta} dr. \tag{3.49}$$

where, $\eta$ is the arbitrary soliton parameters and can take the form, i.e., $\eta(t) = A(t)$, $R(t)$, $C(t)$ and $\phi(t)$, where, $\eta' = \partial\eta/\partial t$ and $E^*$ is the complex conjugate of $E$. The variations of Lagrangian with respect to the amplitude $A(t)$, inverse width $R(t)$, chirp $C(t)$ and phase $\phi(t)$ yield the following set of equations:

$$(\frac{\partial \phi}{\partial t} - m_{20}) + \frac{D}{2} R^2 (\frac{\partial C}{\partial t} + \frac{1}{R^4} + 4C^2) - 2m_{40}A^2 - 3m_{60}A^4 = 0, \tag{3.50}$$

$$(\frac{\partial \phi}{\partial t} - m_{20}) + (\frac{D}{2} + 1) R^2 (\frac{\partial C}{\partial t} + \frac{1}{R^4} + 4C^2) - \frac{2}{R^2} - m_{40}A^2 - m_{60}A^4 = 0, \tag{3.51}$$

$$\frac{\partial}{\partial t}(A^2 R^{(D+2)}) - 8A^2 C R^{D+2} = 2m_{10}A^2 R^{D+2} + 2m_{30}A^4 R^{D+2} + 2m_{50}A^6 R^{(D+2)}, \tag{3.52}$$

and

$$\frac{\partial}{\partial t}(A^2 R^D) = 2m_{10}A^2 R^D + 2m_{30}A^4 R^D + 6m_{50}A^6 R^D. \tag{3.53}$$

Equations (3.52) and (3.53) show that the power ($P = A^2 R^D$) is not a constant quantity with respect to the evolution time, usually, which is a constant for conservative systems. Solving equations (3.50), (3.51), (3.52) and (3.53) the evolution equations of $A$, $R$, $C$ and $\phi$ takes the following form:

$$T_1 = \frac{\partial A}{\partial t} = 2DAC - m_{10}A - (\frac{D}{2} + 2)m_{30}A^3 - (D+3)m_{50}A^5, \tag{3.54}$$

$$T_2 = \frac{\partial R}{\partial t} = 4CR - m_{30}A^2R - 2m_{50}A^4R, \tag{3.55}$$

$$T_3 = \frac{\partial C}{\partial t} = \frac{1}{R^4} - 4C^2 - m_{40}\frac{A^2}{R^2} - 2m_{60}\frac{A^4}{R^2}, \tag{3.56}$$

and

$$\frac{\partial \phi}{\partial t} = m_{20} - \frac{D}{R^2} + (\frac{D}{2} + 2)m_{40}A^2 + (D+3)m_{60}A^4. \tag{3.57}$$

### 3.3.1 Stability Analysis

Equations (3.54), (3.55) and (3.56) can be employed to analyze the system stability. The steady state solution of the peak amplitude can attain two possible values as follows:

$$A_{\pm} = \sqrt{\frac{-m_{30} \pm \sqrt{m_{30}^2 - 3m_{50}m_{10}}}{3m_{50}}}. \tag{3.58}$$

In dissipative systems, the solutions corresponding to the higher amplitudes generally result in stable solutions. The unstable solutions are the separatrix between the stable and HSS solution [159]. The steady state solutions for chirp and width of CS are given by following relations:

$$C = \frac{m_{30}}{4}A^2 + \frac{m_{50}}{2}A^4, \tag{3.59}$$

$$R_{\pm} = \sqrt{\frac{-(m_{40}A^2 + 2m_{60}A^4) \pm \sqrt{(m_{40}A^2 + 2m_{60}A^4)^2 + 16C^2}}{8C^2}}. \tag{3.60}$$

One of the important difference between the soliton solutions obtained in the dissipative systems to that in conservative systems is that the dissipative systems always

support non-zero soliton chirp-value [159]. However, the stability of each steady state solution is required to be checked in order to get the robust soliton solution. Therefore, further analytical treatment of the obtained soliton solutions is necessary. To establish stability criteria, Lyapunov stability analysis along with Hurwitz criteria is applied to the system. The evolution equations (3.54), (3.55), (3.56) and (3.57) are the initial points to establish the stability criteria for the system. The Jacobi determinant for the set of evolution equations (3.54), (3.55) and (3.56) can be constructed as: $|J-\lambda I|=0$ at an equilibrium, such that:

$$\left|\begin{array}{ccc} \frac{\partial T_1}{\partial A}-\lambda & \frac{\partial T_1}{\partial R} & \frac{\partial T_1}{\partial C} \\ \frac{\partial T_2}{\partial A} & \frac{\partial T_2}{\partial R}-\lambda & \frac{\partial T_2}{\partial C} \\ \frac{\partial T_3}{\partial A} & \frac{\partial T_3}{\partial R} & \frac{\partial T_3}{\partial C}-\lambda \end{array}\right|_{eq}=0. \tag{3.61}$$

Corresponding to an isotropic perturbations, the characteristic eigenvalue equation is formed as follows:

$$\lambda^3+\alpha_1\lambda^2+\alpha_2\lambda+\alpha_3=0 \tag{3.62}$$

where, the coefficients $\alpha_1$, $\alpha_2$ and $\alpha_3$ are as follows:

$$\alpha_1=2(2-D)C+m_{10}+(\frac{3D}{2}+5)m_{30}A^2+(5D+17)m_{50}A^4, \tag{3.63}$$

$$\begin{aligned}\alpha_2=&-8(D+4)C+4(D+8)m_{30}A^2C+(12D+76)m_{50}A^4C+\frac{16}{R^4}\\ &+(4C+m_{30}+2m_{50}A^2)m_{10}A^2+3(\frac{D}{2}+2)m_{30}^2A^2+10(D+3)m_{50}^2A^8\\ &+(8D+27)m_{30}m_{50}A^6+4(D-2)m_{40}\frac{A^2}{R^2}+16(D-1)m_{60}\frac{A^4}{R^2},\end{aligned} \tag{3.64}$$

$$\begin{aligned}\alpha_3 = (2m_{10} - 4DC + (D+12)A^2 + 10(D+3)m_{50}A^4)\frac{8}{R^4} + 3(D+4)m_{30})A^5RC \\ -16(m_{60}(2DC + m_{10}) + 3m_{30}m_{40})\frac{A^4}{R^2} + 8m_{50}(10(D+3)m_{50}A^2 + 64DC^3 \\ +8((D-12)m_{30}m_{60}A^2 - 6m_{30}m_{40} - 15m_{40}m_{50}A^2 - 2(D+15)m_{50}m_{60}A^4)\frac{A^4}{R^2} \\ -((64D+198)m_{30} + 32m_{10} + 32m_{50}DA^3R + 160(D+3)m_{50}A^4)C^2 \\ +8m_{50}(5(D+3)m_{30}A^2C - 8DR^4)A^4.\end{aligned} \tag{3.65}$$

The steady state of evolution equations are stable only if the real part of the roots of the eigenvalue equation (equation (3.62)) are positive. To establish the Lyapunov stability criteria, Hurwitz's conditions must be satisfied, i.e. all the coefficients of equation (3.62) should attain positive real values. Hurwitz principal minors are given by the following relations:

$$\alpha_4 = \alpha_1\alpha_2 - \alpha_3, \tag{3.66}$$

and

$$\alpha_5 = -(\alpha_1)^2(\alpha_2)^2 + 4(\alpha_2)^3 + 4(\alpha_1)^3\alpha_3 - 18\alpha_1\alpha_2\alpha_3 + 27(\alpha_3)^3. \tag{3.67}$$

To satisfy the Hurwitz conditions in addition to positive $\alpha_1$, $\alpha_2$ and $\alpha_3$, the value of $\alpha_4$ also need to be positive. The coefficient $\alpha_5$ categorizes the nature of dynamical behavior of the system. The positive coefficient of the real part of $\alpha_5$ indicates the stable focus, whereas, the negative coefficient indicates a stable node. To identify the stability region the contour plots of all $\alpha_i$'s are plotted with $\sigma$ and $\mu$ as independent variables. The positive contour regions are identified, indicating the positive values of all the $\alpha_i$'s. Figures (3.9) and (3.10) present the contour lines corresponding to each $\alpha_i$ and, subsequently, the stability regions (shaded), for one- and two-dimensional

system, respectively. In each Figure curves 'a', 'b', 'c' and 'e' represent the contours corresponding to $\alpha_1$, $\alpha_3$, $\alpha_4$ and $\alpha_2$, respectively. Curves marked with 'd' represent the discriminant of steady state solution of amplitude in the quadratic equation of $A^2$ (equation 3.58). In Figures (3.9) and (3.10) the shaded region corresponds to the stable parametric region, where each $\alpha_i$ and the discriminant of quadratic equation of $A^2$ (equation (3.58)) have positive real values. It is checked numerically that all the ($\sigma$, $\mu$)-values combination lying in the shaded region of the stability plot give the stable CS solution. It is observed that with an increase in the dimension of the system, the corresponding area of stability shrinks considerably. It is evident that stabilizing a soliton at higher dimension is tougher. After the stability region in parametric space is

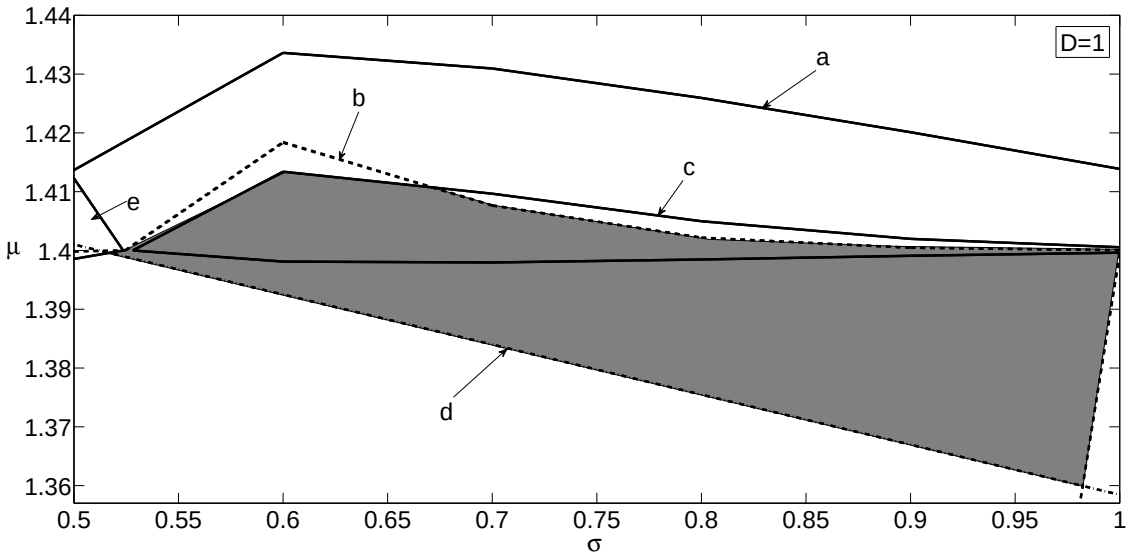


**Figure 3.9:** Stability region in the ($\sigma$, $\mu$)-parameter space corresponding to D=1. Here, $\theta = 1.2$, $\alpha = 2.7$, $\beta = 1$, $\lambda = 0.03$, $\gamma = 0.5$, $s = 10$ and $\Omega_0 = 0.1$.

identified, now it is necessary to study the influence of other system parameters on the global behavior of the system. In nonlinear dynamics, bifurcation behavior of solutions are always the subject of substantial analytical interest. The nature of the transition points and any qualitative change therein decides the system behavior. The variations of steady state of $A$, $R$ and $C$ with respect to feedback strength parameter $\sigma$ for $D = 1$

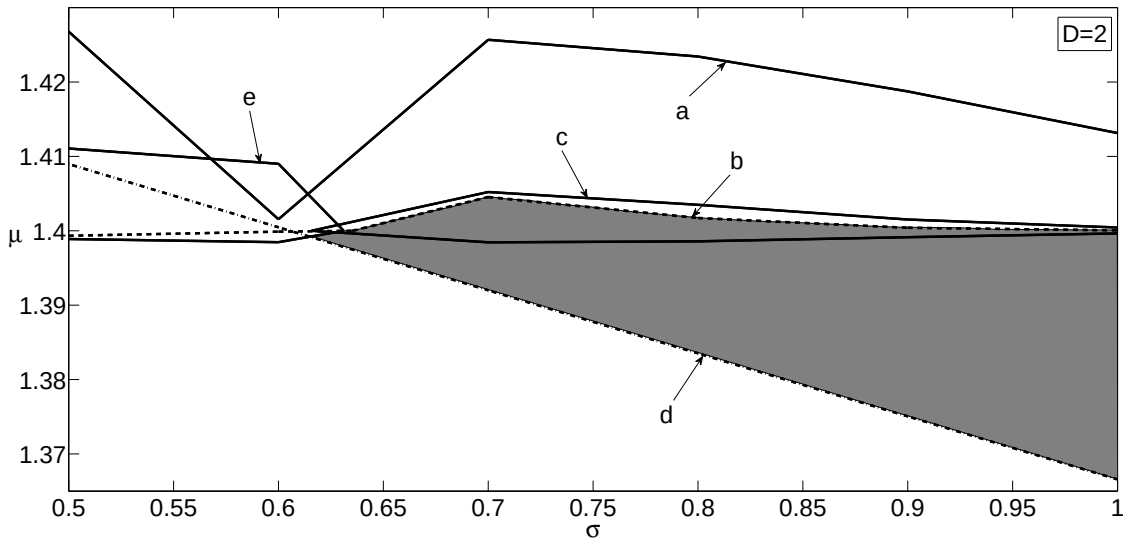


**Figure 3.10:** Stability region in the ($\sigma$, $\mu$)-parameter space corresponding to D=2. Other parameters are the same as stated in Figure (3.9).

and 2, are shown in Figures (3.11) and (3.12), respectively. The steady state value of $A$, given by equation (3.58), undergoes the fold-bifurcation at a particular value of $\sigma(= 0.610)$. As a result, a stable branch (solid line, $A_+$) and an unstable branch (dashed line, $A_-$) are formed as shown in Figure (3.11)($a$). For both the positive and negative solution branches, the stability is comprehensively checked using analytical and numerical techniques. Similar to Figure (3.11)($a$), Figure (3.11)($b$) shows the bifurcation of $R$ at same $\sigma$ value, however, $R_+$ and $R_-$ intersects once thereafter. Analytical and numerical analyses reveal that positive solution of $R$ ($R_+$) corresponds to stable CS solution, while the negative solution of $R$ ($R_-$) yields unstable CS solution. Figure (3.11)($c$) shows the bifurcation analysis of steady state of wavefront chirp $C$. $C_+$ and $C_-$ stand for the steady state value of $C$ (given by equation (3.59)) corresponding to $A_+$ and $A_-$, respectively. In this investigation, a positive $C$ ($C_+$) and a negative $C$ ($C_-$) solution emerge as stable and unstable branches, respectively. For higher dimensional system, i.e., $D = 2$, the bifurcation dynamics is explored and presented in the Figures (3.12). It is observed that as the dimension of the system increases,

the bifurcation occurs at stronger feedback strength (higher $\sigma$-value: $\sigma = 0.702$ for $D = 2$). Not only the CS, the background cavity field ($E = 0$) should be stable for sustained CS. Generally, cavity parameters decide the stability of background. In this case for a stable background, $m_1$ (which is a function of pump parameters for active and passive materials, feedback strength, bandwidth of filter reflection and resonance frequency) should be negative.

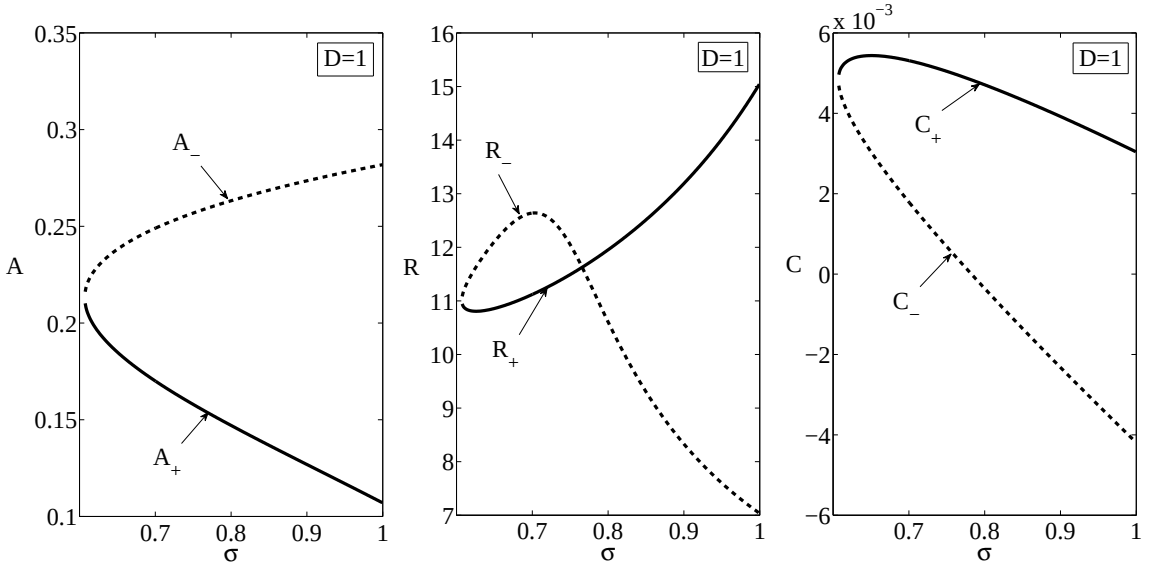


**Figure 3.11:** Bifurcation of steady state solutions of ($a$) amplitude $A$, ($b$) inverse width $R$ and ($c$) chirp $C$ with respect to the feedback strength $\sigma$ for $D = 1$. Solid lines represent the stable solutions corresponding to the positive values of amplitude and dashed lines represent unstable solutions which corresponds to the negative amplitude relation.

At this point it is in order to discuss how different the CS obtained with VCSEL-SA-FSF configuration from those obtained either with FSF or SA. The presence of SA in VCSEL-SA-FSF configuration expands the CS stability zone considerably. Figure (3.13) portrays the spreading of CS stability zone with increasing strength of SA for $D = 1$. The wider parametric zone provides greater freedom to set input values in experimental setup that eventually eases the search of CS. The bifurcation diagrams in Figures (3.11) and (3.12) indicate the bistable behavior of CS. Removal of SA terms from equation (3.10) immediately ceases the bifurcation nature of the system. This

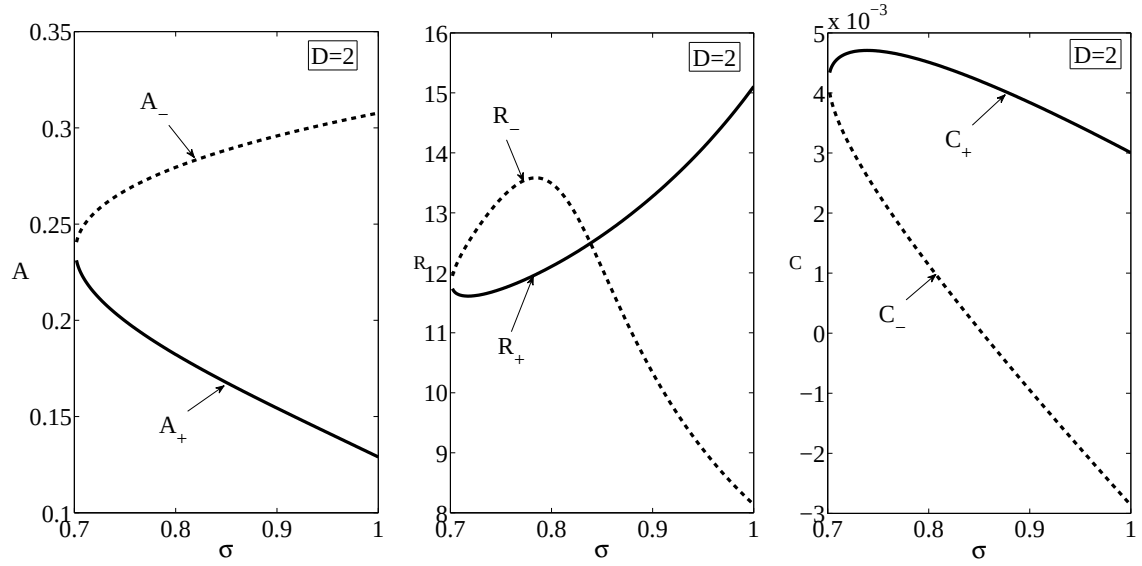


**Figure 3.12:** Bifurcation of steady state solutions of ($a$) amplitude $A$, ($b$) inverse width $R$ and ($c$) chirp $C$ with respect to the feedback strength $\sigma$ for D=2. Solid lines represent the stable solutions corresponding to the positive values of amplitude and dashed lines represent unstable solutions which corresponds to the negative amplitude relation.

confirms that SA is responsible for bistabitity. This is further supported by Figure (3.14), wherein the bistable CS exist in the range $\mu_{tp} < \mu < \mu_{th}$. Here, $\mu_{th} = 1+\gamma-a$, measures the pump parameter corresponding to laser threshold for which bistability is observed and $\mu_{tp} = (\sqrt{(1-a)(s-1)} + \sqrt{\gamma})^2/s$ determines the pump parameter value at the turning point of the hyperbolic bistability curve. The stability criterion is found to be $s > 1 + (1-a)/\gamma$ as in the case of section (3.1). In this case too, the bistability of CS immediately ceases in absence of SA. Further, both $\mu_{th}$ (= 1.4395) and $\mu_{tp}$ (= 1.3068) corresponding to the combined scheme (VC) is smaller than those without FSF (1.5 and 1.3743, respectively). This indicates with combined scheme the bistable CS can be generated at lower pump parameter. More importantly, the bistability range ($\delta\mu = \mu_{th} - \mu_{tp}$) of CS is significantly large (= 0.1327) for the combined scheme in comparison to the scheme without FSF (i.e., = 0.1257). Thus our combined scheme of VCSEL-SA-FSF in one hand spawns bistability of CS, on the other hand enlarges the CS stability range and lowers the requirement of pump energy for CS generation. All

these factors may make our new model preferable for experiments and applications.

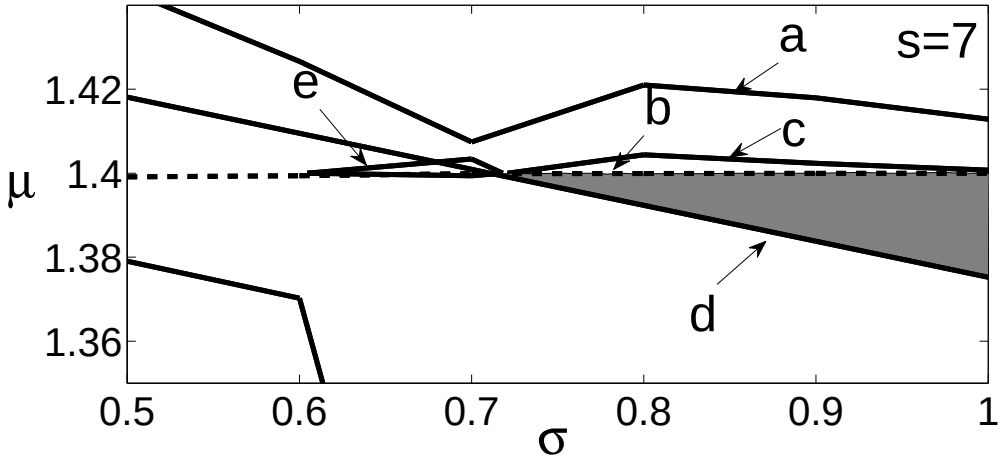


**(a)**

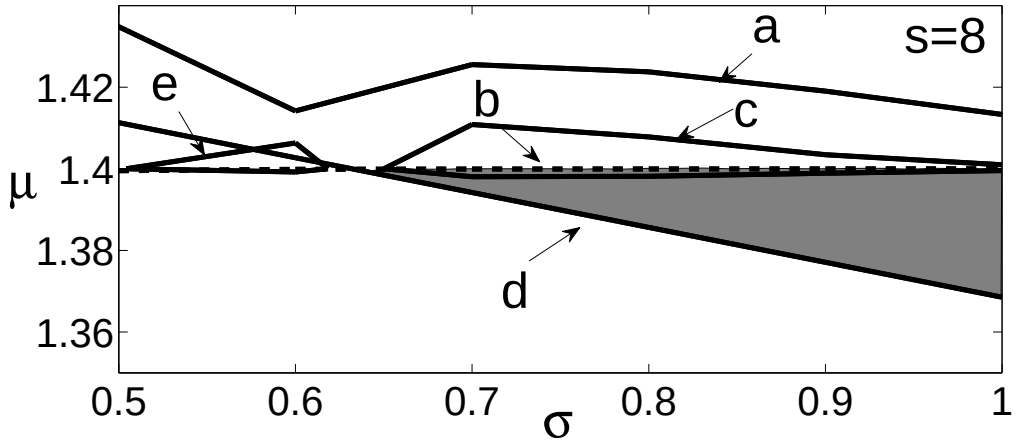


**(b)**

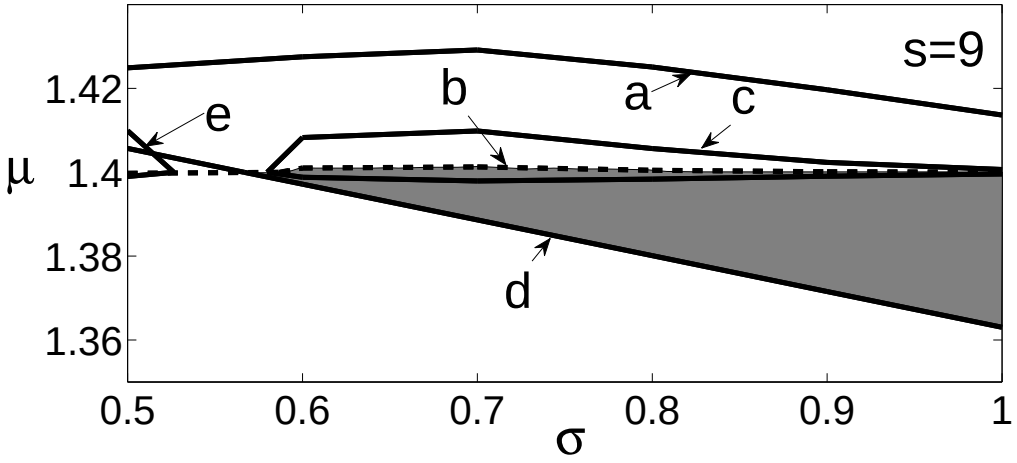


**(c)**

**Figure 3.13:** Expansion of stability region with increase in saturation parameter for $D = 1$. $(a)$, $(b)$ and $(c)$, respectively, correspond to the saturation parameter $s = 7$, 8 and 9.

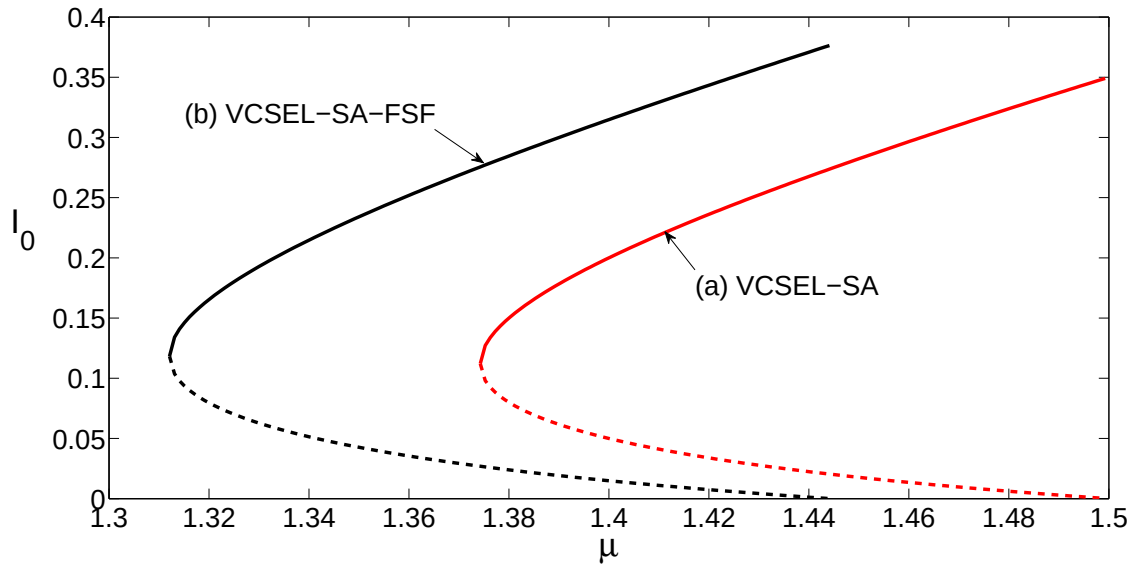


**Figure 3.14:** Variation of field intensity ($I_0$) of CS with pump parameter $\mu$ for the schemes VCSEL-SA (curve $a$) and combined (VCSEL-SA-FSF) (curve $b$). The 'C' like curves show bistablity of CS. Upper branches of both the curves correspond to stable CS, while the dotted lower branch correspond to unstable CS solution.

### 3.3.2 Excitation of one- and two- dimensional cavity solitons

With the knowledge of parametric stability region and bifurcation behavior of the soliton parameters, now we proceed to find the evolution of $A_+$, $R_+$ and $C$. Henceforth, for brevity, $A_+$, $R_+$ and $C_+$ are written as $A$, $R$ and $C$ respectively. The variationally obtained evolution equations are now solved taking parameters from stability region (Figures 3.9 and 3.10) and setting points of stable branch of bifurcation diagram (Figures 3.11 and 3.12) as initial conditions. Figures (3.15) represents the time evolution of $A$, $R$, $C$ and $\phi$ in $D = 1$, while Figure (3.16) portrays the same for $D = 2$. Evolution of phase $\phi$ can be obtained from the equation (3.57) with the steady state value of $A$, $R$ and $C$ obtained from equations (3.54), (3.55) and (3.56). For both the dimensions, $A$, $R$, $C$ and $\phi$ show steady state evolution. A magnified view (in the insets of Figures (3.15) and (3.16)) reveals some tiny initial fluctuations that quickly settle in periodic oscillations of very small amplitudes. All these confined minor oscillations suggest

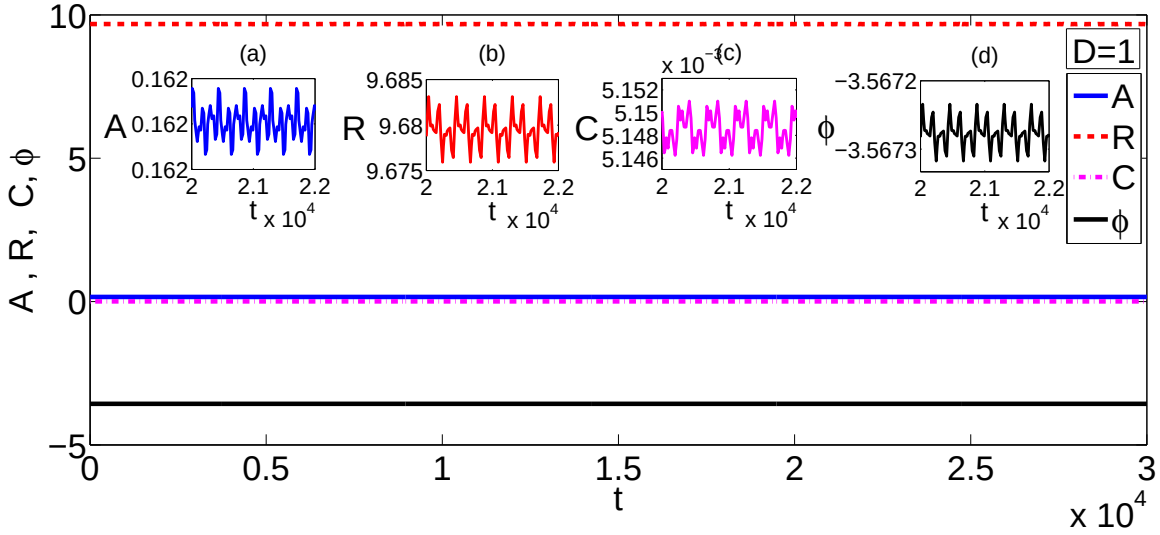


**Figure 3.15:** The steady state evolution of $A$, $R$, $C$ and $\phi$ in D=1. $\sigma = 0.7323$, $\mu = 1.3919$ and rest of the parameters taken from the stability region of in Figure (3.9). Insets show the zoom in view of the time-evolution of parameters $(a)$ $A$, $(b)$ $R$, $(c)$ $C$ and $(d)$ $\phi$.

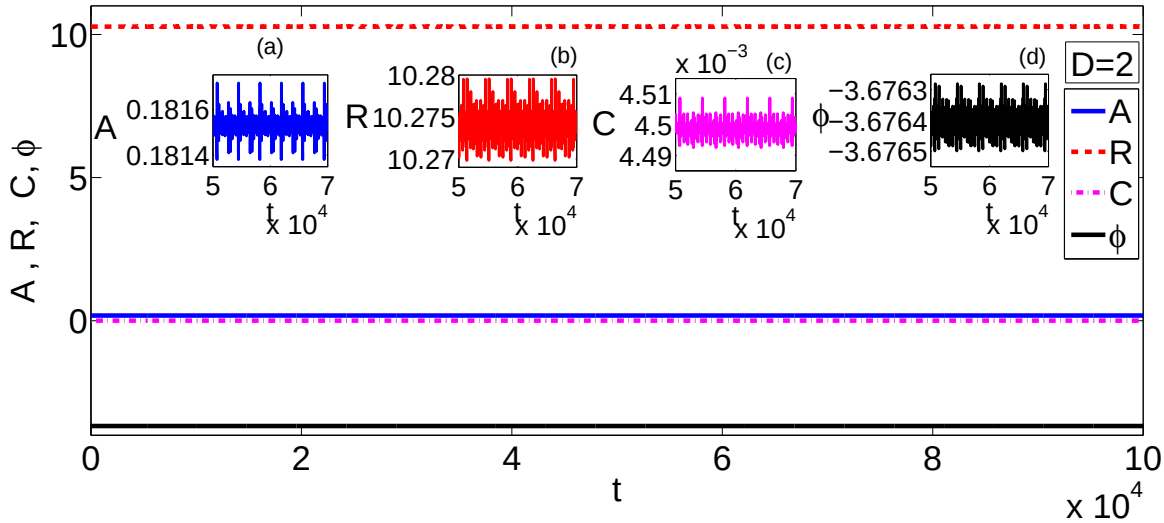


**Figure 3.16:** The steady state evolution of $A$, $R$, $C$ and $\phi$ in D=2. $\sigma = 0.8023$, $\mu = 1.3919$ and other parameter are taken from the stability region in Figure (3.16). Insets show the zoom in view of the time-evolution of parameters $(a)$ $A$, $(b)$ $R$, $(c)$ $C$ and $(d)$ $\phi$.

the evolution of stable CS. The evolution pattern is checked extensively for numerous points in the stability regions of Figures (3.9) and (3.10) for both the dimensions and similar stable evolution of soliton parameters are obtained. Phase diagrams for $D = 1$ and 2, drawn in Figure (3.17a) and (3.17c) respectively, show the confinement of $A$ and $R$. The system of smaller dimension is less prone to fluctuations as compared to higher dimensional system. Figures (3.17b) and (3.17d) show that power of the CS is not constant, rather it shows bound oscillations as the system evolves with time. The steady time-evolution of soliton parameters and confined phase diagrams indicate the generation and robustness of the stable CS in both the dimensions.

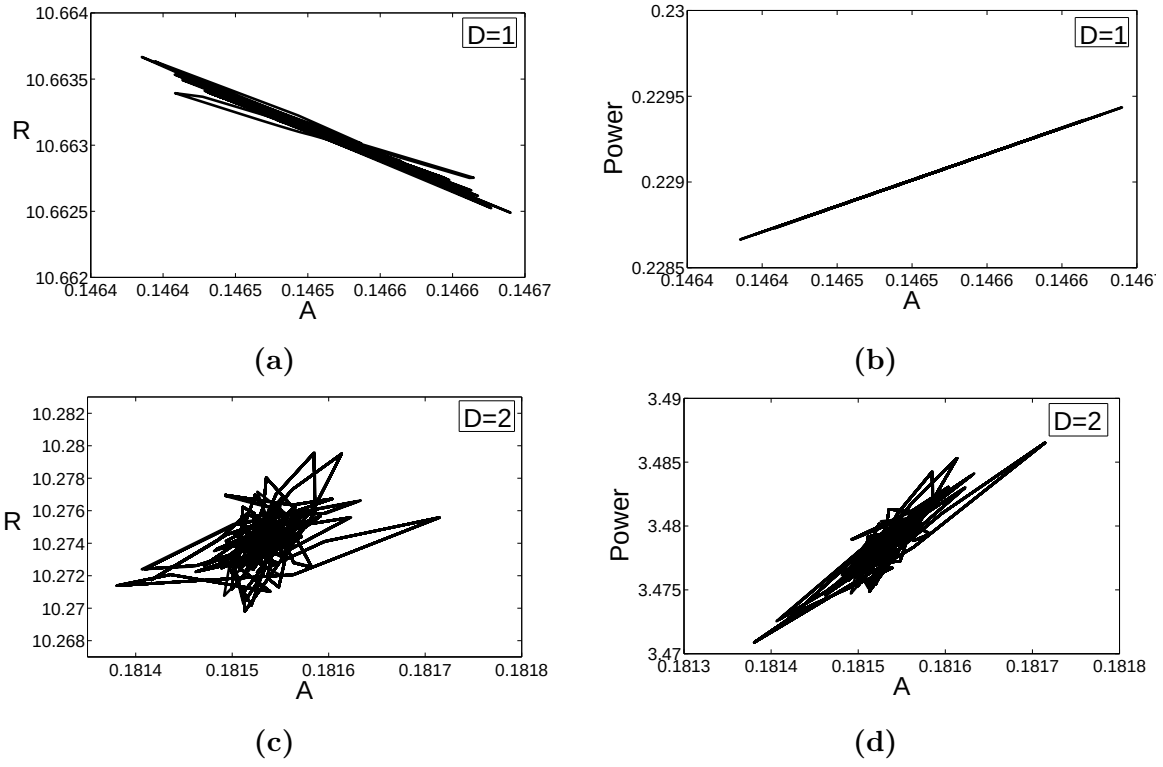


**Figure 3.17:** Phase plots ($A$ versus $R$) for (a) $D = 1$ and (c) $D = 2$. Amplitude of oscillation increases with dimension but remains confined. Power versus $A$ during evolution for (b) $D = 1$ and (d) $D = 2$.

In order to validate the variationally obtained results, direct numerical solution of equation (3.40) is in order. Crank-Nicolson [136], Split-step Fourier method (SSFM) [6] and Runge-Kutta method are commonly used numerical methods for solving CGLE.

For the present investigation SSFM is adopted to find CS corresponding to the points

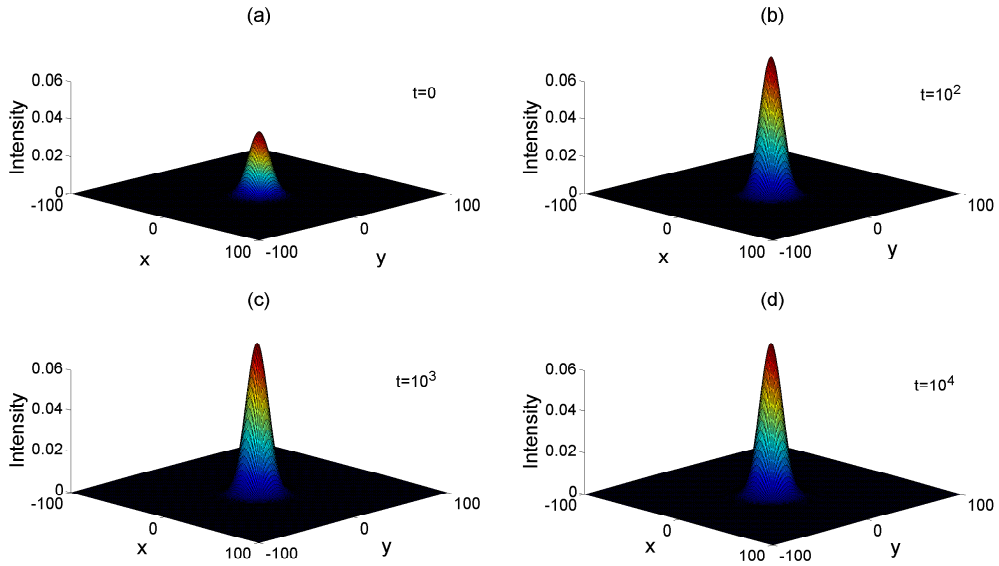


**Figure 3.18:** Numerical evolution of CS in $D = 2$ at different time-steps. Parameters used are same as in Figure (3.16) with integration step-size $h = 0.01$.

in the analytically obtained stability region. To our utter satisfaction, almost all the points corresponding to the stability region yield CS numerically. A typical numerically obtained CS is portrayed through several snapshots in Figure (3.18). Thus our variational result is successful in predicting CS efficiently. In a further attempt to find the snaking, a typical behavior of pattern forming or CS's host system [1], the steady state values of $A$ and $R$ (in $D = 1$) are calculated for a range of bifurcation parameter $\sigma$. $A$ versus $R$ plot shows snaking in Figure (3.19) (dashed curve). However, one may not expect many 'stairs' in the snaking diagram through variational results. Points on the dashed line yield stable CS following analytical method. However, numerically, stable CS is found for the particular range of bifurcation parameter $\sigma = 0.6320$ to 0.7550. Solid line on Figure (3.19) corresponds to such numerically obtained stable CS. For the $\sigma$ -values near 0.7550, initially a breather-like soliton behavior is observed, that quickly, i.e. after few hundreds of initial steps, converts to the stable CS (Figure (3.20)). Below $\sigma = 0.7500$, the initial turbulence almost disappears and stable CS is

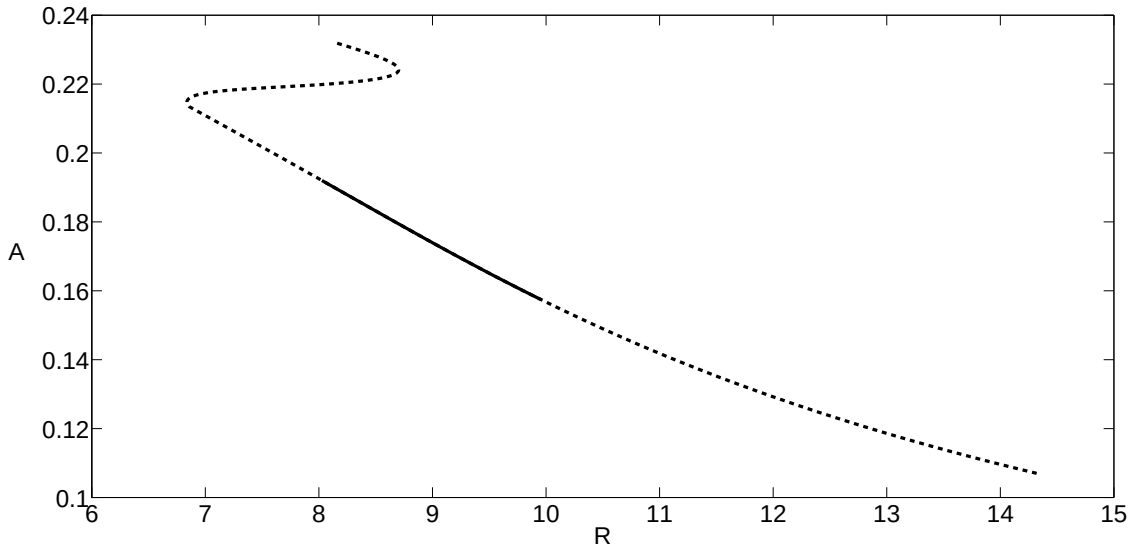


**Figure 3.19:** Snaking curve obtained by variation in steady state values of $A$ and $R$ with respect to the bifurcation parameter $\sigma$ $(0 < \sigma < 1)$ for $D = 1$. Dashed line corresponds to analytically predicted stable CS, whereas solid line (overlaps with dashed line segment) corresponds to the numerically obtained CS. Numerically stable CS occurs for the set of $A$ and $R$ that corresponds to $\sigma = 0.6320$ to $0.7550$.

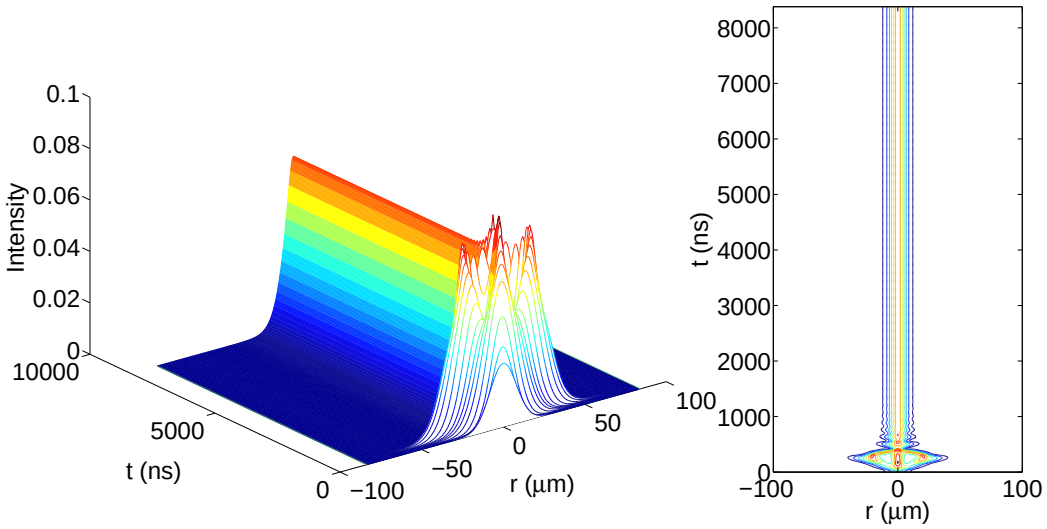


**Figure 3.20:** Evolution of CS obtained by numerical method for $D = 1$. Initially, a breather like profile is observed, later on it regains solitonic shape and evolves undistorted. Here, $\sigma = 0.7542$, rest of the parameters are same as those used in 3.15 with integration step-size $h = 0.01$. $(a)$ spatio-temporal intensity plot and $(b)$ shows the contour plot of the evolving profile.

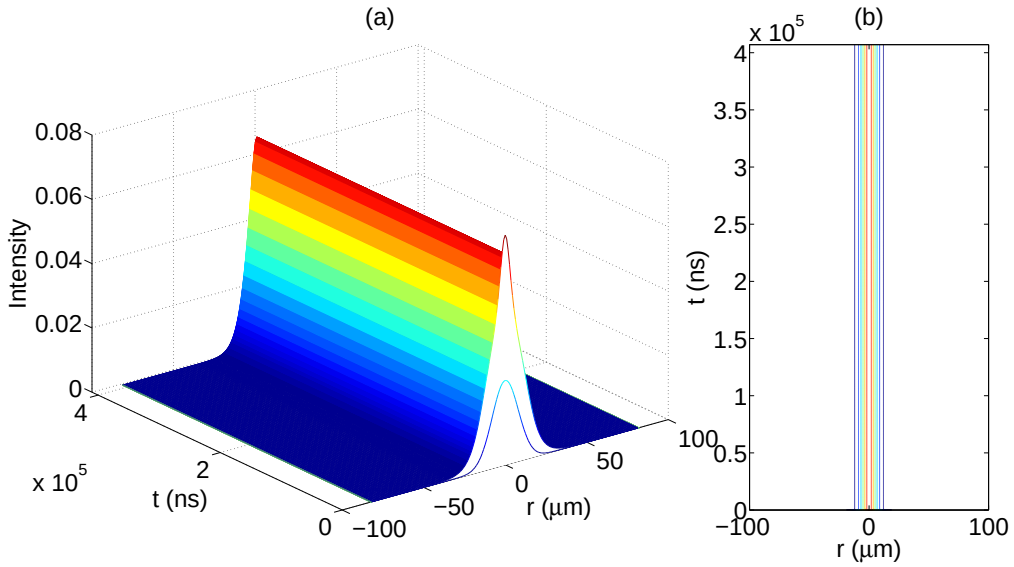


**Figure 3.21:** Evolution of CS obtained by numerical method, for $\sigma = 0.7323$, $D = 1$ and rest of the parameters as same as those in Figure (3.15). Integration step-size $h = 0.01$. $(a)$ the spatio-temporal intensity plot and $(b)$ the contour plot of the evolving profile. After initial turbulence, the amplitude increases and then get fixed to a steady amplitude.

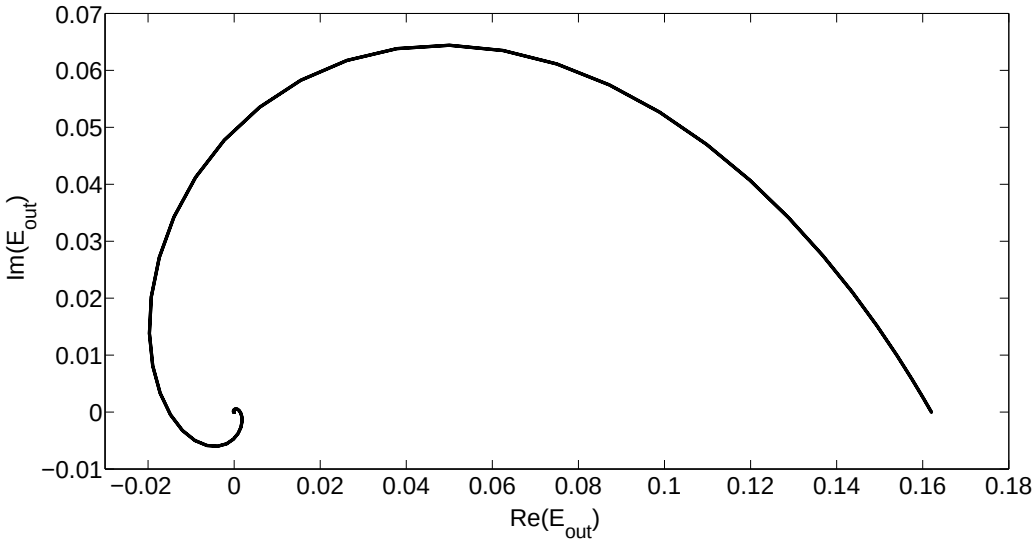


**Figure 3.22:** The phase diagram (real versus imaginary part of the amplitude) of the output CS corresponding to Figure (3.21).

observed. Figure (3.21) shows a typical CS in that range of $\sigma$ in spatio-temporal domain. Corresponding phase portrait (Figure (3.22)), which is an inward spiral, clearly indicates the localization of CS.

## Conclusion

In this chapter, the analytical stability of VCSEL-SA-FSF model is studied. The effect of variation in cavity parameters on the stability of the microcavity is presented. The variation in turning point and threshold limits of pump parameter in VCSEL-SA and VCSEL-SA-FSF model is shown. Analytical solutions of the microcavity with cubic and cubic-quintic nonlinearities are obtained through variational method. It is observed that the soliton parameters, such as amplitude, width and chirp has the dependence on the order of nonlinearity.

# Chapter 4

## Generation of Cavity Soliton Molecules: A Numerical Approach

In this chapter, the existence and stability region of CS is explored in different nonlinear cavities, mostly through analytical approach. In the current chapter, we investigate complete numerically the CS and CS cluster formation in cavity with SA and coupled with FSF.

## 4.1 Cavity Soliton Molecules in Microcavity: VCSEL-SA-FSF Model

The model under investigation comprises of a VCSEL with SA, coupled with the FSF element provided by Bragg's reflector with negligible delay. Such optically injected broad area semiconductor cavity, exhibiting higher order saturation nonlinearity and coupled with FSF element can be represented by the dimensionless dynamical equation (3.10). For a quick recall, equation (3.10) is written below:

$$\frac{\partial E}{\partial t} = [-(1-i\theta) + \frac{\mu(1-i\alpha)}{1+|E|^2} - \frac{\gamma(1-i\beta)}{1+s|E|^2} + i\nabla_\perp^2]E + (a-ib)E, \tag{4.1}$$

This dimensionless dynamical equation (3.10) is solved numerically by the SSFM with parameters chosen from the stable region predicted in section 3.1. Throughout the numerical study, the step-size is fixed to 0.01, and simulation is performed for 10 soliton periods. Following unchirped 'sech' function is considered as the profile function of CS:

$$E(x,t) = A\ sech(Kr)e^{-i\omega t}, \tag{4.2}$$

where, $A$ represents the peak amplitude of CS and always assumes positive non-zero values, $K$ represents the inverse width and $\omega$ is the angular frequency (a real constant). The system parameters those significantly control CS dynamics are the feedback strength $\sigma$ and resonance frequency $\Omega_0$. As discussed in stability analysis (in the previous chapter), the saturation parameter 's' has to follow the inequality condition (equation (3.14)) and 's' assumes the value greater than unity. Line-width enhancement factor for active material should always be greater as compared to that of passive material ($\alpha > \beta$). Considering this condition, the onset of Turing instability can be eluded [14]. Pump parameters for both active and passive medium ($\mu$ and $\gamma$) should follow the conditions stated in the stability analysis (equation (3.13)). In the present investigation $\beta = 0$. The values of rest of the normalized parameters are set as: $\alpha = 2.7$, $\mu = 1.37$, $\gamma = 0.5$, $s = 10$ and $\theta = 1.3$, unless mentioned otherwise. The parameters are chosen in accordance to the stability region.

Generally, a highly intense field undergoes initial perturbations and splits into almost equal amplitude atoms, and then retains shape, size and amplitude (Figure (4.1)). However, another perspective suggests that the velocity matching of the interacting CSs during interaction increases the chance of splitting the initial pulse into two or

four CSs [160]. Also, the presence of higher order nonlinearities supports fission, fusion and annihilation of dissipative solitons [161].

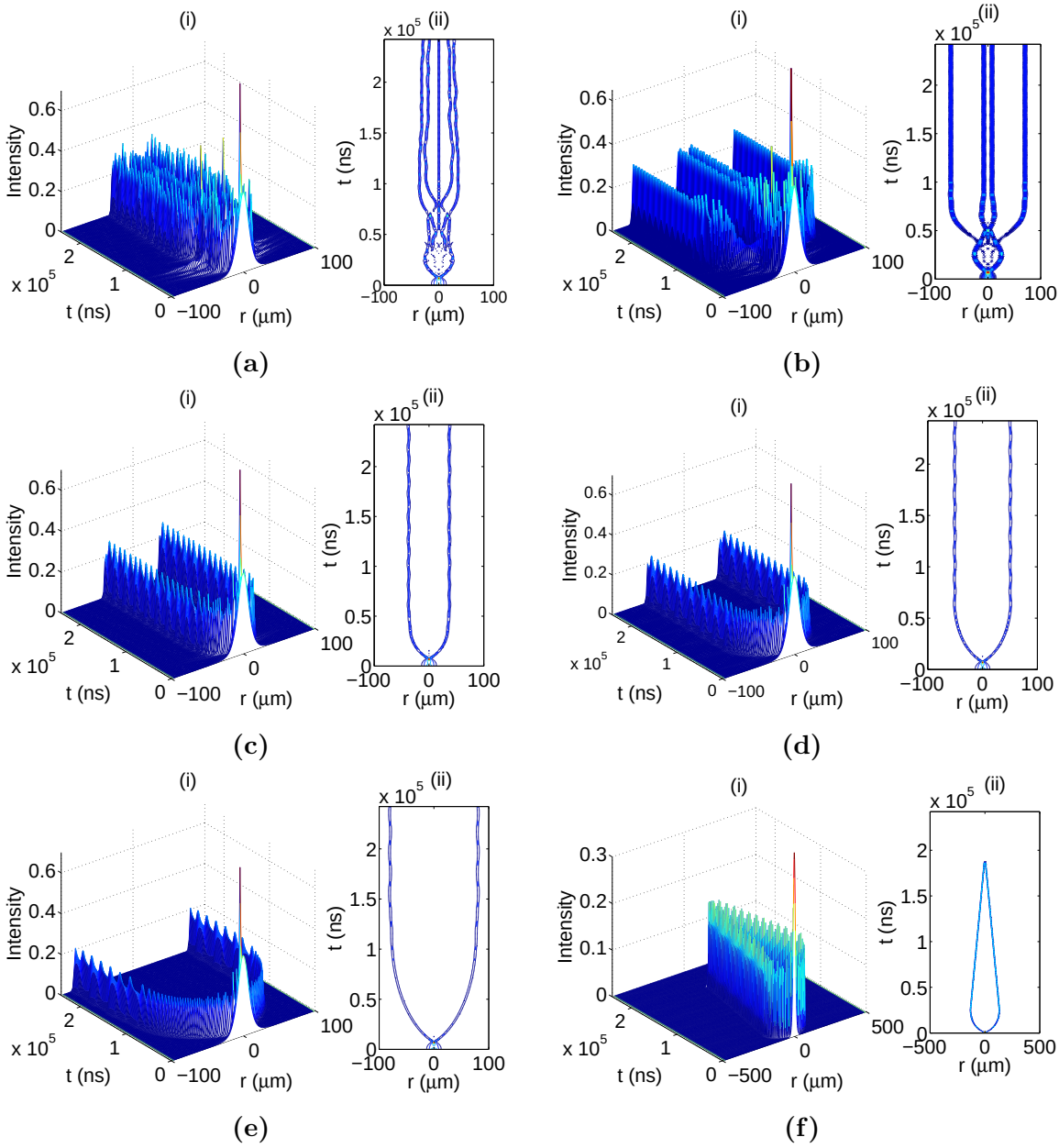


**Figure 4.1:** Effect of variation of resonant frequency ($\Omega_0$) on CS generation at (a) $\Omega_0 = 1.98$, (b) $\Omega_0 = 1.99$, (c) $\Omega_0 = 2.2$, (d) $\Omega_0 = 2.5$, (e) $\Omega_0 = 2.8$ and (f) $\Omega_0 = 3$. Here, $\sigma = 0.7$, $A = 0.6278$, $\alpha = 2.7$, $\mu = 1.37$, $\gamma = 0.5$, $\beta = 0$, $s = 10$ and $\lambda = 0.5$.

Our numerical investigation yields different stable bound state structures comprising of two or more CSs. For example, with $A = 0.6278$ and $\sigma = 0.7$, such bound state CSs are formed for $\Omega_0 > 1.97$ (Figure (4.1)). At a lower $\Omega_0$ (=1.98 and 1.99) bound state of four CSs are formed (Figures (4.1a) and (4.1b)). The two-CS bound

state is formed for $1.99 < \Omega_0 < 3$ (Figures (4.1c)-(4.1e)). The CSs of the bound state vibrate periodically. As these CSs are born from same source, they can be considered as coherent pairs [6]. Such bound state of CSs can be referred to as linear diatomic or tetra-atomic CS molecules. $\Omega_0 \geqslant 3$ leads to the annihilation of CSs. The annihilation occurs due to the phase difference developed between the co-propagating CSs.

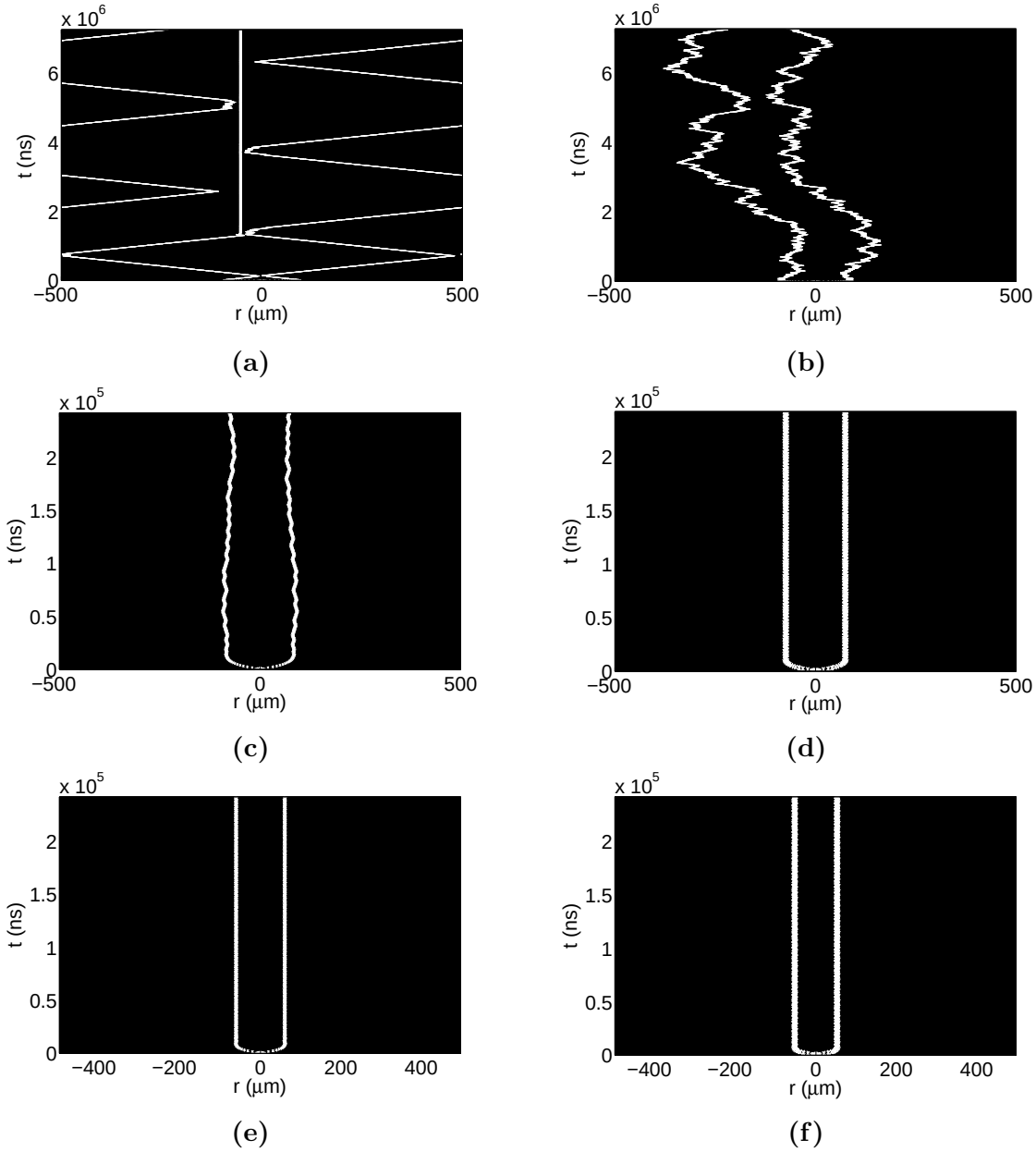


**Figure 4.2:** Transition to a stability from oscillating state with the variation in feedback strength parameter for constant resonant frequency $\Omega_0 = 3$ and injected field amplitude $A = 0.6278$. (a) $\sigma = 0.75$, (b) $\sigma = 0.76$, (c) $\sigma = 0.78$, (d) $\sigma = 0.81$, (e) $\sigma = 0.91$ and (f) $\sigma = 0.99$ and other parameters are same as in Figure (4.1).

However, this annihilation can be opposed by increasing $\sigma$ (Figure (4.2)). The role of $\sigma$ can be well understood now by keeping $\Omega_0$ constant. As the value of $\sigma$ increases the two-CSs system tends to stabilize (Figure (4.2)). Figure (4.2) corresponds to the parameter values $\Omega_0 = 3.0$ and $A = 0.6278$. At $\sigma = 0.75$, one stationary and one moving soliton are generated (Figure (4.2a)). The stationary CS repels the moving CS. Corresponding to $\sigma = 0.76$, the CS pair oscillates and show a slight random motion (Figure (4.2b)). The presence of small phase gradient induces such oscillations in the spatial position of the CSs [162]. The oscillating CS atoms has potential application in tuning the optical clocks [15]. Figure (4.2c) corresponds to the stable CS pair, which is almost stationary. Each CS oscillates about its mean position at $\sigma = 0.78$. Increase in $\sigma$-value makes the CSs more stable as well as stationary; also the separation between the CSs also decreases. However, as $\sigma$-value approaches unity, the system tends to be more stable. At very large $\sigma$, CS molecules get annihilated. The limiting value of $\sigma$ for which CS molecules survives catastrophic collapse, however, is dependent on peak amplitude $A$.

In order to investigate the effect of $\Omega_0$ on the system, the evolution corresponding to the resonant frequency $\Omega_0 = 1.7$ and input amplitude $A = 0.527$ is studied (Figure (4.3)). For this particular set of parameters the system behaved differently. At $\sigma = 0.25$, a CS pair originated out of single initial input field, move away from each other and decay while reaching the boundaries (Figure 4.3a). As the $\sigma$-value is increased, two stable CSs are formed. Figures (4.3b), (4.3c) and (4.3d) represent a stable di-atomic CS molecule. It is observed that the distance between two stable CSs decrease with an increase in the $\sigma$-value. As the value of $\sigma$ crosses 0.33 (i.e., $\sigma > 0.33$), the di-atomic CS destabilizes. As $\sigma$ crosses the value of 0.35, multiple CSs start to form.

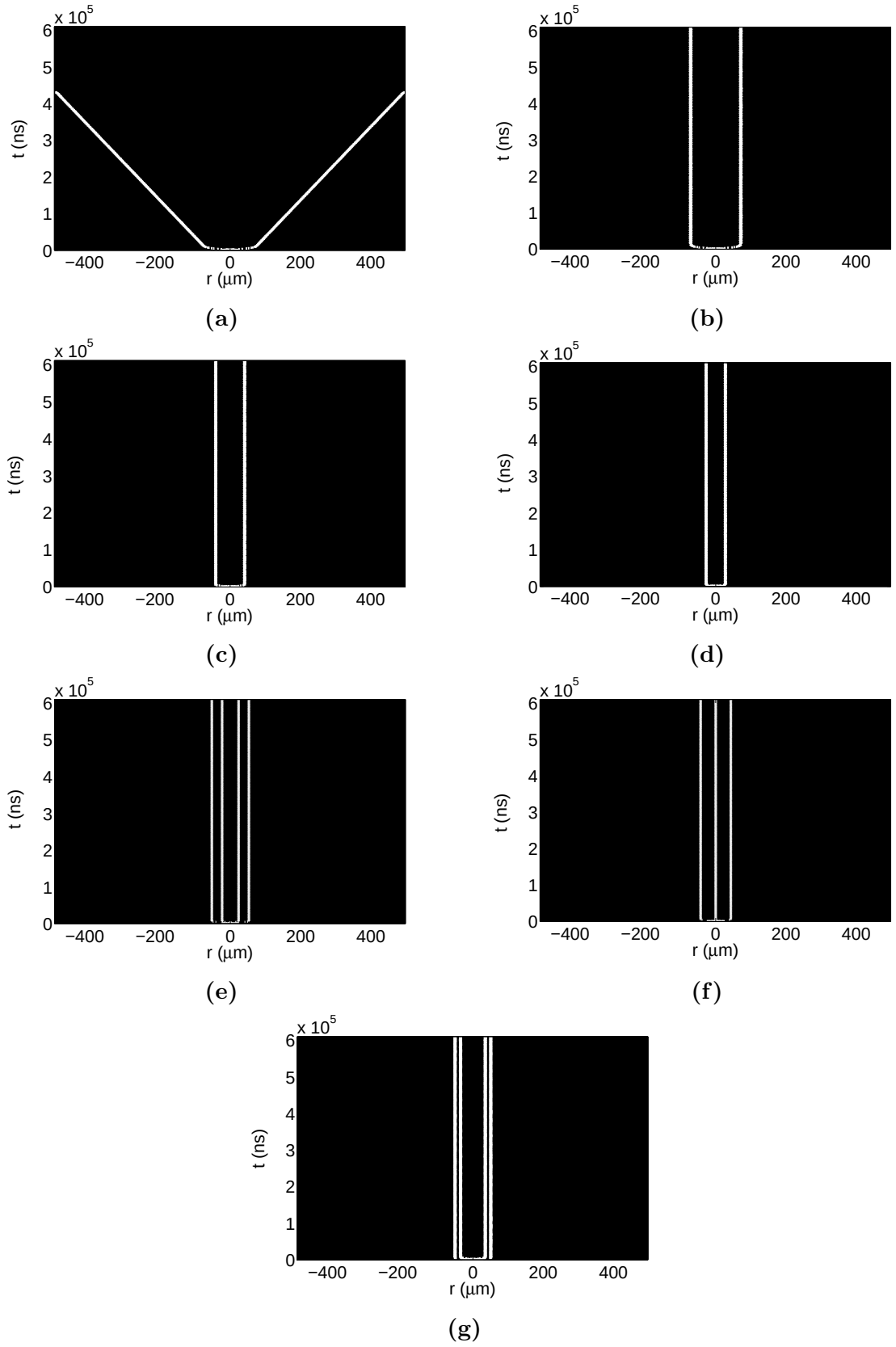


**Figure 4.3:** The effect of feedback strength parameter $\sigma$ on CS. . (a) $\sigma = 0.25$, (b) $\sigma = 0.26$, (c) $\sigma = 0.31$, (d) $\sigma = 0.33$, (e) $\sigma = 0.46$, (f) $\sigma = 0.48$ and (g) $\sigma = 0.49$, Here, $\Omega_0 = 1.7$ and $A = 0.527$, rest of the parameters are same as in Figure (4.1).

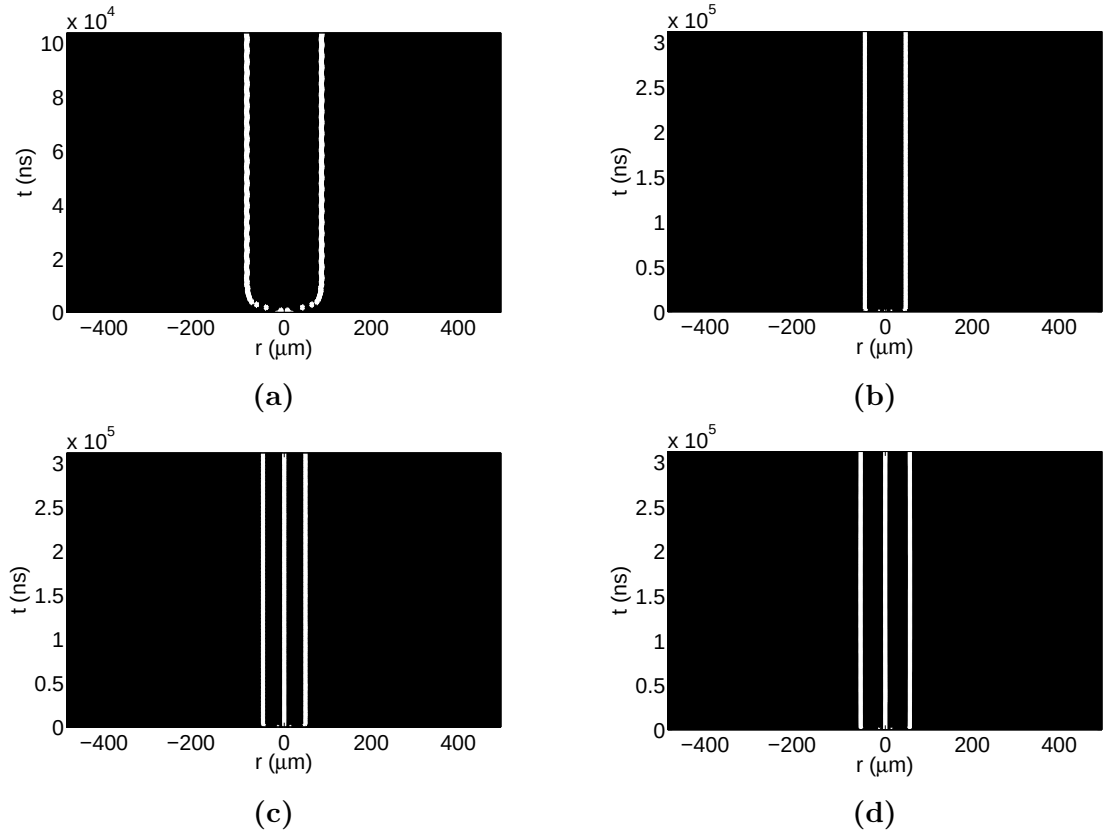


**Figure 4.4:** Generation of diatomic and triatomic CS molecules with increasing values of feedback strength $\sigma$. (a) $\sigma = 0.28$, (b) $\sigma = 0.43$, (c) $\sigma = 0.44$ and (d) $\sigma = 0.53$. Here, $\Omega_0 = 1.7$, $A = 0.27$, rest of the parameters are same as in Figure (4.1).

$0.33 < \sigma < 0.35$ is the unstable range for $\sigma$. Then, the four-CSs system, which can be referred as tetra-atomic CS molecules, are formed as shown in Figures (4.3e) and (4.3g) for $\sigma = 0.46$ and $\sigma = 0.49$ respectively. Also, a tri-atomic CS molecule (three-CSs system) can be generated (Figure (4.3f)) for $\sigma = 0.48$. Hence, $\sigma$ can even control the number of atoms in the CS molecules.

To get more idea of the system, formation of CS molecules is observed with different values of $A$ as lower as 0.27. Other parameters are kept same as stated in Figure (4.1f). Amplitude variation can also influence the CS generation, which is evident from the comparison of Figures (4.3) and (4.4). In Figure (4.4), only two- or three- CSs are formed. $\sigma = 0.28$ to $\sigma = 0.43$ exhibit two-CS system Figures (4.4a) and (4.4b). As the value of $\sigma$ crosses 0.43, the two-CSs system transits to three-CSs system. Figures (4.4c)

and (4.4d) depict typical three-CSs system for $\sigma = 0.44$ and $\sigma = 0.53$, respectively. As $\sigma$-value exceeds 0.53, the system collapses catastrophically.

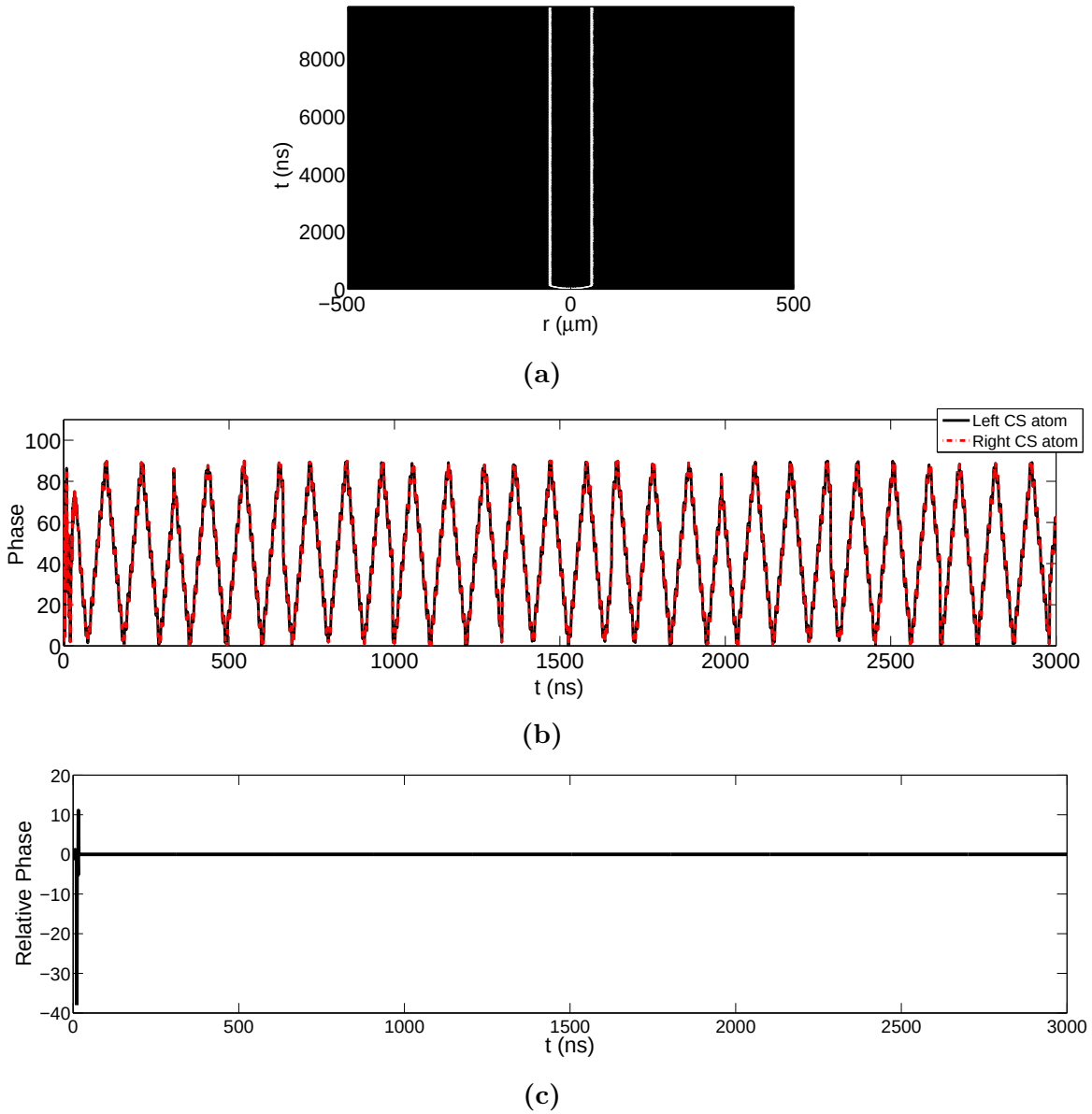


**Figure 4.5:** (a) Evolution of diatomic CS molecule, (b) Variation in phase during evolution, and (c) Relative phase change experienced by diatomic CS molecule. $A = 0.520$, $\sigma = 0.30$ and $\Omega_0 = 1.7$, rest of the parameters are same as in Figure (4.1).

Relative phase study of the co-existing CSs is also an important aspect to analyze the phase variations incurred by CS. Just as a case, for $\sigma = 0.30$, $\Omega_0 = 1.7$ and $A = 0.520$ the variation in phase and relative phase are recorded for co-existing (or diatomic) CSs. Figure (4.5a) shows the evolution of the spontaneously created CSs

from a single input field. The co-propagating CSs are almost in the same phase after experiencing the phase mis-matching during initial few time-steps of evolution (Figure (4.5b)). Figure (4.5c) shows the relative phase difference between the CSs. CSs are in phase during the evolution, except experiencing the phase mismatching during few initial time-steps.

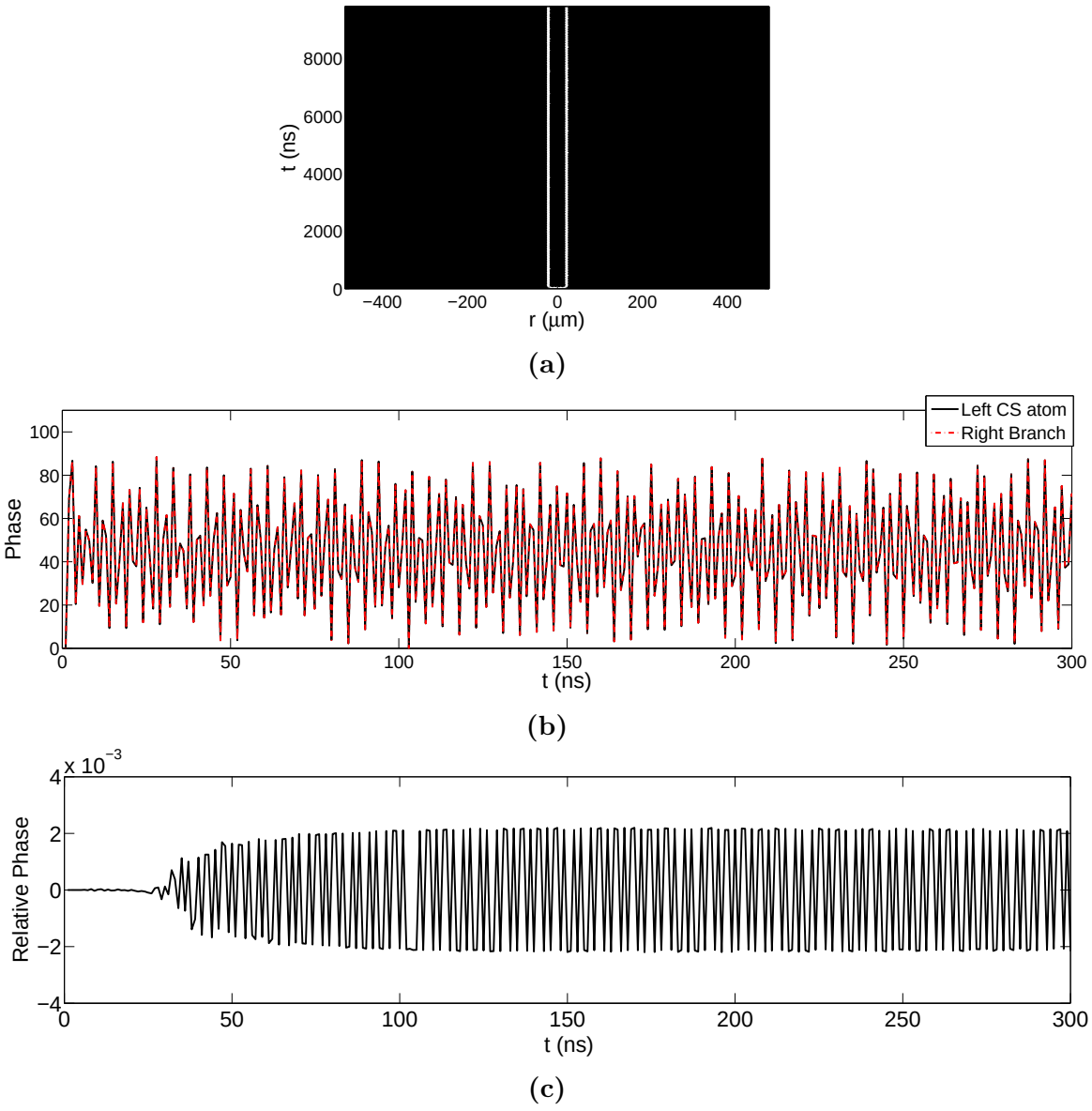


**Figure 4.6:** (a) Evolution of diatomic CS molecule, (b) Variation in phase during evolution, and (c) Relative phase change experienced by diatomic CS molecule. $A = 0.527$, $\sigma = 0.35$ and $\Omega_0 = 1.7$, rest of the parameters are same as in Figure (4.1).

The separation distance between the diatomic CSs has influence on their relative

phases. For peak amplitude $A = 0.527$, feedback strength $\sigma = 0.35$ and resonant frequency $\Omega_0 = 1.7$, the separation between the spontaneously induced CSs is relatively less as compared to diatomic CS molecule in Figure (4.5a). During the evolution, the bound CSs experience XPM due to their presence of each other in the vicinity. Therefore, the bound state CS experience relative phase difference. The corresponding phase of each CS atom and relative phase are shown in Figures (4.6b) and (4.6c), respectively.

## 4.2 Flat-top Solutions

Till now we have obtained CSs of bell-shaped profile. Interesting CS profiles are found in the form of a ∩-shaped ( $A = 0.2667$, Figure (4.7)) and flat-top ($A = 0.667$, Figure (4.8)) CS. Flat-top solutions for CGLE are generated by transition of the roots of the general soliton solution. As the two distinct positive soliton-solutions of a system approach each other, the soliton shape experiences a transition from standard shape (sech/bell-shape) to a flat-top shape [5, 163]. When two distinct real roots of the solution of CGLE become equal to each other, fronts are formed. The pulse width becomes infinite and it fragments into two fronts. The phase assumes constant value in the fronts region.

We extensively study the generation of CS with different profiles for different set of parameters. CGLE possesses different solutions in the form of fronts and pulses. Figure (4.9) identifies ($A$, $\Omega_0$) parametric region of different soliton-solutions, such as, flat-top, fronts, ∩-shaped and region in which the input field decays. The change in parameter values can easily transform one solution into the other [5]. In the present case, the transition of soliton- solution shape is shown in terms of resonant frequency

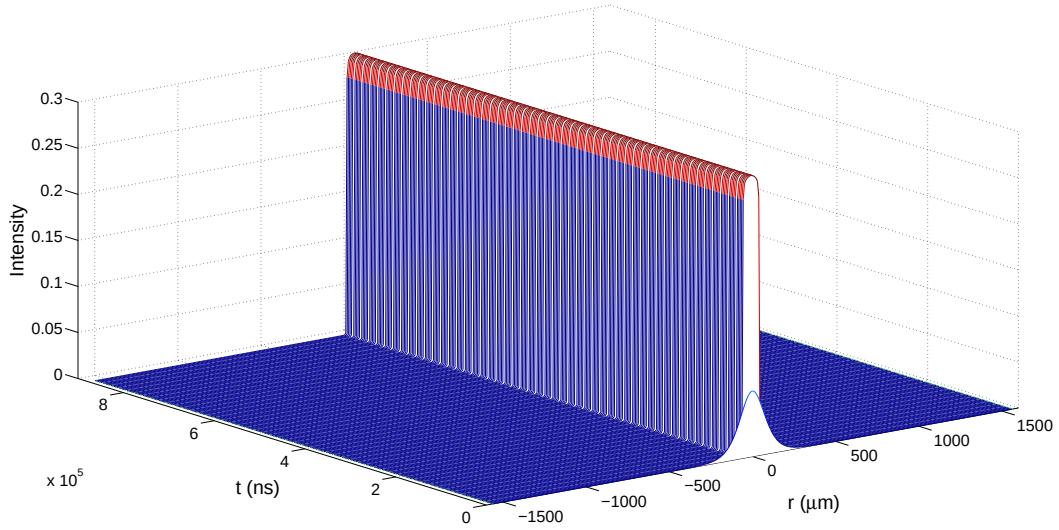


**Figure 4.7:** Generation of ∩-shaped CS with $A = 0.667$. Here, $\sigma = 0.7$, $\omega_0 = 2.12$, $K = 100$ and rest of the parameters same as in Figure (3.1). Here $\alpha = 2.7$, $\mu = 1.37$, $\gamma = 0.5$, $\beta = 0$, $s = 10$, $\lambda = 0.5$ and $K = 100$.

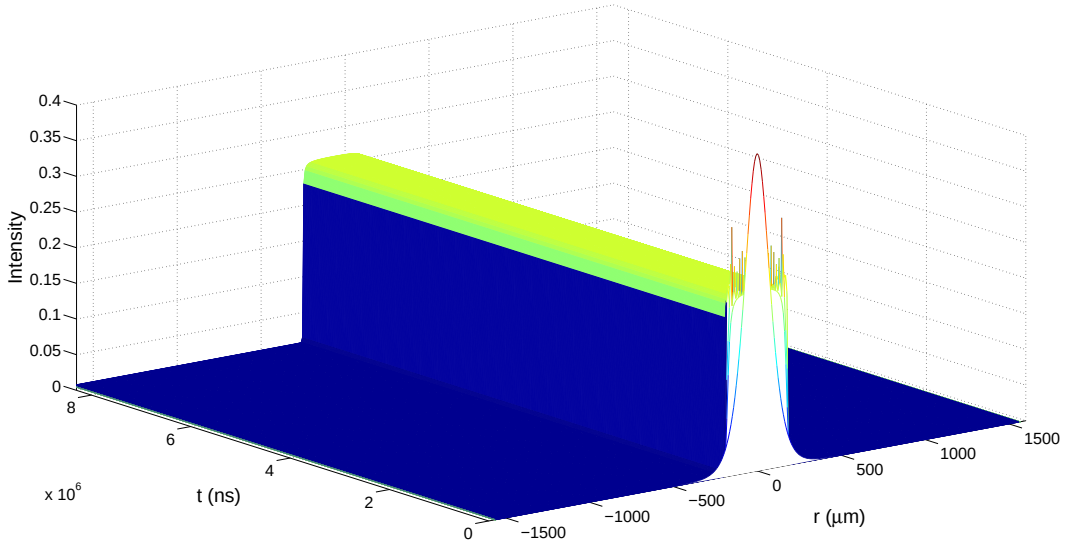


**Figure 4.8:** Evolution of *sech* to a Flat-top CS with $A = 0.2667$. Here, $\sigma = 0.7$, $\omega_0 = 2.12$, $K = 100$ and rest of the parameters same as in Figure (4.7).

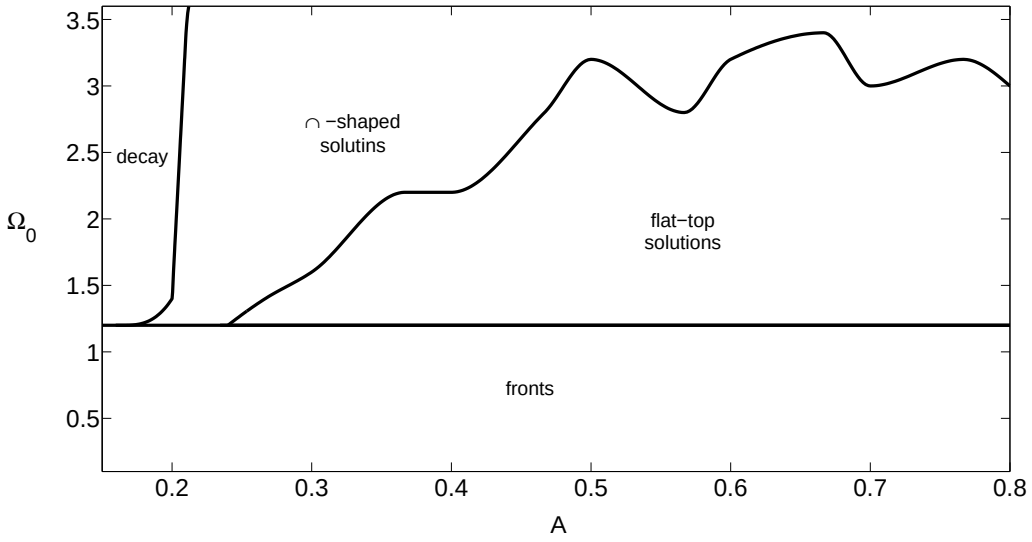


**Figure 4.9:** Regions for ∩-shaped, fronts and flat-top solutions in $A$-$\Omega_0$ plane for $\sigma = 0.7$ and keeping rest of the parameters same as in Figure (4.7).

of feedback $\Omega_0$ and input field amplitude $A$ at a constant feedback strength $\sigma$ (figure (4.9)). Here, $\sigma = 0.7$, $\Omega_0 = 2.12$, $A = 0.667$ and $K = 100$. Fronts are formed for $\Omega_0 < 1$, flat-top solutions are obtained for $1.0 < \Omega_0 < 3.0$. The amplitude and width of CS decreases with the increase in $\Omega_0$-value. For $A = 0.2667$, fronts are formed for $\Omega_0 \leq 1$, a flat-top CS/soliton solution is obtained for $1.0 < \Omega_0 < 1.5$ and ∩-shaped CS for $1.5 < \Omega_0 < 2.6$. For $\Omega_0 > 2.6$, the CS decays quickly. The parameter $\Omega_0$ has significant impact on the amplitude of the CS during evolution. As the value of $\Omega_0$ increases, the evolution amplitude also increases, but on the other hand the soliton width decreases significantly.

# Conclusion

A large family of linear CS molecules is explored in VCSEL-SA-FSF model by controlling the cavity as well as soliton parameters. Diatomic, triatomic and tetra-atomic CS molecules can be excited. Besides, a proper choice of system parameters, particularly,

amplitude leads to the evolution of a ∩-shaped or a flat-top CS or even a 'fronts' type solutions. Regions for ∩-shaped, a flat-top CS, 'fronts' as well as decay region have been identified in the parametric region. The influence of component CSs of a CS molecule on each other's phase are well portrayed to have the insight of the dynamics of the bound CSs.

# Chapter 5

## Cavity Solitons Dynamics

In preceeding chapters, the generation and stability of CSs are presented. We then investigated both the interactional and spontaneous dynamics of CSs. The motivation comes from the fundamental curiosity to validate the interactional behavior of CSs and from the quest of novel all-optical phenomena that may lead to all-optical devices.

## 5.1 Cavity Soliton Dynamics: An Overview

CS has some interesting features that made them competent for versatile applications. A CS can be excited at any desired point in the transverse plane of the cavity. The stationary CS can be set in motion, in principle, by breaking translational symmetry due to the spatial modulation on any system parameter. In fact, any gradient or inhomogeneity in the media leads to the movement of CS. Gradients in the cavity can be introduced through injection beam [164], generating gradients in the cavity background [52], time delay, feedback field strength [58, 165] and feedback field phase [166]. Gradients in the cavity such as intensity [167], phase [123, 167, 168], detuning [169], amplitude [167, 168, 169], thermal [168, 169], inhomogeneous cavity resonance [52, 168], cavity length [52] and field gradients [164] play a major role in defining the dynamics of the CSs. A moving CS can come to rest when it attains an equilibrium

state or the corresponding gradient vanishes [164]. The presence of gradient may be related to the uniform variation of detuning parameter in the semiconductor resonator, here, VCSEL [52]. Alternatively, CS dynamics can be envisaged through a bifurcation of the system, which can be done by exploiting variation of a suitable cavity parameter. The spontaneous and gradient driven movements of CSs is studied in VCSEL with periodic phase modulation of injected beam, as well as detuning [169]. CS dynamics and interactions in broad-area semiconductor laser (particularly VCSEL) coupled with FSF element is reported in ref. [170]. Theoretical prediction is made for the existence and stability of oscillating, oscillating-rotating and traveling twin CS pair [15].

To have a complete idea about any soliton and hence CS, the study of interaction phenomenon is indispensable. Interaction phenomenon is greatly influenced by the relative phase of the participating CSs as well as their individual field profiles. Also, the seperation between CSs play a vital role in the dynamics of interacting solitons or CS. Competing CS either survive or die out depending on the initial gap. Small range interactions between two solitons in saturable absorber allow only one CS to survive, whereas the medium range interactions may allow the survival of new CS in addition to the pre-existing CS [171]. Optical thermal nonlinearities support the long range interactions, i.e., for the range of about ten soliton widths [171]. Any spatial soliton is a self-trapped structure that arises when the strong optical field interacts with the medium, locally modifies the medium's refractive index profile as per the optical field profile and the medium in turn modifies the optical field. Therefore, the self-trapping area can be considered as a perturbed zone. Any other optical field (and hence soliton) that would come closer to it would get modified. This outlines the basic mechanism of soliton interaction [6]. In quantum mechanical sense, the optical

wave packet creates a potential well and gets confined by the same [161]. Therefore, the soliton interaction can be interpreted as an interaction between wave packets of two closely spaced potential wells or wave packets of two jointly induced potential wells. CS being a spatial soliton follows the same mechanism of confinement and interaction. Of course, a big difference is that due to the dissipative nature of the medium, additional energy is required and the loss-gain has to be balanced in the perturbed zone. Correspondingly, inside the potential well the potential will be no more zero. Thus, the confinement of CS occurs at a point far from an equilibrium. In Kerr cavity, mutually coherent in-phase solitons simply attract each other, whereas, mutually coherent but out-of-phase CS repel each other. It is always an attraction for mutually incoherent solitons [161, 172].

Interacting CSs affect the dynamics of each other significantly. Asymmetric spectral broadening of interacting CSs is a resultant of the cross-phase modulation (XPM). XPM generally occurs along with the self-phase modulation when multiple localized structures simultaneously evolve in the cavity. The XPM induced coupling between interacting solitons results in modulation instability, thus, leads to the asymmetric spectral broadening. XPM may not be included explicitly in the initial incident field, but evolution dynamics of interacting CSs encounter its effect [6]. The relative phase and separation between CS change during interactions [120] and the presence of inhomogeneities induces drift in CS [173]. Interactions of CSs in higher order nonlinear medium, such as materials exhibiting saturating nonlinearities or higher order nonlinearities, other than Kerr nonlinearity, present intriguing dynamics such as fission, fusion and annihilation [161]. Two mutually in-phase coherent CSs always experience the attraction, whereas, out-of-phase CSs always lead to the repulsion.

However, the intermediate phase difference results in the interactions influenced by the energy exchange. Intensity in the overlapping region increases (decreases) for the in-phase (out-of-phase) CSs. This results in the local increase (decrease) of refractive index in the material, and eventual attraction (repulsion) between the CSs. However, in homogeneous materials, generally the phase difference of the interacting solitons explicitly influence the trajectories of motion [172]. The afore mentioned CS dynamics can be used for the realization of actual device only if the dynamics is controllable as well as predictable. It may be noted that, non-stationary solitons inside a resonator undergo symmetry breaking corresponding to the direction of motion in addition to the symmetry breaking of location, which is essential for stationary soliton [174].

We study the interaction as well as spontaneous dynamics of CSs in microcavity of VCSEL-SA-FSF in the following section.

## 5.2 Cavity Soliton Dynamics in Microcavity: VCSEL-SA-FSF Model

Now we present the results of our investigation on the interaction between two coherently injected CSs at different relative phases in VCSEL with saturating (approximated to cubic-quintic) nonlinearity and coupled with FSF. Gradient in the cavity can be introduced in terms of intensity, phase, amplitude, temperature, cavity resonance and cavity length [52, 57, 164]. Spatial drift of CS in the cavity can be influenced by any of the above stated gradients and the CS comes to rest when the gradient vanishes or CS reaches at an equilibrium state [164]. In this section, the drift experienced by coupled CSs is due to the phase difference introduced between the interacting CSs. It

is observed that, if the initial separation between the two interacting CSs is less than two CS widths and the relative phase is zero, then fusion of the interacting CS occurs. Similar fusion occurs for a relative phase less than $\pi/2$. For a relative phase of $\pi/2$ one, CS remains stationary while the other starts moving, collide with the former one to annihilate it and eventually bounces back. The soliton interaction is to be inelastic as the system is non-integrable. Separation of more than two CS widths results in no interaction between the incident CSs. Therefore, in this section, the initial separation of two soliton widths in-between the incident CSs is maintained and the interaction is studied at different relative phases (Figure (5.1)). In-phase interacting CSs experience catastrophic collapse after propagating for about 1400 time-steps (i.e., 1400 cavity round trip time) (Figure (5.1a)). The in-phase CSs drift toward each other, as a result of attraction, and at a point their intensity profile overlaps and hence intensity profile shoots up, leading to the instantaneous self-focusing. Abrupt increase of the self-focusing imbalances the delicate balance with the diffraction, leading to the instability of the CS and thus resulting to the catastrophic collapse of CSs. As phase difference is increased between the two CSs, the phase gradient is introduced in the system, causing the spatial drift of both the CSs. Figures (5.1b), (5.1c), (5.1d),(5.1e) and (5.1f) represent the spatial drift of CSs for different relative phases, namely, $\pi/10$, $\pi/8$, $\pi/4$, $\pi/3$ and $\pi/2$, respectively. Due to the presence of higher order nonlinearity, the CS dynamics in this case is much more intriguing than the case of a Kerr cavity. In general, the partially out-of-phase CSs (Figures (5.1b)-(5.1f)) show several attraction-repulsion cycles and eventually one gets annihilated, while the other moves with a uniform speed thereafter. The speed of the surviving CS decreases nonlinearly with the increase in relative phase (Figure (5.2)). For the sake of symmetry, central

point of the spatial axis is marked as zero; left CS (LCS) represents the CS formed on the negative spatial axis, whereas right CS (RCS) corresponds to the CS formed on the positive spatial axis. Also, increasing relative phase delays the annihilation of the CS. As the relative phase crosses a value of $\pi/2$, the CS velocity decreases significantly, while preserving the nature of its dynamics. For completely out-of-phase situation, CS velocity is very low, but increases with the evolution. As relative phase crosses the value of $\pi$, the CS pair starts drifting in opposite direction with the increasing velocity.

More insight can be obtained by precisely looking on the velocities of an individual CS. Considering Figure (5.1d), wherein the velocities of both CSs change with time. The variation in velocities of LCS and RCS are represented in the Figure (5.3). RCS starts with almost uniform velocity, whereas, the LCS starts with an acceleration. As LCS approaches RCS, the transfer of momentum is experienced by RCS, resulting in an increase of velocity. On the other hand, LCS retards. Again the accelerated RCS approaches the retarded LCS. The transfer of momentum from the RCS to LCS is observed. LCS gains momentum, therefore starts moving with high velocity and RCS retards. Eventually, the LCS accelerates during the retardation phase of the RCS and vice-versa. The cycle of acceleration and retardation of LCS and RCS is repeated several times (see supplementary media). Figure (5.3) depicts one cycle of velocity variation at relative phase difference of $\pi/4$.

Two completely out-of-phase CSs repel and attract each other periodically (Figure (5.4)). The frequency of oscillation as well as the velocity of the interacting CSs increase with evolution, keeping the motion confined. The relative phase of the two interacting CSs also get modulated with evolution (Figure (5.4b)). The CSs are ini-

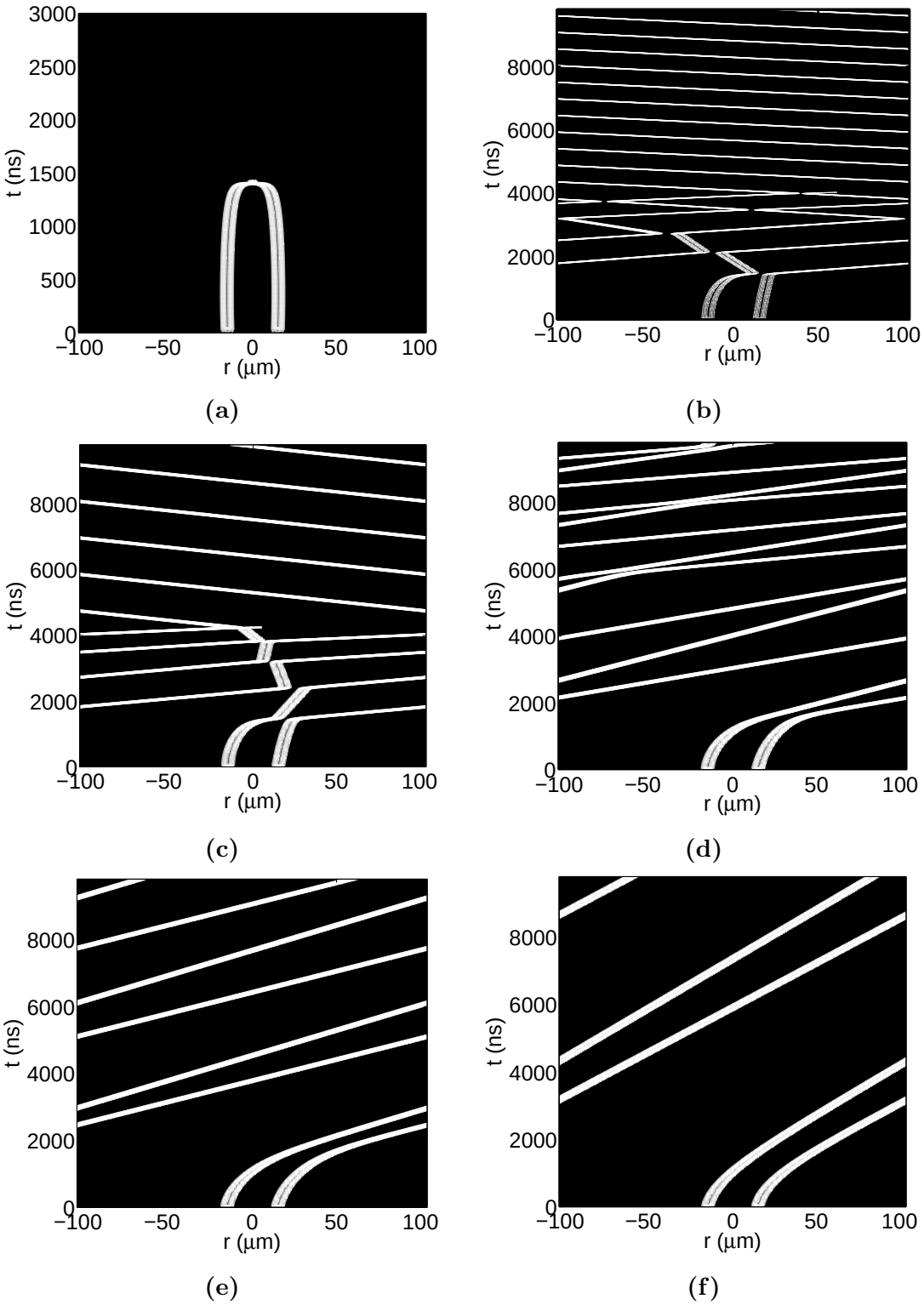


**Figure 5.1:** Interaction of two CS at the following relative phases ($\Delta\phi$): (a) for $\Delta\phi = 0$ interacting CS experiences Catastrophic collapse, (b) and (c) for $\Delta\phi = \pi/10$ and $\Delta\phi = \pi/8$ one soliton annihilates whereas another travels with almost constant velocity, (d) for $\Delta\phi = \pi/4$ each soliton moves with changing velocity during evolution, (e) for $\Delta\phi = \pi/3$ evolution of solitons with approximately constant velocity and (f) for $\Delta\phi = \pi/2$ evolution of solitons with slightly different velocities.

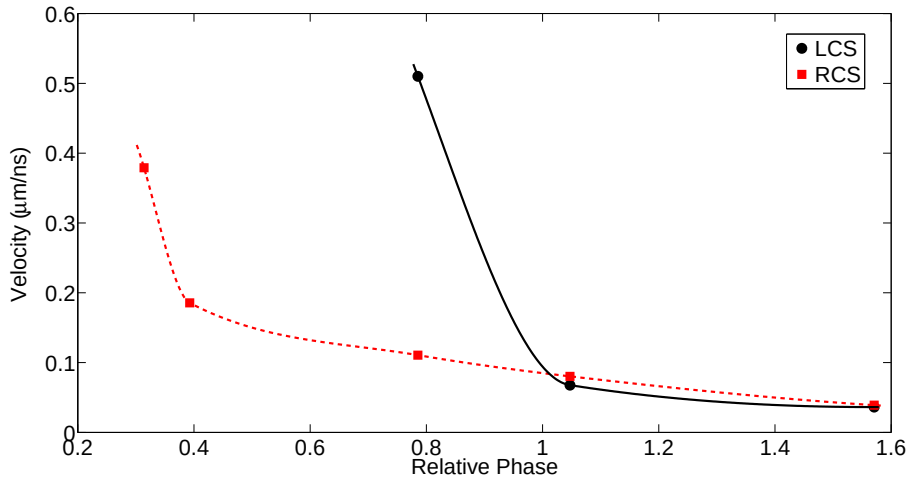


**Figure 5.2:** Relative phase versus velocity plot for interacting CSs. Solid black line represents the velocity of LCS where as dashed red line corresponds to the RCS. For phase difference = $\pi/4$, the velocity changes with time, therefore, corresponding average velocity is considered.

tially locked in out-of-phase mode, gradually move out of this locking. Besides phase, the motion of CS can be controlled by other cavity parameters, like feedback strength, delay in the feedback and even detuning. However, the study shows that the velocity increases with the stronger feedback strength, which is discussed in the following section of this chapter.

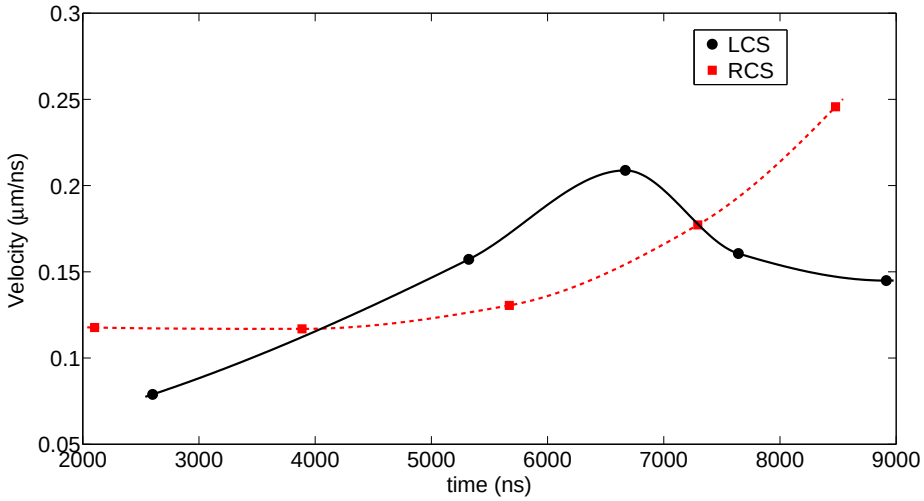


**Figure 5.3:** Variation of the velocity of LCS and RCS with evolution for the relative phase $\pi/4$. Solid black line represents the velocity of LCS where as dashed red line corresponds to the RCS.

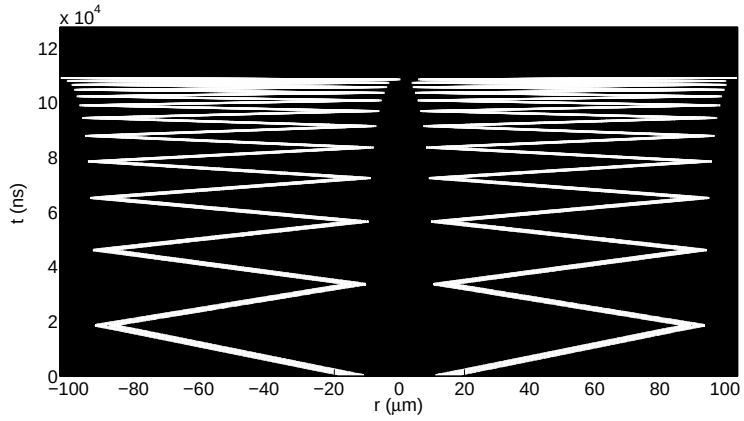


**(a)**

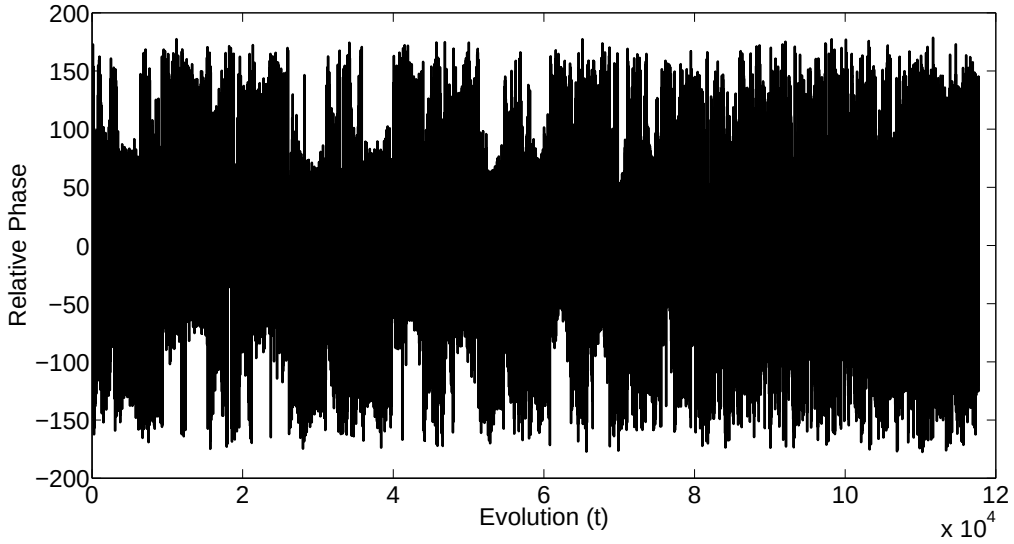


**(b)**

**Figure 5.4:** (a) Space-time evolution of out-of-phase CSs. (b) Relative phase of the CSs originating in positive and negative spatial domains.

## 5.3 All-Optical Push-broom Effect, Marching Cavity Soliton and Migrating Cavity Soliton

Any inhomogeneity, spatial disorder, the presence of the defects and impurities in the semi-conductor materials strongly influence the spatial positioning as well as drift of spatial dissipative solitons or CSs. For certain applications, such random motion can be controlled by introducing parameter modulations greater than noise amplitudes

[1, 69]. Apart from the spatial disorder or defects, the variation in the feedback strength $\sigma$, resonant frequency of the feedback field $\Omega_0$, line-width enhancement factor $\beta$ and amplitude of injected optical field $A$ of the system affect the dynamics of the system.

Chapter 4 dealt with $\beta = 0$, although it is not a rule of thumb, the CSs are stationary in most of the cases for this particular case. In contrary, for $\beta > 0$, we witness intriguing dynamics of the generated CS. The most appealing one is Figure (5.5) where two CSs initially oscillate and eventually one of them starts pushing the other. Such phenomena is observed for a range of $\sigma$, i.e., $0.60 < \sigma < 0.83$, keeping $\beta = 1$, $\Omega_0 = 2.12$, $A = 0.2667$ and rest of the parameters are the same as in Figure (3.1). This one of its kind novel phenomenon can be termed as 'Push-broom effect'.

Although, de Sterke *et al.* and Broderick *et al.* [91, 175, 176] used the same term (push-broom) in different context, those were merely compression of the signal pulse not an actual movement. In the present study, one CS pushes the other and swipe along the transverse plane of the cavity, therefore, shows a 'true' all-optical push-broom effect. The push-broom effect is observed for very limited range of $\beta$, $\sigma$ and $\Omega_0$. With variation of $\sigma$ the dynamics also varies, but eventually leads to push-broom. For $\sigma = 0.61$ (Figure (5.5a)) and $\sigma = 0.64$ (Figure (5.5b)), the initially colliding CSs never come to rest before showing the push-broom effect. However, for $\sigma = 0.65$ (Figure (5.5c)), 0.70, 0.81 and 0.82 (Figure (5.5d)), one of the colliding CS momentarily comes to rest.

In the course of evolution when both the CSs collide and interact with each other, the phenomenon of XPM plays an important role between the stationary and moving CS. As a result, the stationary CS is swept by the moving CS along with it. The

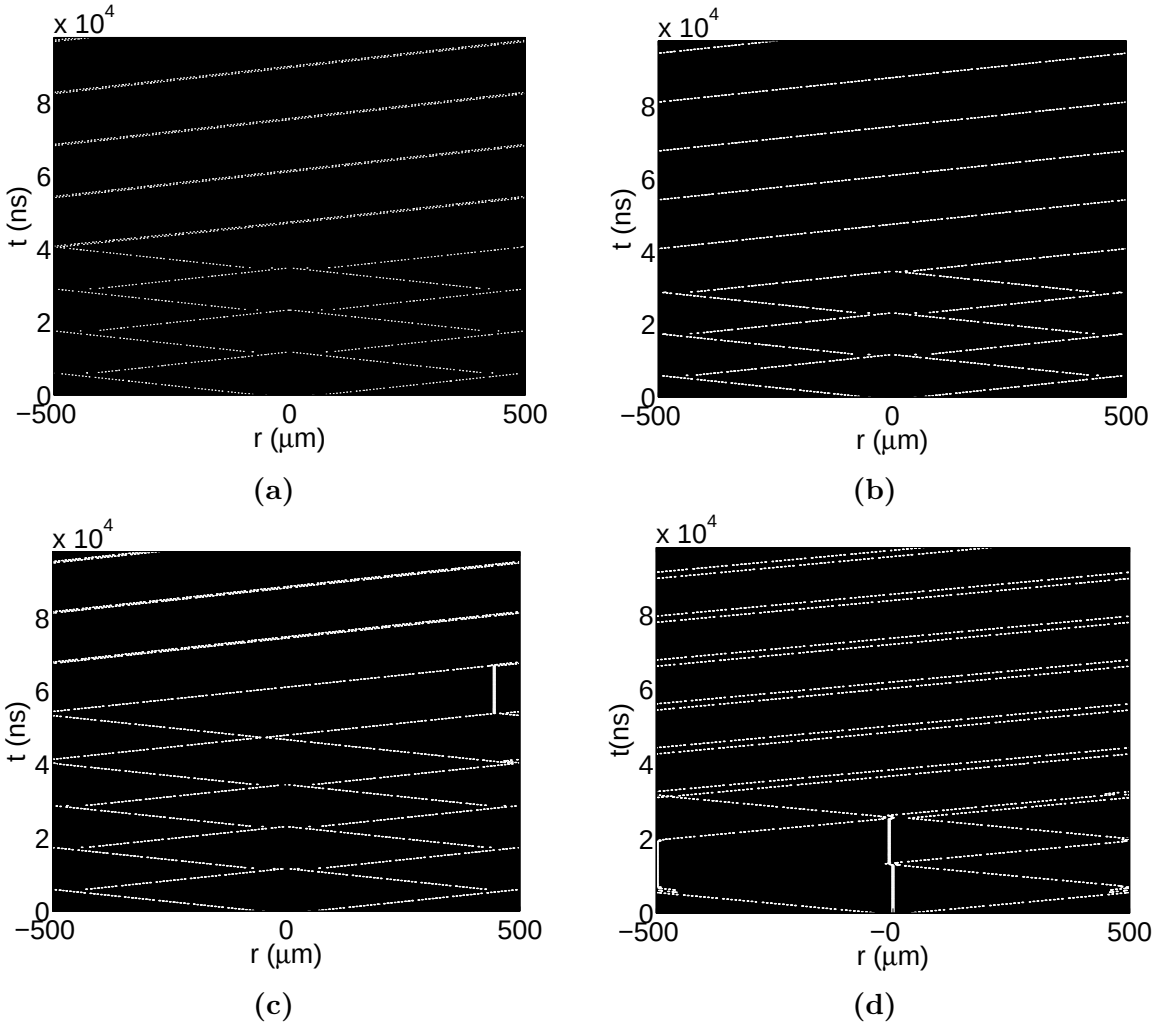


**Figure 5.5:** All-optical Push-broom: some selective push-broom dynamics of CS with increasing feedback strength. (a) $\sigma = 0.61$, (b) $\sigma = 0.64$, (c) $\sigma = 0.65$ and (d) $\sigma = 0.82$. For all panels $\beta = 1$, $\Omega_0 = 2.12$, $A = 0.2667$, $\alpha = 2.7$, $\mu = 1.37$, $\gamma = 0.5$, $\beta = 1$, $s = 10$ and $\lambda = 0.5$.

velocity of the push-broom CSs significantly increases with feedback strength and eventually saturates (Figure (5.8)). Push-broom is also observed with more than two CSs.

For example, at $\sigma = 0.76$, the initial field splits into five CSs those eventually start moving in the same direction (Figure (5.6)) as if they are marching. Such 'marching CSs' maintain constant gap during marching or evolution. By controlling the feedback strength not only push-broom dynamics can be influenced but also a stationary CS molecule can be drifted along the transverse axis of the VCSEL. For instance, a change

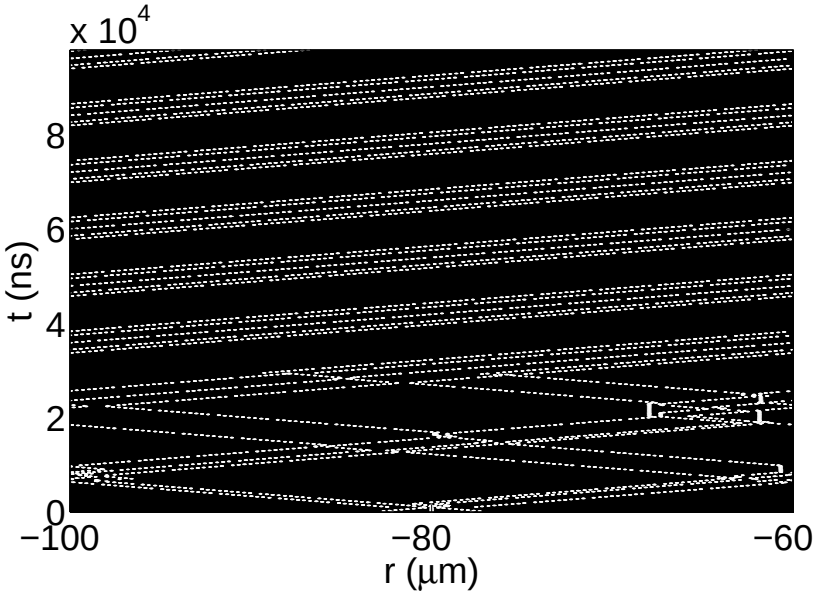


**Figure 5.6:** Generation of 'Marching CSs' for $\sigma = 0.76$. Other parameters are same as in Figure (5.5).

in $\sigma$ from 0.84 (Figure (5.7a)) to 0.83 (Figure (5.7b)) force to migrate a CS molecule by approximately $150\mu m$ across the transverse plane of cavity (Figure (5.7)). Also, the symmetric triatomic CS molecules turns to asymmetric.

The all-optical push-broom CSs, marching CSs and migrating CSs found in the present study are found to be controllable and predictable; thus can open a new horizons in all-optical devising. Since, any local defect, gradient or inhomogeneity of the material can be probed using such CSs, they have potential for applications in soliton force microscopy, shift register and serial-parallel converter. Also, memory relocation can be done by tuning CS parameters. Feedback strength parameter $\sigma$ explicitly affects the velocity of push-broom CS, which is shown in Figure (5.8). As the value of feedback strength is increased, correspondingly CS velocity also increases. The feedback strength versus velocity plot observes an abnormal kink for $\sigma = 0.76$, which apparently corresponds to the velocity of 'marching CS'.

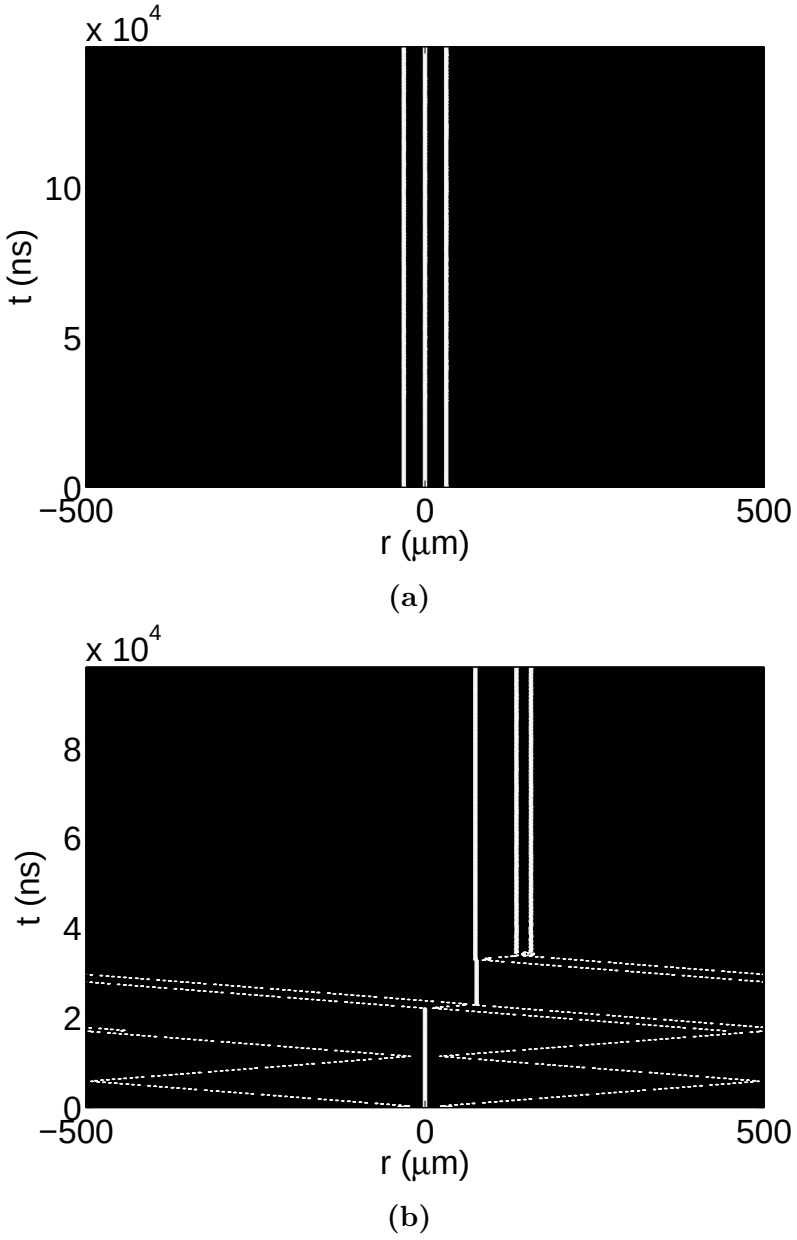


**Figure 5.7:** Migration of CS molecules: (a) a stationary tri-atomic CS molecule for $\sigma = 0.84$, (b) migration of the CS molecule for $\sigma = 0.83$. Other parameters are same as in Figure (5.5).

# Conclusion

Interaction between two CS shows interesting dynamics. The phase induced dynamics is explored. Threshold separation for interaction, influence of relative phase on CS velocity, variation of CS velocity with time are quantitatively determined. A true push-broom effect in a cavity is a novel phenomenon. This effect is observed only for

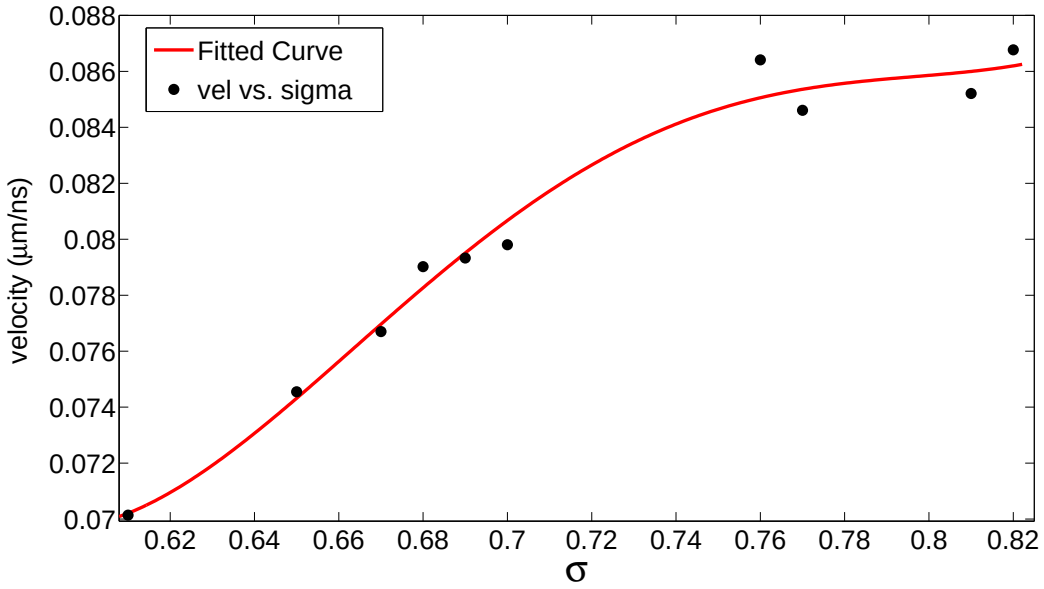


**Figure 5.8:** Variation of the velocity of Push-broom CS with the feedback strength. Other parameters are same as in Figure (5.5).

a special set of parameters particularly for non-zero value of line-width enhancement factor of the passive material. This effect can have potential for the applications in all-optical devices creating a buzz in industrial, research and development as well as in the commercial applications, such as, in still emerging areas: soliton force microscopy [1], signal processing and transmission, device characterization [177]. The movement of CS can be induced by parameter gradient, which has prospective applications in: all-optical reconfiguration of the memory array, shift register and serial-parallel converter. Local defects or the presence of gradients and inhomogeneities in the materials and devices can be probed using CS [173, 178]. CSs formed are controllable, predictable and efficient thus can open a new horizon in all-optical data processing, delay lines and development erasable memory devices.

# Chapter 6

## Cavity Soliton Generation by Standing Wave Method: An Alternate Approach

Analytical method to solve the governing equations of CS are limited. Most of the theoretical investigations emphasize on finding the stability region, bifurcation behavior etc. instead of directly solving for soliton solution. A noteworthy analytical-numerical approach is the separation method, where the governing equation is split into two eigenvalue problems and solved graphically to find CS. An investigation on CS first ever completely by variational method based analytical approach has been presented in Chapter 3. In this chapter, we propose an analytical approach to achieve CS following the standing wave method. CS can be considered as a 'soliton in a box', or a bound state of a propagating soliton bouncing between the cavity mirrors. Based on this concept, we first determined traveling wave soliton solutions (TWSS) in a VCSEL coupled with FSF and then superposed counter-propagating TWSS to achieve standing wave localized structures (SWLS). Those standing wave patterns inside dissipative cavity can be considered as CSs, provided the three basic features, namely, exponential localization, bistability and freedom of location are satisfied.

In this chapter, we derived bright (sech pulses) and exotic (with cosh-Gaussian pulses) TWSS and, subsequently, SWLS for two models based on VCSEL: one with

perturbation gradient and the other is with constant perturbation. A parametric region that corresponds to stable CS generation is identified. The cosh-Gaussian soliton solutions can be used to realize CS based all-optical tunable devices.

## 6.1 Model 1

A dissipative cavity comprising VCSEL coupled with FSF is considered. At steady state, the pulse dynamics in the laser cavity is represented by the following CGLE [121]:

$$(\frac{\partial}{\partial t}+1)E(x,t)-i\frac{\partial^2 E(x,t)}{\partial x^2}-\mu(1-i\alpha)(1-|E|^2)E(x,t)-\sigma(a-ib)E(x,t)=0, \tag{6.1}$$

where, $E(x,t)$ is the slowly varying wave envelope of the electric field of the laser pulse, $t$ is cavity round trip time and $x$ is the coordinate transverse to the cavity axis. Here, $a=\Gamma_0/(\Gamma_0^2+\Omega_0^2)$ and $b=\Omega_0/(\Gamma_0^2+\Omega_0^2)$, while $\Omega_0$ represents resonant frequency and $\Gamma_0$ is the line-width enhancement parameter of the feedback field, $\sigma$ represents the coupling constant or feedback strength, $\mu$ represents scaled gain that is responsible for the stabilization of the off-state in VCSEL. The line-width enhancement parameter $\alpha$ usually attains large positive values for VCSEL. In equation (6.1), the first term represents evolution of the wave envelope $E(x,t)$ and linear loss inside the cavity. The second term is the diffraction term. The third term contains Kerr nonlinearity and nonlinear loss/gain (depending upon the sign of the coefficients) incurred in the transverse direction of cavity. The last term in the equation represents the contribution of frequency selective feedback. Equation (6.1) can be rewritten as a perturbed nonlinear

Schrdinger equation (NLSE) as follows:

$$i\frac{\partial E}{\partial t} + \frac{\partial^2 E}{\partial x^2} - (\sigma b + \alpha\mu)E + \alpha\mu|E|^2 E = iR(E, E^*), \tag{6.2}$$

where, $R(E, E^*) = (\sigma a - 1 + \mu)E - \mu|E|^2 E$ is the perturbation term, nullifying which one can retrieve an unperturbed NLSE. Both the forms of equations (6.1) and (6.2) are well explored in different fields of study, particularly, in cavity dynamics. In the present investigation, the following perturbation term can be introduced:

$$R(E, E^*) = \frac{\partial}{\partial x}[(\sigma a - 1 + \mu)E - \mu|E|^2 E], \tag{6.3}$$

The above form represents the slope of the perturbation, which is used in anticipation to include the effect of modulation of perturbation in a spatially distributed system. This slope could add a pseudo 3D effect in the resultant soliton profile, which may be even better than an actual 3D profile as far as visualization is concerned.

Equation (6.1) is generally, non-integrable by means of inverse scattering transform method, hence no general exact solution is possible. However, a particular exact solution can be obtained [179, 180, 181]. Several analytical approaches, such as Painlevé analysis and its variant [182], Hirota bilinear method [183] have been employed to solve the CGLE. Soliton solutions of discrete CGLE has been obtained using extended hyperbolic function approach [184]. Besides, separation method has been found to be a very strong tool to solve such CGLE [121]. Approximate analytical method, like, variational method has been successfully used to find the dynamics of CGLE system [158, 136]. Numerical solution of such CGLE mostly relies on Crank-Nicholson method. Time splitting spectral method is another strong contender [136].

The TWSS of the system are obtained in the presence of dissipation using He's semi-inverse variational method [185, 186, 187]. Its an appreciated method to find

TWSS in a wide variety of systems including nanofibers [188]. Besides Kerr nonlinear media, the suitability of this method now is established in studying optical soliton perturbation in media having different nonlinearities, namely, non-Kerr-law nonlinearity [140], dual power-law nonlinearity [189] and log-law nonlinearity [190]. In addition to provide the best suitable solution to the system, this method gives an excellent overview of the nature of solutions [191]. It is one of the strongest approximate methods, which has been successfully applied to solve numerous systems like Helmholtz equation, Broer-Kaup (BK) systems, Whitham Broer-Kaup (WBK) systems [192], cubic-quintic Duffing oscillators [193] and periodic solutions of some nonlinear oscillators with strong nonlinearity [185]. The step-by-step derivation of TWSS is presented below.

In order to find the 1-soliton TWSS, the following ansatz is considered [185, 194]:

$$E(x,t) = g(\xi)e^{(-kz+\omega t+\theta)}, \tag{6.4}$$

where, $g(\xi)$ represents the pulse shape. $\xi = x - vt$, $v$ is the velocity of the soliton, $k$ is the soliton wave number, $\omega$ is the soliton frequency and $\theta$ is the phase constant. Hereafter we will refer $g(\xi)$ as profile function. Substituting equation (6.4) in equation (6.2) that incorporates the new perturbation term given by equation (3) and separating the real and imaginary parts, the following set of equations are obtained:

$$g'' + (-\omega - \sigma b + k^2 - \alpha\mu)g + \alpha\mu g^3 = k(\sigma a - 1 + \mu)g + \mu k g^3 \tag{6.5}$$

and

$$(-2k - v)g' = (\sigma a - 1 + \mu)g' - 3\mu g^2 g', \tag{6.6}$$

where $g' = \partial g/\partial \xi$ and $g'' = \partial^2 g/\partial \xi^2$ Solving equation (6.6) for $g$ we get,

$$g = \pm\sqrt{\frac{v + 2k + \sigma a - 1 + \mu}{3\mu}} \tag{6.7}$$

Equation (6.7) indicates that the soliton solution exists if $3\mu(v+2k+\sigma a-1+\mu) > 0$. Therefore, for any acceptable profile function '$g$', the wave velocity needs to satisfy the following relation:

$$v > 1 - 2k - \sigma a - \mu \tag{6.8}$$

Taking into account the limiting condition of velocity, as stated in equation (6.8), the velocity of the traveling wave can be kept constant. Also, the velocity need to be a positive quantity. For a suitable choice of parameters ($\alpha = 2.7$, $\mu = 1.397$, $\sigma = 0.7$, $\Gamma_0 = 0.5$ and $\Omega_0 = 0.1$) and obeying the inequality relation as stated in equation (6.8), the value of velocity is obtained as $v = 2.7568$, which is used throughout the investigation. Multiplying equation (6.5) by $g'$ and then integrating it over the entire space results in:

$$\frac{g'^2}{2} + (k^2 - \sigma b - \omega - \alpha\mu - \sigma a + 1 - \mu)\frac{g^2}{2} + (\alpha\mu - \mu k)\frac{g^4}{4} = K \tag{6.9}$$

where, $K$ is the constant of integration. For this system, a new quantity $J$ can be defined as follows [140, 186]:

$$J = \int_{-\infty}^{\infty} K d\xi \tag{6.10}$$

On substituting equation (6.9) in equation (6.10), the following equation is obtained:

$$J = \int_{-\infty}^{\infty} (\frac{g'^2}{2} + (k^2 - \sigma b - \omega - \alpha\mu - \sigma a + 1 - \mu)\frac{g^2}{2} + (\alpha\mu - \mu k)\frac{g^4}{4})ds. \tag{6.11}$$

A proper choice of the profile function $g(\xi)$ is now required to proceed further. To

solve equation (6.1) two different profile functions are considered. One is hyperbolic secant *sech* function; a widely studied standard function for bright soliton and the other is a *cosh*-Gaussian function; an exotic function that can generate a number of profiles by tuning *cosh* parameter. The former is adopted to reveal the nature of the basic TWSS, while the latter is considered in the anticipation of achieving a versatile TW profile.

### 6.1.1 Case-I: '*sech*' profile function

The fundamental modes emitted by lasers are generally modeled as either '*sech*' or Gaussian profile. *sech* function is the exact solution of an unperturbed cubic NLSE. Gaussian function is also equally popular for the ease of mathematical modeling and calculations without altering the background physics. In the present case, we choose the standard *sech* type (bright) one-soliton solution of the following form:

$$g(\xi) = S\ sech(T\xi). \tag{6.12}$$

The parameters $S$ and $T$ represent the amplitude and inverse of the width of soliton, respectively. Our primary target is to determine the values of $S$ and $T$. Substituting equation (6.12) in equation (6.13), the following equation is formed:

$$J = \frac{S^2T}{3} + \mu(\alpha - k)\frac{S^4}{3T} + (k^2 - \sigma b - \omega - \alpha\mu - \sigma a + 1 - \mu)\frac{S^2}{T}. \tag{6.13}$$

The values of $S$ and $T$ can be obtained using the principle of variation, i.e., $\partial J/\partial S = 0$ and $\partial J/\partial T = 0$. These conditions in conjugation with equation (6.13) lead to the following relations:

$$T^2 + 3(k^2 - \sigma b - \omega - \alpha\mu - \sigma a + 1 - \mu) + 2(\alpha - k)\mu S^2 = 0 \tag{6.14}$$

and

$$-T^2 + 3(k^2 - \sigma b - \omega - \alpha\mu - \sigma a + 1 - \mu) + (\alpha - k)\mu S^2 = 0 \tag{6.15}$$

Solving equations (6.14) and (6.15):

$$S = \sqrt{\frac{2(k^2 - \sigma b - \omega - \alpha\mu - \sigma a + 1 - \mu)}{\mu(k - \alpha)}}, \tag{6.16}$$

$$T = \sqrt{(k^2 - \sigma b - \omega - \alpha\mu - \sigma a + 1 - \mu)}. \tag{6.17}$$

Therefore, the final TWSS for the VCSEL-FSF system reads as:

$$E(x,t) = \sqrt{\frac{2(k^2 - \sigma b - \omega - \alpha\mu - \sigma a + 1 - \mu)}{\mu(k - \alpha)}}$$
$$sech(\sqrt{(k^2 - \sigma b - \omega - \alpha\mu - \sigma a + 1 - \mu)}e^{i(-kx+\omega t+\theta)} \tag{6.18}$$

Figure (6.1) depicts the intensity profile of the *sech* TWSS. This solution is found to be valid for a large choice of system parameters.

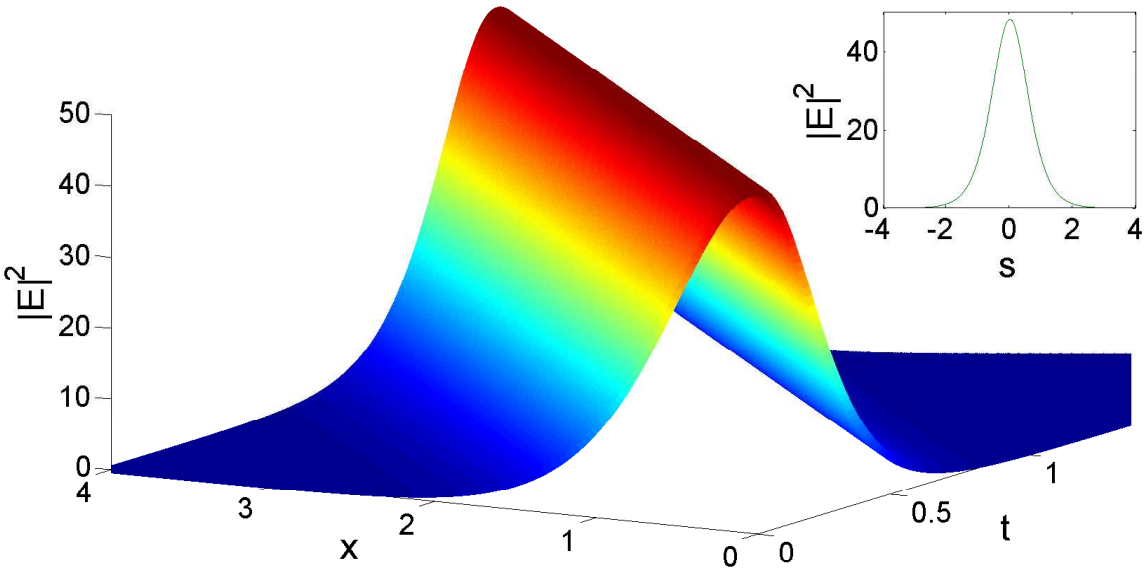


**Figure 6.1:** 3D profile of sech traveling wave soliton solution. Inset shows 2D profile, i.e., cross-section of the 3D profile. Here, $\alpha = 2.7$, $\mu = 1.397$, $\sigma = 0.7$, $\Gamma_0 = 0.5$ and $\Omega_0 = 0.1$.

### 6.1.2 Case-II: Exotic cosh-Gaussian profile function

The possibility to achieve soliton solution with a profile different from the standard *sech* form is explored in this section. *cosh*-Gaussian profile function of the following form is considered as an ansatz for the system:

$$g(\xi) = Pcosh(Q\xi)e^{-\frac{\xi^2}{R^2}}. \tag{6.19}$$

Here, $P$ represents the pulse amplitude, $Q$ is the *cosh* parameter and $R$ represents the pulse width. This type of pulse can be generated by superposing two de-centered Gaussian pulses [76]. To the best of our knowledge, this is the first use of *cosh*-Gaussian profile in the study of VCSEL as well as of equation (6.1). The *cosh*-Gaussian ansatz is found to be more generic as it gives rise to a number of different profiles for different values of *cosh*-Gaussian parameter. At a very small value of *cosh*-parameter the pulse is almost Gaussian, which will transform to a deformed Gaussian, then flat-top and finally to one with a central dip with increasing value of *cosh*-parameter. This seems to be more interesting in comparison to the common *sech* profile for the spontaneous emergence and tunability of self-organized structures. This profile promises more intriguing spatio-temporal patterns in spatially extended systems. *cosh*-parameter also decides the steepness of the profile, which in turn influences the other optical localized structures nearby. Thus the *cosh*-parameter renders a controlling tool and hence has potential applications in all-optical tunable devices [195]. Besides, a large 3D *cosh*-Gaussian function, which is of annular intensity profile, may trap a small optical structure and in principle, quantum particles.

Substituting the *cosh*-Gaussian shape function, i.e., equation (6.19) in equation

(6.13), the following relation for $J$ is obtained:

$$J = \frac{\sqrt{2\pi}P^2}{8R}(Q^2R^2 - e^{\frac{Q^2R^2}{2}} - 1) + \frac{\sqrt{\pi}\mu(\alpha-k)P^4R}{16}(e^{Q^2R^2} + 4e^{\frac{Q^2R^2}{4}} + 3) + \frac{\sqrt{2\pi}}{8}(k^2 - \sigma b - \omega - \alpha\mu - \sigma a + 1 - \mu)P^2R(e^{\frac{Q^2R^2}{2}} + 1). \quad (6.20)$$

Similar to the case of *sech* solution the values of $P$, $Q$ and $R$ can be determined by varying $J$ with respect to each of the system parameter, i.e., $\partial J/\partial P = 0$, $\partial J/\partial Q = 0$ and $\partial J/\partial R = 0$, which yield the following equations, respectively:

$$\sqrt{2}(k^2 - \sigma b - \omega - \alpha\mu - \sigma a + 1 - \mu)R^2(e^{\frac{Q^2R^2}{2}} + 1) - \sqrt{2}(Q^2R^2 - e^{\frac{Q^2R^2}{2}} - 1) + \mu(\alpha - k)P^2R^2(e^{Q^2R^2} + 4e^{\frac{Q^2R^2}{4}} + 3) = 0, \quad (6.21)$$

$$\sqrt{2}(k^2 - \sigma b - \omega - \alpha\mu - \sigma a + 1 - \mu)R^2e^{\frac{Q^2R^2}{2}} + \mu(\alpha - k)P^2R^2(e^{Q^2R^2} + e^{\frac{Q^2R^2}{4}}) - \sqrt{2}(2 - e^{\frac{Q^2R^2}{2}}) = 0, \quad (6.22)$$

and,

$$\frac{\sqrt{2}}{R^2}(Q^2R^2 - e^{\frac{Q^2R^2}{2}} - 1) + \sqrt{2}(k^2 - \sigma b - \omega - \alpha\mu - \sigma a + 1 - \mu)(e^{\frac{Q^2R^2}{2}} + 1) - \sqrt{2}Q^2(2 - e^{\frac{Q^2R^2}{2}}) + \sqrt{2}(k^2 - \sigma b - \omega - \alpha\mu - \sigma a + 1 - \mu)Q^2R^2e^{\frac{Q^2R^2}{2}} + \mu(\alpha - k)P^2Q^2R^2(e^{Q^2R^2} + 4e^{\frac{Q^2R^2}{4}}) + \frac{\mu}{2}(\alpha - k)P^2(e^{Q^2R^2} + 4e^{\frac{Q^2R^2}{4}} + 3) = 0. \quad (6.23)$$

The solutions of equations (6.21) - (6.23) give the values of $P$, $Q$ and $T$. Solving the equations (6.21) - (6.23) analytically is a cumbersome process. Therefore, graphical method is adopted. Figure (6.2) depicts the plot of equations (6.21) and (6.22) for a constant value of $T$. The intersection points are the solutions of equations (6.21) and (6.22). In Figure (6.2), instead of few discrete solution points, a long overlapping

region that signifies a large family of parametric solution is obtained. The curves intersect at region where value of $P$ is less than 1. Any point on the intersecting region, with the fixed $R$-value corresponds to a possible solution. Considering the

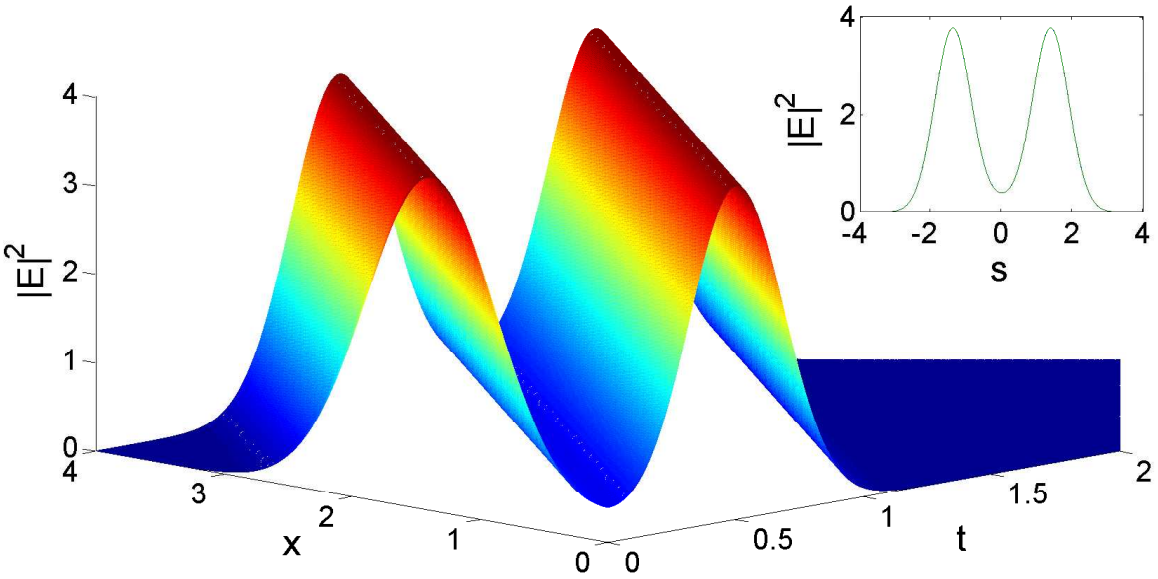


**Figure 6.2:** Plots of equations (6.21) and (6.22) with $R = 1.02$. The long intersecting/overlapping region corresponds to the stable soliton solution. Rest of parameters are same as in Figure (6.1).

different solution points from Figure (6.2), different solution profiles are plotted. For the point considering values $P = 0.6236$, $Q = 2.6505$ and $R = 1.02$, a $3D$ cosh-Gaussian function profile is plotted, which is shown in Figure (6.3). Inset shows the corresponding $2D$ profile with same parametric values. It is evident from the Figure that the pulse propagates as a stable soliton with a central dip. Figures (6.4) and (6.5) show the cosh-Gaussian profile functions with ($P = 0.2599$, $Q = 3.1874$) and ($P = 0.0255$, $Q = 4.3832$), respectively, at a constant value ($R = 1.02$). As the value of $P$ decreases and $Q$ increases, the dip between two humps changes its shape and depth, which is clearly evident from the inset of Figures (6.3), (6.4) and (6.5), respectively.

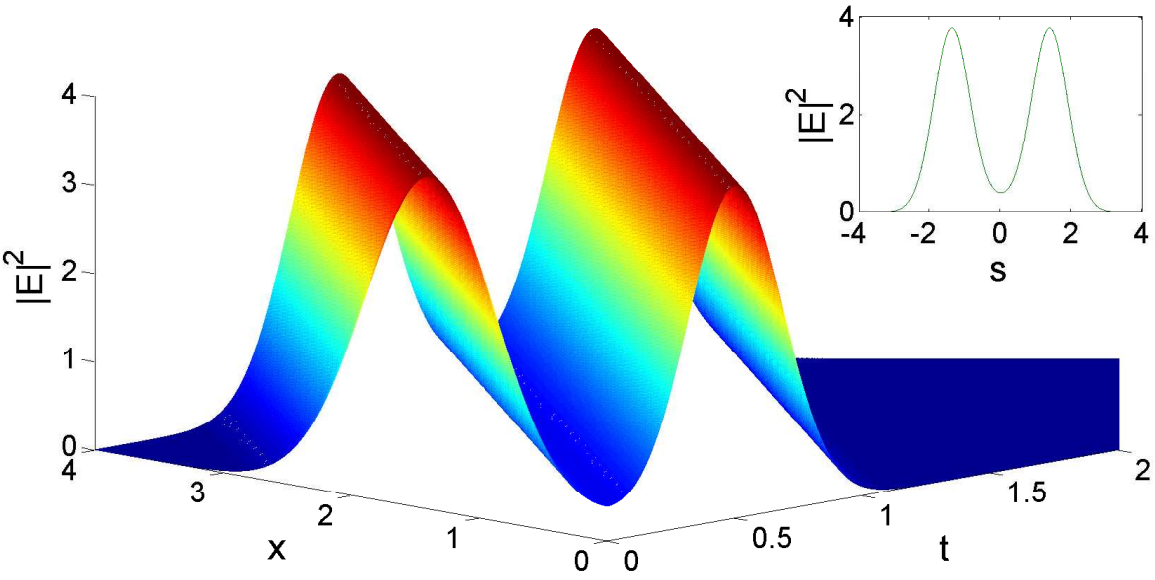


**Figure 6.3:** TWSS of cosh-Gaussian profile for $P = 0.6236$, $Q = 2.6505$ and $R = 1.02$. 2D profile is in the inset. Rest of parameters are same as in Figure (6.1).

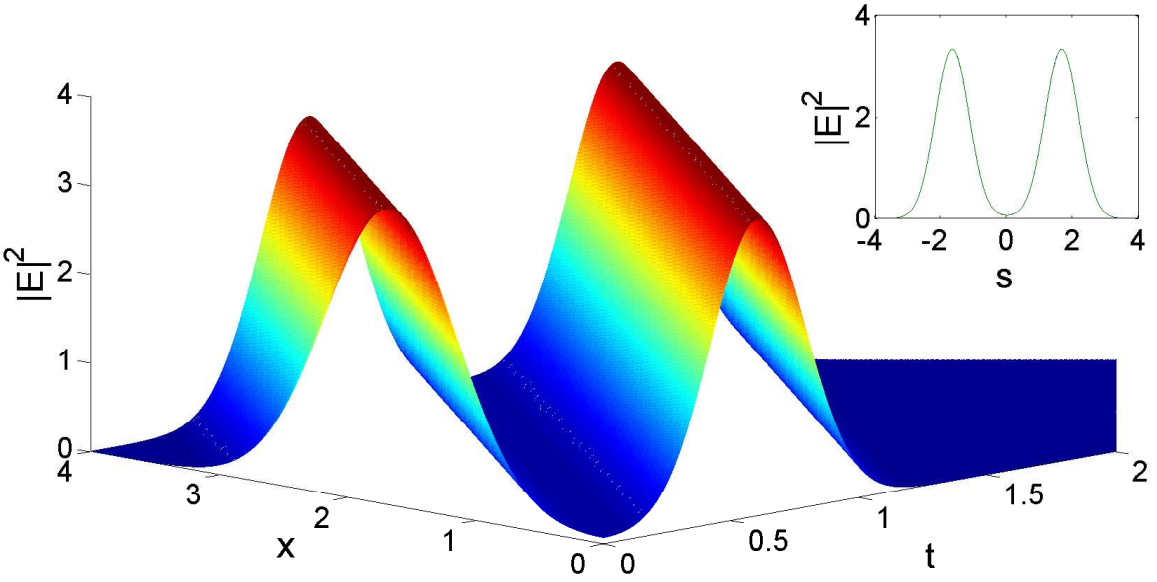


**Figure 6.4:** Cosh-Gaussian TWSS for $P = 0.2599$, $Q = 3.1874$ and $R = 1.02$. 2D profile is in the inset. As $P$ decreases and $R$ increases, the dip tends to touch the bottom line. Rest of parameters are same as in Figure (6.1).

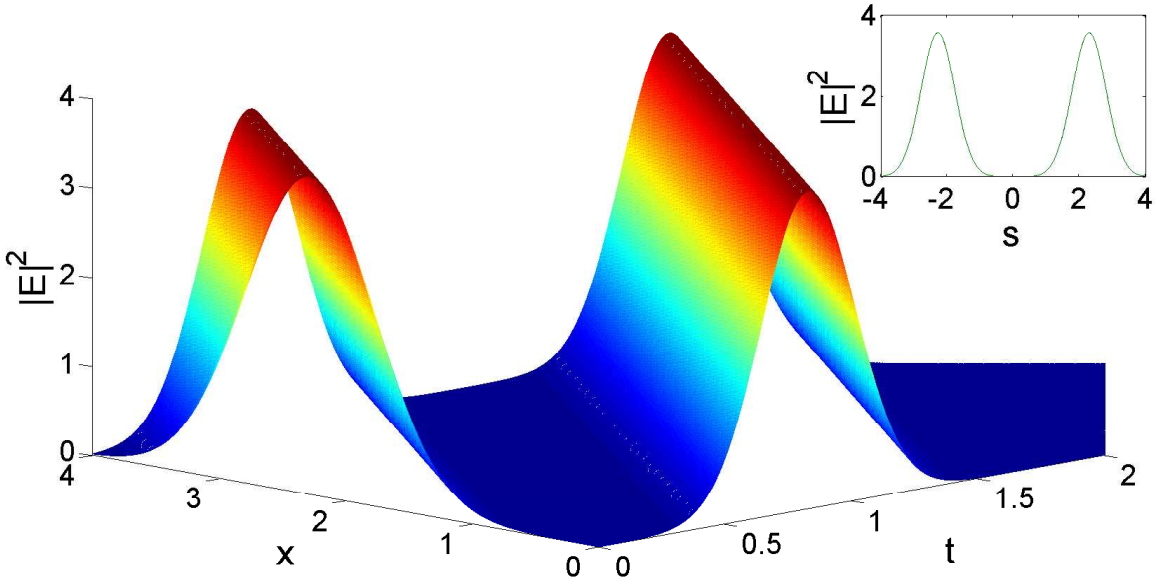


**Figure 6.5:** Cosh-Gaussian TWSS for $P = 0.0255$, $Q = 4.3832$, $R = 1.02$. Inset is the corresponding 2D profile. Rest of parameters are same as in Figure (6.1).

## 6.2 Generation of Standing Wave Patterns in Dissipative cavity

A true CS can be envisaged as localized TWSS. In a VCSEL coupled with feedback, many tilted TWSS can be excited [9]. They coexist, in some parametric region only, with the stable trivial solutions that correspond to the laser 'off' state. The tilted TWSS interact with each other. The introduction of an annular spatial filter into the feedback path leads to a single dominant localized TWSS. Such localized structures are the basic requirement for CS generation. In this section, TWSS are obtained from the standing wave patterns. CS is considered as soliton bouncing back and forth by the cavity mirrors. To imitate the situation, tilted TWSS are superposed multiple times to create SWLS. For all types of TWSS, such SWLS that resemble CS are formed. Figure (6.6) presents a typical SWLS for *sech* type TWSS for a tilt angle of $\pi/6$. Here, the snapshots during evolution, for only one period, are presented. These SWLSs change

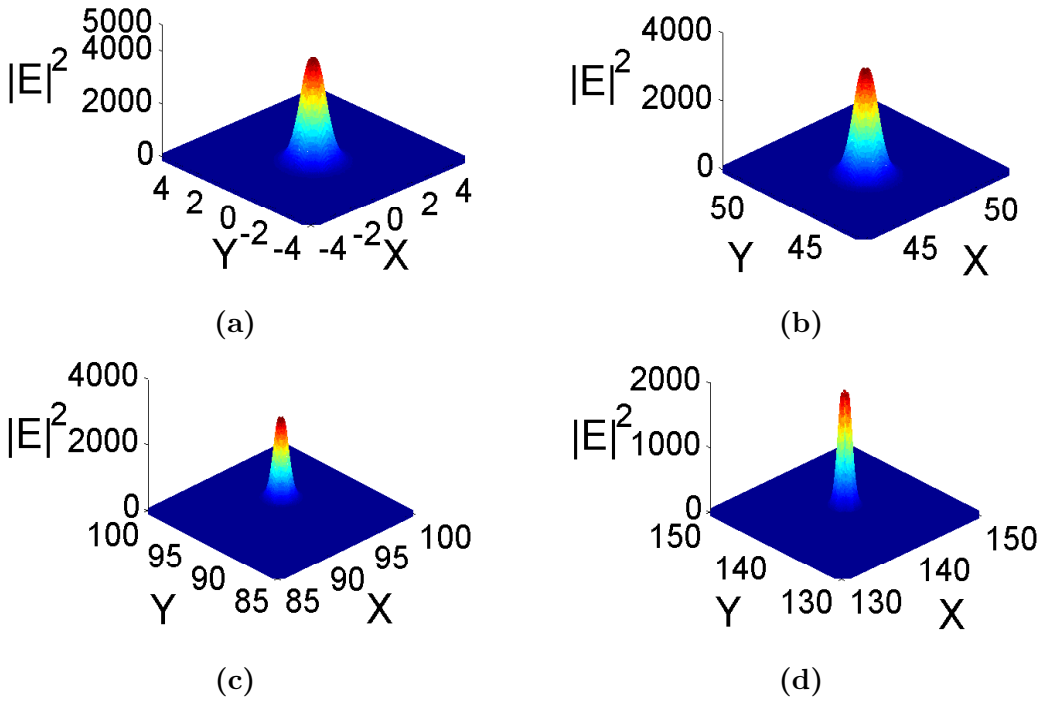


**Figure 6.6:** Snapshots of SWLS of *sech* profile at (a) $t = 0$, (b) $t = 4$, (c) $t = 8$ and (d) $t = 12$ time-steps at a fixed tilt angle $\theta = \pi/6$. As 't' increases the profile vary periodically. One period is shown in this figure.

periodically with time.

SWLS for cosh-Gaussian type TWSS are portrayed in Figure (6.7) for one oscillation period. SWLS for Gaussian type TWSS are portrayed in Figure (6.8). In Figure (6.8), all these localized structures are found to be stable against time evolution. These SWLSs exhibit bistability, exponential localization and freedom of location thus can be considered as CS. Following the aforesaid method, one can also generate elliptical CS of *sech* or *cosh*-Gaussian or Gaussian type. For example, Figure (6.9) displays the generation of cosh-Gaussian CS for different ellipticity. Also, by varying tilt angle, a large variety of CS can be generated. Few examples of *cosh*-Gaussian type CSs are compiled in Figure (6.10). The mirrors of the VCSEL basically comprises of DBR. DBR is periodic structured mirror that consist of alternate dielectric layers of refractive index $n_1$ and $n_2$. The reflection coefficient is determined by the number of layers

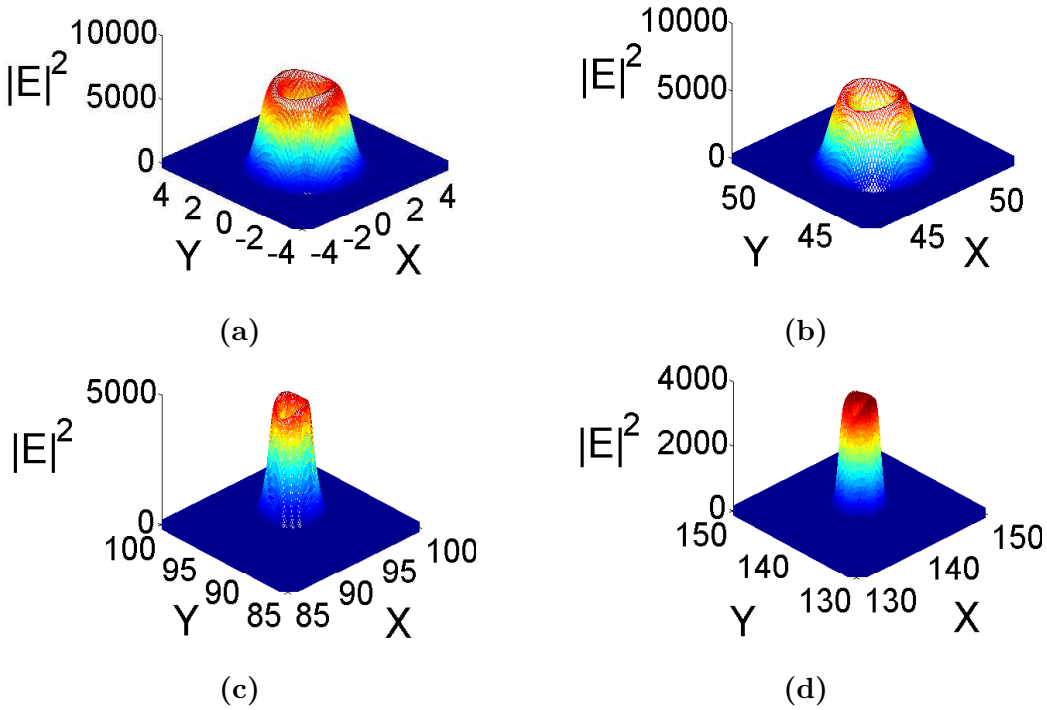


**Figure 6.7:** Snapshots of SWLS of $cosh - Gaussian$ profile at (a) $t = 0$, (b) $t = 4$, (c) $t = 8$ and (d) $t = 12$ time-steps at a fixed tilt angle $\theta = \pi/6$.

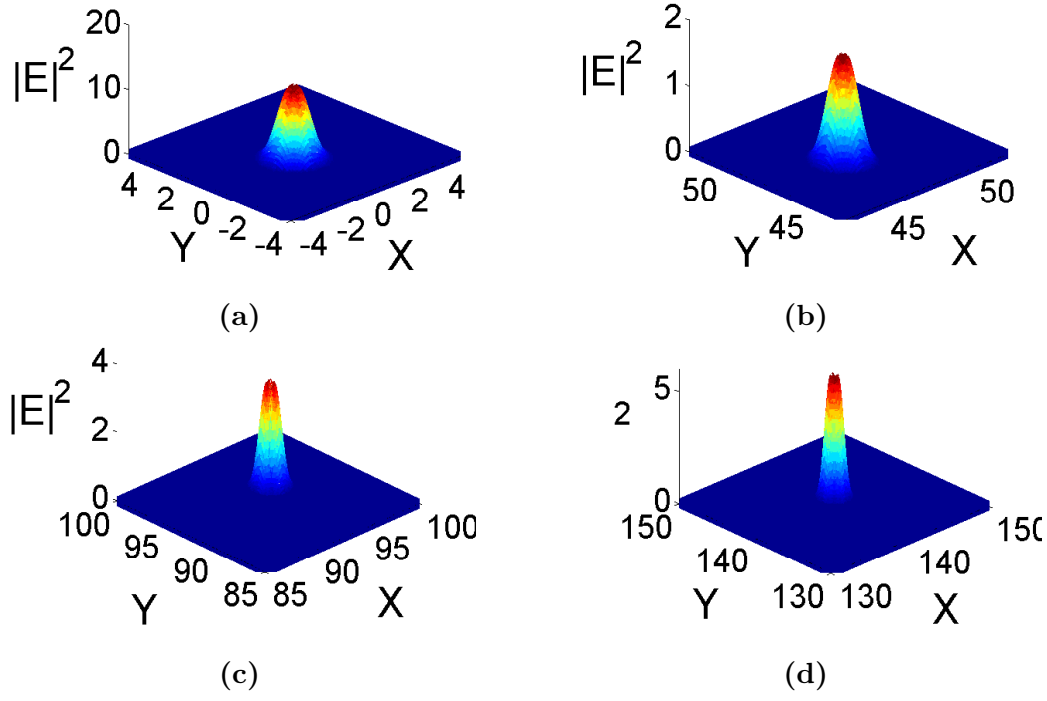


**Figure 6.8:** Snapshots of SWLS of *Gaussian* profile at (a) $t = 0$, (b) $t = 4$, (c) $t = 8$ and (d) $t = 12$ time-steps at a fixed tilt angle $\theta = \pi/6$.

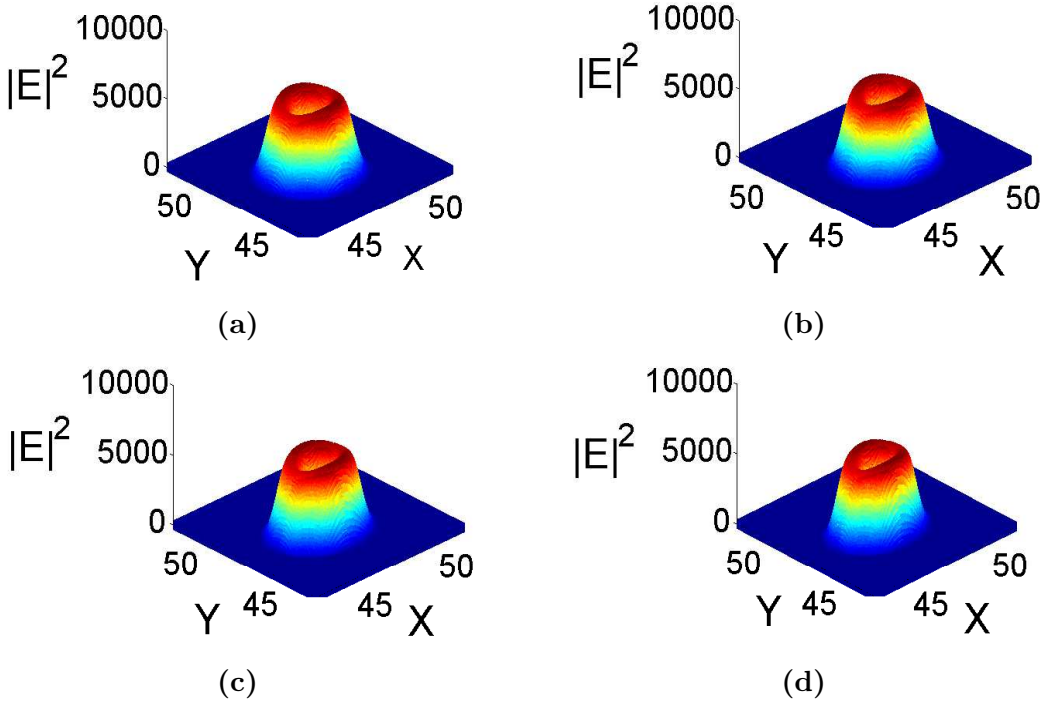


**Figure 6.9:** Snapshots of SWLS of *cosh*-Gaussian profile at $t = 4$ time-step and fixed tilt angle $\theta = \pi/6$ with different ellipticity (a) $e = 1.1$, (b) $e = 1.2$, (c) $e = 1.3$ and (d) $e = 1.4$.

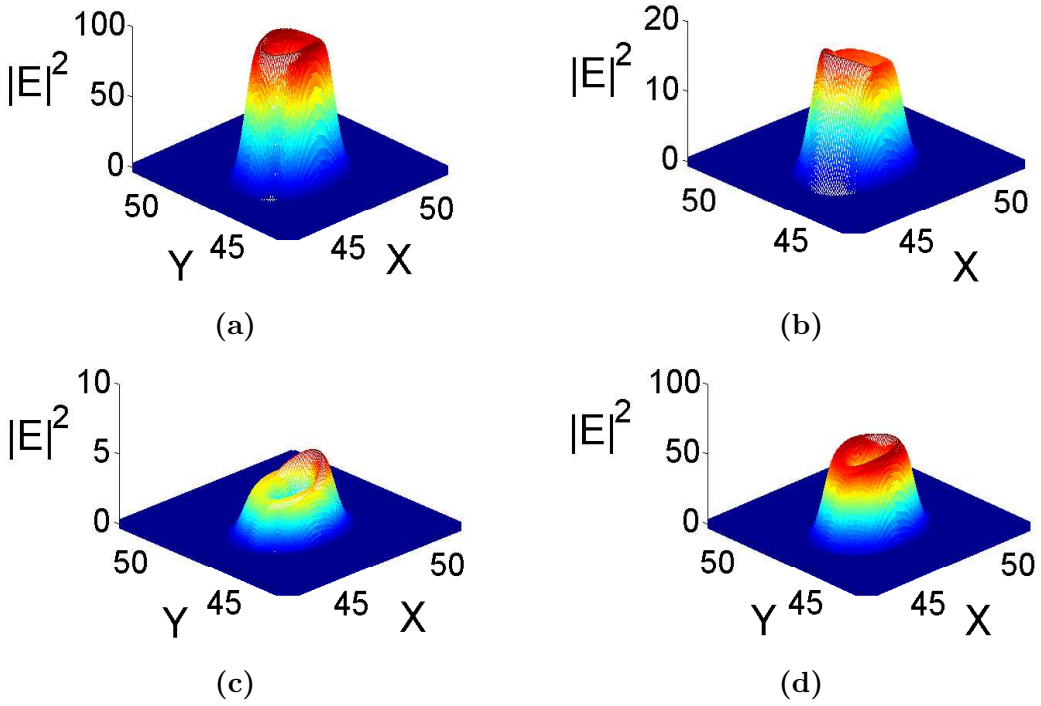


**Figure 6.10:** Snapshots of SWLS of *cosh*-Gaussian profile at $t = 4$ time-step at different tilt angle (a) $\theta = 0°$, (b) $\theta = 2°$, (c) $\theta = 4°$ and (d) $\theta = 6°$.

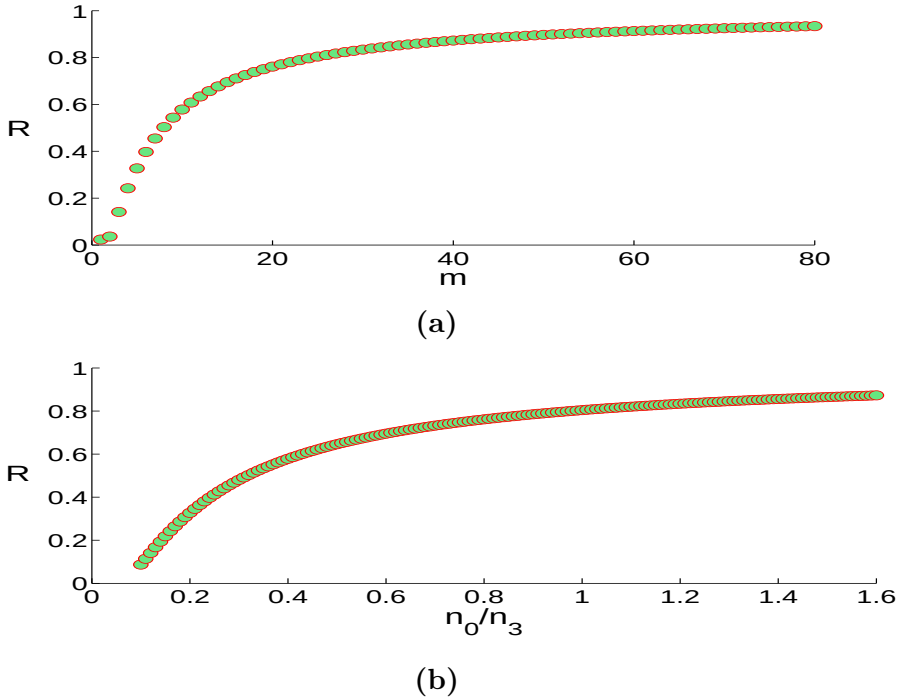


**Figure 6.11:** Variation in the reflection coefficient with respect to (a) number of periods of DBR, and (b) the ratio of refractive indices of top and bottom layers.

following the formula below:

$$R(\lambda_B) = \frac{(\frac{n_2}{n_1})^{2m}(\frac{n_0}{n_3} - 1)}{(\frac{n_2}{n_1})^{2m}(\frac{n_0}{n_3} + 1)}, \tag{6.24}$$

where, $\lambda_B$ is the value of wavelength at which reflectivity is at its peak. $m$ represents the number of periods. $n_0$ and $n_3$ are the refractive indices of the top and bottom layers of DBR, respectively,. The reflection coefficient profile is presented in Figure (6.11). This reflection coefficient saturates at larger number of layers.

The reflection coefficient of the mirrors has a significant role in CSs intensity profile. Increasing value of reflection coefficients intensifies the CS manifold. A variety of CS is achieved for different reflection coefficients of the DBR (Figure (6.12)).

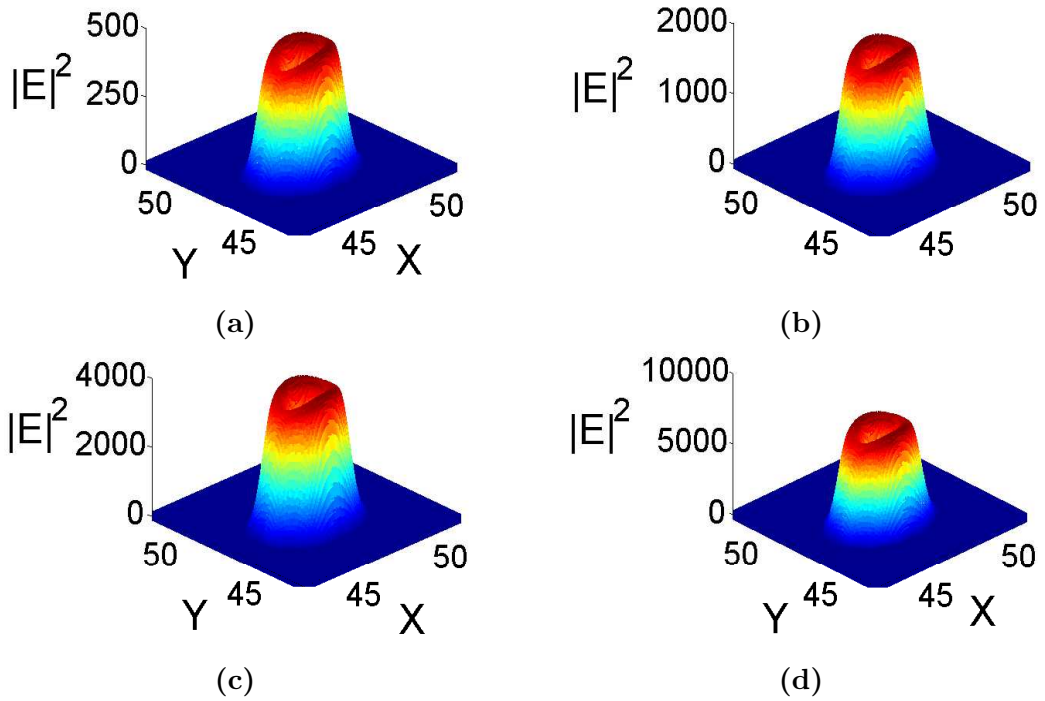


**Figure 6.12:** Snapshots of SWLS of *cosh*-Gaussian profile at $t = 4$ time-step and fixed tilt angle $\theta = \pi/6$ with different reflection coefficient (a) $r = 0.25$, (b) $r = 0.5$, (c) $r = 0.75$ and (d) $r = 1$.

## 6.3 Model 2

This section explores the standing wave pattern in the dissipative cavity with a classic model of CGLE as given below:

$$(\frac{\partial}{\partial t} - \epsilon)E = (1 + ic_1)\frac{\partial^2 E}{\partial x^2} - (1 - ic_3)|E|^2 E, \tag{6.25}$$

where, $E$ is the slowly varying field envelope, $x$ is the spatial co-ordinate transverse to the cavity axis, and $t$ is the cavity round trip time. The prototype CGLE model described by equation (6.25) has wide application in variety of physical phenomena starting from its preliminary field of application, superconductivity to a recent field dealing with Bose-Einstein condensation [147]. Here some primary references are brought forward. The study of traveling wave (TW) solution [196], spatiotemporal intermittency regime of Nozaki-Bekki holes [197] and Benjamin-Feir stable region [198],

localized TW solution [9, 196], controlling of TW with feedback [179], turbulence in electromagnetic fields [199] and instability in nonlinear chemical kinetics [200] are to cite but a few. It is also sought after in superfluidity, second-order phase transitions and Rayleigh-Benard convection [128]. The CGLE is also a commonly chosen model for pattern-forming systems and supports a variety of coherent and complex patterns [132, 201]. This classic equation has been also investigated in context to find localized structure in spatially extended non-equilibrium systems [132]. Several path breaking experiments have been performed in optical systems that can be described by the equation (6.25) and its variants.

This classic form of CGLE is deliberately used to show the relation of dissipative cavity system with the extremely wide fraternity of CGLE. To connect it with VCSEL, the coefficients $\epsilon$, $c_1$ and $c_3$ should be considered as real valued cavity parameters. Here, $(\partial_t - \epsilon)$ describes the basic cavity dynamics. The system is considered to be simple and lossy, where $\epsilon$ represents the cavity loss coefficient, scaled with respect to the evolution coordinate $t$. The term $(1 + ic_1)\partial_{xx}$ describes the spatial coupling, wherein the real part represents diffusive coupling and imaginary part captures diffractive coupling. The last term $(1 - ic_3)|E|^2E$ is the nonlinearity induced loss/gain term in the system. The real and imaginary part of the term describes, respectively, cubic nonlinear loss and nonlinear gain/absorption processes depending upon its sign. Equation (6.25) transforms to real Ginzburg-Landau equation for $c_1 = c_3 = 0$, thus resulting to the onset of stationary periodic solution or stationary bifurcations [132].

### 6.3.1 Traveling wave solutions

Considering the TW hypothesis, the TWSS for the system can be taken as in model 1:

$$E(x,t) = g(\xi)e^{i(-kz+\omega t+\theta)}, \tag{6.26}$$

Employing the standard procedure of He's method the limiting condition for velocity comes out to be:

$$v > -2c_1k + 2\sqrt{\epsilon - k^2}. \tag{6.27}$$

**Case I:** Standard sech type TWSS

To proceed further, following profile function is considered:

$$g(\xi) = Ssech(T\xi) \tag{6.28}$$

where, parameter $S$ represents the amplitude and $T$ represents the inverse width, are represented as follows:

$$S = \sqrt{\frac{2(\omega + c_1k^2 + \frac{2k(k^2-\epsilon)}{v+2c_1k})}{c_3 - \frac{2k}{v+2c_1k}}}, \tag{6.29}$$

and

$$T = \sqrt{-\frac{\omega + c_1k^2 + \frac{2k(k^2-\epsilon)}{v+2c_1k}}{c_1 + \frac{2k}{v+2c_1k}}}. \tag{6.30}$$

**Case II:** Non-standard *cosh*-Gaussian TW ansatz

In this case, the following unchirped *cosh*-Gaussian ansatz as profile function is considered as in equation (6.19):

$$g(\xi) = P\ cosh(Q\xi)e^{-\frac{\xi^2}{R^2}}, \tag{6.31}$$

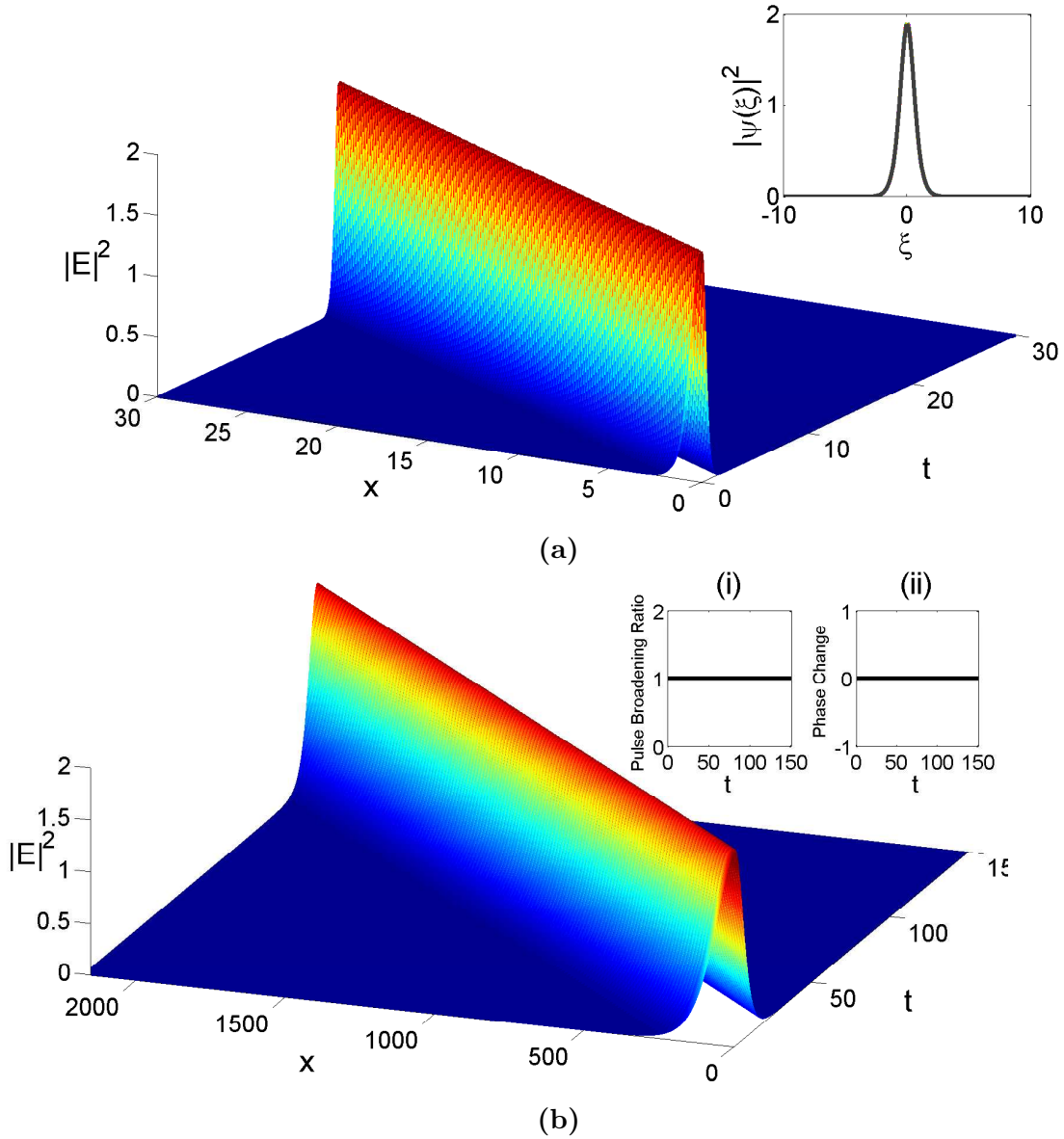


**Figure 6.13:** (a) 3D Intensity profile for *sech* TWSS with 2D profile in inset., (b) Numerically obtained spatio-temporal evolution of field envelop for *sech* input profile. Inset plots correspond to (i) pulse broadening ratio with respect to time $t$ and (ii) phase change countered by the field envelop with respect to time $t$. Here, $c_1 = 0.3$, $c_3 = -0.8$, $\epsilon = 1$, $\omega = c_3$, $k = 0.3$ and $v = 11.7279$

where, $P$ represents the amplitude, $Q$ is the cosh parameter and $R$ is the pulse width parameter of the profile. The standard procedure of He's method leads to the following three equations:

$$\frac{\sqrt{2}a_1}{4}PR(1+e^{\frac{Q^2R^2}{2}})+\frac{a_2}{16}P^3R(e^{Q^2R^2}+4e^{\frac{Q^2R^2}{4}}+3) \\ -\frac{\sqrt{2}a_3P}{4R}(1-Q^2R^2+e^{\frac{Q^2R^2}{2}})=0, \tag{6.32}$$

$$\frac{\sqrt{2}a_1}{8}P^2R^3Qe^{\frac{Q^2R^2}{2}}+\frac{a_2}{32}P^4R^3Q(e^{Q^2R^2}+e^{\frac{Q^2R^2}{4}})-\frac{\sqrt{2}a_3}{8}P^2QR(-2+e^{\frac{Q^2R^2}{2}})=0, \tag{6.33}$$

and

$$\frac{\sqrt{2}a_1}{8}P^2(1+e^{\frac{Q^2R^2}{2}})+\frac{\sqrt{2}a_1}{8}P^2Q^2R^2e^{\frac{Q^2R^2}{2}}+\frac{a_2}{64}P^4(e^{Q^2R^2}+4e^{\frac{Q^2R^2}{4}}+3) \\ +\frac{a_2}{32}P^4Q^2R^2(e^{Q^2R^2}+e^{\frac{Q^2R^2}{4}})+\frac{\sqrt{2}a_3P^2}{8R^2}(1-Q^2R^2+e^{\frac{Q^2R^2}{2}}) \\ -\frac{\sqrt{2}a_3}{8}P^2Q^2(-2+e^{\frac{Q^2R^2}{2}})=0. \tag{6.34}$$

where $a_1 = (\omega + c_1k^2 + (2k(k^2-\epsilon))/(v+2c_1k))$, $a_2 = (2k/(v+2c_1k) - c_3)$ and $a_3 = (c_1 + 2k/(v+2c_1k))$. Equations (6.32), (6.33) and (6.34) are solved to determine the parameters $P$, $Q$ and $R$. However, analytically it is very cumbersome to solve equations (6.32), (6.33) and (6.34). Therefore, these equations are solved graphically. Different values of the parameters generate different solution points, hence different nature of profiles are witnessed for each case. One of the possible cases is discussed in this study. Figure (6.14) depicts the first quadrant of solution plot for equations (6.32), (6.33) and (6.34) with variation in parameters $P$ and $Q$, keeping $R(=0.3)$ constant for parametric values $c_1 = 0.3$, $c_3 = -0.8$, $\epsilon = 1$, $I_0 = \epsilon$, $\omega = c_3$, $k = 0.3$

and $v = 11.7279$. It may be noted that all the Figures in this section, obtained from both analytical as well as numerical analysis. Figure (6.15)(i) shows the intensity pro-

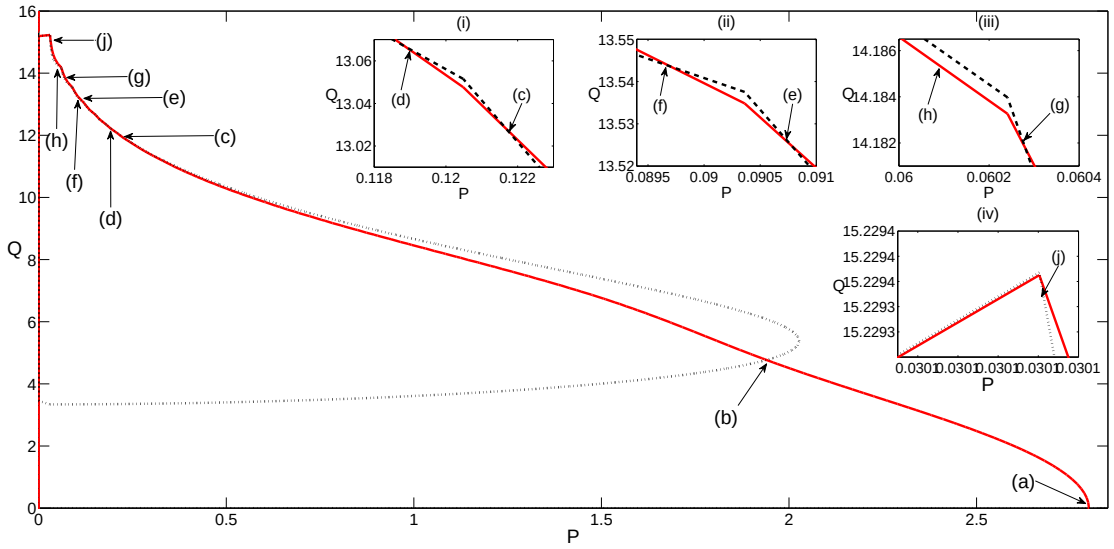


**Figure 6.14:** Parametric solution space plot for parameters $P$ and $Q$ in equations (6.29), (6.30) and (6.31) for constant $R$ ($= 0.3$). Insets are zoom in view of solution points marked in main plot: (i) correspond to points (c) and (d), (ii) correspond to points (e) and (f), (iii) corresponds to points (g) and (h), and (iv) corresponds to point (j).

file plots in $3D$ with $2D$ plot in the Figure (6.15)(ii) for point (a) that corresponds to $P = 2.7994$ and $Q = 0$. Intensity profile in Figure (6.15)(i) is a purely Gaussian shape profile, closely matching the nature of standard *sech* profile shape. Figure (6.15)(iii) is the 3D intensity profile for $P = 1.9402$ and $Q = 4.7740$ corresponding to the point (b) in Figure (6.14) with 2D profile shape is shown in Figure (6.15)(iv). It is a flat-top profile. Typical *cosh*-Gaussian profile with $3D$ and cross-sectional $2D$ are plotted for the solution point (i) in Figure (6.15)(v) and (6.15)(vi), respectively. Solution points (c)-(h) in Figure (6.14) generates a similar pulse with a dip in between two equally distributed maxima. These points represent typical *cosh*-Gaussian nature of the profile. The points of intersection that corresponds to TWSS are obtained as (c) $((P, Q) = (0.1217, 13.0282))$ and (d) $((P, Q) = (0.0908, 13.5247))$, (e) $((P, Q) = (0.0897, 13.5435))$, (f) $((P, Q) = (0.0603, 14.1817))$, (g) $((P, Q) = (0.0600, 14.1859))$

and (h) ($(P, Q) = (0.0301, 15.2294)$). The analytically obtained TWSS profile corresponding to those points are shown in Figures (6.16)(i) and (6.16)(ii), (6.16)(iii), (6.16)(iv), (6.16)(v) and (6.16)(vi), respectively. A direct numerical solution using the aforesaid parameters yields similar profiles of TWSS portrayed in Figures (6.17) and (6.18) with parameters corresponding to the analytically found solution points in Figure (6.14).

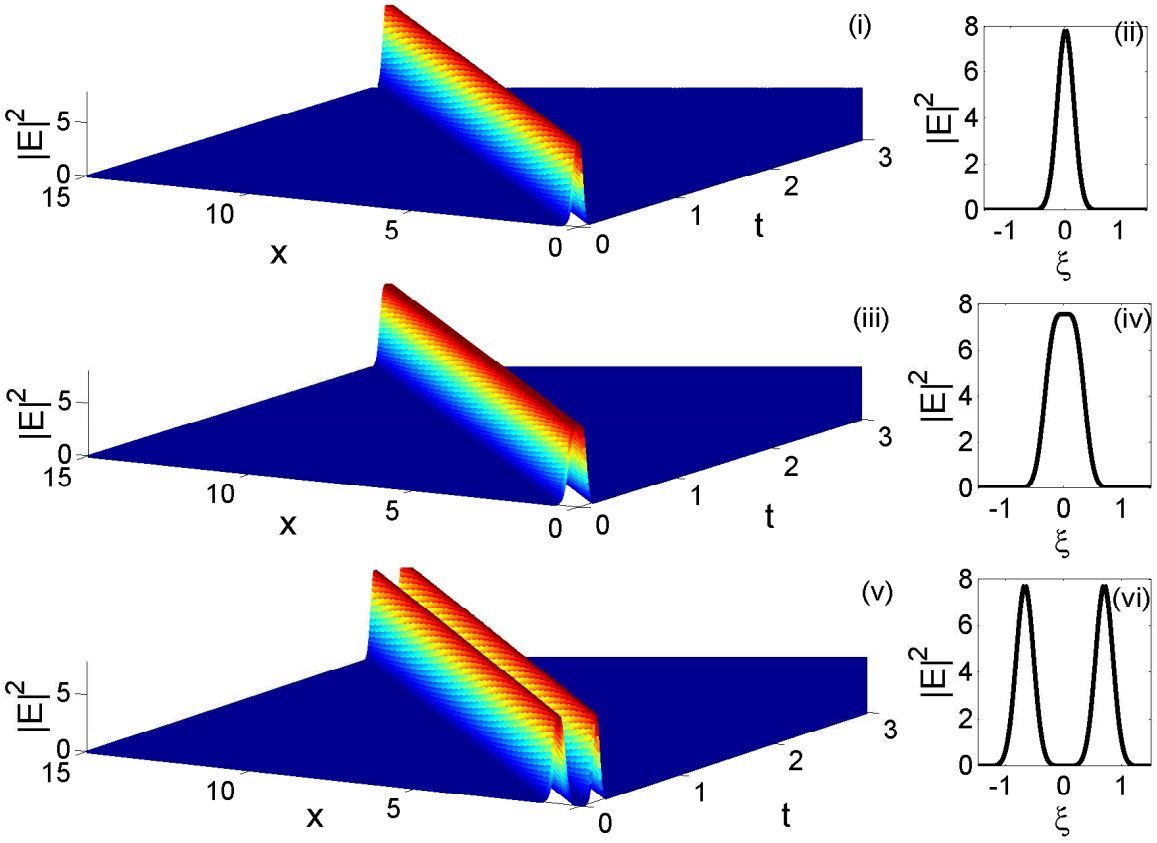


**Figure 6.15:** 3D intensity TWSS profile for (i) solution point 'a', i.e.,$(P, Q) = (2.7994, 0)$, (iii) solution point 'b', i.e., $(P, Q) = (1.9402, 4.7740)$, (v) solution point 'j', i.e., $(P, Q) = (0.0301, 15.2294)$. Respective 2D profiles are plotted in (ii), (iv) and (vi).

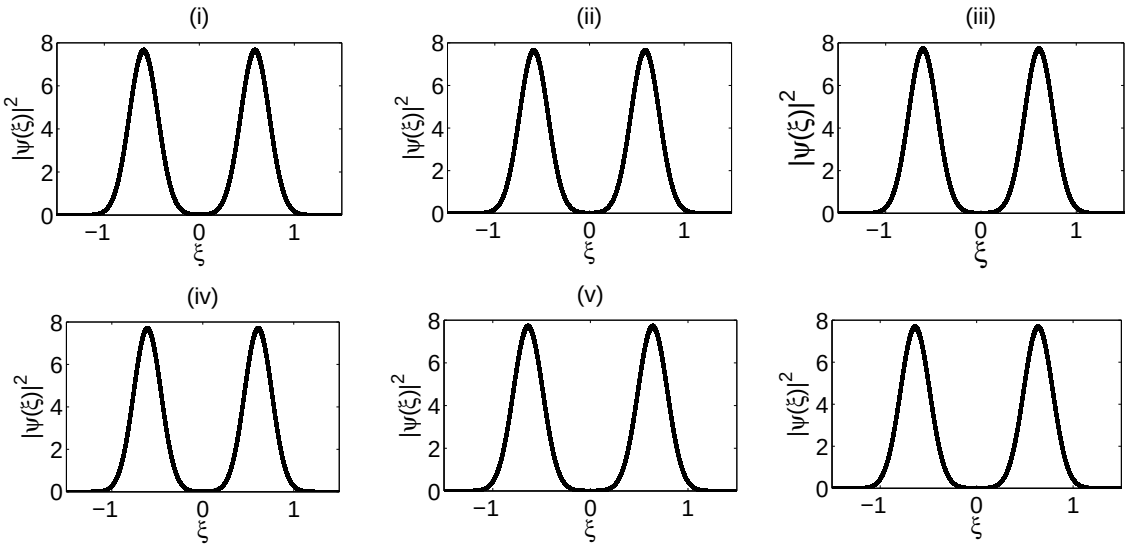


**Figure 6.16:** 2D intensity profiles corresponding to solution points (i) 'c' ($(P,Q) = (0.1217, 13.0282)$), (ii) 'd' ($(P,Q) = (0.1189, 13.0664)$), (iii) 'e' ($(P,Q) = (0.0908, 13.5247)$), (iv) 'f' ($(P,Q) = (0.0897, 13.5435)$), (v) 'g' ($(P,Q) = (0.0603, 14.1817)$) and (vi) 'h' ($(P,Q) = (0.0600, 14.1859)$) at constant $R = 0.3$.

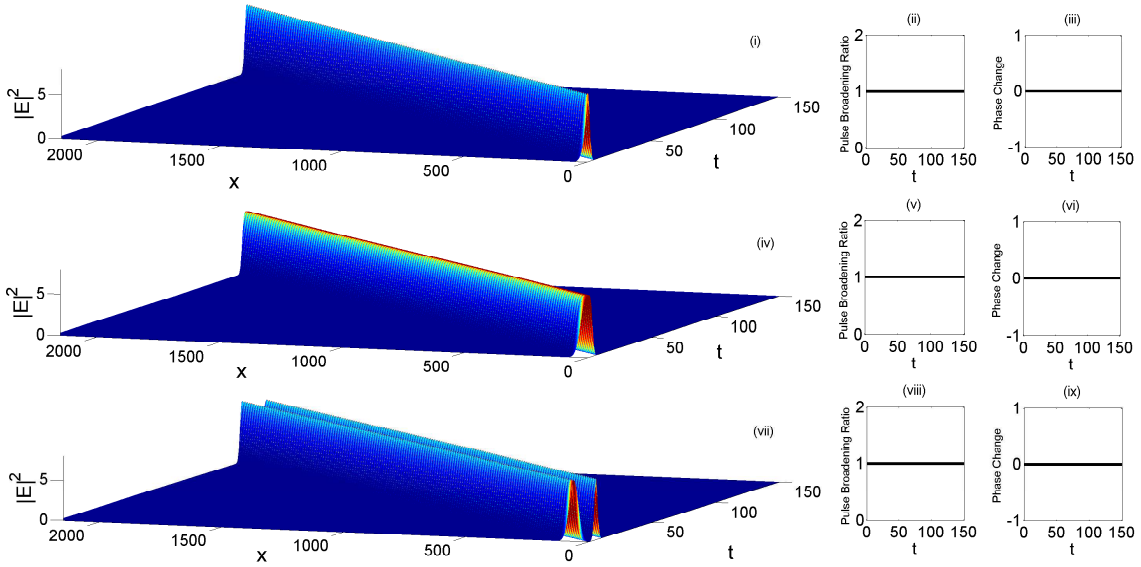


**Figure 6.17:** Numerically obtained spatio-temporal evolution of *cosh*-Gaussian field profile $|\psi(x,t)|^2$ for points: (i) solution point 'a', (iv) solution point 'b', (vii) solution point 'c', marked in Figure (6.14). Corresponding pulse broadening ratio and phase change countered by the field envelop with respect to time $t$ are shown in sub-Figures (ii) and (iii), (v) and (vi), and (viii) and (ix), respectively.

### 6.3.2 Standing Wave Localized Structures

SWLS inside the dissipative cavity can be achieved by superposing the TWSS of various profiles. Here, we show the SWLS for points 'b', 'e', 'g' and 'j' in Figure

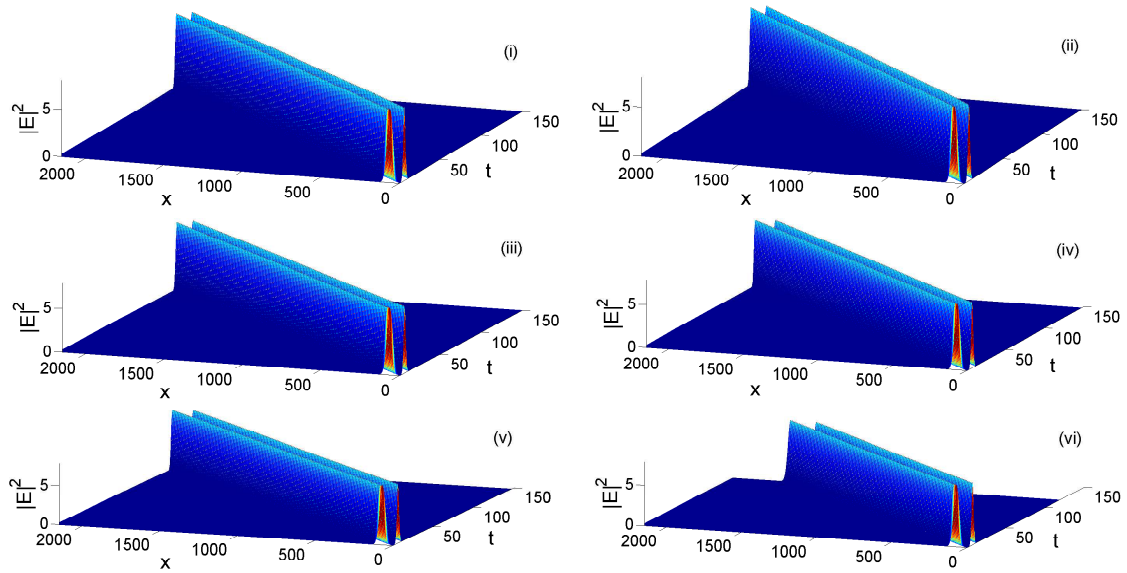


**Figure 6.18:** Numerically obtained spatio-temporal evolution of cosh-Gaussian field profile $|\psi(x,t)|^2$ for solution points (i) 'd', (ii) 'e', (iii) 'f', (iv) 'g', (v) 'h', and (vi) 'j', marked in the Figure (6.14).

(6.19). The same for other points can also be achieved similarly. Like Model 1, in this case also one can generate a large variety of SWLS by changing tilt angles of the DBR mirrors and reflection coefficient.

### 6.3.3 Standing Wave Localized Structures versus Cavity Soliton

In the whole chapter, a large variety of self-localized structures (what we mentioned also as CS) are presented for different tilt angle of cavity mirrors, i.e. DBR, reflection coefficients and profiles. Before terming them unambiguously as CS, the availability of the three major characteristics of CS in the localized structures need to be checked. These are exponential localization, bistability and plasticity, i.e., freedom of location. The profile of SWLS shows exponential localization. Like other CS these SWLS can be made 'on' and 'off' at same condition with a beam of opposite phase. Thus bistability can be achieved. Since we can inject the traveling waves at any desired point in the

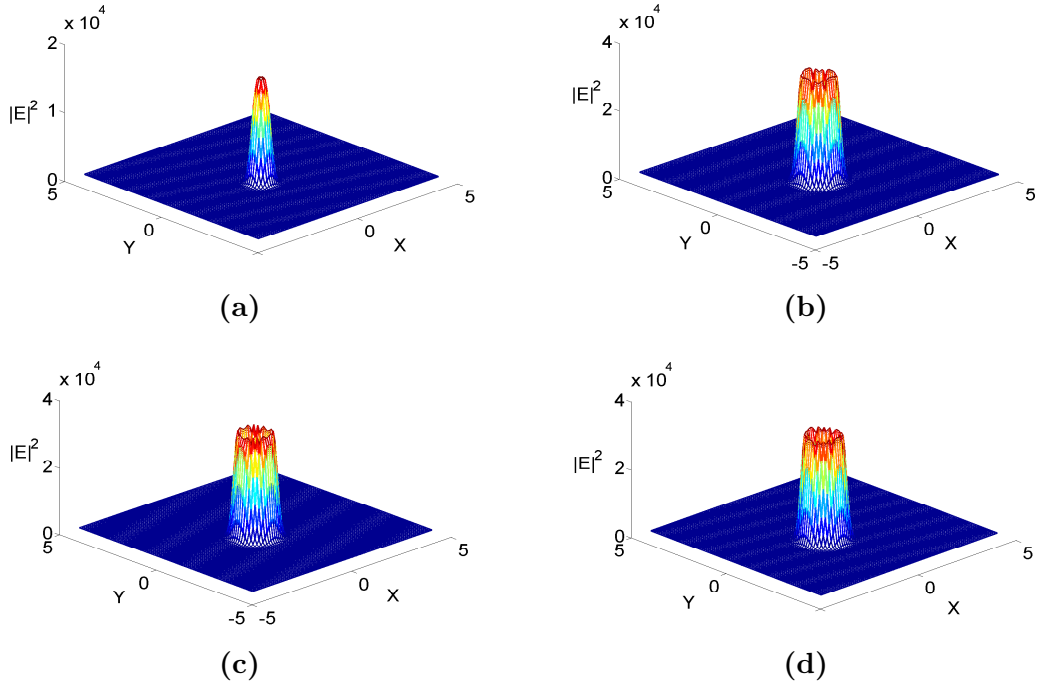


**Figure 6.19:** Snapshots of SWLS of *cosh*-Gaussian profile at different solution points: (a) 'b', (b) 'e', (c) 'g' and (d) 'j'.

transverse cavity plane and can change the tilt angle of the mirrors, the plasticity can be achieved. Thus the SWLS of these two models can be considered as CS.

# Conclusion

We generated sech and cosh-Gaussain type SWLS that resemble CSs following an alternate approach- the standing wave method. This method is capable to generate CS at any desired position of the transverse cavity plane. A large family of CS can be generated by changing the tilt angle of the mirrors as well as number of layers in the DBR. Also, this method can predict versatile profiles of the CS. This approach may open the possibility of generation of more fascinating self-localized patterns and CS variety in dissipative cavities.

# Chapter 7

## Application of Stability Analysis Mechanism

Stability analysis is an important criteria to study the behavior and sustainability of any localized structure or system of particles or even tools. Analysis of the stability and multi-stability of microcavity systems used in the preceding chapters could be potentially applied to other fields of science and technology (by going beyond optics) to extract useful information for better fundamental understanding and modeling of a wide range of physical/biological systems. In an effort to investigate the versatility of the stability analysis technique used for CS, we proceeded to undertake the task of performing stability analysis in two interdisciplinary, yet apparently sharply contrasting areas: an application to 'Multi-Phase Flow Engineering' and 'Medical Sciences' (tumor cell growth dynamics). The details of the study are compiled in the following sections of this chapter.

## 7.1 Multi-Phase Flow Dynamics

Of the different types of multi-phase flow situations, gas-solid transport phenomenon is chosen for the study in this thesis. Fluidized dense-phase pneumatic transport is the preferred method for conveying fine powders in several industries, such as coal fired thermal power plants, chemical, pharmaceutical, petrochemical plants, cement, food

industries, etc. due to the reasons of high solids to gas mass ratio, low gas flow requirement (i.e. smaller compressor and savings in operating power requirement), smaller size of pipes and fittings, reduced conveying velocity resulting in lowering of wear rate of pipelines and bends, decreased rate of product attrition, reduced size of solids-gas separation unit etc. [202, 203]. In spite of having several merits, fundamentally understanding the flow mechanisms and reliably designing fluidized dense-phase systems have made only limited progress so far. The existing models to determine energy loss are based on dimensionless numbers [203, 204, 205, 206, 207, 208], but these have not taken into consideration the important flow attributes, such as, the flow characteristics and stability of the dunes. Therefore, stability of the dunes are to be examined along the length of flow. Number of methods for stability analysis exist in literature, such as Lyapunov exponents method [144], linear stability analysis [209], perturbation method [145] and von Neumann Stability analysis [210]. There have been some cases where the researchers have used stability analysis to study the particle-fluid systems, such as Chen et al. [211] to Fullmer and Hrenya [212]. These work were carried out either with granular products or coarser particles in standpipes or with fluidized beds. Very little research has been conducted in the area of stability analysis for fluidized dense-phase pneumatic conveying of fine powders through pipes. This work investigates into the stability of moving dunes of fine aerated powders through pipelines.

### 7.1.1 Flow Model for Gas-Solids Transport

The governing equations for the flow are developed considering the following assumptions: one-dimensional flow along the bulk flow direction (x-direction); in an infinitesimal control volume, the gas-solids composition is uniform with no concentration gradi-

ent of particles across the diameter of pipe; the gas-solids flow is in steady state; ideal gas equation of state is obeyed by gas-phase in an isothermal system. Considering mass, momentum and energy balance across a small control volume (see Figure (7.1)), the following governing equations are obtained: Net accumulation of momentum along

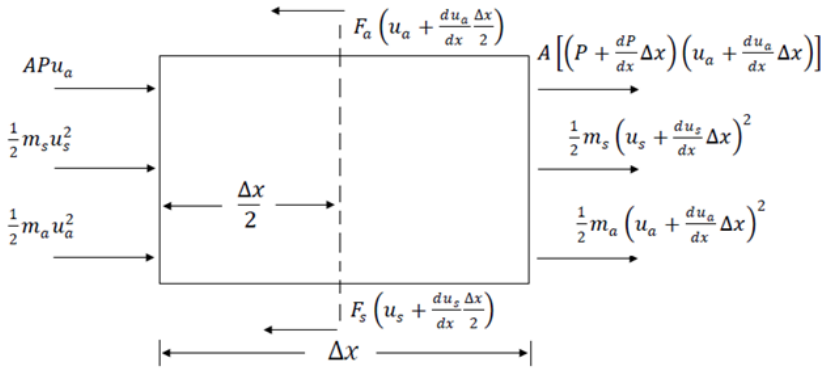


**Figure 7.1:** Variation of dune velocity for different air flows along the flow direction.

X-direction is:

$$= APu_a - A[(P + \frac{dP}{dx}\Delta x)(u_a + \frac{du_a}{dx}\Delta x)] - [F_a(u_a + \frac{du_a}{dx}\frac{\Delta x}{2}) + F_s(u_s + \frac{du_s}{dx}\frac{\Delta x}{2})]. \quad (7.1)$$

Along x- direction, net accumulation of kinetic energy:

$$= \frac{1}{2}m_a u_a^2 + \frac{1}{2}m_s u_s^2 - \frac{1}{2}m_a(u_a + \frac{du_a}{dx}\Delta x)^2 - \frac{1}{2}m_s(u_s + \frac{du_s}{dx}\Delta x)^2. \quad (7.2)$$

Assuming, at steady state there is no net accumulation of energy in the control volume and neglecting the higher order terms, following equation is formed:

$$P\frac{dua}{dx} + u_a\frac{dP}{dx} + u_a f_a + u_s f_s + \rho_a \epsilon_a u_a^2\frac{dua}{dx} + \rho_s \epsilon_s u_s^2\frac{dus}{dx} = 0, \quad (7.3)$$

For gas-solids flow, the conservation of momentum is written as:

$$\begin{aligned}
&[(\rho_a \epsilon_a A u_a)(u_a + \frac{du_a}{dx}\Delta x) - (\rho_a \epsilon_a A u_a) u_a] \\
&+[(\rho_{fl} \epsilon_s A u_s)(u_s + \frac{du_s}{dx}\Delta x) - (\rho_{fl} \epsilon_s A u_s) u_s] \\
&= [PA - (P + \frac{dP}{dx}\Delta x)A] - F_a - F_s.
\end{aligned} \tag{7.4}$$

Dividing both sides of equation (7.4) by elemental volume ($A\Delta x$),

$$\epsilon_a \rho_a u_a \frac{du_a}{dx} + \epsilon_s \rho_{fl} u_s \frac{du_s}{dx} + \frac{dP}{dx} = -f_a - f_s. \tag{7.5}$$

Mass conservation for gas-phase and solids-phase are given by:

$$\frac{d}{dx}(\epsilon_a \rho_a u_a) = 0, \tag{7.6}$$

$$\frac{d}{dx}(\epsilon_s \rho_{fl} u_s) = 0. \tag{7.7}$$

Gas-phase and solids-phase are related by the following relation:

$$\epsilon_a + \epsilon_s = 1. \tag{7.8}$$

Following equations represent the evolution of parameters $u_s$, $u_a$, $\epsilon_s$ and $P$ with respect to the pipleline distance $x$ and are known as evolution equations of the system.

$$\frac{du_s}{dx} = \frac{u_s}{\epsilon_s(\rho_{fl} u_s^2 (u_s - u_a) - \frac{u_a P}{1-\epsilon_s})}[-(u_s - u_a) f_s + \frac{u_a P}{\rho_a}\frac{d\rho_a}{dx}], \tag{7.9}$$

$$\frac{du_a}{dx} = -\frac{u_a}{\rho_a}\frac{d\rho_a}{dx} - \frac{u_a}{(1-\epsilon_s)(\rho_{fl} u_s^2 (u_s - u_a) - \frac{u_a P}{1-\epsilon_s})}[-(u_s - u_a) f_s + \frac{u_a P}{\rho_a}\frac{d\rho_a}{dx}], \tag{7.10}$$

$$\frac{d\epsilon_s}{dx} = -\frac{1}{(\rho_{fl}u_s^2(u_s-u_a) - \frac{u_aP}{1-\epsilon_s})}[-(u_s-u_a)f_s + \frac{u_aP}{\rho_a}\frac{d\rho_a}{dx}], \tag{7.11}$$

$$\frac{dP}{dx} = \frac{(rho_a u_a^2 - rho_s u_s^2)}{(\rho_{fl}u_s^2(u_s-u_a) - \frac{u_aP}{1-\epsilon_s})}[-(u_s-u_a)f_s + \frac{u_aP}{\rho_a}\frac{d\rho_a}{dx}] \\ -f_a - f_s + (1-\epsilon_s)u_a^s\frac{d\rho_a}{dx}. \tag{7.12}$$

Physical properties of the fly ash and pipeline conditions are given in table (7.2). Test data to carry out the present work of performing stability analysis for gas-solids flow systems are obtained from [203].

| Fly ash no. | $d_{10}$ $(\mu m)$ | $d_{50}$ $(\mu m)$ | $d_{90}$ $(\mu m)$ | $\rho_s$ $(kg/m^3)$ | $\rho_b$ $(kg/m^3)$ | D (mm) | L (m) |
|---|---|---|---|---|---|---|---|
| 1 | 5 | 30 | 145 | 2300 | 700 | 69 | 168 |

**Table 7.1:** Physical properties of the fly ash conveyed.

### 7.1.2 Numerical determination of flow parameters

The entire horizontal pipeline length is divided into a number of different sections consisting of straight pipe sections and bends. A set of coupled ODEs (equations (7.9)-(7.12)) are solved section by section with numerical technique based on the fourth-fifth-order Runge-Kutta-Fehlberg (RKF45) method [213, 214]. The values used for parameters $f_s$, $f_a$, $\rho_a$ and $\frac{d\rho_a}{dx}$ are obtained from the experiments. The initial values for the succeeding section are the numerical values obtained from the exit point of the preceding section. This practice has been followed throughout the pipeline till the exit point. System parameters, i.e. $u_s$, $u_a$, $\epsilon_s$ and $P$, are calculated at each small interval of the pipeline section. Numerically determined values of parameters obtained at the end of the first pipe section serve as the initial conditions for the successive section. The

results (variation of $u_s$ and $u_a$ along the length of pipe) are provided in the following Figures (7.2) and (7.3). Some results correspond to solids mass flow rate of 19 t/h, two different air mass flow rates (0.04 and 0.08 $kg/s$) and fluidized bulk densities of 300 and 400 $kg/m^3$.

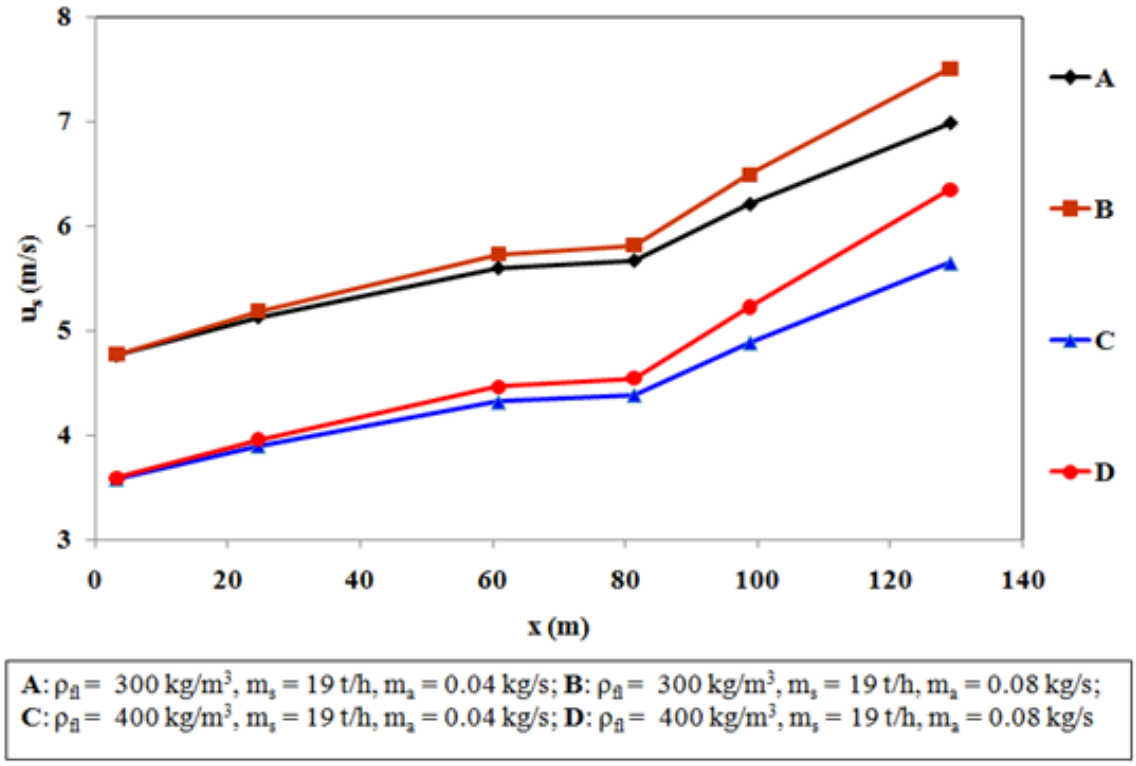


**Figure 7.2:** Variation of dune velocity for different air flows along the flow direction.

### 7.1.3 Stability Analysis

Stability analysis is discussed in details for gas-solids flow mechanism considering linearization and Lyapunov analysis [202]. In the present investigation, the linearization approach is adopted to study the stability of the system. Actual gas and solids velocity, volume fraction of solids and pressure are studied through eigenvalue and phase space analysis. In order to proceed with the stability analysis of the system, it is necessary

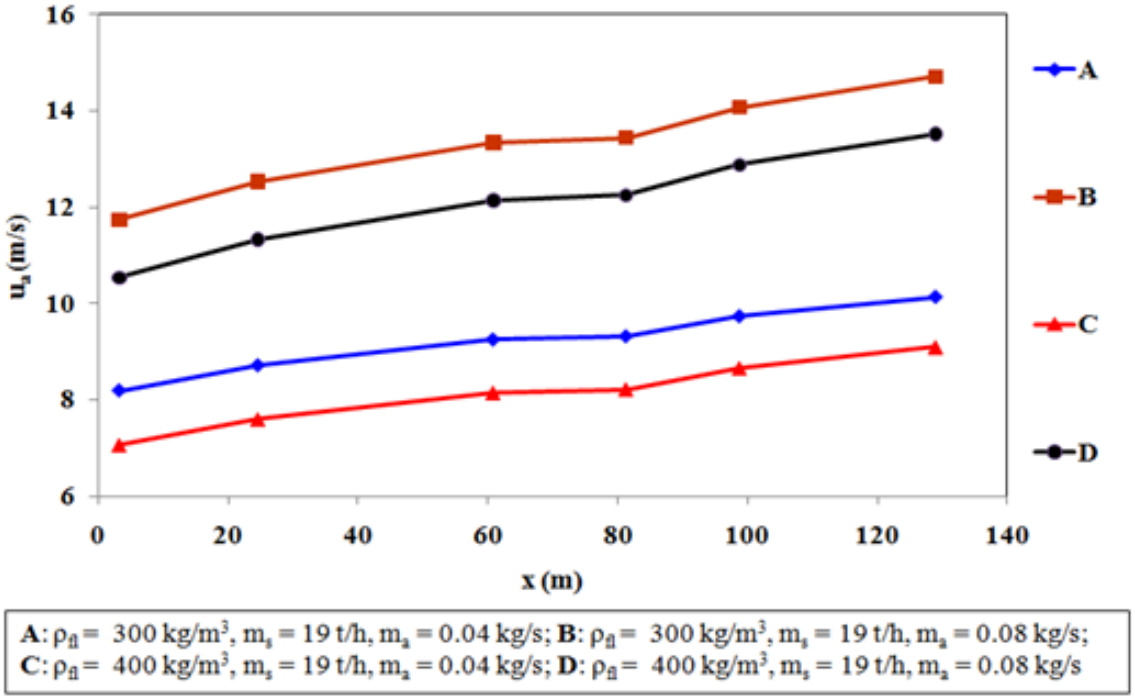


**Figure 7.3:** Variation of actual air velocity for different air flows along the flow direction.

to linearize the nonlinear evolution equations (7.9)-(7.12).

$$\frac{du_s}{dx} = A_{11}u_s + A_{12}u_a + A_{13}\epsilon_s + A_{14}P, \tag{7.13}$$

$$\frac{du_a}{dx} = A_{21}u_s + A_{22}u_a + A_{23}\epsilon_s + A_{24}P, \tag{7.14}$$

$$\frac{d\epsilon_s}{dx} = A_{31}u_s + A_{32}u_a + A_{33}\epsilon_s + A_{34}P, \tag{7.15}$$

$$\frac{dP}{dx} = A_{41}u_s + A_{42}u_a + A_{43}\epsilon_s + A_{44}P, \tag{7.16}$$

From linearized equations (7.13)-(7.16), the following Jacobi determinant can be constructed from the derivatives with respect to solids velocity, actual air velocity, volume

fraction for solids and pressure at an equilibrium state.

$$\begin{vmatrix} A_{11}-\lambda & A_{12} & A_{13} & A_{14} \\ A_{21} & A_{22}-\lambda & A_{23} & A_{24} \\ A_{31} & A_{32} & A_{33}-\lambda & A_{34} \\ A_{41} & A_{42} & A_{43} & A_{44}-\lambda \end{vmatrix}_{eq} = 0. \tag{7.17}$$

where, $\lambda$ is the eigenvalue of the Jacobi determinant. The steady state solutions of the linearized evolution equations are stable if the coefficients of the resultant Eigen value equation assume positive real part. The resultant eigenvalue in its general form can be represented as:

$$\lambda^4 + c_1\lambda^3 + c_2\lambda^2 + c_3\lambda + c_4 = 0, \tag{7.18}$$

where, the coefficients $c_i$'s ($i$ = 1 to 4) are the functions of $A_{kl}$'s ($k$,$l$ = 1 to 4). The solutions of eigenvalue equation (7.18) give information about the stability, quasi-stability and instability of the system at an equilibrium state. The system is stable if the real part of its eigenvalues are a negative real numbers, and are unstable if the real part of the eigenvalues are positive [149]. For this system, the eigenvalues obtained are the combination of negative and positive real numbers, thus indicating that the system behaves like saddle point, it is neither stable nor unstable. The phase portraits obtained converge in every case under study, thus demonstrating that the system is operating under the stable conditions. However, on the contrary, it is indicating that the dunes formed at the initial point of the pipe (blow tank discharge) are deforming gradually as the flow moves towards the exit point of the pipeline. As the gas-solids flow develops along the pipeline, the solids and actual gas velocity increases and the pressure drops down with the reduction in volume fraction of solids (see paper 5 in List

of Publications). To determine the stability behavior of the system near equilibrium, the associated phase portraits demonstrate the system behavior very intricately. Phase plot of gas and solids velocity are shown in Figure (7.4). Figure (7.4) shows that the

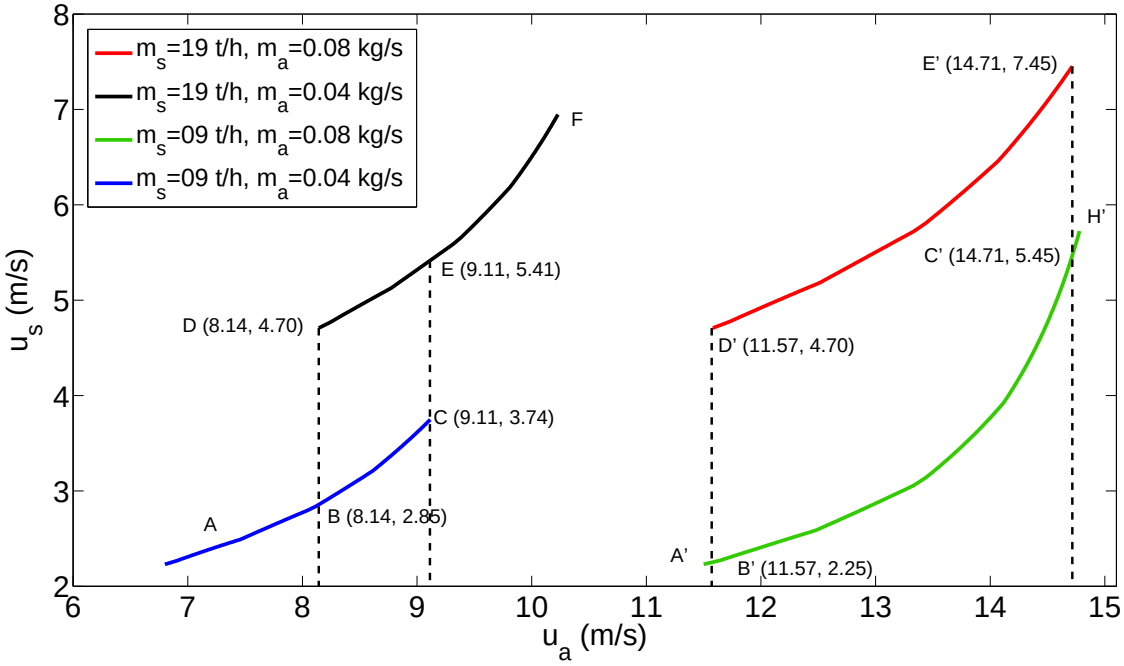


**Figure 7.4:** Variation in particle velocity with increasing actual gas velocity along the pipeline.

velocity of gas and solids increase as the flow develops. The rate of increase of particle velocity is steeper as compared to that of gas velocity. The overlapping region of two different mass flow rates, the region between the pairs of dashed lines (DB and EC; DB and EC) defines the bistability for the different combination of mass flow rate of solids under the same mass flow rate conditions for air. As the range of operating steady state characteristics for mass flow rates of the air increases, the corresponding overlapping region defining the multi-stability tends to shrink. In the velocity phase portrait (Figure (7.4)), as the flow evolves from point A to C, there is no operation zone for the corresponding mass flow rate of solids ($m_s = 9t/h$) beyond point C. On increasing the air velocity, there is a step-wise rise to the higher mass flow rate of solids at point E ($m_s = 19t/h$). Such sudden change is referred to as bifurcation instability.

However, as we move from point F to D, the system will follow the path F to E to D, until the critical point D ($m_s = 19t/h$) is reached, the system will undergo a step drop, therefore, falling to point B at lower mass flow rate of solids ($m_s = 9t/h$). Therefore, it can be inferred that for higher solid flow rate (i.e. $m_s = 19t/h$) , larger particle velocity (us = 4.7 m/s) would be required to make the flow to start compared to lower solids flow rate (i.e. corresponding to $m_s = 9t/h$). Other plots between the remaining parameters are provided in the Figures (7.5), (7.6) and (7.7).

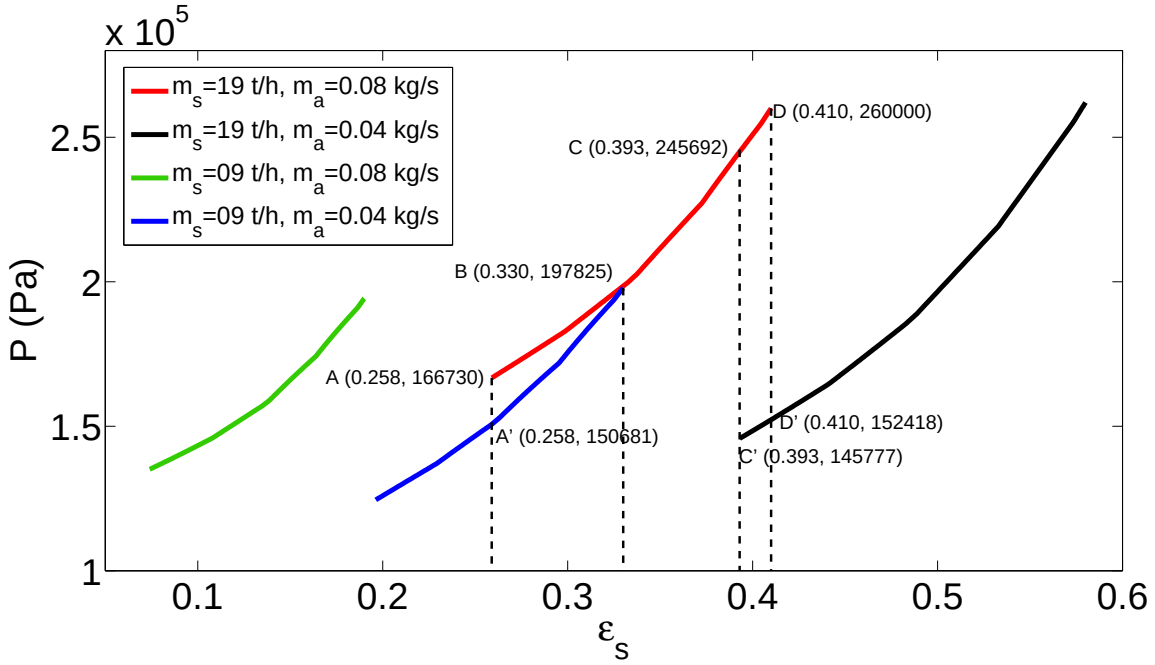


**Figure 7.5:** Variation in pressure with increasing solids volumetric fraction.

Figure (7.8) shows the 3-Dimensional representation of pressure drop versus actual air velocity and particle velocity. As can be comprehended from the Figure (7.8), corresponding to the different combinations of $u_s$ and $u_a$, pressure drops can be determined. Increase in the air and solids velocity results in the pressure drop in the system along the pipeline.

Flow dynamics of gas-solids flow and stability of four critical conveying parameters: pressure drop, particle and solids velocities, and solid volume fraction has been studied

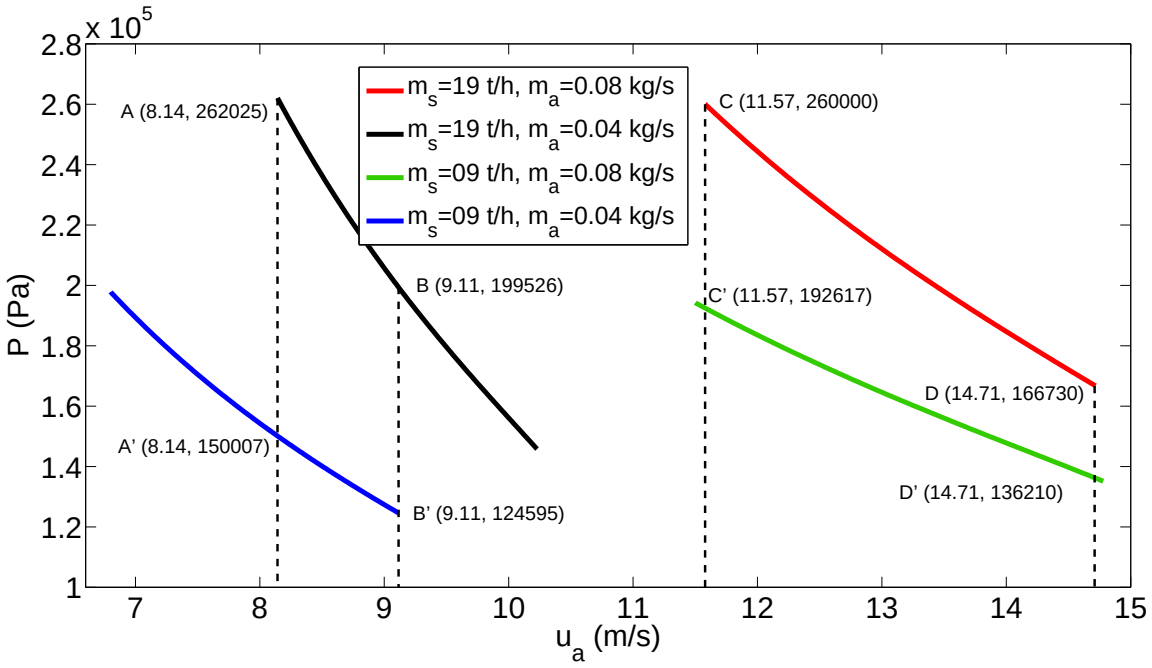


**Figure 7.6:** Variation in pressure with increasing actual air velocity.

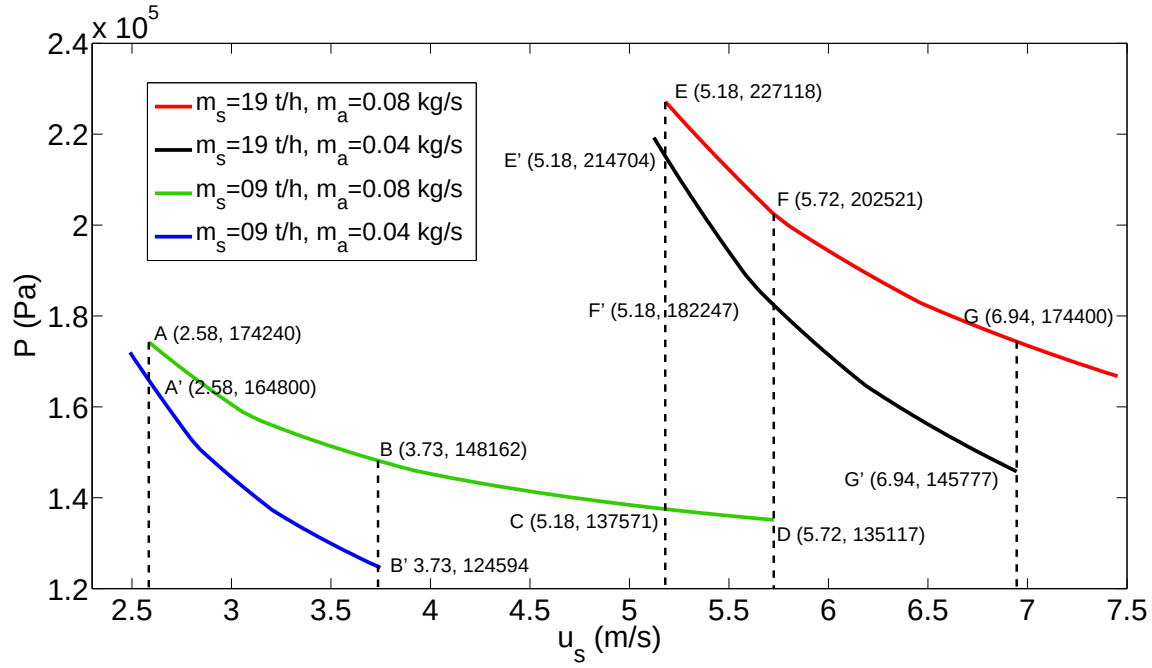


**Figure 7.7:** Variation in pressure with increasing particle velocity.

for fly ash samples. Two- and three-dimensional phase space portraits with different combinations of conveying parameters show that as the flow develops, solids and actual air velocities increase, solids volume fraction decreases (along the direction of flow) and pipeline pressure drops. Multi-stable operating zones for the sample of fly ash are

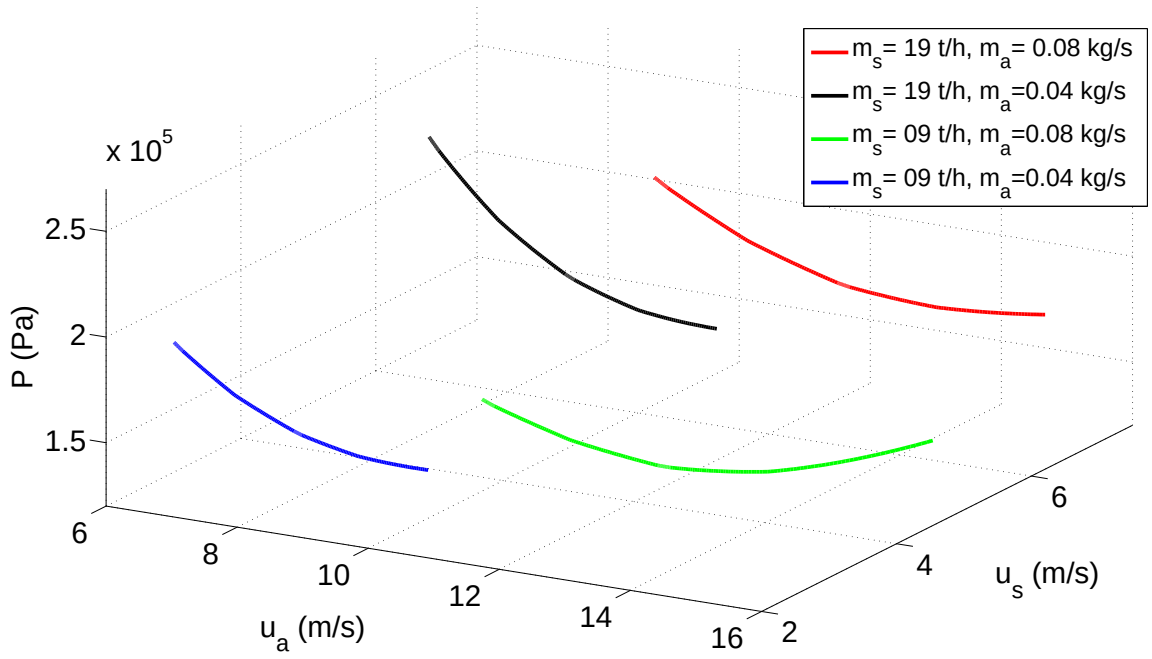


**Figure 7.8:** Variation in pressure ($P$) with increasing particle velocity ($u_s$) and actual air velocity ($u_a$).

predicted at certain mass flow rate of air and solids. Further extension of the work can be found in Kaur et al. (2017a), Kaur et al. (2017b) and Kaur et al. (2017c) (papers 5, 6 and 9 in List of Publications). The work can be extended for better fundamental understanding and modeling of the gas-solids flow systems and to predict feasible operating regimes.

The following section deals with the stability analysis of the cancer cell growth dynamics.

## 7.2 Cancer Cell Dynamics

Mathematical models provide promising approaches that can be tested in laboratories, which are otherwise very expensive, risky and time consuming. In this section, such a study is conducted mathematically to determine the growth dynamics of cancer cell under the effect of drug dosages and time delay.

### 7.2.1 Mathematical Modeling

The uncontrolled growth and spread of mutated cells in the body indicate cancer. A set of delay differential equations (DDE) constitute the mathematical model of cancer cell dynamics. These DDEs govern the population dynamics of various tumor cells present in different phases of a cell cycle, viz., interphase, mitosis phase and quiescent phase. These DDEs are solved to identify a stability region that is related to the stable state for tumor cell growth. Also, the population dynamics of tumor cells have been studied with different drug activity, delay time and at different dosage schedules [215, 216].

$$\frac{T_M(t)}{dt} = a_1 T_I(t-\tau) - d_3 T_M(t) - a_4 T_M(t) - c_3 T_M(t) I(t) - u_2(t) T_M(t), \tag{7.19}$$

$$\frac{T_I(t)}{dt} = 2a_4 T_M(t) - a_5 T_I(t-\tau) + a_6 T_Q(t) - c_1 T_I(t) I(t) - d_2 T_I(t) - a_1 T_I(t-\tau), \tag{7.20}$$

$$\frac{T_Q(t)}{dt} = a_5 T_I(t-\tau) - a_6 T_Q(t) - d_4 T_Q(t) - c_5 I(t) T_Q(t) - u_1(t) T_Q(t), \tag{7.21}$$

$$\frac{I(t)}{dt} = k + \frac{\rho I(t)(T_I(t) + T_M(t))^n}{\alpha + (T_Q(t) + T_I(t) + T_M(t))} - c_2 I(t) T_I(t) - c_4 T_M I(t) - d_1 T(t) - c_6 T_Q(t) I(t) - u_3(t) I(t). \tag{7.22}$$

where, $T_I(t)$, $T_M(t)$ and $T_Q(t)$ represent the population of tumor cells during interphase, mitosis phase and quiescent phase at any time $t$. $I(t)$ represents the pop-

ulation of immune cells at time $(t)$. The total cell population is given by $N(t) = T_Q(t) + T_I(t) + T_M(t)$. The term $\frac{\rho I(t)(T_I(t)+T_M(t))^n}{\alpha+(T_Q(t)+T_I(t)+T_M(t))}$ gives the nonlinear growth of the immune cells. The parameters $\rho$, $n$ and $\alpha$ are explicitly dependent on the tumor type and immune system health. $a_1$ and $a_4$ represent the tumor cell population growth and regulate the rate of cell division. The parameter $k$ represents the constant rate of growth of immune cells in the absence of any tumor cells. $c_i$ are the loss terms, which emerge as resultant of encounters between tumor cells and immune cells. $d_i$'s represent the fractional losses due to natural process of cell death. $u_1(t)$, $u_2(t)$ and $u_3(t)$ are the other control functions in the system, which are defined as:

$$u_1(t) = k_5(1 - e^{-k_6\omega t}), \tag{7.23}$$

$$u_2(t) = k_1(1 - e^{-k_2\omega t}), \tag{7.24}$$

$$u_3(t) = k_3(1 - e^{-k_4\omega t}), \tag{7.25}$$

and $\omega$ is the linear combination of states $\omega_1$ and $\omega_2$, given as:

$$\omega(t) = r_1\omega_1(t) + r_2\omega_2(t). \tag{7.26}$$

where, $\omega_1' = -\lambda_1\omega_1(t) + c(t)$ and $\omega_2' = -\lambda_2\omega_2(t) + c(t)$. $c(t)$ is the concentration of drug at any time $t$. $\lambda_1$ and $\lambda_2$ are the constants and are case specific.

### 7.2.2 Stability Analysis

In order to analyze the stability and no cancer cell growth zone, four different cases are considered, which are discussed as following:

**Case 1: Drug free system; without immune response; and no delay $\tau = 0$**

In the first case, the drug free system without immune response is considered without delay. The equations (7.19)-(7.22) take the following form for this case:

$$\frac{T_M(t)}{dt} = a_1 T_I(t) - d_3 T_M(t) - a_4 T_M(t). \tag{7.27}$$

$$\frac{T_I(t)}{dt} = 2a_4 T_M(t) - a_5 T_1(t) + a_6 T_Q(t) - d_2 T_I(t) - a_1 T_I(t), \tag{7.28}$$

$$\frac{T_Q(t)}{dt} = a_5 T_I(t) - a_6 T_Q(t) - d_4 T_Q(t), \tag{7.29}$$

The fixed point for this condition is given as $(0, 0, 0)$. The eigenvalues of the Jacobi determinant for the set of equations (7.27)-(7.29) are given by:

$$\lambda_1 = \pm \frac{tr_1 \pm \sqrt{tr_1^2 - 4\Delta_1}}{2} \tag{7.30}$$

where, $tr_1 = -(d_3 + a_4 + d_2 + a_1 + a_5 + a_6 + d_4)$ and the $\Delta_1$ is given by the following relation:

$$\Delta_1 = -(d_3 + d_4)(d_2 a_6 + d_4 a_5) + (a_4 - d_3)(a_1 a_6 + d_4 a_1). \tag{7.31}$$

Positive values of equation (7.31) represent that the system lie in the stable fixed point zone, however, tumor cell would grow if $\Delta < 0$ or if the following condition would be satisfied:

$$(a_4 - d_3)(a_1 a_6 + d_4 a_1) < (d_3 + d_4)(d_2 a_6 + d_4 a_5). \tag{7.32}$$

The tumor free state $\Delta > 0$, and this condition is dependent on both death and growth rate of cells. Solid line in Figure (7.9) corresponds to $\Delta_1 = 0$. Combination of regions R II and R III in Figure (7.9) represent the positive values of $\Delta_1$, whereas, R III

presents the negative values. Following set of parameters are used in the calculation: $a_1 = 0.98$. $a_4 = 0.85$, $a_5 = 0.0001$, $a_6 = 0.00015$, $c_1 = 0.9$, $c_2 = 0.085$, $c_3 = 0.9$, $c_4 = 0.085$, $c_5 = 50e-3$, $c_6 = 0.00085$, $d_1 = 0.29$, $d_2 = 0.11$, $d_4 = 0.1$,$k = 0.036$, $\rho = 0.1$, $n = 3$, $\alpha = 0.2$, $k_1 = 0.47$, $k_2 = 0.57$, $k_3 = 0.49$, $k_4 = 0.061$, $k_5 = 0.47$, $k_6 = 0.57$, $r_1 = 0.73$ and $r_2 = 0.27$.

**Case 2: Drug free system; without immune response; and delay $\tau > 0$**

In this case the effect of delay is introduced, the Jacobian eigenvalue determinant at equilibrium takes the following form:

$$\begin{vmatrix} -d_3 - a_4 - \lambda & a_1 & 0 \\ 2a_4 & -d_2 - (a_5 + a_1)(t-\tau) - \lambda & a_6 \\ 0 & a_5(t-\tau) & -(a_6 + d_4) - \lambda \end{vmatrix} = 0. \tag{7.33}$$

The resultant characteristic equation around the fixed point $(0, 0, 0)$ takes the following form:

$$F_1(\lambda) = P_1(\lambda) + e^{-\tau\lambda} Q_1(\lambda), \tag{7.34}$$

where, $P_1(\lambda) = -(d_3 + a_4 + \lambda)(d_2 + \lambda)(a_6 + d_4 + \lambda) + 2a_1a_4(a_6 + d_4 + \lambda)$ and $Q_1(\lambda) = (d_3 + a_4 + \lambda)(a_5 + a_1 - a_5a_6)$. Dashed curve in Figure (7.9) represents zeros of the solution for *case 2*. Region R I and R II attain negative values of the solution, whereas, combination of R III and R IV have positive values. Regions with negative values of the solutions represent the unstable region where tumor cells multiplies. Thus such regions are unstable regions. From Figure (7.9), it is concluded in region R III (shaded region) the tumor growth is stabilized.

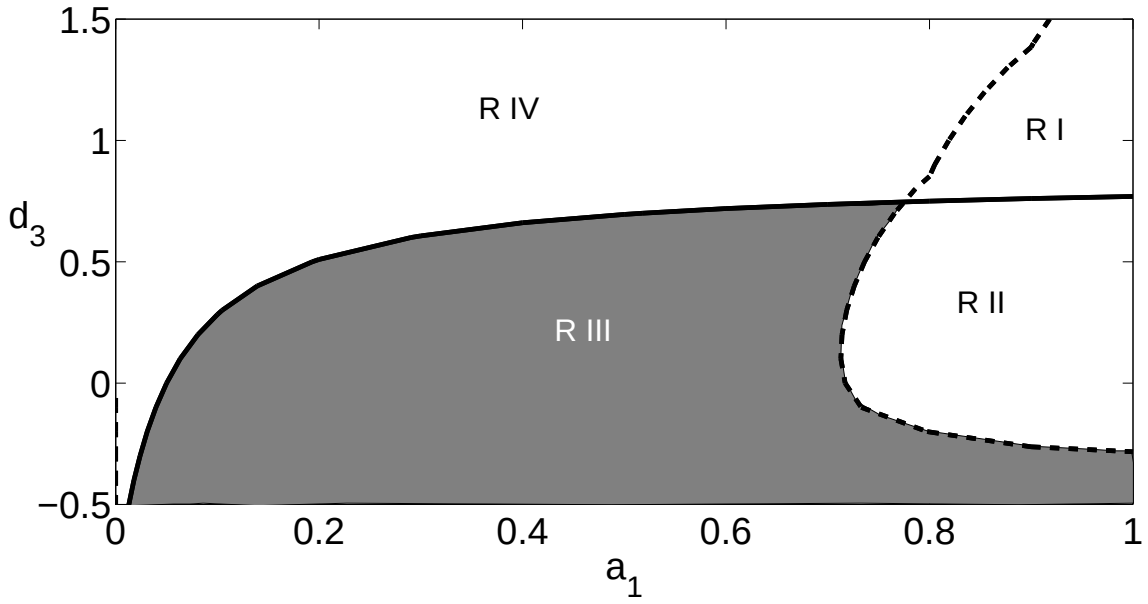


**Figure 7.9:** Stability diagram for Drug free system with no immune response. Solid line corresponds to no delay and dashed line corresponds to the case with delay. Shaded region (R III) is the stability region where tumor cell growth is stabilized.

**Case 3: Drug activity; immune response; and no delay $\tau = 0$**

Drug activity and immune suppression are considered without the delay, i.e., $\tau = 0$. The fixed points for this case are $(0, 0, 0, \frac{c+3k}{d_1+u_3})$. Considering the equations (7.19)-(7.22) without delay, the corresponding Jacobian determinant takes the form:

$$\begin{vmatrix} -\beta_1 - \lambda_3 & a_1 & 0 & 0 \\ 2a_4 & -\beta_2 - \lambda_3 & a_6 & 0 \\ 0 & a_5 & -\beta_3 - \lambda_3 & 0 \\ -\frac{c_4 k}{d_1+u_3} & -\frac{c2k}{d_1+u_3} & -\frac{c_6 k}{d_1+u_3} & -d_1 - \lambda_3 \end{vmatrix} = 0, \tag{7.35}$$

where, $\beta_1 = d_3 + a_4 + c_3\frac{k}{d_1+u_3} + u_2$, $\beta_2 = a_5 + c_1\frac{k}{d_1+u_3} + d_2 + a_1$, $\beta_3 = a_6 + d_4 + u_1 + \frac{c_5 k}{d_1+u_3}$, $\beta_4 = a_5 a_6$ and $\beta_5 = 2a_1 a_4$. On solving the determinant the following eigenvalue equation is formed:

$$(-d_1 - \lambda_3)[-(\beta_1 + \lambda_3)((\beta_2 + \lambda_3)(\beta_3 + \lambda_3) - \beta_4) + \beta_6(\beta_3 + \lambda_3)] = 0, \tag{7.36}$$

where, $\beta_1 = d_3 + a_4 + c_3\frac{k}{d_1+u_3} + u_2$, $\beta_2 = a_5 + c_1\frac{k}{d_1+u_3} + d_2 + a_1$, $\beta_3 = a_6 + d_4 + u_1 + \frac{c_5 k}{d_1+u_3}$, $\beta_4 = a_5 a_6$ and $\beta_5 = 2a_1 a_4$. Trace of the determinant is calculated as: $tr_3 = -(\beta_1 + \beta_2 + \beta_3 + d_1)$ and always assume the negative values. $\lambda_3 = -d_1$ is one of the eigenvalues of the system without delay.

In reduced form, the characteristic equation representing the system is written as:

$$\lambda_3^3 + (\beta_1 + \beta_2 + \beta_3)\lambda_3^2 + (\beta_1\beta_2 + \beta_1\beta_3 + \beta_2\beta_3 - \beta_4 - \beta_5)\lambda_3 + \beta_1\beta_2\beta_3 - \beta_1\beta_4 - \beta_3\beta_5 = 0. \quad (7.37)$$

Equation (7.37) can be written as:

$$\alpha_1\lambda_3^3 + \alpha_2\lambda_3^2 + \alpha_3\lambda_3 + \alpha_4 = 0. \quad (7.38)$$

The corresponding discriminant is given by:

$$\Delta_3 = 18\alpha_1\alpha_2\alpha_3\alpha_4 - 4\alpha_2^2\alpha_4 + \alpha_2^2\alpha_3^2 - 4\alpha_1\alpha_3^3 - 27\alpha_1^2\alpha_4^2. \quad (7.39)$$

If the discriminant ($\Delta_1 > 0$), the system was in stable state for the fixed point $(0, 0, 0)$ in the case 1, therefore, the stability can also be achieved in this case where fixed points are given as $(0, 0, 0, \frac{c+3k}{d_1+u_3})$ However, $\Delta < 0$ is the suitable condition for the tumor growth which is represented by region R II and R III combined in Figure (7.10).

The decrease in the tumor cells, in stability zone with increasing immune response during interphase, mitosis and quiescent phase are given in Figures (7.11), (7.12) and (7.13), respectively. The values of parameters considered in these plots are same as in Figure (7.10).

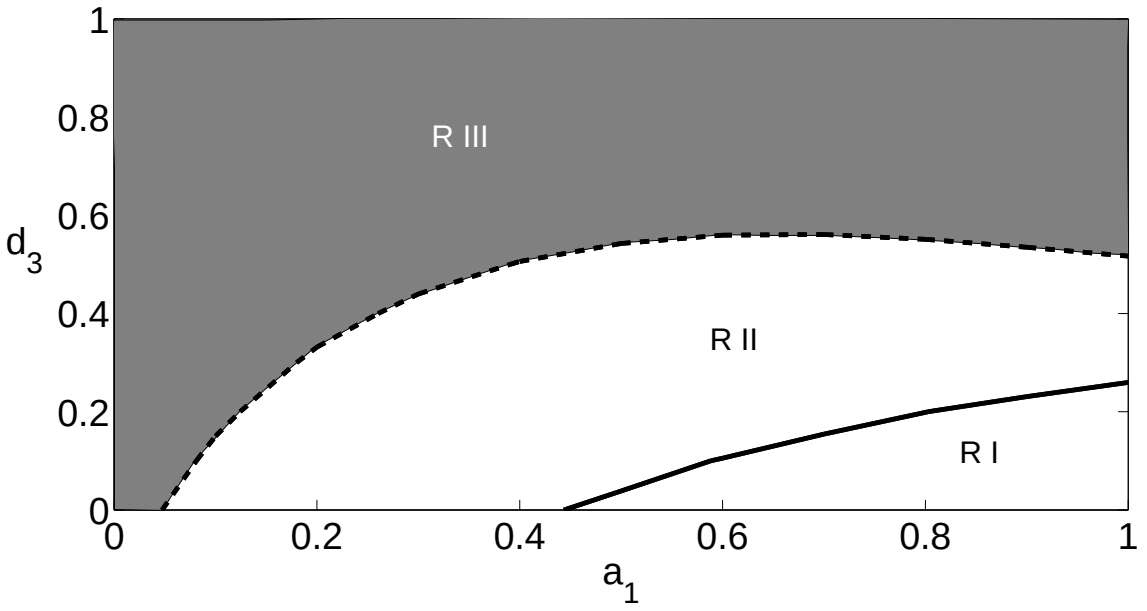


**Figure 7.10:** Stability diagram for a system with drug activity and immune response. Solid Curve represents the case for no-delay (Case 3), dashed curve represents the study with delay (case 4). Shaded region corresponds to region where tumor growth is stabilized.

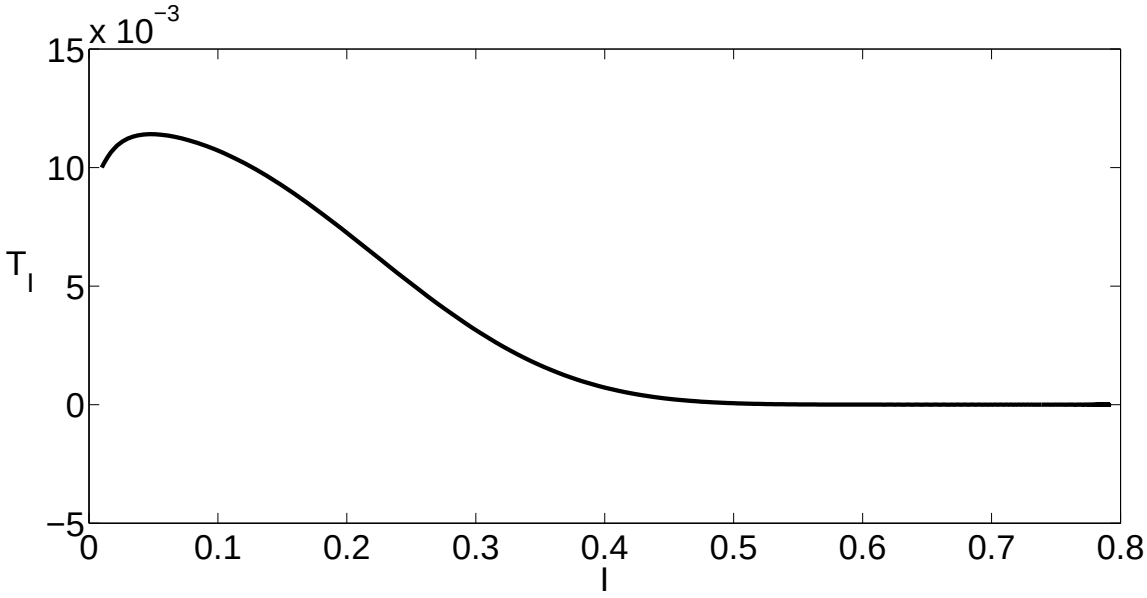


**Figure 7.11:** Decrease in the tumor cells with the increase in immune response during interphase.

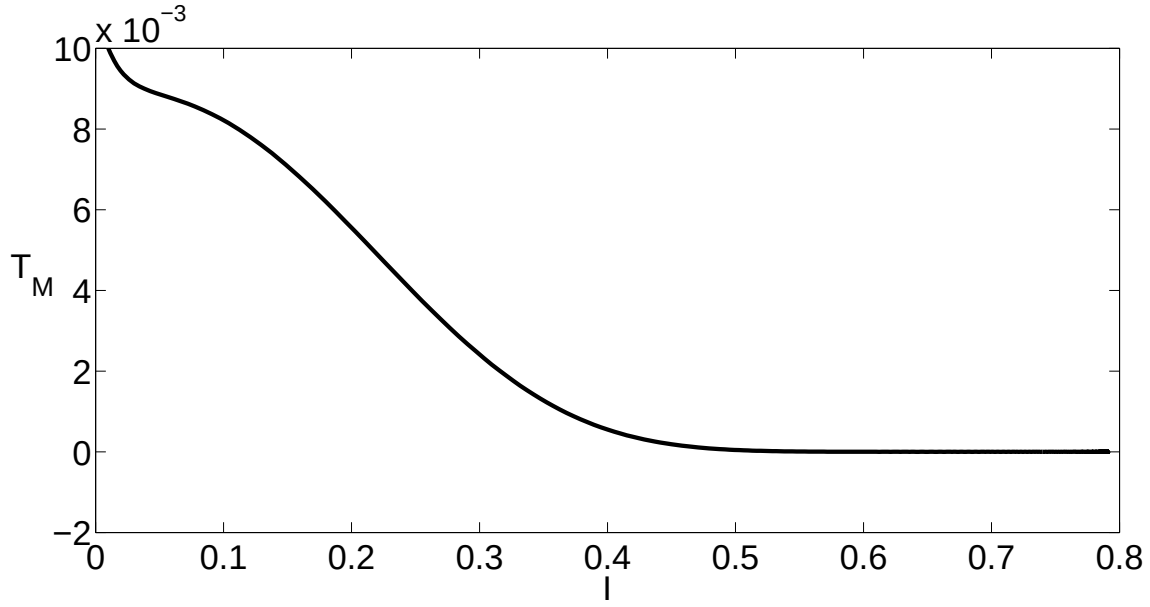


**Figure 7.12:** Decrease in the tumor cells with the increase in immune response during mitosis phase

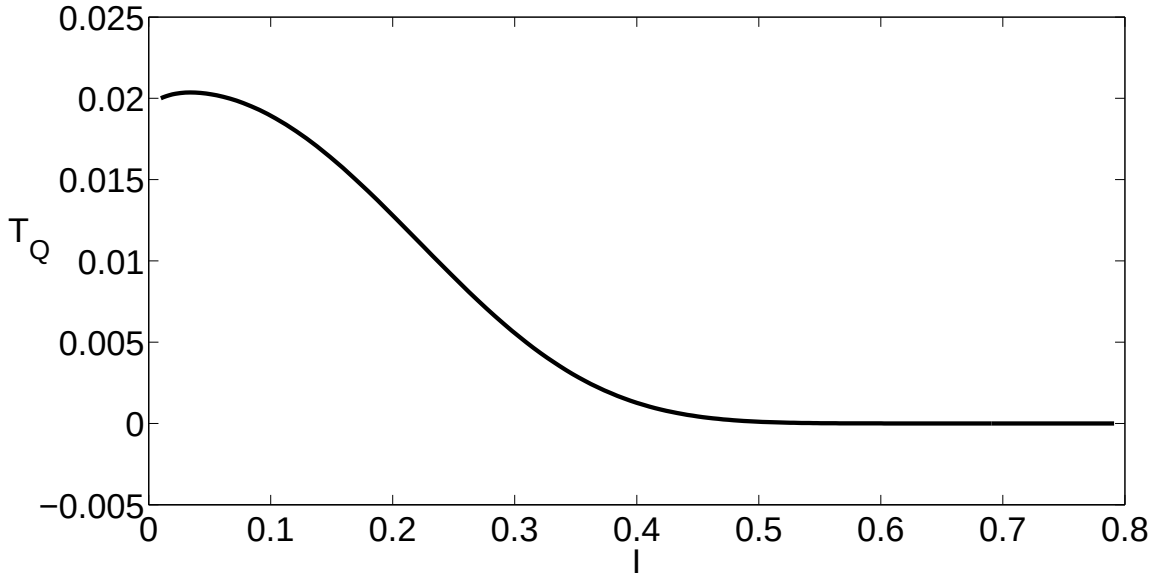


**Figure 7.13:** Decrease in the tumor cells with the increase in immune response during quiescent phase.

**Case 4: Drug activity; immune response; and delay $\tau > 0$**

For this case, the Jacobian determinant takes the following form:

$$\begin{vmatrix} -\beta_1 - \lambda_4 & a_1(t-\tau) & 0 & 0 \\ 2a_4 & -\beta_2' - \lambda_4 & a_6 & 0 \\ 0 & a_5(t-\tau) & -\beta_3 - \lambda_4 & 0 \\ -\frac{c_4 k}{d_1+u_3} & -\frac{c2k}{d_1+u_3} & -\frac{c_6 k}{d_1+u_3} & -d_1 - \lambda_4 \end{vmatrix} = 0, \tag{7.40}$$

where, $\beta_2' = a_5 + c_1\frac{k}{d_1+u_3} + d_2 + a_1(t-\tau)$. Similar to the *Case-3*, one of the eigenvalue of the determinant is calculated as: $\lambda_4 = -d_1$. The characteristic equation takes the following form:

$$-(\beta_1 + \lambda_4)[(\beta_6 + \lambda_4)(\beta_3 + \lambda_4) + \beta_7((\beta_3 + \lambda_4) - \beta_4)(t-\tau)] + \beta_5(\beta_3 + \lambda_4)(t-\tau) = 0, \tag{7.41}$$

where, $\beta_6 = \frac{c_1 k}{d_1+u_3}$ and $\beta_7 = a_5 + a_1$. The linearized characteristic equation around the fixed point $(0, 0, 0, \frac{c+3k}{d_1+u_3})$ can be written as:

$$F(\lambda_4) = P(\lambda_4) + e^{-\tau\lambda_4}Q(\lambda_4), \tag{7.42}$$

where, $P(\lambda_4) = -(\beta_1 + \lambda_4)(\beta_3 + \lambda_4)(\beta_6 + \lambda_4)$ and $Q(\lambda_4) = [-\beta_7(\beta_3 + \lambda_4) + \beta_4](\beta_1 + \lambda_4) + \beta_5(\beta_3 + \lambda_4)$. The stability of such system can be studied using the Theorem 1 in ref. [215, 217]. Dashed curve in Figure (7.10) represents the zeros of the solution in the study with delay and immune suppression. Region R III presents the positive solutions, whereas the negative solutions are presented by R II and R I. Region R II supports the tumor growth. By comparing the results of *case 3* and *case 4*, it is concluded that the region R III is the region where tumor growth can be stabilized.

## Conclusion

We successfully extended the skill of stability analysis learnt from the investigation of CS in to two diverse fields: multi-phase flow and cancer model. Stability region in both the cases are identified. For gas-solids flow, the results are at par with the experimental data (refer to the publications serial number 5 and 6 in the publication list). However, for cancer model, experimental verification is subject to availability of adequate systems and clearance of several strict regulations (which forms a part of the future scope of work).

| Symbol | Abbreviations |
|---|---|
| $A$ | Cross sectional area of control volume $[m^2]$ |
| $A_{11}$, $A_{12}$, $A_{21}$, $A_{22}$, $A_{33}$, $A_{44}$ | Coefficients of linearized evolution equations $[1/m]$ |
| $A_{13}$, $A_{23}$ | Coefficients of linearized evolution equations $[1/s]$ |
| $A_{1,4}$, $A_{24}$ | Coefficients of linearized evolution equations $[ms/kg]$ |
| $A_{31}$, $A_{32}$ | Coefficients of linearized evolution equations $[s/m^2]$ |
| $A_{34}$ | Coefficients of linearized evolution equations $[s^2/kg]$ |
| $A_{41}$, $A_{42}$ | Coefficients of linearized evolution equations $[kg/(m^3 s)]$ |
| $A_{43}$ | Coefficients of linearized evolution equations $[Pa/m]$ |
| $c_1$ | Coefficient of eigenvalue equation $[1/m]$ |
| $c_2$ | Coefficient of eigenvalue equation $[1/m^2]$ |
| $c_3$ | Coefficient of eigenvalue equation $[1/m^3]$ |
| $c_4$ | Coefficient of eigenvalue equation $[1/m^4]$ |
| $d_{50}$ | Median particle diameter $[\mu m]$ |
| $F_a$ | Frictional force due to air phase [N] |
| $F_s$ | Frictional force due to solids phase [N] |
| $f_a$ | Frictional force per unit volume due to air phase $[N/m^3]$ |
| $f_s$ | Frictional force per unit volume due to solids phase $[N/m^3]$ |
| $m_a$ | Mass flow rate of air $[kg/s]$ |
| $m_s$ | Mass flow rate of solids $[kg/s]$ |
| $P$ | Pressure [Pa] |
| $u_a$ | Actual gas velocity $[m/s]$ |
| $u_s$ | Particle velocity [m/s] |
| $V_a = m_a/\rho_a$ | Volumetric flow rate of air $[m^3/s]$ |
| $V_s = m_s/\rho_s$ | Volumetric flow rate of solids $[m^3/s]$ |
| $\rho_a$ | Density of air $[kg/m^3]$ |
| $\rho_s$ | Particle Density $[kg/m^3]$ |
| $\lambda$ | Eigenvalue $[1/m]$ |
| $\epsilon_a = V_a/(V_a + V_s)$ | Volume fraction of air |
| $\epsilon_s = V_s/(V_a + V_s)$ | Volume fraction of solids |

**Table 7.2:** List of symbols and abbreviations used in section (7.1).

# Chapter 8

## Conclusions

This thesis presents the study of the existence, stability and dynamics of cavity solitons in a broad area microcavity, particularly in a vertical-cavity surface-emitting laser. Different system configurations based on VCSEL are considered. Emphasis is given to VCSEL with saturating nonlinearity coupled with frequency-selective feedback having very short or negligible time delay. Different cavity nonlinearity, namely, cubic, cubic-quintic and saturation nonlinearity are considered. Complex Ginzburg-Landau equation and perturbed NLSE that describes the cavity dynamics is solved analytically with the help of Lagrangian based variational method. The analytical results are validated with approach based on split-step Fourier method. The trivial and non-trivial homogeneous steady state solutions of VCSEL-SA-FSF model are determined. Corresponding regions for the stable, unstable and cavity soliton solutions are identified. The existence and stability criteria of the VCSEL-FSF model considering cubic and cubic-quintic nonlinearity are established through Lyapunov exponents method along with Hurwitzs criteria. The amplitude, width, chirp, phase and the power of the evolving CS are found to be confined, but not constant throughout the evolution. The steady state solutions of the amplitude, width and chirp bifurcate with an increase in feedback strength parameter.

The VCSEL-SA-FSF model demonstrated the spontaneous fission of the initial

beam and eventual formation of bound state CSs or CS molecules. These CS molecules are linear and comprise of two or more CS 'atoms'. Nevertheless, the spontaneous annihilation of the CS molecules is observed. Amplitude, feedback strength and resonance frequency of feedback element are the important factors determining the stability of the CS molecules in such systems. The study indicates that different combinations of feedback strength, amplitude and resonance frequency generate the multi-molecule CSs through single injected beam.

After exploring the existence and stability conditions, the dynamics of CS and CS molecules are investigated. Both the phase controlled dynamics and interaction dynamics of CSs are studied. Phase controlled drift velocity of CS is demonstrated in VCSEL-FSF with cubic-quintic nonlinearity. In-phase CSs attract each other, after sometime the CSs annihilate due to catastrophic collapse. Out-of-phase CSs tends to repel each other. A true 'optical push-broom' effect is observed in VCSEL-SA -FSF, where a CS pushes another in controlled manner. The velocity of the CSs can be increased by increasing the feedback strength. The parametric zone for observing this novel effect is however narrow.

An alternate approach of finding CS is established through the standing wave method. Traveling wave soliton solution in VCSEL-FSF exhibiting cubic nonlinearity are obtained through He's Variational method. Standing wave localized structures are created through super-imposing the TWSS in the dissipative cavity. A large family of CS having *sech* and *cosh*-Gaussian profiles are generated. CS profiles are also found with different tilt angles, reflection coefficients and ellipticity of the beam.

The stability analysis methods is extended to analyze multi-phase flow and cancer growth. Stable operating zone of the gas-solid flow system is identified. For the cancer

model, a parametric zone is marked where tumor cell growth gets stabilized.

## 8.1 Applications of Cavity Solitons

### 8.1.1 All-optical memories

The CS and CS molecules presented in this thesis have their primary application in all-optical memory arrays. Particularly, the multi atomic linear CS molecules may be used through unconventional way. The freedom of location, possibility of multiplication and annihilation and capability of relocation made them more attractive than ever.

### 8.1.2 Mapping surface and bulk optical inhomogeneity in materials

The CS dynamics showed some interesting effects, such as 'all-optical push broom', 'marching CSs'. Probably, the most important application of these findings will be in mapping surface and bulk optical inhomogeneity in materials. Inhomogeneity or gradients in the background of the cavity can lead to spontaneous motion of CS. CSs tend to move continuously until it reaches an equilibrium spatial position or the gradient vanishes. Any spontaneous motion of the cavity solitons in the semiconductor devices indicates the presence of defects. This technique can be used to map inhomogeneity of semiconductor materials or even soft biological samples placed in the external cavity. This technique may be applied to realize 'soliton force microscopy'.

### 8.1.3 All-optical delay lines

For high speed switching, all-optical routers are required in optical communication devices. For the moment a wave packet is being processed, the succeeding wave-packet needs to be buffered or delayed. Therefore, in order to escape the interference of two independent signals delay lines are key elements for such types of systems. The phase induced dynamics discussed in section 5.2 and all-optical push-broom discussed in section 5.3 can give an optimal conceptual background to develop the all-optical delay lines.

### 8.1.4 Tuning the optical clocks

The oscillating pair discussed in section 4.1 can be helpful in tuning optical clocks as oscillating CS pair can be considered as the coherently coupled CS pair. The frequency of oscillation of CS pair can be matched with the clock for tuning the optical clocks.

### 8.1.5 Application to Medical Research, Engineering and Technology

The concept of stability could be successfully applied to other fields of science and technology to extract useful information for better fundamental understanding and modeling of a wide range of physical/biological systems. An effective application of the stability analysis in these thermodynamically irreversible 'far-from-equilibrium' systems could go a long way towards generating improved fundamental understanding of the system dynamics and could present a far reaching yet seemingly exciting prospect of developing simulation models that could reliably predict such dynamics. This con-

cept of stability analysis learned for investigating CS is successfully applied in this thesis to two interdisciplinary, yet apparently contrasting areas: an application to multi-phase flow engineering (gas solids flow systems) and medical sciences (tumor cell growth dynamics).

## 8.2 Future Scope

In future, investigation can be done on gradient induced CS dynamics and mapping to realize a soliton force microscope. In this context, Graphene or other 2D material embedded VCSEL may be promising. The concept of cavity solitons can be extended to the realization of optical memory devices with better capacity. The concept of stability can be extended to the study of behavior of dissipative complex systems in biological, physical and chemical sciences, technology and in social sciences.

# Bibliography


[1] T. Ackemann, W. J. Firth, and G.-L. Oppo, Fundamentals and applications of spatial dissipative solitons in photonic devices, in *Advances in Atomic Molecular and Optical Physics*, edited by E. Arimondo, P. R. Berman, and C. C. Lin, volume 57, chap. 6, pp. 323–421, Academic Press, 2009.

[2] N. Akhmediev and A. Ankiewicz, in *Dissipative Solitons*, edited by N. Akhmediev and A. Ankiewicz, volume 661 of *Lecture Notes in Physics*, Springer-Verlag Berlin Heidelberg, 2005.

[3] N. N. Rozanov, S. V. Fedorov, and A. N. Shatsev, *Opt. Spectrosc.* **91**, 232-234 (2001).

[4] N. Radwell and T. Ackemann, *IEEE J. Quant. Electron.* **45**, 1388-1395 (2009).

[5] N. Akhmediev and A. Ankiewicz, *Solitons: Non-linear pulses and beams* (Springer US, 1997).

[6] G. P. Agarwal, *Nonlinear Fiber Optics*, Fourth ed. (Academic Press, San Diego, 2006).

[7] R. Menzel, *Photonics: Linear and Nonlinear Interactions of Laser Light and Matter* (Springer-Verlag Berlin Heidelberg, 2001).

[8] I. Prigogine and G. Nicolis, Self-organisation in nonequilibrium systems: Towards a dynamics of complexity, in *Bifurcation Analysis: Principles, Applications and Synthesis*, edited by M. Hazewinkel, R. Jurkovich, and J. H. P. Paelinck, pp. 3–12, Springer Netherlands, Dordrecht, 1985.

[9] P. V. Paulau, A. J. Scroggie, A. Naumenko, T. Ackemann, N. A. Loiko, and W. J. Firth, *Phys. Rev. E* **75**, 056208 (2007).

[10] L. A. Lugiato, *IEEE J. Quant. Electron.* **39**, 193-196 (2003).

[11] W. J. Firth and C. O. Weiss, *Opt. & Photon. News* **13**, 54-58 (2002).

[12] A. J. Scroggie, W. J. Firth, and G.-L. Oppo, *Phys. Rev. A* **80**, 013829 (2009).

[13] N. N. Rozanov, *Opt. Spectrosc.* **88**, 238-241 (2000).

[14] M. Bache, F. Prati, G. Tissoni, R. Kheradmand, L. Lugiato, I. Protsenko, and M. Brambilla, *Appl. Phys. B* **81**, 913-920 (2005).

[15] M. Eslami, R. Kheradmand, P. Bahari, and H. Tajalli, *Eur. Phys. J. D* **69**, 222 (2015).

[16] N. N. Akhmediev and A. Ankiewicz, Solitons around us: Integrable, Hamiltonian and Dissipative Systems, in *Optical Solitons: Theoretical and Experimental Challenges*, edited by K. Porsezian and V. C. Kuriakose, pp. 105–126, Springer, Berlin, Heidelberg, 2003.

[17] W. J. Firth, Theory of cavity solitons, in *Soliton-driven Photonics*, edited by A. D. Boardman and A. P. Sukhorukov, pp. 459–485, Springer Netherlands, Dordrecht, 2001.

[18] A. Larraza and S. Putterman, *Phys. Lett. A* **103**, 15-18 (1984).

[19] A. Hasegawa and F. Tappert, *Appl. Phys. Lett.* **23**, 142-144 (1973).

[20] A. Hasegawa and F. Tappert, *Appl. Phys. Lett.* **23**, 171-172 (1973).

[21] Y. S. Kivshar, G. P. Agrawal, and G. P. Agrawal, *Optical Solitons: From Fibers to photonic Crystals*, first ed. (Academic Press, Burlington, 2003).

[22] N. J. Zabusky and M. D. Kruskal, *Phys. Rev. Lett.* **15**, 240-243 (1965).

[23] H. Kuwayama and S. Ishida, *Sci. Rep.* **3**, 2272 (2013).

[24] E. D. Giudice, S. Doglia, and M. Milani, *Phys. Scr.* **23**, 307 (1981).

[25] J. Ross, S. C. Müller, and C. Vidal, **240**, 460-465 (1988).

[26] P. Manneville, *Dissipative Structures and Weak Turbulence*, first ed. (Academic Press, Boston, 1990).

[27] J. S. Russell, Report on waves, volume Report of the 14th meeting, pp. 311–390, London, September 1844, Brit. Assoc. Adv. Sci.

[28] C. S. Gardner, J. M. Greene, M. D. Kruskal, and R. M. Miura, *Phys. Rev. Lett.* **19**, 1095-1097 (1967).

[29] T. H. Maiman, *Nature* **187**, 493-494 (1960).

[30] P. A. Franken, A. E. Hill, C. W. Peters, and G. Weinreich, *Phys. Rev. Lett.* **7**, 118-119 (1961).

[31] R. W. Terhune, P. D. Maker, and C. M. Savage, *Phys. Rev. Lett.* **8**, 404-406 (1962).

[32] E. J. Woodbury and W. K. Ng, *Proc. IRE.* **50**, 2347-2348 (1962).

[33] J. A. Armstrong, N. Bloembergen, J. Ducuing, and P. S. Pershan, *Phys. Rev.* **127**, 1918-1939 (1962).

[34] V. F. Zakharov and A. B. Shabat, *Sov. Phys. JETP* **34**, 62-69 (1972).

[35] H. M. Gibbs, S. L. McCall, and T. N. C. Venkatesan, *Phys. Rev. Lett.* **36**, 1135-1138 (1976).

[36] N. N. Rozanov and V. E. Semenov, *Opt. Spectrosc.* **48**, 59-63 (1980).

[37] D. W. McLaughlin, J. V. Moloney, and A. C. Newell, *Phys. Rev. Lett.* **51**, 75-78 (1983).

[38] L. F. Mollenauer, R. H. Stolen, and J. P. Gordon, *Phys. Rev. Lett.* **45**, 1095-1098 (1980).

[39] L. A. Lugiato, Theory of optical bistability, in *Progress in Optics*, edited by E. Wolf, volume 21, pp. 69–216, Elsevier, 1984.

[40] H. M. Gibbs, *Optical Bistability: Controlling Light with Light* (Academic Press, Orlando, 1985).

[41] N. N. Rozanov and G. V. Khodova, *Opt. Spectrosc.* **65**, 449-450 (1988).

[42] N. N. Rozanov and G. V. Khodova, *J. Opt. Soc. Am. B* **7**, 1057-1065 (1990).

[43] S. V. Fedorov, G. V. Khodova, and N. N. Rozanov, *Proc. SPIE* **1840**, 208-215 (1992).

[44] V. Y. Bazhenov, V. B. Taranenko, and M. V. Vasnetsov, *Proc. SPIE* **1840**, 183-193 (1992).

[45] M. Kreuzer, H. Gottschling, and T. Tschudi, *Mol. Cryst. Liq. Cryst.* **207**, 219-230 (1991).

[46] R. Neubecker and T. Tschudi, *J. of Mod. Opt.* **41**, 885-906 (1994).

[47] N. N. Rozanov and S. V. Fedorov, *Opt. Spectrosc.* **72**, 782-785 (1992).

[48] N. Rozanov, Solitons in laser systems with saturable absorption, in *Dissipative Solitons*, edited by N. Akhmediev and A. Ankiewicz, volume 661 of *Lecture Notes in Physics*, pp. 101–130, Springer Berlin Heidelberg, 2005.

[49] A. G. Vladimirov, S. V. Fedorov, N. A. Kaliteevski, G. V. Khodova, and N. N. Rozanov, *J. Opt. B: Quant. Semiclass. Opt.* **1**, 101 (1999).

[50] N. N. Rozanov, *J. Opt. Technol.* **76**, 187-198 (2009).

[51] L. A. Lugiato, F. Prati, G. Tissoni, M. Brambilla, S. Barland, M. Giudici, and J. R. Tredicce, Cavity solitons in semiconductor devices, in *Dissipative Solitons: From Optics to Biology and Medicine*, edited by N. Akhmediev and A. Ankiewicz, pp. 1–42, Springer Berlin Heidelberg, Berlin, Heidelberg, 2008.

[52] S. Barland, J. R. Tredicce, M. Brambilla, L. A. Lugiato, S. Balle, M. Giudici, T. Maggipinto, L. Spinelli, G. Tissoni, T. Knodl, M. Miller, and R. Jager, *Nature* **419**, 699-702 (2002).

[53] Y. Tanguy, T. Ackemann, W. J. Firth, and R. Jäger, *Phys. Rev. Lett.* **100**, 013907 (2008).

[54] F. Pedaci, S. Barland, E. Caboche, P. Genevet, M. Giudici, J. R. Tredicce, T. Ackemann, A. J. Scroggie, W. J. Firth, G.-L. Oppo, G. Tissoni, and R. Jger, *Appl. Phys. Lett.* **92**, 011101 (2008).

[55] M. Brambilla, T. Maggipinto, G. Patera, and L. Columbo, *Phys. Rev. Lett.* **93**, 203901 (2004).

[56] N. Veretenov and M. Tlidi, *Phys. Rev. A* **80**, 023822 (2009).

[57] P. V. Paulau, D. Gomila, P. Colet, M. A. Matías, N. A. Loiko, and W. J. Firth, *Phys. Rev. A* **80**, 023808 (2009).

[58] M. Tlidi, A. G. Vladimirov, D. Pieroux, and D. Turaev, *Phys. Rev. Lett.* **103**, 103904 (2009).

[59] M. Tlidi, A. G. Vladimirov, D. Turaev, G. Kozyreff, D. Pieroux, and T. Erneux, *Eur. Phys. J. D* **59**, 59-65 (2010).

[60] E. Caboche, F. Pedaci, P. Genevet, S. Barland, M. Giudici, J. Tredicce, G. Tissoni, and L. A. Lugiato, *Phys. Rev. Lett.* **102**, 163901 (2009).

[61] E. Caboche, S. Barland, M. Giudici, J. Tredicce, G. Tissoni, and L. A. Lugiato, *Phys. Rev. A* **80**, 053814 (2009).

[62] P. Genevet, S. Barland, M. Giudici, and J. R. Tredicce, *Phys. Rev. A* **79**, 033819 (2009).

[63] F. Prati, G. Tissoni, L. A. Lugiato, K. M. Aghdami, and M. Brambilla, *Eur. Phys. J. D* **59**, 73-79 (2010).

[64] C. McIntyre, A. M. Yao, G.-L. Oppo, F. Prati, and G. Tissoni, *Phys. Rev. A* **81**, 013838 (2010).

[65] P. Genevet, S. Barland, M. Giudici, and J. R. Tredicce, *Phys. Rev. Lett.* **101**, 123905 (2008).

[66] P. Genevet, L. Columbo, S. Barland, M. Giudici, L. Gil, and J. R. Tredicce, *Phys. Rev. A* **81**, 053839 (2010).

[67] P. V. Paulau, D. Gomila, P. Colet, B. A. Malomed, and W. J. Firth, *Phys. Rev. E* **84**, 036213 (2011).

[68] F. Prati, L. A. Lugiato, G. Tissoni, and M. Brambilla, *Phys. Rev. A* **84**, 053852 (2011).

[69] T. Ackemann, N. Radwell, Y. Noblet, and R. Jäger, *Opt. Lett.* **37**, 1079-1081 (2012).

[70] O. A. Egorov and F. Lederer, *Opt. Lett.* **38**, 1010-1012 (2013).

[71] A. G. Vladimirov, A. Pimenov, S. V. Gurevich, K. Panajotov, E. Averlant, and M. Tlidi, **372** (2014).

[72] G. J. de Valcárcel and K. Staliunas, *Phys. Rev. A* **87**, 043802 (2013).

[73] W. J. Firth and A. Lord, *J. of Mod. Opt.* **43**, 1071-1077 (1996).

[74] W. J. Firth, G. K. Harkness, A. Lord, J. M. McSloy, D. Gomila, and P. Colet, *J. Opt. Soc. Am. B* **19**, 747-752 (2002).

[75] F. Leo, L. Gelens, P. Emplit, M. Haelterman, and S. Coen, *Opt. Express* **21**, 9180-9191 (2013).

[76] S. Konar and S. Jana, *Opt. Commun.* **236**, 7-20 (2004).

[77] X. Hachair, F. Pedaci, E. Caboche, S. Barland, M. Giudici, J. Tredicce, F. Prati, G. Tissoni, R. Kheradmand, L. Lugiato, I. Protsenko, and M. Brambilla, *IEEE J. Sel. Top. Quantum Electron.* **12**, 339-351 (2006).

[78] T. Elsass, K. Gauthron, G. Beaudoin, I. Sagnes, R. Kuszelewicz, and S. Barbay, *Eur. Phys. J. D* **59**, 91-96 (2010).

[79] T. Ackemann, A. Heuer, Y. A. Logvin, and W. Lange, *Phys. Rev. A* **56**, 2321-2326 (1997).

[80] G. Khitrova, J. F. Valley, and H. M. Gibbs, *Phys. Rev. Lett.* **60**, 1126-1129 (1988).

[81] N. Radwell, C. McIntyre, A. J. Scroggie, G.-L. Oppo, W. J. Firth, and T. Ackemann, *Eur. Phys. J. D* **59**, 121-131 (2010).

[82] G. Tissoni, K. M. Aghdami, F. Prati, M. Brambilla, and L. A. Lugiato, Cavity soliton laser based on a VCSEL with saturable absorber, in *Localized States in Physics: Solitons and Patterns*, edited by O. Descalzi, M. Clerc, S. Residori, and G. Assanto, pp. 187–211, Springer Berlin Heidelberg, Berlin, Heidelberg, 2011.

[83] P. V. Paulau, D. Gomila, T. Ackemann, N. A. Loiko, and W. J. Firth, *Phys. Rev. E* **78**, 016212 (2008).

[84] A. J. Scroggie, W. J. Firth, G. S. McDonald, M. Tlidi, R. Lefever, and L. A. Lugiato, *Chaos, Solitons & Fractals* **4**, 1323-1354 (1994).

[85] V. L. Kalashnikov, *Phys. Rev. E* **80**, 046606 (2009).

[86] X. Hachair, S. Barland, L. Furfaro, M. Giudici, S. Balle, J. R. Tredicce, M. Brambilla, T. Maggipinto, I. M. Perrini, G. Tissoni, and L. Lugiato, *Phys. Rev. A* **69**, 043817 (2004).

[87] R. Kheradmand and M. Eslami, *Jpn. J. Appl. Phys.* **50**, 05FG07 (2011).

[88] R. Kheradmand and M. Eslami, *J. Phys. Conf. Ser.* **248**, 012050 (2010).

[89] D. Mihalache, D. Mazilu, L.-C. Crasovan, B. A. Malomed, F. Lederer, and L. Torner, *J. Opt. B: Quant. Semiclass. Opt.* **6**, S333 (2004).

[90] M. Eslami, R. Kheradmand, and F. Prati, *Phys. Rev. A* **89**, 013818 (2014).

[91] C. M. de Sterke, *Opt. Lett.* **17**, 914-916 (1992).

[92] W. J. Firth, L. Columbo, and T. Maggipinto, *Chaos* **17**, 1-8 (2007).

[93] S. Barbay, X. Hachair, T. Elsass, I. Sagnes, and R. Kuszelewicz, *Phys. Rev. Lett.* **101**, 253902 (2008).

[94] H. Susanto and P. C. Matthews, *Phys. Rev. E* **83**, 035201 (2011).

[95] P. C. Matthews and H. Susanto, *Phys. Rev. E* **84**, 066207 (2011).

[96] J. A. Goldstone and E. Garmire, *Phys. Rev. Lett.* **53**, 910-913 (1984).

[97] R.-K. Lee, Y. Lai, and B. A. Malomed, *J. Opt. B: Quant. Semiclass. Opt.* **6**, 367 (2004).

[98] M. M. Gupta and S. Medhekar, *Optik* **127**, 1221-1228 (2016).

[99] R. W. Boyd, *Nonlinear Optics*, Third ed. (Academic Press, Burlington, 2008), pp. 1–613.

[100] B. A. Malomed, D. Mihalache, F. Wise, and L. Torner, *J. Opt. B: Quant. Semiclass. Opt.* **7**, R53 (2005).

[101] J. Atai and B. A. Malomed, *Phys. Rev. E* **54**, 4371-4374 (1996).

[102] B. A. Malomed and H. G. Winful, *Phys. Rev. E* **53**, 5365-5368 (1996).

[103] B. A. Malomed, *Chaos* **17**, 037117 (2007).

[104] H. Triki, K. Porsezian, P. T. Dinda, and P. Grelu, *Phys. Rev. A* **95**, 023837 (2017).

[105] R. Pradhan, S. Saha, and P. K. Datta, *J. Opt. Soc. Am. B* **31**, 2956-2964 (2014).

[106] U. Keller, K. J. Weingarten, F. X. Kartner, D. Kopf, B. Braun, I. D. Jung, R. Fluck, C. Honninger, N. Matuschek, and J. A. der Au, *IEEE J. Sel. Top. Quantum Electron.* **2**, 435-453 (1996).

[107] S. Husaini and R. G. Bedford, *Proc. SPIE* **8966**, 896608-896608-8 (2014).

[108] X. M. Liu *et al.*, *Sci. Rep.* **6**, 26024 (2016).

[109] S. Bhattachraya, R. Maiti, A. C. Das, S. Saha, S. Mondal, S. K. Ray, S. N. B. Bhaktha, and P. K. Datta, *J. Appl. Phys.* **120**, 013101 (2016).

[110] Y. Kodama, *J. Phys. A: Math. and Theor.* **43**, 434004 (2010).

[111] S. Samaranayake, G. Samaranayake, and A. K. Bajaj, *Chaos, Solitons & Fractals* **11**, 1519-1534 (2000).

[112] C. Becker, S. Stellmer, P. Soltan-Panahi, S. Dorscher, M. Baumert, E. Richter, J. Kronjager, K. Bongs, and K. Sengstock, *Nature Phys.* **4**, 496-501 (2008).

[113] A. Picozzi, *Nat. Photon.* **2**, 334-335 (2008).

[114] X. T. Tran and N. N. Rozanov, *Opt. Spectrosc.* **105**, 432-477 (2008).

[115] N. B. Abraham and W. J. Firth, *J. Opt. Soc. Am. B* **7**, 951-962 (1990).

[116] T. Ackemann and W. Lange, *Appl. Phys. B* **72**, 21-34 (2001).

[117] F. Arecchi, S. Boccaletti, and P. Ramazza, *Phys. Rep.* **318**, 1-83 (1999).

[118] A. C. Newell, *Solitons in Mathematics and Physics* (SIAM, Philadelphia, 1985).

[119] J. Murray, *Mathematical Biology II* (Springer-Verlag New York, 2003).

[120] N. N. Akhmediev, A. Ankiewicz, and J. M. Soto-Crespo, *Phys. Rev. Lett.* **79**, 4047-4051 (1997).

[121] W. J. Firth and P. V. Paulau, *Eur. Phys. J. D* **59**, 13-21 (2010).

[122] S. V. Gurevich, C. Schelte, M. Tlidi, and K. Panajotov, *Proc. SPIE* **9892**, 98921G-98921G-7 (2016).

[123] Y. Tanguy, N. Radwell, T. Ackemann, and R. Jäger, *Phys. Rev. A* **78**, 023810 (2008).

[124] C. Zhan, D. Zhang, D. Zhu, D. Wang, Y. Li, D. Li, Z. Lu, L. Zhao, and Y. Nie, *J. Opt. Soc. Am. B* **19**, 369-375 (2002).

[125] K. W. Chow, I. M. Merhasin, B. A. Malomed, K. Nakkeeran, K. Senthilnathan, and P. K. A. Wai, *Phys. Rev. E* **77**, 026602 (2008).

[126] P. P. Paltani and S. Medhekar, *Optik* **122**, 70-75 (2011).

[127] P. Mandel and M. Tlidi, *J. Opt. B: Quant. Semiclass. Opt.* **6**, R60 (2004).

[128] I. S. Aranson and L. Kramer, *Rev. Mod. Phys.* **74**, 99-143 (2002).

[129] G. Cruz-Pacheco, C. D. Levermore, and B. P. Luce, *Physica D: Nonlin. Phenom.* **197**, 269-285 (2004).

[130] M. C. Cross and P. C. Hohenberg, *Rev. Mod. Phys.* **65**, 851-1112 (1993).

[131] L. A. Lugiato and R. Lefever, *Phys. Rev. Lett.* **58**, 2209-2211 (1987).

[132] W. van Saarloos and P. C. Hohenberg, *Physica D: Nonlin. Phenom.* **56**, 303-367 (1992).

[133] N. Akhmediev, General theory of solitons, in *Soliton-Driven Photonics*, edited by A. D. Boardman and A. P. Sukhorukov, NATO Science Series II, Springer Netherlands, 2001.

[134] C. McIyntre, *Dynamics and Interactions of Cavity Solitons in Photonics Devices*, PhD thesis, Dept. of Physics, University of Strathclyde, 2013.

[135] A. Scroggie, *Spontaneous Optical Patterns in two and four level atomic systems*, PhD thesis, Dept. of Physics, University of Strathclyde, 1995.

[136] V. Skarka and N. B. Aleksić, *Phys. Rev. Lett.* **96**, 013903 (2006).

[137] S. Gangopadhyay and S. N. Sarkar, *Fib. Int. Opt.* **20**, 191-195 (2001).

[138] G. Das and S. N. Sarkar, *Opt. Eng.* **35**, 3413-3417 (1996).

[139] V. M. Nair, S. Sarkar, and S. K. Khijwania, *IEEE Photonics Technology Letters* **20**, 1381-1383 (2008).

[140] R. Kohl, D. Milovic, E. Zerrad, and A. Biswas, *J. Infrared Milli. Terahz. Waves* **30**, 526-537 (2009).

[141] K. Chow, B. A. Malomed, and K. Nakkeeran, *Phys. Lett. A* **359**, 37-41 (2006).

[142] J.-H. He, *Int. J. Mod. Phys. B* **20**, 1141-1199 (2006).

[143] G. H. Weiss and A. A. Maradudin, *J. Math. Phys.* **3**, 771-777 (1962).

[144] H. K. Khalil, *Nonlinear systems* (Prentice Hall, Upper Saddle River, (N.J.), 1996).

[145] D. Puzyrev, S. Yanchuk, A. G. Vladimirov, and S. V. Gurevich, *SIAM J. Appl. Dyna. Sys.* **13**, 986-1009 (2014).

[146] B. Janiaud, A. Pumir, D. Bensimon, V. Croquette, H. Richter, and L. Kramer, *Physica D: Nonlin. Phenom.* **55**, 269-286 (1992).

[147] G. Dangelmayr and L. Kramer, *Mathematical Tools for Pattern Formation* (Springer Berlin Heidelberg, Berlin, Heidelberg, 1998), pp. 1–85.

[148] B. Krauskopf, *AIP Conf. Proceed.* **548**, 1-30 (2000).

[149] S. H. Strogatz, *Nonlinear Dynamics and Chaos* (Westview Press, 2014).

[150] N. Akhmediev and A. Ankiewicz, Dissipative solitons in the complex Ginzburg-Landau and Swift-Hohenberg equations, in *Dissipative Solitons*, edited by N. Akhmediev and A. Ankiewicz, volume 661 of *Lecture Notes in Physics*, chap. 1, Springer-Verlag Berlin Heidelberg, 2005.

[151] S. V. Fedorov, A. G. Vladimirov, G. V. Khodova, and N. N. Rozanov, *Phys. Rev. E* **61**, 5814-5824 (2000).

[152] K. Panajotov and M. Tlidi, *Opt. Lett.* **39**, 4739-4742 (2014).

[153] J. Atai and B. A. Malomed, *Phys. Lett. A* **244**, 551-556 (1998).

[154] N. Bekki and K. Nozaki, *Phys. Lett. A* **110**, 133-135 (1985).

[155] P. Marcq, H. Chate, and R. Conte, *Physica D: Nonlin. Phenom.* **73**, 305-317 (1994).

[156] K. Pushkarov, D. Pushkarov, and I. Tomov, *Opt. Quant. Electron.* **11**, 471-478 (1979).

[157] C. De Angelis, *IEEE J. Quant. Electron.* **30**, 818-821 (1994).

[158] V. Skarka, N. B. Aleksić, H. Leblond, B. A. Malomed, and D. Mihalache, *Phys. Rev. Lett.* **105**, 213901 (2010).

[159] B. Aleksic, B. Zarkov, V. Skarka, and N. Aleksic, *Phys. Scr.* **2012**, 014037 (2012).

[160] H. Leblond, The Davey-Stewartson model in quadratic media: a way to control pulses, in *Soliton-driven Photonics*, edited by A. D. Boardman and A. P. Sukhorukov, pp. 215–218, Springer Netherlands, Dordrecht, 2001.

[161] G. I. Stegeman and M. Segev, *Science* **286**, 1518-1523 (1999).

[162] L. Spinelli, G. Tissoni, L. A. Lugiato, and M. Brambilla, *Phys. Rev. A* **66**, 023817 (2002).

[163] N. N. Akhmediev, V. V. Afanasjev, and J. M. Soto-Crespo, *Phys. Rev. E* **53**, 1190-1201 (1996).

[164] F. Pedaci, P. Genevet, S. Barland, M. Giudici, and J. R. Tredicce, *Appl. Phys. Lett.* **89**, 221111 (2006).

[165] K. Panajotov and M. Tlidi, *Eur. Phys. J. D* **59**, 67-72 (2010).

[166] A. Pimenov, A. G. Vladimirov, S. V. Gurevich, K. Panajotov, G. Huyet, and M. Tlidi, *Phys. Rev. A* **88**, 053830 (2013).

[167] T. Maggipinto, M. Brambilla, G. K. Harkness, and W. J. Firth, *Phys. Rev. E* **62**, 8726-8739 (2000).

[168] Y. Menesguen, S. Barbay, X. Hachair, L. Leroy, I. Sagnes, and R. Kuszelewicz, *Phys. Rev. A* **74**, 023818 (2006).

[169] A. J. Scroggie, J. M. McSloy, and W. J. Firth, *Phys. Rev. E* **66**, 036607 (2002).

[170] T. Ackemann, J. Jimenez, Y. Noblet, N. Radwell, G. Ren, P. V. Paulau, C. McIntyre, G.-L. Oppo, J. P. Toomey, and D. M. Kane, Dynamics and interaction of laser cavity solitons in broad-area semiconductor lasers, in *Nonlinear Optical Cavity Dynamics*, edited by P. Grelu, chap. 3, pp. 41–76, Wiley-VCH Verlag GmbH & Co. KGaA, 2016.

[171] H. Vahed, R. Kheradmand, H. Tajalli, G. Tissoni, L. A. Lugiato, and F. Prati, *Phys. Rev. A* **84**, 063814 (2011).

[172] B. Luther-Davies, Spatial solitons in saturating nonlinear optical materials, in *Soliton-Driven Photonics*, edited by A. D. Boardman and A. P. Sukhorukov, NATO Science Series II, Springer Netherlands, 2001.

[173] P. Parra-Rivas, D. Gomila, L. Gelens, M. A. Matas, and P. Colet, Dynamics of dissipative solitons in presence of inhomogeneities and drift, in *Nonlinear Optical Cavity Dynamics*, edited by P. Grelu, chap. 5, pp. 107–128, Wiley-VCH Verlag GmbH & Co. KGaA, 2016.

[174] C. Weiss, V. Taranenko, M. Vaupel, K. Staliunas, G. Slekys, and M. Tarroja, Spatial solitons on nonlinear resonators, in *Soliton-Driven Photonics*, edited by A. D. Boardman and A. P. Sukhorukov, NATO Science Series II, Springer Netherlands, 2001.

[175] M. J. Steel and C. M. de Sterke, *Phys. Rev. A* **49**, 5048-5055 (1994).

[176] N. G. R. Broderick, D. Taverner, D. J. Richardson, M. Ibsen, and R. I. Laming, *Phys. Rev. Lett.* **79**, 4566-4569 (1997).

[177] M. Tlidi, E. Averlant, A. Vladimirov, A. Pimenov, S. Gurevich, and K. Panayotov, Localized structures in broad area VCSELs: Experiments and delay-induced motion, in *Structural Nonlinear Dynamics and Diagnosis*, edited by M. Belhaq, volume 168 of *Springer Proceedings in Physics*, pp. 417–437, Springer International Publishing, 2015.

[178] G. Tissoni, K. Aghdami, M. Brambilla, and F. Prati, *Eur. Phys. J. Special Topics* **203**, 193-205 (2012).

[179] K. A. Montgomery and M. Silber, *Nonlinearity* **17**, 2225 (2004).

[180] A. V. Porubov and M. G. Velarde, *J. of Math. Phys.* **40**, 884-896 (1999).

[181] L. Cheng-Shi, *Commun. Theor. Phys.* **43**, 787 (2005).

[182] R. Conte and M. Musette, *Physica D: Nonlin. Phenom.* **69**, 1-17 (1993).

[183] K. Nozaki and N. Bekki, *J. Phys. Soc. Jpn.* **53**, 1581-1582 (1984).

[184] L. Hua-Mei, L. Ji, and X. You-Sheng, *Commun. in Theor. Phys.* **44**, 79 (2005).

[185] A. Amani, D. D. Ganji, A. A. Jebelli, M. Shahabi, and N. S. Nosar, *Int. J. Appl. Math. Comput.* **2**, 33-43 (2010).

[186] A. Biswas, *PIER* **96**, 1-7 (2009).

[187] A. Biswas, S. Johnson, M. Fessak, B. Siercke, E. Zerrad, and S. Konar, *J. Mod. Opt.* **59**, 213-217 (2012).

[188] A. Biswas, D. Milovic, M. Savescu, M. F. Mahmood, K. R. Khan, and R. Kohl, *J. Nonlinear Opt. Phys. Mat.* **21**, 1250054 (2012).

[189] A. Bhrawy, A. Alshaery, E. Hilal, K. R. Khan, M. F. Mahmood, and A. Biswas, *Optik* **125**, 4945-4950 (2014).

[190] A. Biswas, D. Milovic, and R. Kohl, *Inverse Probl. Sci. Eng.* **20**, 227-232 (2012).

[191] Z. L. Tao, *Zeitschrift fr Naturforschung A* **63**, 634-636 (2014).

[192] M. F. El-Sabbagh and S. I. El-Ganaini, *Int. Math. Forum* **7**, 2131-2141 (2012).

[193] H. B. S. S. Ganji, D. D. Ganji and S. Karimpour, *PIER M* **4**, 23-32 (2008).

[194] A. Zavyalov, R. Iliew, O. Egorov, and F. Lederer, *Phys. Rev. A* **79**, 053841 (2009).

[195] S. Jana and S. Konar, *Opt. Commun.* **267**, 24-31 (2006).

[196] A. Doelman, *J. Nonlin Sci.* **3**, 225-266 (1993).

[197] M. van Hecke, *Phys. Rev. Lett.* **80**, 1896-1899 (1998).

[198] H. Chate, *Nonlinearity* **7**, 185 (1994).

[199] J. Xiao, G. Hu, J. Yang, and J. Gao, *Phys. Rev. Lett.* **81**, 5552-5555 (1998).

[200] Y. Kuramoto and T. Tsuzuki, **55**, 356-369 (1976).

[201] J. Q. Anderson, R. A. Ryan, M. Wu, and L. D. Carr, *New J. of Phys.* **16**, 023025 (2014).

[202] G. Klinzing, R. Marcus, F. Rizk, and L. Leung, *Pneumatic Conveying of Solids - A Theoretical and Practical Approach* (Springer Netherlands, 2010).

[203] S. Mallick, *Modelling dense-phase pneumatic conveying of powders*, PhD thesis, University of Wollongong, 2009.

[204] R. Pan and P. Wypych, *Powder Handl. Process.* **4**, 167-172 (1992).

[205] M. G. Jones and K. C. Williams, *Part. Sci. Technol.* **21**, 45-56 (2003).

[206] G. Setia, S. Mallick, and P. Wypych, *Powder Technol.* **257**, 88-103 (2014).

[207] G. Setia, S. Mallick, R. Pan, and P. Wypych, *Powder Technol.* **294**, 80-92 (2016).

[208] N. Behera, V. K. Agarwal, M. Jones, and K. C. Williams, *Part. Sci. Technol.* **31**, 136-146 (2013).

[209] C. Narayanan, D. Lakehal, and G. Yadigaroglu, *Powder Technol.* **125**, 122-130 (2002).

[210] J. G. Charney, R. Fjrtoft, and J. Von Neumann, *Tellus* **2**, 237-254 (1950).

[211] Y. M. Chen, S. Rangachari, and R. Jackson, *Industrial & Engineering Chemistry Fundamentals* **23**, 354-370 (1984).

[212] W. D. Fullmer and C. M. Hrenya, *Annu. Rev. Fluid. Mech.* **49**, 485-510 (2017).

[213] E. Fehlberg, *NASA Technical Report* **315**, 1-43 (1969).

[214] L. F. Shampine, H. A. Watts, and S. M. Davenport, *SIAM Rev.* **18**, 376-411 (1976).

[215] M. Villasana and A. Radunskaya, *J. Math. Biol.* **47**, 270-294 (2003).

[216] D. Kalyan, Modelling and solving cancer equation, Master's thesis, Thapar University, 2014.

[217] J. M. Mahaffy, *Quart. Appl. Math.* **40**, 193-202 (1982).